

## INFORMATION TO USERS

This manuscript has been reproduced from the microfilm master. UMI films the text directly from the original or copy submitted. Thus, some thesis and dissertation copies are in typewriter face, while others may be from any type of computer printer.

**The quality of this reproduction is dependent upon the quality of the copy submitted.** Broken or indistinct print, colored or poor quality illustrations and photographs, print bleedthrough, substandard margins, and improper alignment can adversely affect reproduction.

In the unlikely event that the author did not send UMI a complete manuscript and there are missing pages, these will be noted. Also, if unauthorized copyright material had to be removed, a note will indicate the deletion.

Oversize materials (e.g., maps, drawings, charts) are reproduced by sectioning the original, beginning at the upper left-hand corner and continuing from left to right in equal sections with small overlaps.

Photographs included in the original manuscript have been reproduced xerographically in this copy. Higher quality 6" x 9" black and white photographic prints are available for any photographs or illustrations appearing in this copy for an additional charge. Contact UMI directly to order.

ProQuest Information and Learning  
300 North Zeeb Road, Ann Arbor, MI 48106-1346 USA  
800-521-0600

UMI<sup>®</sup>



**University of Alberta**

Intensity modulated arc therapy technique using sliding window dynamic multileaf  
collimation

by

Marc Alexander MacKenzie



A thesis submitted to the Faculty of Graduate studies and Research in partial  
fulfilment of the requirements for the degree of Doctor of Philosophy

in

Medical Physics

Department of Physics

Edmonton, Alberta  
Fall 2000



National Library  
of Canada

Acquisitions and  
Bibliographic Services

395 Wellington Street  
Ottawa ON K1A 0N4  
Canada

Bibliothèque nationale  
du Canada

Acquisitions et  
services bibliographiques

395, rue Wellington  
Ottawa ON K1A 0N4  
Canada

*Your file* *Votre référence*

*Our file* *Notre référence*

The author has granted a non-exclusive licence allowing the National Library of Canada to reproduce, loan, distribute or sell copies of this thesis in microform, paper or electronic formats.

The author retains ownership of the copyright in this thesis. Neither the thesis nor substantial extracts from it may be printed or otherwise reproduced without the author's permission.

L'auteur a accordé une licence non exclusive permettant à la Bibliothèque nationale du Canada de reproduire, prêter, distribuer ou vendre des copies de cette thèse sous la forme de microfiche/film, de reproduction sur papier ou sur format électronique.

L'auteur conserve la propriété du droit d'auteur qui protège cette thèse. Ni la thèse ni des extraits substantiels de celle-ci ne doivent être imprimés ou autrement reproduits sans son autorisation.

0-612-59624-9

**Canada**

**University of Alberta**

**Library Release Form**

Name of Author: Marc Alexander MacKenzie

Title of Thesis: Intensity modulated arc therapy technique using sliding window dynamic multileaf collimation

Degree: Doctor of Philosophy

Year this Degree Granted: 2000

Permission is hereby granted to the University of Alberta Library to reproduce single copies of this thesis and to lend or sell such copies for private, scholarly or scientific purposes only.

The author reserves all other publication and other rights in association with the copyright in the thesis, and except as hereinbefore provided neither the thesis nor any substantial portion thereof may be printed or otherwise reproduced in any material form whatever without the author's prior written permission.



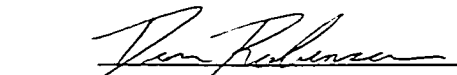
10644 65 Ave.  
Edmonton, AB  
T6H 1V4

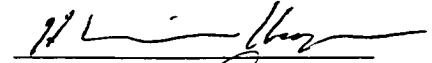
September 26, 2000

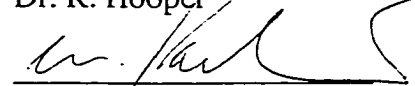
University of Alberta

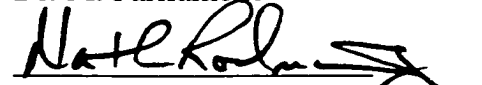
Faculty of Graduate Studies and Research

The undersigned certify that they have read, and recommended to the Faculty of Graduate Studies and Research for acceptance, a thesis **Intensity modulated arc therapy technique using sliding window dynamic multileaf collimation** submitted by **Marc Alexander MacKenzie** in partial fulfilment of the requirements for the degree of **Doctor of Philosophy in Medical Physics**.

  
Dr. D. Robinson

  
Dr. R. Hooper

  
Dr. M. Parliament

  
Dr. N. Rodning

  
Dr. D. Hube

  
Dr. J.J. Battista

September 26, 2000

## *Abstract*

The goal of external beam radiotherapy is to deliver a homogeneous tumouricidal radiation dose to a planned target volume (PTV) while sparing surrounding healthy tissue and avoiding critical structures. The PTV should encompass the tumour as well as subclinical invasions, with margins to account for variations in patient set up and allowance for tumour movement.

Traditional radiation therapy planning techniques employ the application of a number of open rectangular fields to achieve this aim. These fields may be shaped with lead blocks or a multileaf collimator in order to conform better to the target outline. Further improvements in delivery can be realised by employing fields that have non-uniform intensity profiles in order to correct for tissue heterogeneities and surface irregularities, as well as to conform high dose regions as closely as possible to prescribed treatment volumes or conformally avoid critical structures. Using non-uniform intensity fields is known as intensity modulated radiation therapy (IMRT).

While non-uniform intensities have been traditionally realised with static physical attenuators, there is increasing use of dynamic multileaf collimation (DMLC). These can modulate either single incident fields (as in step and shoot or sliding window DMLC), or a series of contiguous transverse slices delivered by a rotating modulated slit beam. The latter technique, called tomotherapy, requires a dedicated unit or a linac fitted with a specialised modulator. Alternately, a highly conformal 3D-dose distribution can be achieved by using multiple concentric arcs with an aperture defined at all angles by a varying MLC shape. This has been referred to as intensity modulated arc therapy (IMAT). IMAT has been touted as an alternative to tomotherapy that requires no specialised equipment beyond what is often present.

A model is presented for an improved IMAT delivery scheme. This involves the determination of multileaf motions as a function of gantry angle, which will produce conformal dose distributions in a single arc. The aperture is delivered using a series of sliding window DMLC segments during gantry rotation. Dosimetric verification of fields delivered, as well as comparisons to other conformal techniques, is presented.

## *Acknowledgements*

I would like to offer my deep and sincere thanks to everyone who supported me throughout my second degree and throughout my research. In general, I would like to thank all those in the Medical Physics Department who provided a supportive, friendly and productive atmosphere. I would also like to thank the faculty and staff of the Physics Department who have been helpful with courses and administrative details. At the risk of forgetting someone, I would nonetheless like to thank in particular:

A number of professors who taught or mentored me during my undergraduate degree, notably Drs. Hussein, Sharp, Lees, DeMille, Ross, Ross and Young.

I would like to thank everyone at Bill's Excavating near Fox Creek, Alberta who helped me out of a terrible mess just prior to the start of this degree (and they fed me a good breakfast, too!).

I would like to thank all those friends who have made my time in Edmonton an enjoyable one. I would like to thank my family (especially my sisters, Veronique and Michele, my uncle Arch, aunt Tib and cousin Alex) who counselled me to stay with my degree when I was having doubts.

I would like to thank all the members of my examining committee for generously agreeing to devote their time to meetings and to reading my thesis.

There are a few people in the Medical Physics department I would like to thank in particular. Thanks to Sherry Connors for her sage and invaluable advice on numerous professional matters. Thanks to Colin Field for all his help, especially with the Helax computer system, and for buying beer at conferences. The biggest thanks in physics goes, of course, to my supervisor Don Robinson for all his guidance, as well as for all his general support.

Finally I would like to thank, most of all, my wife Christine Lesiak and my two sons Alexander and Adrian, for their support, love and understanding throughout my work on this degree. Without their support, none of this could have happened. I offer no thanks to the cats, whom I suspect of secretly plotting against me. *Meow!*  
*Hiss!*

# TABLE OF CONTENTS

Page

<b>CHAPTER 1 INTRODUCTION .....</b>	<b>1</b>
1.1 THE CANCER PROBLEM.....	1
1.2 TREATMENT MODALITIES .....	1
1.3 CONFORMAL THERAPY WITH EXTERNAL BEAM RADIATION.....	3
1.3.1 <i>Box treatments</i> .....	11
1.3.2 <i>Field shaping</i> .....	14
1.3.3 <i>3D CRT</i> .....	17
1.3.4 <i>IMRT techniques and inverse treatment planning (ITP)</i> .....	19
1.3.4.1 DMLC techniques.....	21
1.3.4.2 Tomotherapy.....	21
1.3.4.3 IMAT and its niche.....	22
<b>CHAPTER 2 TREATMENT PLANNING .....</b>	<b>27</b>
2.1 VOLUMES AND TARGET DEFINITION .....	27
2.2 DOSE CALCULATION ALGORITHMS .....	28
2.2.1 <i>Dosimetric function based algorithms</i> .....	31
2.2.2 <i>Monte Carlo based algorithms</i> .....	42
2.2.3 <i>Convolution / Superposition based algorithms</i> .....	42
2.2.3.1 Single convolution approximation.....	46
2.2.3.2 Fourier theory .....	47
2.2.3.3 KERMA, TERMA and Dose deposition.....	48
2.3 THE INVERSE PLAN.....	51
2.3.1 <i>Projection, Radon transform, Filtering and Smoothing</i> .....	53
2.3.2 <i>Initial profile prediction</i> .....	57
2.3.3 <i>Profile refinement through iterative search techniques</i> .....	58
2.3.3.1 Genetic Algorithms.....	59
2.3.3.2 Simulated annealing.....	60
2.3.3.3 Quasi Newton Methods.....	63
2.3.3.4 Computational artefacts .....	65
2.4 PLAN EVALUATION.....	66
<b>CHAPTER 3 BEAM DELIVERY .....</b>	<b>69</b>
3.1 STEP AND SHOOT VS. SLIDING WINDOW TECHNIQUE .....	69
3.2 MLC AND DMLC MODELLING .....	71
3.2.1 <i>The focal and extra-focal source model</i> .....	73
3.2.2 <i>Geometric projection to source plane</i> .....	76
3.2.2.1 Collimator Scatter Factor.....	76
3.2.2.2 Relative Energy Fluence Profile .....	79
3.2.2.3 Dose Output.....	80
3.2.3 <i>Leaf motions</i> .....	84
3.2.3.1 Discrete approximation to continuous motion .....	89
3.2.3.2 Kinematics .....	89
3.3 INTENSITY MODULATED ARC THERAPY.....	91

<b>CHAPTER 4 VERIFICATION .....</b>	<b>93</b>
4.1 DOSIMETRIC CONCEPTS .....	93
4.1.1 <i>Ionising Radiation Fields</i> .....	93
4.1.2 <i>Photon Interactions in Matter</i> .....	97
4.1.3 <i>KERMA and Dose</i> .....	99
4.2 DOSIMETERS .....	100
4.2.1 <i>Film</i> .....	101
4.2.2 <i>Ion chamber and ion chamber array</i> .....	106
4.3 PHANTOMS AND SET-UP USED .....	108
4.4 MEASURING SYSTEMS .....	109
<b>CHAPTER 5 EXPERIMENTAL RESULTS .....</b>	<b>112</b>
5.1 INVERSE PLANNING .....	114
5.1.1 <i>Reducing computational artefacts</i> .....	114
5.2 BEAM MODELLING .....	123
5.2.1 <i>TERMA and dose calculation</i> .....	124
5.2.2 <i>Open field distribution, <math>S_c</math> and dose calculation</i> .....	128
5.2.2.1 $S_c$ values for MLC.....	128
5.2.2.2 Open field energy fluence profiles .....	135
5.2.2.3 Calculation and delivery of single DMLC energy fluence profiles .....	136
5.2.2.4 MLC field dose profiles .....	142
5.2.3 <i>Dynamic field distribution, output and dose calculation</i> .....	150
5.3 ABSOLUTE DOSE FOR DMLC FIELDS .....	153
5.4 VERIFICATION DOSIMETRY .....	156
5.5 DELIVERY OF SIMPLE PLANAR DOSE DISTRIBUTIONS.....	162
5.5.1 <i>Verification of the simple multi-field delivery</i> .....	162
5.5.2 <i>Approximation of continuous motion</i> .....	169
5.5.3 <i>Planning of simple distributions: convergence and calculation times</i> .	173
5.5.4 <i>Delivery of planned profiles</i> .....	178
5.6 DELIVERY OF COMPLEX PLANAR DOSE DISTRIBUTIONS.....	181
5.7 3D MULTI-SLICE DELIVERY .....	192
<b>CHAPTER 6 DISCUSSION, CONCLUSIONS AND FUTURE WORK .....</b>	<b>197</b>
<b>CHAPTER 7 APPENDIX A, CO-ORDINATE SYSTEM OF THE PATIENT</b>	<b>202</b>
<b>CHAPTER 8 BIBLIOGRAPHY.....</b>	<b>203</b>

*List of Figures*

	<u>Page</u>
Figure 1-1 Important components of the treatment head of a typical medical linear accelerator. The linear accelerator and associated structures (not shown) are situated above / before the target. Various photon scattering interactions inside the head are also depicted (arrows and lines). .....	4
Figure 1-2 Schematic of volumes relevant to radiotherapy, as defined by ICRU 50 [ICRU 1993]. .....	5
Figure 1-3 a) An open versus a wedged field b) The use of wedge fields to correct for surface grades. ....	8
Figure 1-4 Correcting for irregular surface contours using either a) bolus or b) retracted missing tissue compensator .....	9
Figure 1-5 Beam shaping performed via static multileaf collimator (MLC) and physical compensator (adapted from Kollar 1996 and Webb 1997) .....	10
Figure 1-6 Open and combinations of open and/or wedged fields: a) single open field, b) parallel opposed open beams, c) a four field box, d) orthogonal wedged pair and e) open and wedge field combination. ....	12
Figure 1-7 Percent depth dose (PDD), dose deposition in a water phantom as a function of depth in phantom, as a percentage of the maximum dose deposited (shown here for a 6MV x-ray beam). ....	13
Figure 1-8 The use of the continuous closing motion of a single secondary collimating jaw to produce a wedged isodose distribution; this technique is known as dynamic wedging. ....	16
Figure 1-9 Various machine parameters that could be varied during a dynamic treatment. ....	18
Figure 1-10 Schematic of the prototype of the tomotherapy unit [Mackie 1993]. ....	23
Figure 1-11 Set up for delivery of proposed IMAT technique. ....	26
Figure 2-1 Extraction of binary mask of region of interest from DICOM CT file. ..	29
Figure 2-2 Treatment of a brain tumour using six non-coplanar wedged fields, planned on a 3D TPS (Gratis™) [Used by permission; ©Sherouse Systems Inc.]. .	30
Figure 2-3 A) Reference dose definition conditions. B) Definition and measurement technique for obtaining the value for the relative dose factor (RDF). ....	33
Figure 2-4 Definition and measurement technique for obtaining the collimator scatter ( $S_c$ ). ....	35
Figure 2-5 Definition and measurement technique for obtaining the value for the phantom scatter ( $S_p$ ). ....	36

Figure 2-6 The definition for the inverse square factor (IS).....	38
Figure 2-7 Definition and measurement technique for obtaining the value for the asymmetric output factor (AOF).....	39
Figure 2-8 Definition and measurement technique for obtaining the tissue phantom ratio (TPR).....	40
Figure 2-9 Dose calculation by Monte Carlo methods using the Peregrine system, as a function of increasing photon histories.....	43
Figure 2-10 The convolution of a TERMA distribution (A) with a polyenergetic dose spread kernel (B) to yield a dose distribution (C).....	44
Figure 2-11 The convolution of a unit value Heaviside function (a) with a Gaussian (b) to yield the 'smeared' distribution (c).....	49
Figure 2-12 Reconstruction of a circular distribution from its projections. The result is shown for a) 2, b) 10, c) 18 and d) 72 out of 72 equally spaced projections.....	55
Figure 2-13 A) a distribution $d(x,y)$ , along with the projection of $d(x,y)$ from an angle $\theta$ , at distances $a$ from the point of rotation. B) The reconstruction of the image in A by forming the 2D Fourier transform at various angles, and then taking the inverse Fourier Transform. ....	56
Figure 2-14 A simple representation of the solution space of a 1D function. There are two minima shown A) a local minimum, of which there are several and B) a global minimum.....	62
Figure 3-1 A simple case of a dynamic treatment STT, shown for a pair of jaws and four control points. ....	72
Figure 3-2 Effective focal and extra-focal source model of linac output. A) The assumed geometry of the source distribution B) Representation of the relative distributions and weighting of the focal and extra-focal sources .....	74
Figure 3-3 Projection of 50% occlusion point for focal and extra-focal sources as a function of jaw position for A) symmetric and B) asymmetric jaw setting.....	77
Figure 3-4 Projections of an example MLC aperture shape from 100 cm SAD onto the focal (red) and extra-focal (blue) source planes, as seen from A) isocentre B) - 4 cm off axis C) -6 cm off axis D) -10 cm off axis .....	78
Figure 3-5 The co-ordinates of a dose calculation point P for a planned dose distribution. This point's position is shown for a given projection relative to isocentre, in terms of a radial distance $p$ and depth difference $\Delta d$ from the isocentre.....	82
Figure 3-6 The tongue and groove effect. ....	88
Figure 4-1 Measurement of the optical density (OD) of a radiographic film. ....	103
Figure 4-2 The characteristic dose to optical density response curve of film, known as the Hunter and Driffield, or H & D, curve. ....	104
Figure 4-3 Experimental set up used for the delivery and verification of IMAT dose distributions. Shown at A) starting position for delivery, B) at midpoint of arc (along with depiction of field area covered), and C) at 90 degrees. ....	110
Figure 5-1 Flowchart for the general calculation process for the planning of the IMAT fields. ....	113

Figure 5-2	Effect of increasing resolution of projections (left) on computational artefact in filtered back projections (right). Resolutions shown: A) 0.5 cm B) 0.2 cm C) 0.1 cm and D) 0.05 cm.....	116
Figure 5-3	Butterworth filter with a cut off value, $\omega_0$ , of A) 2 B) 1.5 C) 1.0 and D) 0.5, alone (at left) and in conjunction with the ramp filter (right); $M=10$ (see Equation 5-14). .....	119
Figure 5-4	Effect of combined high pass (Ramp) and low pass (Butterworth) filter (at left) on the filtered back projection of an ideal disc projection (green) and a discrete disc projection (blue) for cut off values, $\omega_0$ , of A) 1.0, B) 0.5, C) 0.2 ..	121
Figure 5-5	Effect of increasing degree of low pass filtering and smoothing on a discrete disc projection (blue), shown with the ideal projection (green). Cases shown are A) no filtering or smoothing B) just low pass filtering C) same low pass filtering and some smoothing and D) same low pass filtering and increased smoothing .....	122
Figure 5-6	Effect of resampling the non-divergent projection of the incident energy fluence profile, as it would be seen at isocentre. ....	125
Figure 5-7	Phantom co-ordinates for TERMA calculations .....	126
Figure 5-8	Equal areas of extra-focal plane (at level of flattening filter) subtended by different jaw and MLC field size settings.....	129
Figure 5-9	Change in $S_c$ for a variable MLC aperture with jaws fixed at $15 \times 25 \text{ cm}^2$ (green line) versus the change in $S_c$ for variable jaws (MLC fully retracted) over the same aperture variation (blue line). ....	130
Figure 5-10	Relative $S_c$ of rectangular MLC field shapes (red circles with error bars) vs. their respective equivalent square shapes, along with fitted polynomial (blue line). ....	134
Figure 5-11	A) Three measured beam energy fluence profiles: $10 \times 10$ (blue), $10 \times 6$ (green) and an asymmetric $10 \times 4$ (red); measured (green) vs. calculated (blue) values for B) $10 \times 10$ C) $10 \times 6$ D) $10 \times 4$ asymmetric. Secondary collimating jaws are fixed at $15 \times 25 \text{ (XxY) cm}^2$ . ....	137
Figure 5-12	Planned (blue) and measured (green) energy fluence profiles for two single projections (A and B) of required profiles for planar dose deliveries of an elliptical dose distribution. ....	138
Figure 5-13	Planned (blue) and measured (green) energy fluence profiles for two single projections (A and B) of required profiles for planar dose deliveries of an elliptical dose distribution. ....	140
Figure 5-14	Prediction calculation of a beam energy fluence profile of an uncorrected delivery for the penumbral correction, based on a sum of static fields for A) 13 fields, B) 26 fields C) 51 fields and D) 101 fields.....	141
Figure 5-15	Predicted beam energy fluence profile using sum of calculated static fields (blue) compared to measured value (green) for an STT delivery with the $S_c$ correction, but without the penumbral correction.....	143
Figure 5-16	Comparison of desired beam energy fluence profile (red) with the uncorrected profile delivery (green) and A) the $S_c$ corrected profile (blue) and B) the penumbral and $S_c$ correction (blue).....	144

Figure 5-17 Comparison of desired beam energy fluence profile (red) with the uncorrected profile delivery (green) and A) the Sc corrected profile (blue) and B) the penumbral and Sc correction (blue).....	145
Figure 5-18 Beam's eye view of planned leaf motions for profile shown in Figure 5-21A. ....	146
Figure 5-19 Beam's eye view of planned leaf motions for profile shown in Figure 5-22. ....	147
Figure 5-20 Measured (green line) and calculated (blue line) dose profiles for various MLC apertures, namely 10x10 cm <sup>2</sup> , 10x6 cm <sup>2</sup> , 10x4 cm <sup>2</sup> (2 cm off-axis shift), and 10x4 cm <sup>2</sup> (4 cm off-axis shift).....	149
Figure 5-21 Point measurements with error bars (red points, at right) and measured PDDs for open fields of same maximum dimensions (blue line, at right) for various input energy fluence profiles (left).....	151
Figure 5-22 Point measurements with error bars (red points) and measured PDDs for open fields of same maximum dimensions (shown in B, blue line), as well as for an effective field size (shown in C, blue line) for a complex energy fluence profile input (shown in A).....	152
Figure 5-23 A comparison of two film dosimetry system measurements for a single plane delivery of a concave dose distribution using IMAT.....	159
Figure 5-24 A) Measurement of a line dose profile through the experimental phantom for a static 360° arc delivery B) Comparison of dose profile from calibrated film measurement (blue) with in-house TPS (ATP, in green) for an arc distribution to the test phantom.....	160
Figure 5-25 Illustration of the use of Fourier correlation for the alignment of the calculation space with the measured dose region. The shift between the calculation space (A) and measured outline (B) is determined. The planned region of interest is overlaid on the measured distribution (C), and the dose to this region is then extracted (D) for comparison. ....	161
Figure 5-26 Desired dose delivery region (shown in red) in the experimental phantom (shown in green) .....	163
Figure 5-27 Inverse plan based on eight projections designed to deliver a centred elliptical dose delivery, using in-house TPS. Profiles are planned in PC routine and imported into in-house TPS for purposes of comparison. Intensity profiles at gantry angles 0, 45 and 90 degrees are shown in Figure 5-21. ....	165
Figure 5-28 Comparison of two isodose distributions calculated by an in-house treatment planning system (ATP) and by the PC based routine used in this work... ..	166
Figure 5-29 Dosimetric comparison between planned and delivered dose to a central elliptical target. A) Dose difference between planned and delivered in region of interest B) Cumulative dose area histogram of planned (blue) and measured (green) values values C) Histogram of local dose difference between planned and delivered doses. ....	168
Figure 5-30 Continuous arc approximation using 181 individual static fields. The isodose lines are for 100, 80, 60, 50, 40, and 20 percent of the maximum dose (in order, starting at the centre and moving out).....	170

Figure 5-31 Continuous arc approximation as the number of fields goes from a) 4 fields b) 8 fields c) 16 fields d) 24 fields. The isodose lines are for 100, 80, 60, 50, 40, and 20 percent of the maximum dose.....	171
Figure 5-32 Comparison of the 24 beam (dashed line) and 181.....	172
Figure 5-33 Planned region of interest (in red) within the phantom (green) for elliptical dose delivery A) centred about isocentre and B) off isocentre.....	174
Figure 5-34 Inverse plan based on 24 projections for a centred elliptical dose delivery. Relative dose distribution is shown at the A) first iteration, B) eighth iteration and C) last (sixteenth) iteration. D) Relative dose difference shown between planned and desired distributions (units of the axes are pixels).....	176
Figure 5-35 Inverse plan based on 24 projections for an off-centre elliptical dose delivery. Relative dose distribution is shown at the A) first iteration, B) eighth iteration and C) last (sixteenth) iteration. D) Relative dose difference shown between planned and desired distributions (units of the axes are pixels).....	177
Figure 5-36 Results of dose delivery for simple elliptical dose distribution centred about the isocentre. A) dose difference between planned and delivered B) dose difference between planned and delivered in region of interest C) Cumulative dose area histogram of planned (blue) and measured (green) values D) Local error histogram showing local pixel differences between predicted dose and measured dose. ....	180
Figure 5-37 Results of dose delivery for simple elliptical dose distribution centred about a point off the isocentre. A) dose difference between planned and delivered B) dose difference between planned and delivered in region of interest C) Cumulative dose area histogram of planned (blue) and measured (green) values D) Local error histogram showing local pixel differences between predicted dose and measured dose.....	182
Figure 5-38 Planned region of interest (in red) within the phantom (green) for A) an irregular dose distribution and B) a concave dose distribution. ....	183
Figure 5-39 Inverse plan based on 24 projections for an off-centre 'butterfly' shaped dose delivery. Relative dose distribution is shown at the A) first iteration, B) eighth iteration and C) sixteenth and final iteration. D) Relative dose difference shown between planned and desired distributions (units of the axes are pixels).....	184
Figure 5-40 Inverse plan based on 24 projections for a concave dose delivery. Relative dose distribution shown at A) eighth iteration and B) sixteenth and final iteration. C) Relative dose difference shown between planned and desired distributions (units of axes in pixels).....	185
Figure 5-41 Results of dose delivery for a complex off-centre 'butterfly' dose distribution. A) dose difference between planned and delivered B) dose difference between planned and delivered in region of interest C) Cumulative dose area histogram of planned (blue) and measured (green) values D) Local error histogram showing local pixel differences between predicted dose and measured dose. ....	187
Figure 5-42 Results of dose delivery for a complex concave dose distribution. A) dose difference between planned and delivered B) dose difference between planned and delivered in region of interest C) Cumulative dose area histogram of planned	

(blue) and measured (green) values D) Local error histogram showing local pixel differences between predicted dose and measured dose.....	189
Figure 5-43 Local dose error histogram using the desired dose distribution, scaled by predicted dose, for simple dose deliveries A) centred elliptical dose distribution and B) off-centre elliptical dose distribution .....	190
Figure 5-44 Local dose error histogram using the desired dose distribution, scaled by predicted dose, for complex dose deliveries A) irregular 'butterfly' dose distribution and B) concave dose distribution .....	191
Figure 5-45 The desired treatment regions for the multi-planar 3D dose delivery...	193
Figure 5-46 A) Planned single projection (of 24) of required energy fluence profile for a 3D plan (5 slices planned) B) independent software confirmation of net relative intensity resulting from planned leaf motions, assuming simple summed aperture intensity model. ....	195
Figure 5-47 Results from concurrent slice delivery (multi-slice, 3D plan) of highly irregular dose patterns; planned distribution (A), film images (B) and isodose levels (C) for 20 (dk. blue), 40 (lt. blue), 60 (yellow), 74 (red) and 82 (red-brown) cGy. ....	196

*List of Tables*

		<u>Page</u>
Table 1	$S_c$ measured and predicted by extra-focal source model.	132

*List of Abbrs.*

Abbrs.	Abbreviations
ACB	Alberta Cancer Board
AOF	Asymmetric Output Factor
ASCII	American Standard for Character Information Interchange
BEV	Beam's Eye View
CAX	Central Axis
CCI	Cross Cancer Institute
CNS	Central Nervous System
CRT	Conformal Radiotherapy
CT	Computed Tomography
CTV	Clinical Target Volume
DBD	Dynamic Beam Delivery
DICOM	Digital Imaging and Communication in Medicine
$d_{\max}$	Depth of maximum dose
DMLC	Dynamic Multileaf Collimator
dSAR	differential Scatter Air Ratio
EF	Extra-focal
f.s.	field size ( $\text{cm}^2$ )
FWHM	Full Width Half Maximum (cm)
GI	Gastro intestinal
GTV	Gross Tumour Volume ( $\text{cm}^3$ )

ICRP	International Commission on Radiological Protection
ICRU	International Commission on Radiation Units and Measurements
IEC	International Electrotechnical Commission
IMAT	Intensity modulated arc therapy
IMRT	Intensity modulated radiation therapy
ITP	Inverse Treatment Planning
IV	Irradiated volume
KERMA	Kinetic Energy Released per unit Mass (Gy)
MLC	Multileaf Collimator
MRI	Magnetic Resonance Imaging
MU	Monitor Units
MV	Mega Electron Volts (X-ray spectrum)
MeV	Mega Electron Volts (mono energetic photons)
OAR	Organ At Risk
OD	Optical Density
PDD	Percent Depth Dose
PTV	Planning Target Volume
RBE	Radiobiological Effects
RDF	Relative Dose Factor
RTOG	Radiation Therapy Oncology working Group
SAD	Source to Axis Distance (cm)
SAR	Scatter Air Ratio
SBD	Source to Bottom of jaw Distance (cm)

SBL	Source to Bottom of multiLeaf distance (cm)
SCA	Single Convolution Approximation
Sc	Collimator Scatter Factor
SDD	Source to Detector Distance (cm)
Sp	Phantom Scatter Factor
SSD	Source to Surface Distance (cm)
STD	Source to Top of jaw Distance (cm)
STL	Source to Top of multiLeaf distance (cm)
STT	Segmented Treatment Table
TAR	Tissue Air Ratio
TAR0	Tissue Air Ratio for zero field size
TERMA	Total Energy Released per unit Mass (Gy)
TPS	Treatment Planning System
TV	Treated volume (cm <sup>3</sup> )

## *List of Symbols*

D	Dose
E	Energy
K	KERMA
X	Exposure
Z	Atomic number (number of electrons/protons)
$\rho$	Density
$\sigma$	Interaction cross-section
$\Omega$	Solid angle
$\mu$	Linear attenuation coefficient
$\Phi$	Fluence
$\phi$	Fluence rate
$\Psi$	Energy fluence
$\psi$	Energy fluence rate
$\kappa$	Pair production interaction cross-section
$\tau$	Photoelectric effect interaction cross-section
$\omega$	Frequency

## **Chapter 1 Introduction**

### **1.1 *The cancer problem***

Cancer is a class of diseases characterised by the unchecked and improper proliferation of a single cell into a tumourous mass. Broadly speaking, it encompasses four main groups: carcinomas, which are epithelial in origin, sarcomas, which arise from connective tissues, leukaemias which arise from the cells of the bone marrow and lymphomas which arise from the cells of the immune system. Tumours may be benign, that is to say localised and non-invasive to surrounding tissue, or malignant, which may be locally invasive or capable of metastasis (i.e. spreading to distal locations); it is the malignant tumours that are known as cancers. Cancer is responsible for about 40 thousand deaths a year in Canada, and 500 thousand deaths a year in the United States [Rubin 1993].

The typical treatment process for cancer leads from diagnosis, to localisation, to treatment prescription. Once a patient has been diagnosed with a possible cancer their treatment will go through a number of steps. Firstly, the diagnosis must be confirmed. The tumour then is staged based on whether it is a localised or invasive tumour, whether it has local or distal metastatic involvement, and whether there is nodal involvement [Rubin 1993]. Once a tumour has been confirmed, staged, and localised the physician will then decide on the best course of action.

### **1.2 *Treatment modalities***

If the tumour is deemed treatable, then a treatment modality, or combination of modalities, will be selected. If the tumour cannot be treated with a curative intent, then a course of palliative treatment may be prescribed. In broad terms, there are three

main treatment modalities for cancer: surgical intervention, chemotherapy, and radiation therapy. Surgical intervention involves the resection of the primary tumour, as well as perhaps the regional lymph nodes, depending on the staging of the tumour. A round of chemotherapy involves the administration of drugs that seek to inhibit the growth of the tumour by blocking the pathways used by the tumour cells for proliferation. Radiation therapy seeks to deliver a radiation dose to the tumorous region sufficient to kill all tumour cells present. Other experimental modalities (e.g. gene therapy, angiogenesis inhibitors) are experimental and likely many years away from being clinically useful.

Radiation therapy offers a tried and true method of destroying cancer cells. Radiation therapy may be accomplished with external beam radiation, also called teletherapy, and may involve photons, electrons, or heavy particles. It may also be administered by direct insertion of a radiation source into the tumour, through a technique called brachytherapy. It may also involve introducing certain radiopharmaceuticals directly into the patient's bloodstream (such as  $\text{NaI}^{131}$  for thyroid ablation therapy). Cancer therapy is commonly a multidisciplinary effort, often with adjuvant therapies being prescribed to complement each other (e.g. surgical resection, such as a mastectomy, coupled with radiation therapy to kill any remaining cancer cells, and thus to help guard against future recurrence of the tumour).

In the treatment of cancer, radiation therapy can lay claim to being one of the oldest modalities, with radioactivity being used shortly after its discovery by Becquerel in 1896 to treat skin lesions [Carrier and Cormack 1995]. It is no surprise that over the nearly one hundred years which have followed, significant improvements in the techniques, the technology, and results of radiation therapy have been realised. With the invention of the cobalt teletherapy unit here in Canada in the 1950's, external beam radiotherapy became a far more useful tool in the fight against cancer and a new era was ushered in for radiotherapy [Urtasun 1992].

Radiation therapy is used to treat tumours in approximately 55% of all cases here in Alberta [Field 1988], either alone or in conjunction with other treatment modalities, and either with curative or palliative intent. The benefit of modern radiation treatment is evident when one examines the survival figures of those receiving treatment today as compared to those who received treatment in the past [Johns and Cunningham 1983]. Although use has been made of other particles for therapy (e.g. protons, neutrons, and pions) the bulk of treatments are still performed with photons (i.e. X-rays) and electrons. Assuming the treatment prescription involves external beam radiation, there would be pre-treatment imaging for tumour localisation, simulation, and treatment delivery, followed by post-treatment imaging for evaluation of success.

The most common source for external beam radiation is the medical linear accelerator, or linac (see Figure 1-1). These machines are capable of producing high-energy photons (e.g. an x-ray beam spectrum with energies into the tens of MeV), and some are also used to produce high energy electrons. In this work, 6 MV external x-ray beams are used exclusively (note that the MV denotes a polyenergetic beam with a spectrum of Bremsstrahlung photons having a maximum energy of 6 MeV).

### ***1.3 Conformal therapy with external beam radiation***

Treatment planning has, since its inception, always retained a singular goal - the delivery of a tumouricidal dose to a tumour volume while minimising the dose to surrounding healthy tissue and sparing sensitive organs. This goal has become further refined in recent years to include a number of standard defined volumes [ICRU 1993] that are involved in radiotherapy treatment planning (see Figure 1-2).

The gross tumour volume (GTV) is defined as the visible (using imaging techniques) or palpable portion of the tumour mass. The clinical target volume (CTV) includes the GTV, as well as an

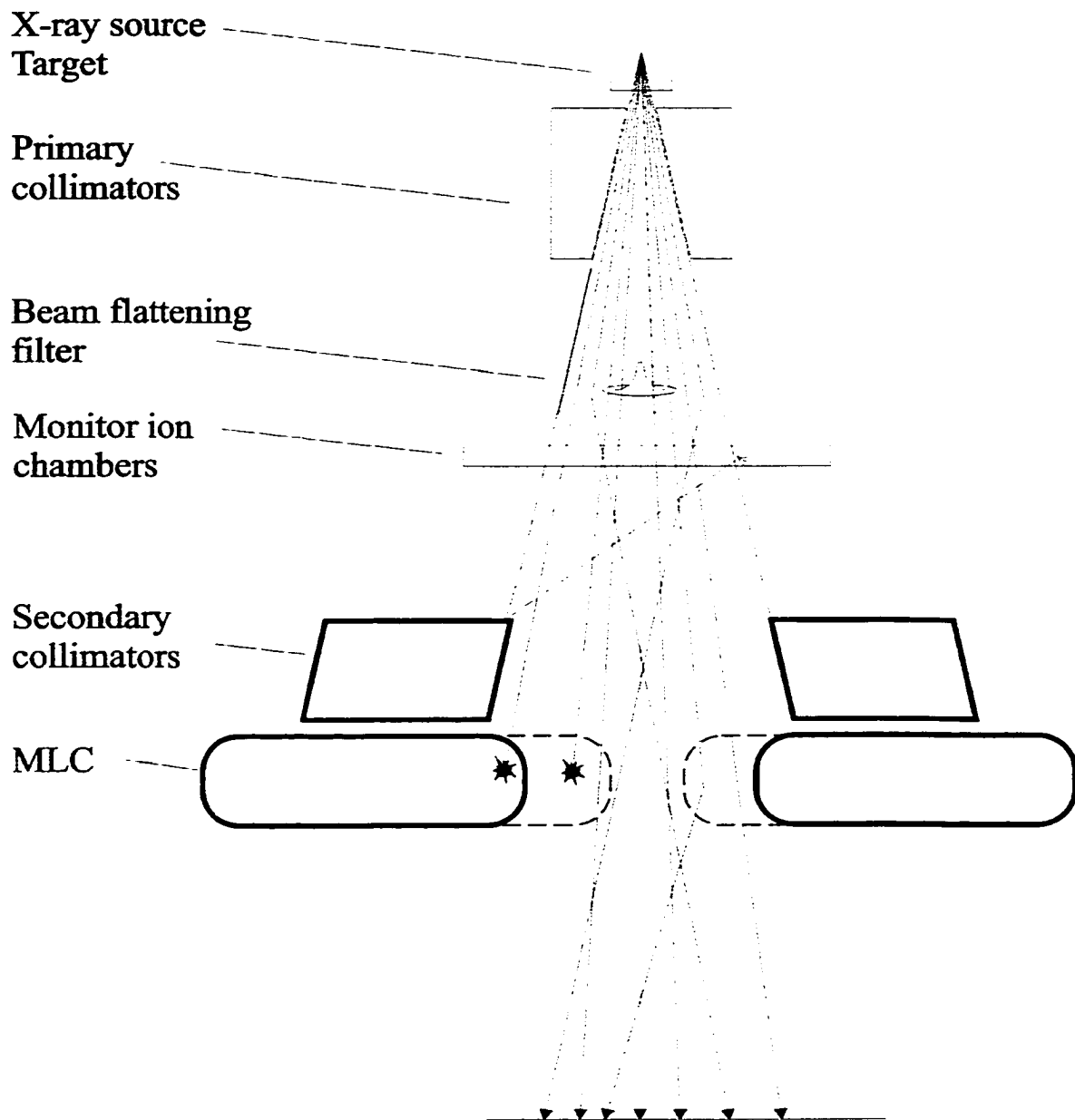


**Figure 1-1** Important components of the treatment head of a typical medical linear accelerator. The linear accelerator and associated structures (not shown) are situated above / before the target. Various photon scattering interactions inside the head are also depicted (arrows and lines).

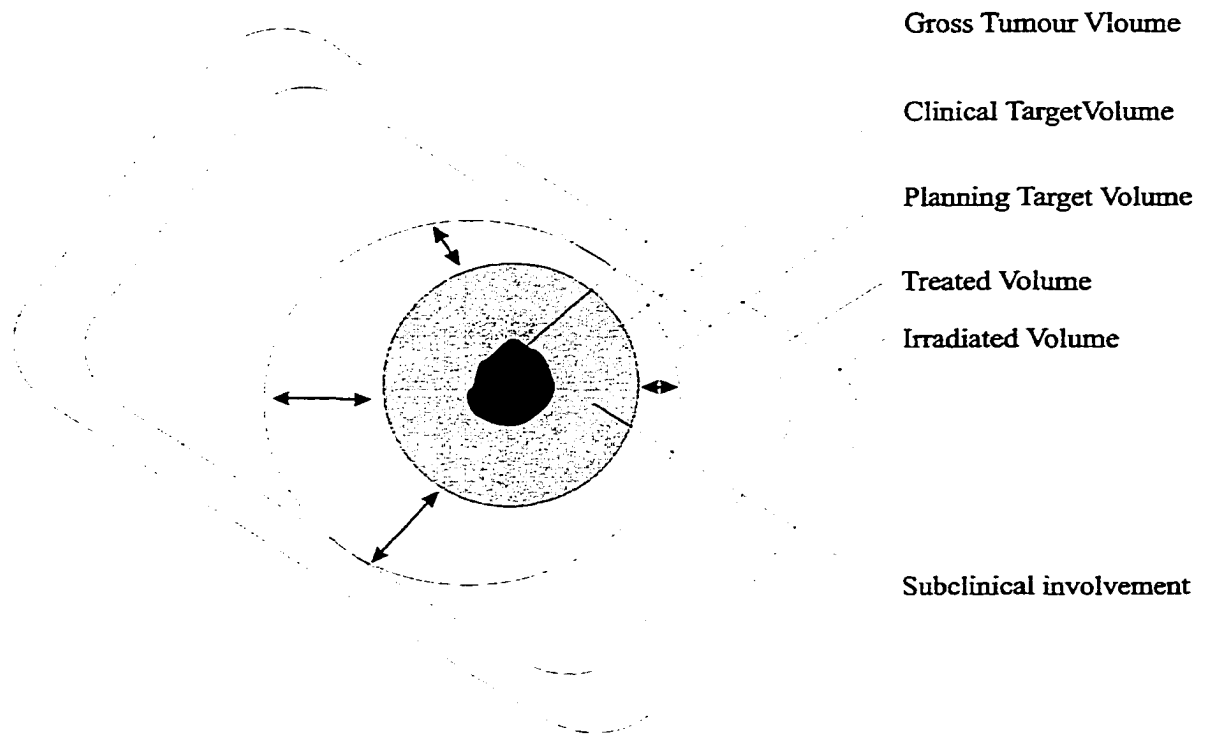


**Figure 1-2 Schematic of volumes relevant to radiotherapy, as defined by ICRU 50 [ICRU 1993].**

area around the tumour which includes the microscopic invasions of tumour cells; this is the volume of clinical concern that must receive a sufficient tumouricidal dose during the course of treatment. The planning target volume (PTV) is a yet larger volume that encompasses the CTV. It is larger than the CTV as the CTV may move relative to beam co-ordinates during the course of treatment due to positioning errors, changes in internal organ positions, or patient movement. This volume must be treated with a tumouricidal dose in order for the CTV to receive a tumouricidal dose, despite the uncertainty in position of the target.

Ideally, the PTV is the volume planned for irradiation, but due to limitations in technique, the treated volume (TV) is the volume that receives a tumouricidal dose. These limitations are in part imposed by the beam shape and arrangement used in an attempt to avoid sensitive structures (e.g. the spinal cord), and also due to unavoidable irradiation of the tissue above and below the tumour along the beam path. The irradiated volume (IV) is that volume which, although not receiving a tumouricidal dose, receives a dose that is considered significant in relation to normal tissue tolerance (e.g. greater than 50% of the dose specified for target dose).

Conformal therapy is the term used to describe the optimisation of radiotherapy delivery to a given PTV, such that the PTV and TV coincide as closely as possible. This optimisation is intended to insure the amount of dose delivered to surrounding healthy tissues and organs at risk is minimised. A concomitant result is that the dose delivered to the tumour may be escalated while keeping the dose to the surrounding tissues below what is judged to be a safe threshold (the tissue tolerance). It has been estimated [Thames 1992] that marked increase in tumour control probability will be realised if the dose can be escalated by 20% over a typical dose prescription.

Advances in external beam radiation therapy over the last several decades have lead to improvements in patient survival figures. Improved dose distributions are

thought to contribute to increased local tumour control and therefore improvements in overall survival [Spirou and Chui 1994, Urtasun 1992]. In order to achieve these improved dose distributions, a typical treatment plan will employ a number of fields from various directions. As well, delivering the desired dose distribution at depth may require the use of non-uniform intensity profiles. This is done to correct for tissue heterogeneities, such as body cavities like the lung or GI tract and surface irregularities (i.e., a non-flat body contour), as well as to conform the high dose regions as closely as possible to the treatment volume. Finally, the treatment must take into account the radiosensitivity of certain organs, notable examples being the spinal cord or parotid glands.

Traditional techniques for conformal beam deliveries involve multiple open and wedged fields<sup>†</sup> (see Figure 1-3), possibly bolus or retracted missing tissue compensators (see Figure 1-4) and beam shaping blocks or multileaf collimator (MLC) shaped fields (see Figure 1-5). Beam delivery is often performed in a coplanar fashion (i.e. beam axes are confined to a single common plane). These modifiers are used either to shape a beam, as in the case of shielding blocks/MLC, or to achieve a differential distribution of radiation across the field. A combination of beam modifying devices and multiple treatment fields is often used. Other techniques have been proposed for the optimisation of beam delivery. These include dynamic collimation (dynamic wedges, dynamic jaws, and DMLC), IMAT, scanning beams, and tomotherapy. Certain techniques are contingent on very specialised equipment (e.g. scanning electron beams, tomotherapy). Others techniques, such as DMLC, IMAT, and dynamic wedge, require only that certain software controls be in place, over and above some common hardware (e.g. MLC). As well, there must be software support for the technique in the treatment planning system (TPS).

Any treatment that involves external beam radiation will require a treatment plan which defines a planning target volume (PTV), as well as the doses that will be

---

<sup>†</sup> beam is attenuated by a wedge shaped filter

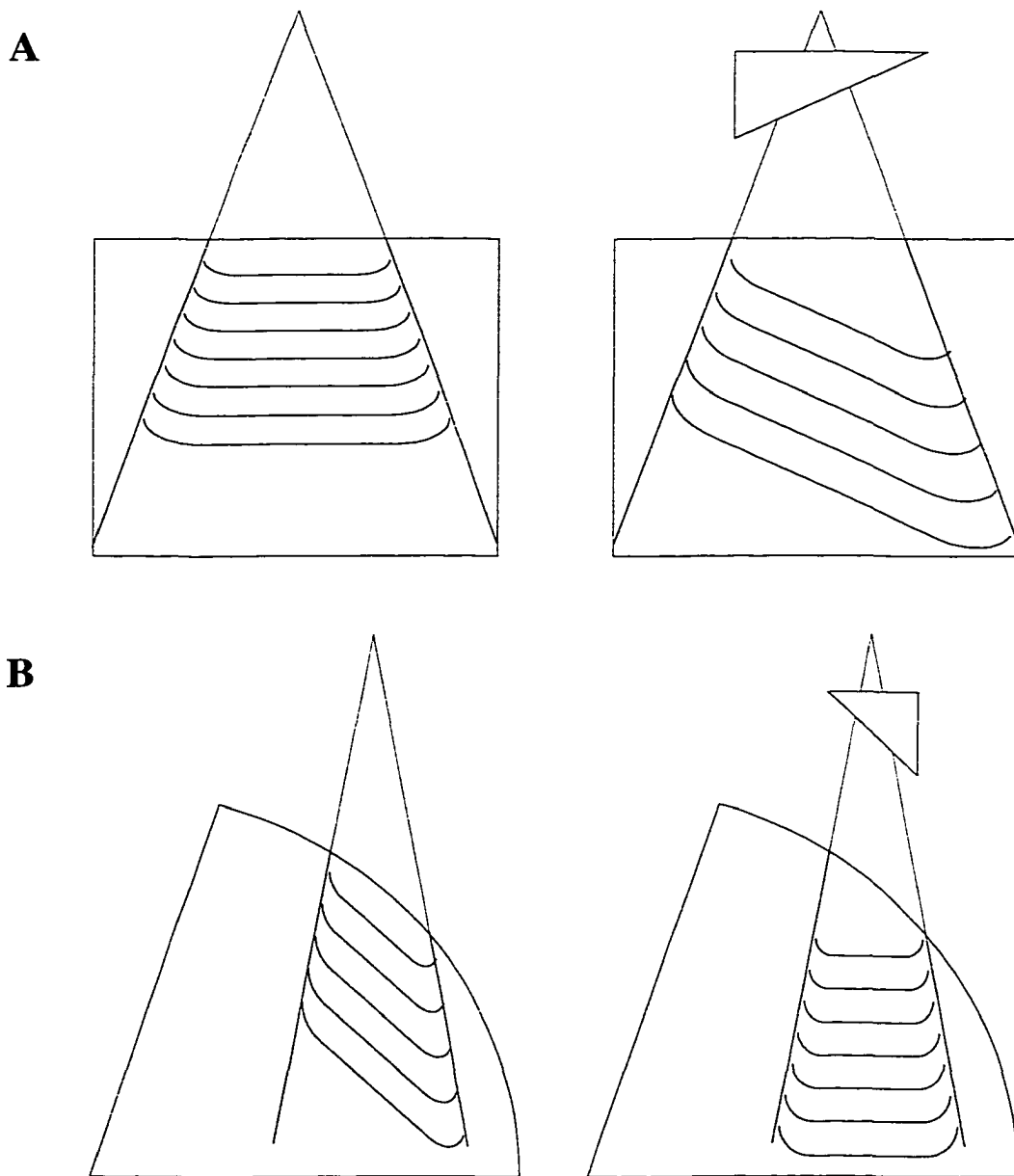


**Figure 1-3 a) An open versus a wedged field b) The use of wedge fields to correct for surface grades.**

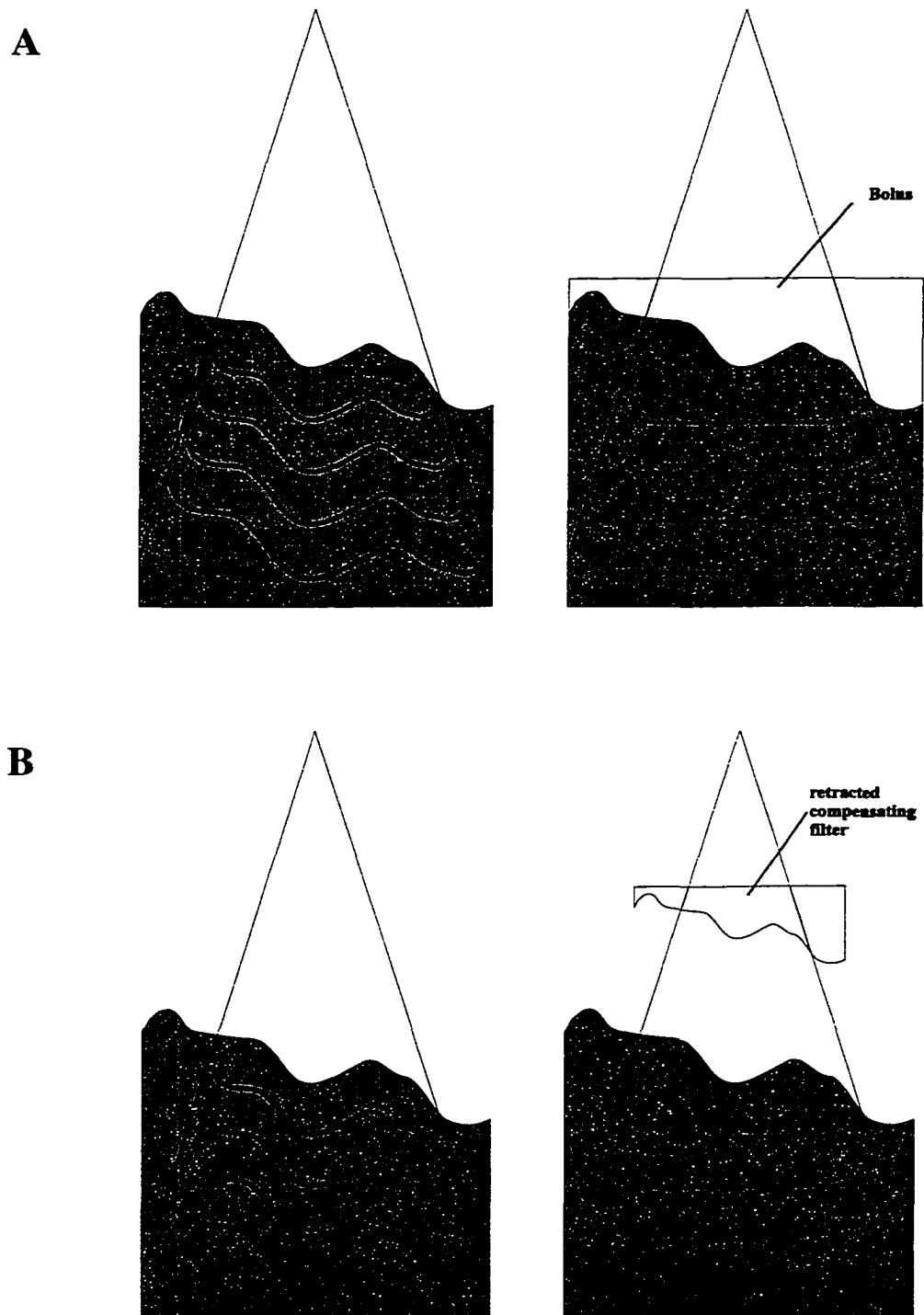


**Figure 1-4** Correcting for irregular surface contours using either a) bolus or b) retracted missing tissue compensator

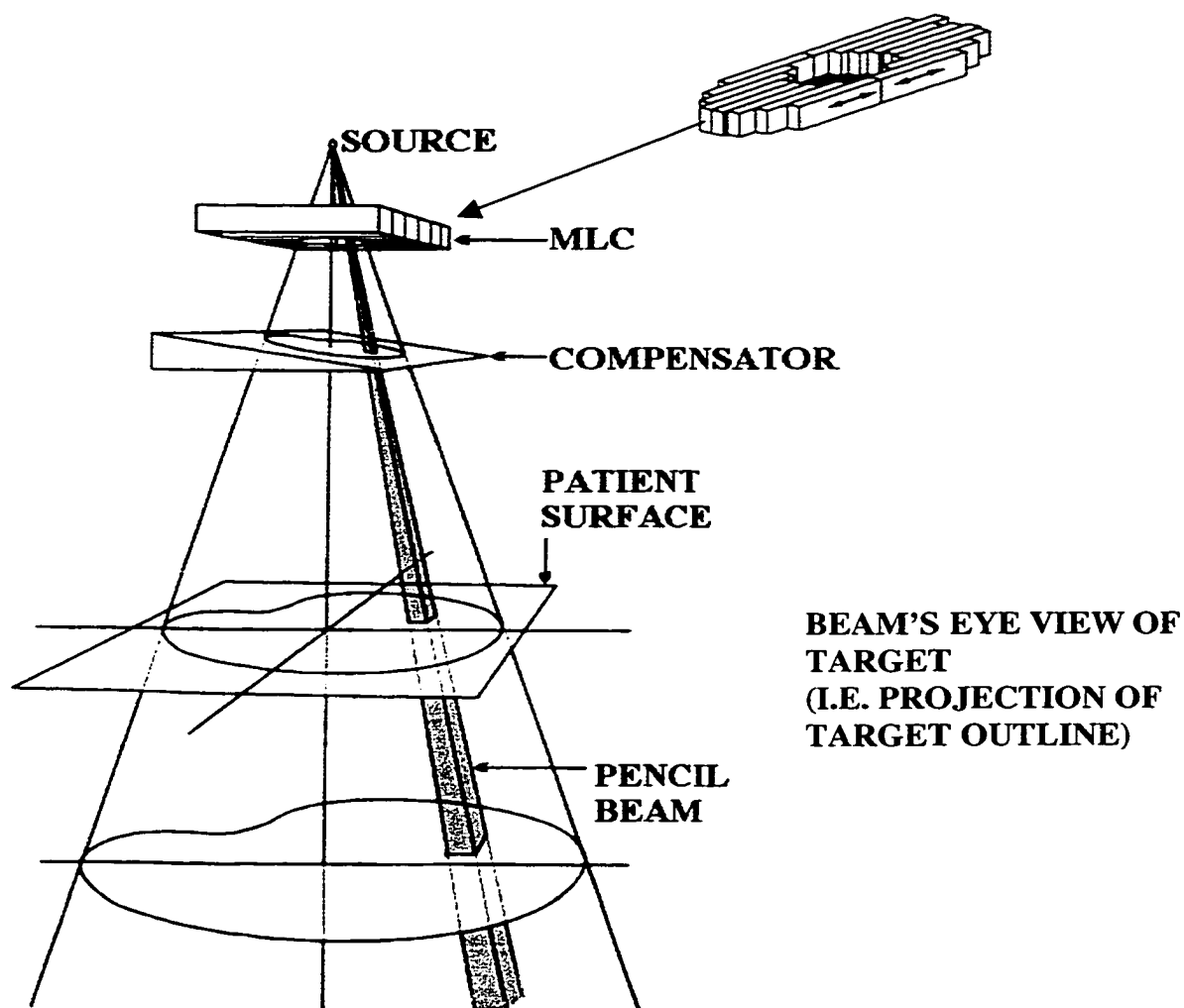


**Figure 1-5** Beam shaping performed via static multileaf collimator (MLC) and physical compensator (adapted from Kollar 1996 and Webb 1997)

delivered to various regions, and the dose delivery schedule (number of fields, dose per field and dose fractionation). The oncologist will define volumes and dose constraints to the organs at risk (OARs). Once the PTV and other desired dose volumes have been defined, the issue becomes one of determining what is sufficient to achieve this dose prescription. Treatment planners will formulate beam arrangements, as well as the shape and relative weighting of each beam in order to achieve the prescribed doses as closely as possible. The consultation of a medical physicist may be required at various stages in this process. This entire process is termed forward planning, and is often iterative. Once the treatment plan is approved, radiation technologists operating a therapy unit (e.g. a cobalt unit or a medical linear accelerator) will execute the plan over a number of treatment sessions (typically 25 daily treatments over 5 weeks).

### 1.3.1 Box treatments

The simplest treatment field is a single open rectangular field. The characteristics of a photon beam from a medical linear accelerator impinging on the flat surface of a homogeneous tissue equivalent volume (see Figure 1-6 a) are well known [Khan 1994; Johns and Cunningham 1983]. Notable features are relatively uniform (flat) dose profiles normal to the beam (within a few percent through the open field), and the decrease of this dose with depth in a well defined manner, defined along the central beam axis (CAX) as characterised by the percent depth dose (PDD) (see Figure 1-7).

For most treatments, multiple fields are used to treat a target volume. There are several advantages to using multiple field arrangements. With the use of several fields, it is possible to achieve a relatively homogeneous dose distribution. As well, it becomes possible to conform the composite dose distribution more closely to the PTV and hence the dose to the tissue outside the PTV can be lowered (e.g. in critical

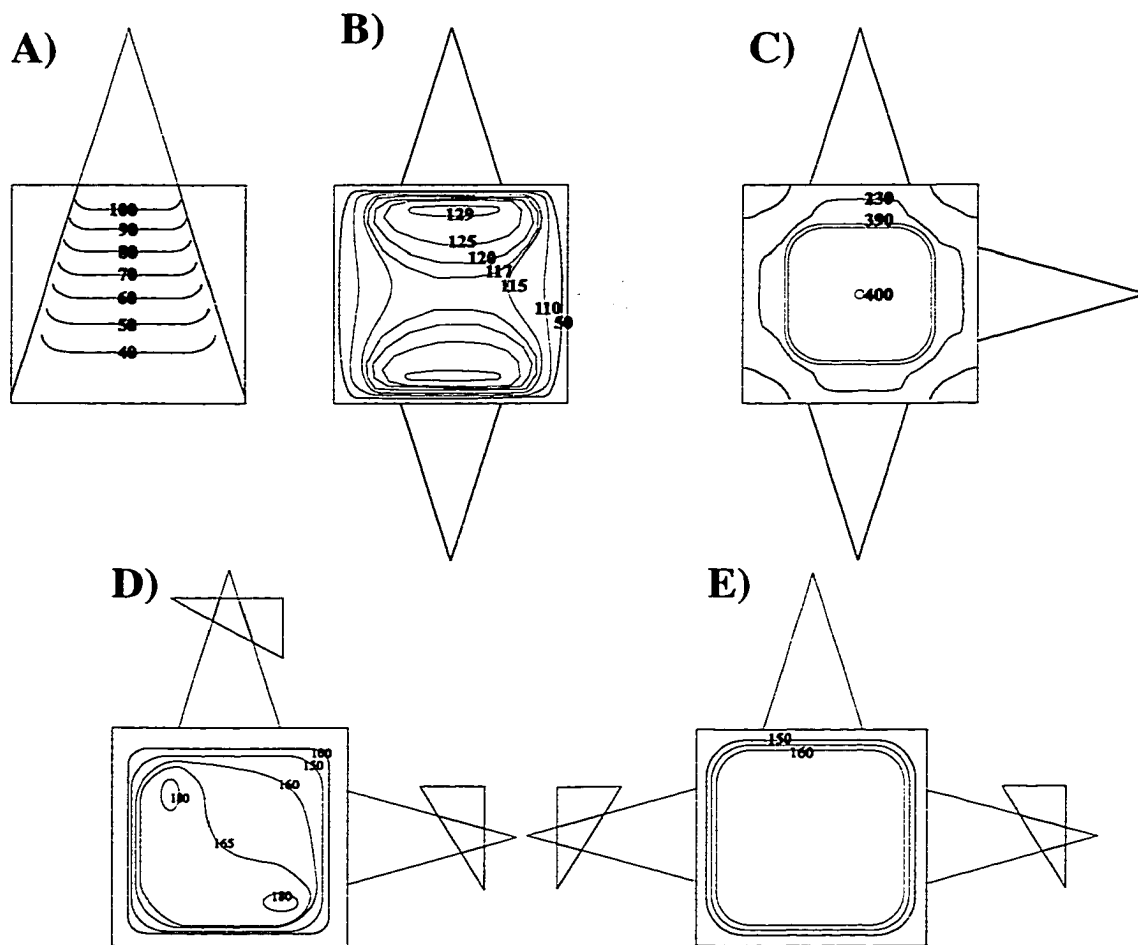


**Figure 1-6** Open and combinations of open and/or wedged fields: a) single open field, b) parallel opposed open beams, c) a four field box, d) orthogonal wedged pair and e) open and wedge field combination.

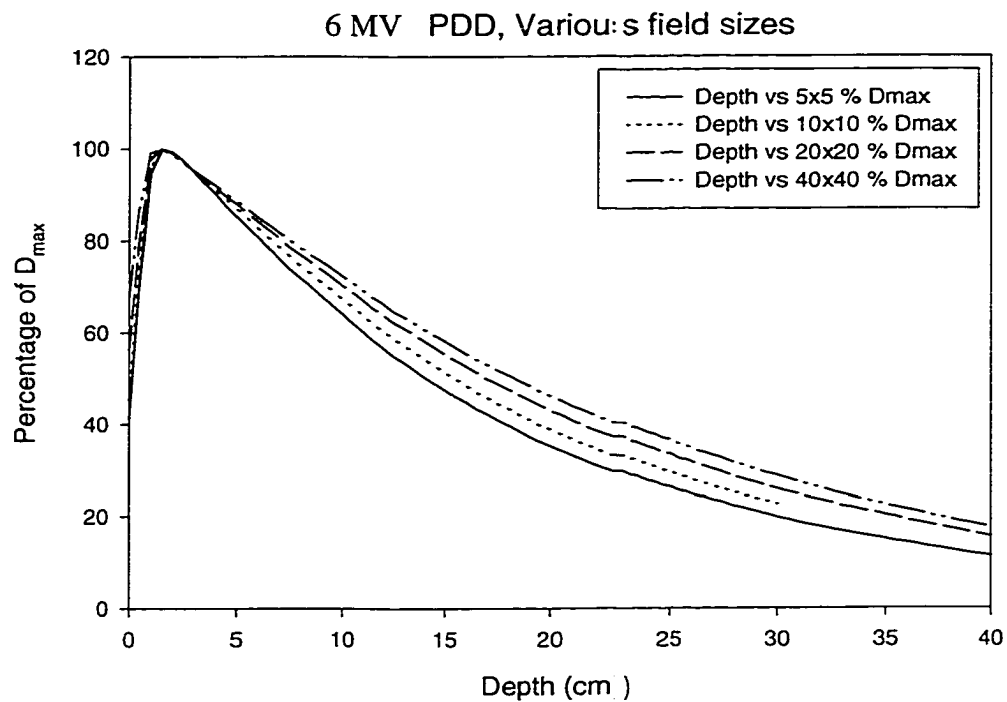


**Figure 1-7** Percent depth dose (PDD), dose deposition in a water phantom as a function of depth in phantom, as a percentage of the maximum dose deposited (shown here for a 6MV x-ray beam).

organs). A relatively simple multiple beam arrangement would be the parallel-opposed open beam pair (see Figure 1-6b).

Slightly more complex set-ups are often used and, through these techniques, varying degrees of dose homogeneity can be realised in the target zone. Using open fields, one can achieve still greater homogeneity with a four-beam arrangement (see Figure 1-6c). For example, a four field box is commonly used in the treatment of prostate cancer.

### 1.3.2 Field shaping

The application of wedged fields is a fairly common example of the use of a beam modifying device. Lead or steel wedges are standard in radiotherapy, and they produce a tilt of 15, 30, 45 and 60 degrees, respectively, in the isodose line passing through the point on the central axis (CAX) at 10 cm depth in a flat water phantom for at least 1/4 of the field size in both directions from the CAX. These wedges find limited use in correcting for one dimensional uniform grades, or internal inhomogeneities with very simple ramp geometries. Wedged fields are often used in combination with open fields and other wedged fields to achieve greater degrees of dose homogeneity about a tumour. Two open orthogonal fields, such as might be used to treat a superficial target volume, result in a very non-uniform dose distribution. By wedging these two fields, the dose homogeneity can be significantly improved (see Figure 1-6d). Open and wedged fields in a T formation may also be employed in a treatment plan to achieve improved dose homogeneity (see Figure 1-6e). Two open and two parallel opposed wedged fields may be combined to achieve a high degree of dose homogeneity, as is often done in some four field prostate treatments where the wedges correct for curvature in the patient's surface.

Bolus is tissue equivalent material that is placed directly against the patient (recall Figure 1-4a). This serves to either provide additional build-up to bring the

depth of maximum dose,  $d_{\max}$ , to the patient surface, or to level out patient contours (thus acting as a missing tissue compensator). The use of bolus as a missing tissue compensator may be undesirable in some cases, namely for megavoltage treatments, as this negates the skin-sparing achieved without bolus present.

In order to correct for more complex surface grades or internal tissue inhomogeneities, retracted compensators may be employed. A retracted missing tissue compensating filter is an irregularly shaped block with a profile varying in one or two dimensions. The thickness as a function of the lateral field co-ordinates ( $x, y$ ) is such that the x-ray beam is attenuated so that the transmitted beam has a relative intensity which is similar, as if it had passed through the 'missing' tissue. The thickness of the filter varies much as would compensating bolus thickness along a coincident diverging ray from the source, in order to correct for the variations in patient contour. Compensators can, in principle, also be shaped to correct for internal heterogeneities.

The drawback of retracted missing tissue compensators is that they are both time consuming and costly to manufacture, and are specific to a single field for an individual patient. As well, they cannot achieve very large dose differences within the compensated field (i.e. intensity modulation), as this is limited by the maximum compensator thickness.

An option in field shaping that has been introduced into the clinic in the last decade is the dynamic wedge (see Figure 1-8). The dynamic wedge seeks to replace standard mechanical wedges with the dynamic motion of one of the collimating jaws during treatment [Kijewski *et. al.* 1978]. Using this technique, one of the collimator jaws of the accelerator is closed during beam delivery in a sweep across the field toward the opposite jaw, until the field is almost closed. The required motion of the moving jaw is pre computed [Kijewski *et. al.* 1978] and these motions are stored as a set of instructions called a Segmented Treatment Table (STT). The STT dictates what discrete positions the jaw should be at, as a function of the total number of monitor

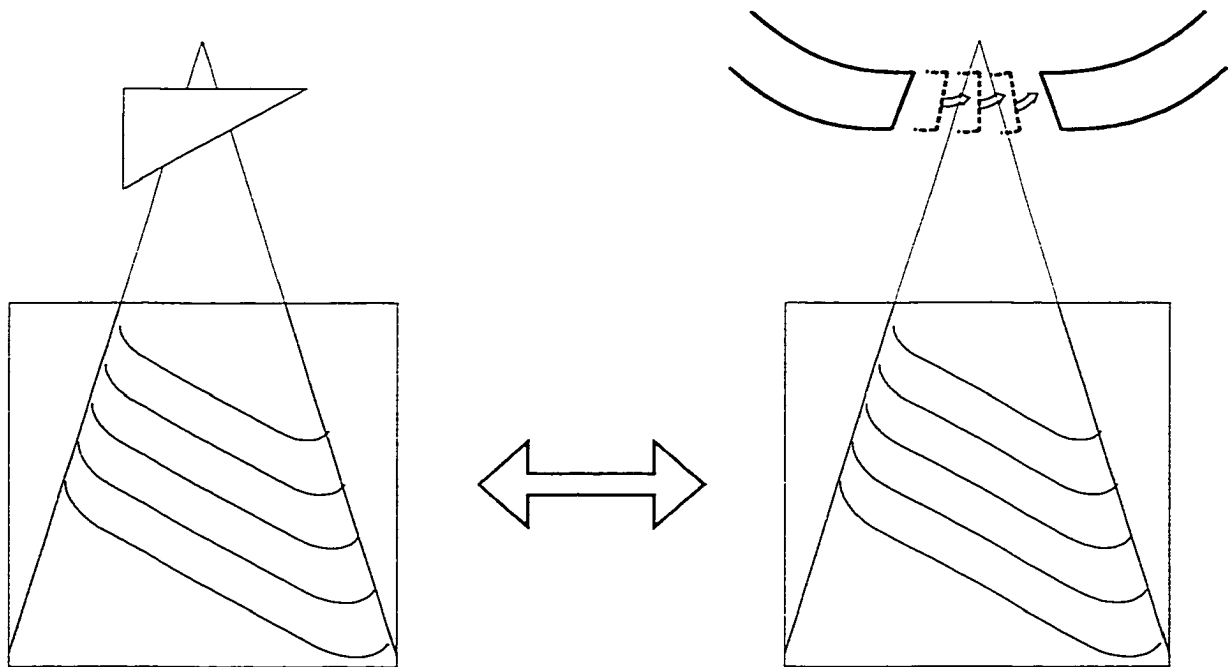


**Figure 1-8** The use of the continuous closing motion of a single secondary collimating jaw to produce a wedged isodose distribution; this technique is known as dynamic wedging.

units (MUs) delivered (see section 2.2.1 for more on MUs), which are related to beam fluence. The mechanical machine settings at these MU values (e.g. the jaw positions) are known as control points. The net effect of these motions, for a dynamic wedge, is to produce a monotonically increasing beam profile in the direction of jaw travel, much as one would achieve with a physical wedge. This motion is used to produce an isodose profile whose wedge angle is the same as that of a physical wedge according to the IEC [IEC 1989] and ICRU [ICRU 1976] definition; indeed any wedge angle may be programmed. This concept has been extended to more complex motions and distribution (see 1.3.4).

The idea of dynamically controlling jaw positions during beam delivery has been extended to other machine parameters (Figure 1-9) in order to achieve more complex dose distributions such as those found in retracted missing tissue compensators, with the possibility of even greater variations or intensity modulation across the field. This shall be reviewed again in section 1.3.4 (IMRT and ITP).

### 1.3.3 3D CRT

With the advent of routine CT and MRI scanning, 3D volumetric patient data have become routinely available. While traditional planning had often been based upon patient contours, single transverse slice (see Appendix A, Co-ordinate system) images or simulator fluoroscopy images, it was proposed that it would be possible to devise better plans based upon volumetric patient data [Goitein 1983, Sherouse 1987]. 3D conformal radiotherapy (3D CRT) is planned based on treating volumes, as opposed to select planes. It exploits non-coplanar beam arrangements, and frequently utilises beam's eye view (BEV) for field shaping. The utility of this approach is still being studied in clinical protocols at numerous institutes, including this one (the Institute where this work was carried out is currently involved in RTOG studies concerning the treatment of prostate cancer and lung cancer using 3D CRT).

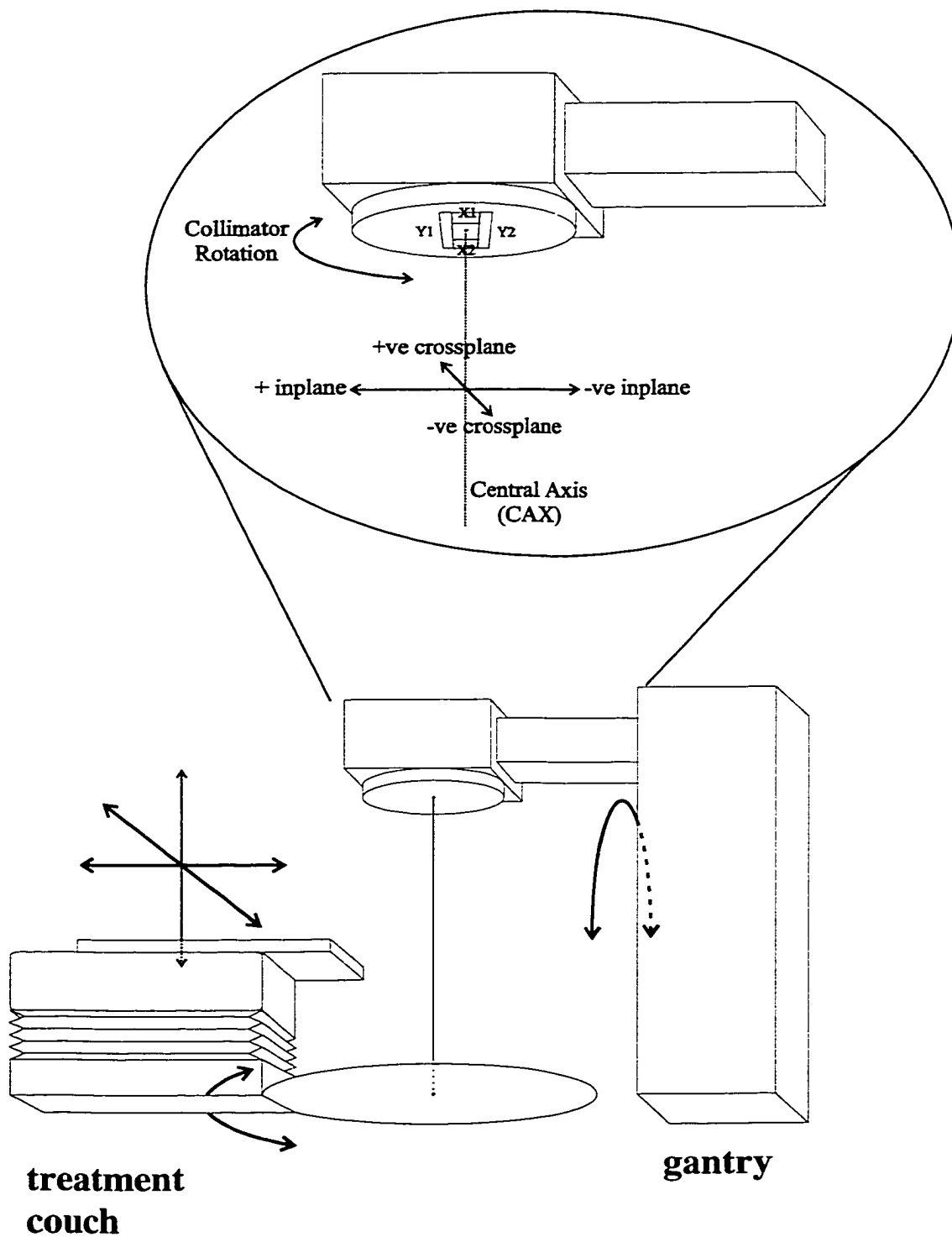


**Figure 1-9** Various machine parameters that could be varied during a dynamic treatment.

It has been suggested, in the case of head and neck tumours, that 3D CRT may play a role in improved deliver to the treatment site [Harari 1995, Roa 1994]. For this site, it has been shown that recurrences most often occur at the site of the original primary tumour [Pigott 1995]. The implication is that failure to control the tumour in the GTV will likely mean failure of the treatment. 3D conformal radiotherapy is one means of dose escalation by having tighter margins and steeper gradients around the tumour site, allowing for a larger dose to be delivered to the treatment site without increasing the normal tissue complication rate.

#### 1.3.4 IMRT techniques and inverse treatment planning (ITP)

Another technique that promises to further increase dose conformity to prescribed target volumes is intensity modulated radiation therapy (IMRT). IMRT refers to a treatment in which beam intensities are non-uniform across a radiation field. They may be changed during the delivery of the field (i.e. a dynamic delivery) or may be the result of static compensators (like a missing tissue compensator). The net result is a non-uniform beam fluence profile. Although technically a missing tissue compensator would qualify as an IMRT delivery, the term IMRT is usually reserved for fields that are optimised to combine with other non-uniform beams to achieve a highly uniform dose in the PTV.

IMRT supplements 3D CRT in a number of important ways. It improves dose conformity, giving the potential for further dose escalation, and therefore possibly even greater local tumour control. It also offers a new possibility in the means of treatment planning. IMRT is usually understood to require not only correcting for internal tissue inhomogeneities, but it also involves a solution to the inverse problem of specifying doses and dose limits to the regions of interest and then back-calculating the required beam profiles to achieve this delivery. The difference between the forward planning of 3D CRT and the inverse planning of IMRT is that in the former, one specifies tentative beams then calculates dose (often iteratively), whereas in the

latter one specifies dose then determines the required beams. As well, the inverse problem may specify limiting the dose to structures at risk, while being more liberal with dose in other regions. This is known as conformal avoidance. The reduced normal tissue dose with IMRT should lead to reduced morbidity and a better quality of life for cancer patients.

Various techniques have been proposed for IMRT delivery. These often include dynamic compensation with the secondary collimators and dynamic multileaf collimator (DMLC). There are also more complex delivery schemes such as scanning electron beams, tomotherapy or intensity modulated arc therapy (IMAT). A number of treatment sites are expected to benefit from IMRT, in particular the breast [Smitt 1997, Hansen 1997], head and neck [Boyer 1997, Verellen 1997, De Neve 1996], lung [Derycke 1997] and prostate [Reinstein 1998]. It was projected that in 1999 there would be 4880 deaths from cancer in Alberta alone [Brasher 1997]. Among these 4880, it was projected that there would be 125 head and neck cases, 1185 respiratory cases, 465 breast cases, 360 prostate cases, and 150 CNS cases. Thus the total number of sites that are expected to benefit from IMRT is 2285, or roughly 47% of all cases. It is therefore evident that research into IMRT techniques may have a large impact on many of the cancer cases treated in Alberta, Canada, and world-wide.

As stated earlier, certain techniques are contingent on having very specialised equipment (scanning electron beam with racetrack microtrons, tomotherapy requiring a specialised unit), but others require only that the software controls be in place (DMLC, IMAT, and dynamic wedge). The initial avenues of research that are of the most interest here are those requiring certain software controls, i.e. 2D dynamic ports with the DMLC and IMAT, or perhaps those requiring some in-house devices and controllers.

### **1.3.4.1 DMLC techniques**

The delivery of 2D dynamic ports with DMLC has been studied by numerous authors [e.g. Mohan 2000, Boyer 1999, Budgell 1999], and the implementation of such methods poses challenging problems for dose modelling, delivery and verification. DMLC software to allow for dynamic control of the MLC has been available for use at the Cross Cancer Institute, where this work has been carried out, since 1999.

There are two main methods of delivering IMRT fields with the multileaf collimator. These are referred to as the ‘Step and Shoot’ method [De Neve 1996, Boyer 1997] and the ‘Sliding Window’ method [Ling 1996, Spirou 1994]. The ‘Step and Shoot’ technique delivers multiple field sub regions by moving the collimating jaws to define the first of these segments, then turning the beam on for a set amount of time, turning the beam off, then repeating this for the subsequent segments. This may be done for a number of segments, on the order of ten to twenty. The ‘Sliding Window’ technique sweeps the opposing leaf pairs across the field with the beam continuously on. Both of these methods are discussed widely in the literature and require slightly different assumptions for the required positions and motions in order to achieve the desired beam intensity profiles in two dimensions.

### **1.3.4.2 Tomotherapy**

Tomotherapy (see Figure 1-10), literally meaning ‘slice therapy’, is conceptually related to imaging. The delivery of treatment is not unlike the delivery of a beam for CT imaging. The difference (aside from beam energy) is that whereas in CT the patient modulates a beam of uniform intensity, in tomotherapy the beam incident on the patient is modulated in order to achieve some desired dose distribution within a transverse slice (see Appendix A, Co-ordinate system).

A current commercial application of the tomotherapy concept is the MIMiC collimator [e.g. Tsai 1999a] This is an “add-on” device for linear accelerators which consists of 20 sets of opposed leaves, each projecting an area of  $1 \times 1 \text{ cm}^2$  at isocentre. These leaves are driven in and out of the treatment beam while the beam gantry rotates about the patient, and so each leaf is responsible for modulating a single ‘pencil beam’ intensity (see Figure 1-5) in a narrow fan beam.

A beta unit of a dedicated tomotherapy unit is due to be installed at the Cross Cancer Institute in the year 2001. It combines a 6 MV compact linear accelerator with a 40 cm wide MLC modulated slit aperture mounted on a CT gantry ring, with megavoltage CT capabilities. The modulated beam is administered in a helical delivery; that is to say the linear accelerator rotates in a spiral fashion about the patient while the treatment table (see Figure 1-10) is translated through the ring.

#### **1.3.4.3 IMAT and its niche**

A technique has been proposed [Yu 1995] for the delivery of conformal fields which has been dubbed intensity modulated arc therapy (IMAT). Although this technique is touted as an alternative to tomotherapy, it has only recently begun to receive more attention [Cotrutz 2000].

IMAT, as it was originally proposed, involved the delivery of a rotational IMRT delivery, similar to that of a tomotherapy unit. The required beam fluence profiles would be delivered over a number of full  $360^\circ$  rotations about the patient (three to five, perhaps more), using a variable MLC aperture to define different beam intensity levels on each pass.

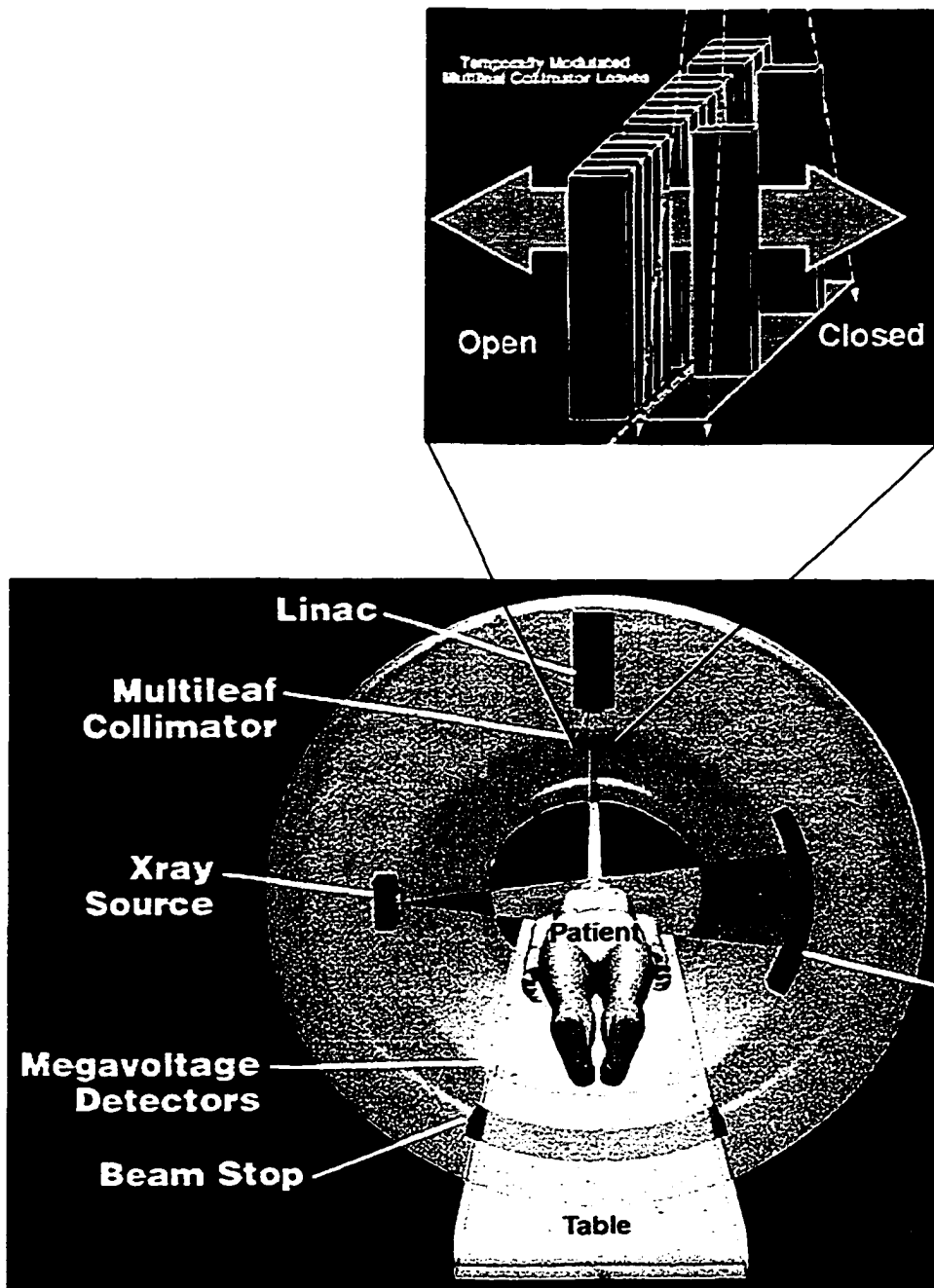


**Figure 1-10** Schematic of the prototype of the tomotherapy unit [Mackie 1993].

This dose delivery technique may be advantageous in terms of normal tissue sparing for certain sites [Zaider 1998]. One reason for early lack of interest may be due to other simpler techniques being widely available, although more complex dose distributions are achievable with IMAT. Other reasons may be the lack of planning systems designed to handle this kind of delivery. As well, the time required to deliver these plans is not short. The work presented here will show that a modified version of this technique provides a potentially attractive solution, in terms of intuitive treatment planning, delivery time, and the use of existing technologies.

Some minor variations on arc therapy have also been investigated [Cotrutz 2000], but the technique presented in this thesis is unique. It combines a single gantry rotation, instead of the multiple arcs suggested by Yu, and using a sliding window technique, instead of variable MLC apertures, to deliver a highly conformal dose distribution. The number of passes for Yu's technique could even double for a non-contiguous mass (e.g. a bifurcated tumour), while the method developed here still uses only one arc.

The major hypothesis of this work is that it is possible to deliver an IMAT rotational treatment in a single gantry pass, instead of the multiple passes invoked by Yu, regardless of the complexity of the tumour. In this respect, the proposed delivery is similar to tomotherapy. The advantage of this technique over tomotherapy, however, is that it requires a single pass for all slices (instead of one rotation per slice treated), and it is contingent only on commonly available hardware (as well as some specialised software). One major difference between this technique and that of Yu is the incorporation of the sliding window MLC for delivery of the required profiles. The leaves of the MLC will make a unidirectional sweep, with a varying leaf separation, from numerous projections on the phantom, as the gantry is rotated about the patient or measurement phantom (see Figure 1-11).

For dynamic beam delivery, the Institute where this work was carried out currently has, in addition to the enhanced dynamic wedge, the Varian dynamic beam delivery (DBD) toolbox. The DBD toolbox is a limited release piece of research software, which allows for the modulation of various machine parameters while the beam is on. As well, this Institute has taken delivery of DMLC software that will allow for the modification of segmented treatment table (STT) files for the MLC, which is essential to the proposed IMAT delivery.

The theoretical underpinnings of this work are presented in three major sections in chapters two, three and four. Firstly, chapter two focuses on the process of the inverse treatment planning methods used in this work. Chapter three examines the beam modelling and calculations used in determined the leaf motions required to achieve the plans calculated (as per chapter two). Finally, chapter four examines the techniques employed in the verification of the IMAT deliveries.

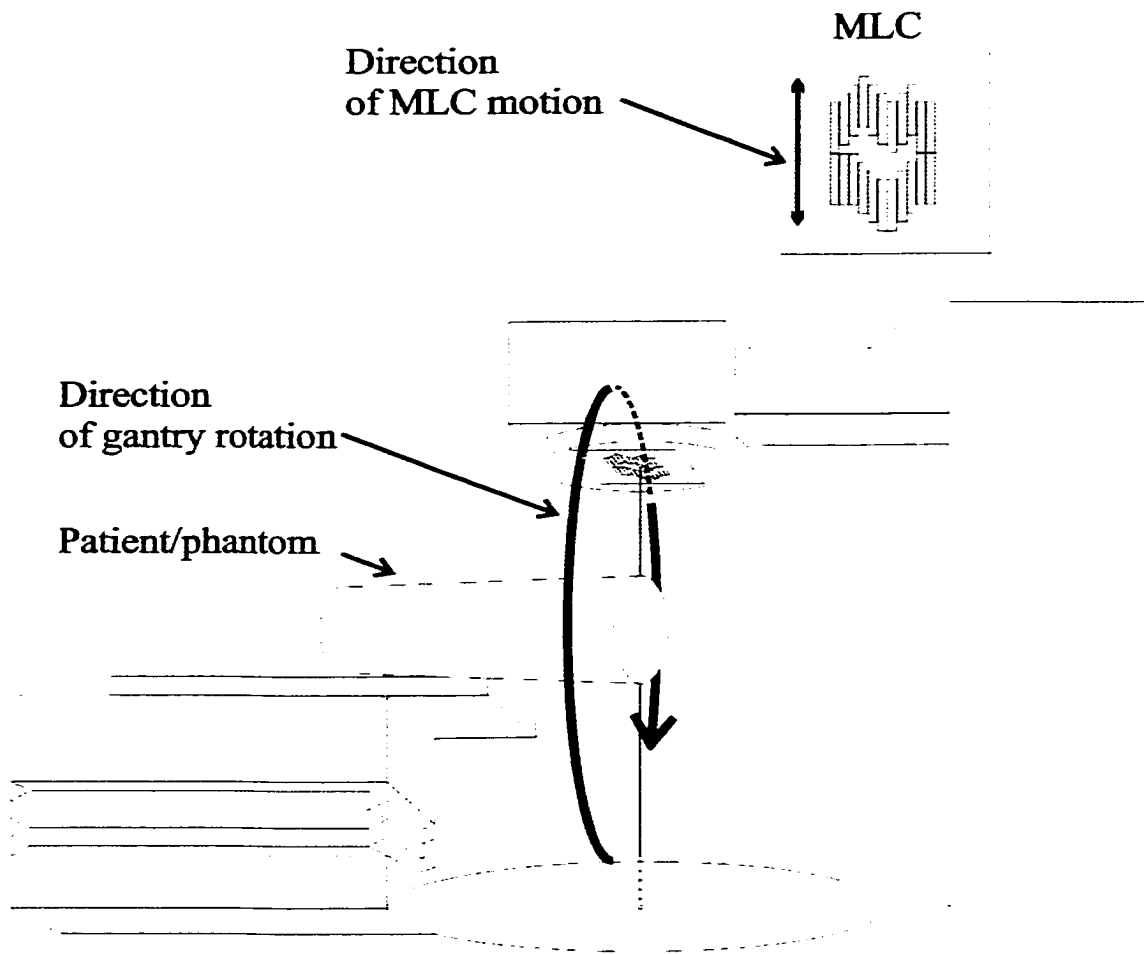


**Figure 1-11** Set up for delivery of proposed IMAT technique.

## **Chapter 2 Treatment planning**

### ***2.1 Volumes and Target definition***

There are numerous criteria for the selection of a PTV larger than a CTV, including patient motion and inter-treatment set up variations. These factors are not considered here -- it is assumed in this work that the PTV has been correctly specified, and any other volumes of interest (e.g. OARs) have also been defined appropriately. The focus of this work will be the planning, delivery and verification of the prescribed dose to the PTV.

Volume and external contours definition was carried out in one of two ways. Either planning was performed on an idealised shape and computer generated phantom contour, or the phantom of interest was scanned using a CT scanner and the external contour and treatment volumes were defined on a treatment planning workstation.

A user interface was developed for use with a PC based planning program, developed for this work, using a commercial math package (Matlab, The Math Works Inc., v5.3). A planner may specify, in the case of idealised shapes, phantom, tumour or critical structure shapes at some desired pixel resolution, and at a given location with respect to isocentre. The shapes allowed were rectangles and ellipses, although it was also possible to introduce arbitrary contours in the planning space using a computer mouse.

For planning on the clinical planning workstation, CT images were transferred from the CT scanner using the Digital Imaging and Communication in Medicine (DICOM) protocol to a planning workstation where contours were introduced to define external limits, as well as a desired treatment region. These modified DICOM images were then transferred to a PC and introduced using a user supplied code into

the PC planning environment (see Figure 2-1). This entailed converting the outlines of the external contour and any regions of interest into 2D matrices of ones and zeros (referred to as binary maps). Similar binary maps were employed with the user-defined shapes.

## **2.2 Dose calculation algorithms**

Traditional forward planning (see 1.3.4) entails the design of beams on a TPS in an attempt to achieve the homogeneous prescribed dose to the PTV, with possible subsequent iterative modification by the planner to improve the initial result. The TPS dose calculation routine that converts these beam shapes and weights into a dose distribution may be of several forms. Treatment planning systems are of two main types, namely 2D and 3D.

Two dimensional treatment planning (2DTP) was the norm until the late 1980's, and early 1990's, and is still in some use today, although this is declining. The chief reason for its continuance is the widespread familiarity with this well established technique. 2DTP assumes that, for the purposes of planning a treatment, the tumour lies in a single plane and that the volumes and internal structures extend unchanged in the dimension orthogonal to that plane. Frequently, the treatment beams used are assumed to have their central axes in that same plane. Critical structures, which lay outside this plane, may be accounted for by calculating the dose in an adjacent transverse slice. The extension to several adjacent slices is sometimes referred to as "2.5 D" treatment planning. This type of planning may be adequate for certain routine treatment plans.

Three dimensional treatment planning (3DTP) is based on volumes rather than on planar slices [Goitein 1983, Sherouse 1987], and it is not simply a multi-planar version of 2DTP (see Figure 2-2). The dose calculation algorithms are of a true 3D nature. Implementation of a 3D TP system requires the collection of a set of 3D

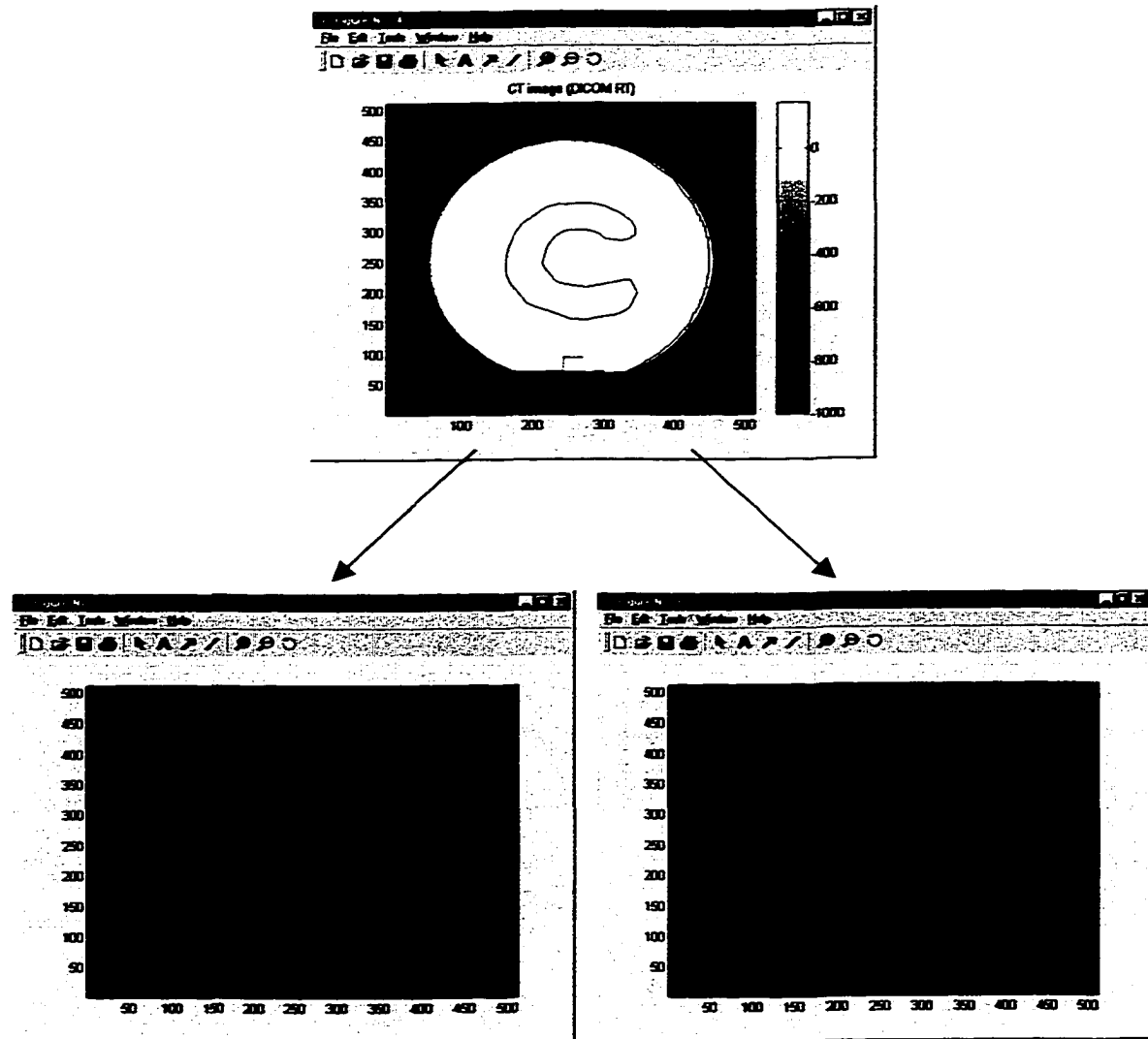


**Figure 2-1** Extraction of binary mask of region of interest from DICOM CT file.

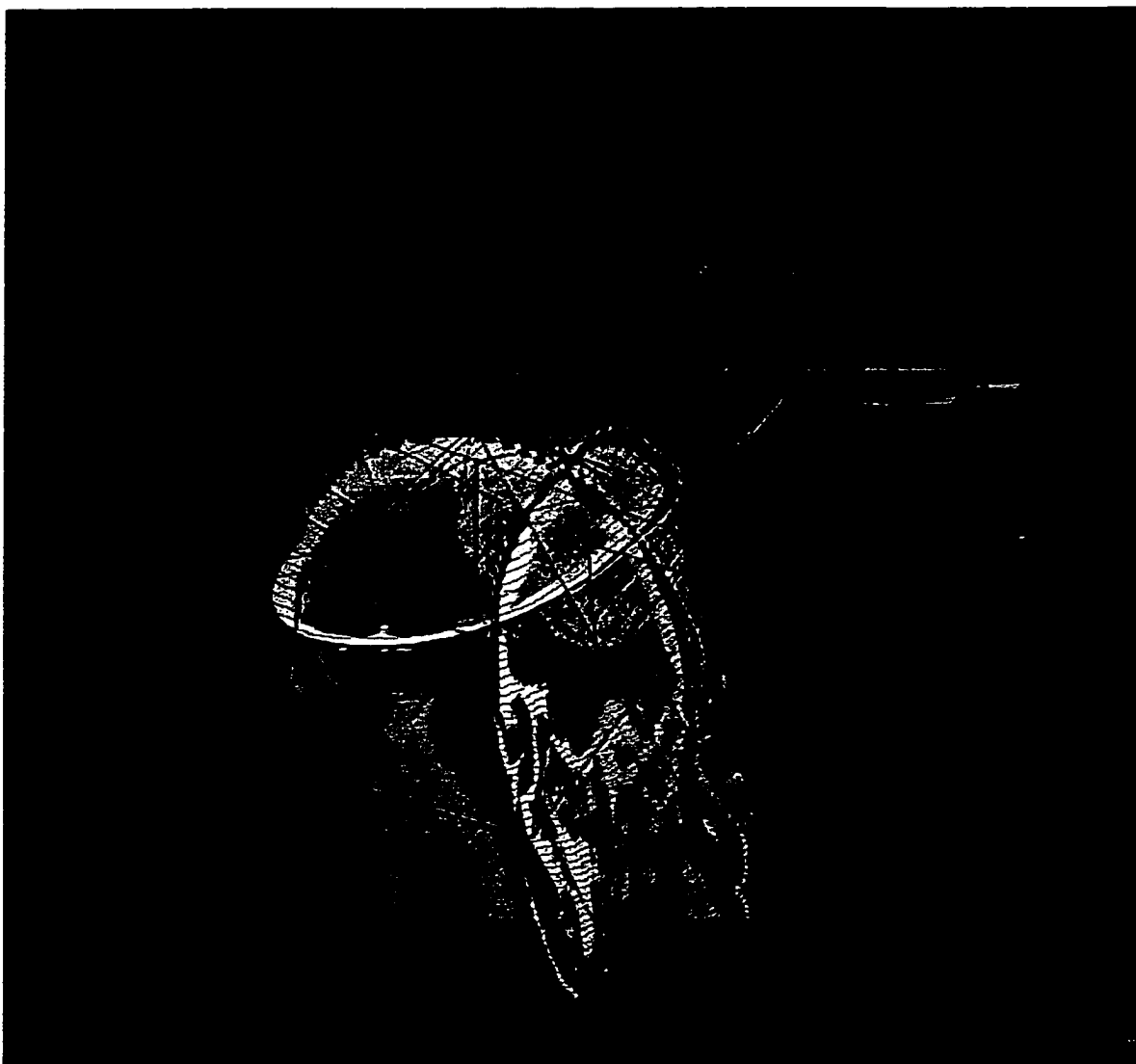


**Figure 2-2** Treatment of a brain tumour using six non-coplanar wedged fields, planned on a 3D TPS (Gratis™) [Used by permission; ©Sherouse Systems Inc.].

commissioning data (i.e. measured beam data), and empirical factors and information regarding the treatment unit's geometry. The 3D TP system also requires a different set of patient data over that of the 2D system; whereas the latter may require a single transverse slice, the former requires a full set of CT data (contiguous planes whose separation is small enough to give accurate 3D spatial information).

Both 2D and 3D treatment planning systems may use a variety of dose calculation algorithms, with various correction factors for computing dose perturbations due to field shaping and inhomogeneities. An overview of these methods is presented in section 2.2.1.

For clinical applicability it is necessary to compute dose in non-homogeneous media. Heterogeneity corrections of various sorts have been proposed over the years. These include the Batho power law, ratio of TPRs and kernel scaling (for convolution calculations). The effect of heterogeneities has not been modelled in this work, as this is seen as just a further refinement to dose calculation, and extraneous to the main thrust of the thesis.

### 2.2.1 Dosimetric function based algorithms

There are numerous dosimetric function based calculation algorithms that are used in treatment planning. These schemes use various empirical factors to implicitly account for particle transport. The measurement and definition of various dosimetric factors are outlined in Figure 2-3 through to Figure 2-8, and further explained below.

The output of each medical linear accelerator, or linac, is calibrated to deliver a known radiation dose to a reference point, under certain reference conditions (see Figure 2-3a). The dose is measured in Grays, which are Joules per kilogram (see end of section 4.1 for further discussion). The machine output is most often set such that one centi Gray (cGy) of dose is deposited per machine unit of output (typically known

as a monitor unit, or MU; these units correspond to arbitrary units of ionisation in the beam monitor chamber, shown in Figure 1-1) at the reference point, under reference conditions.

The reference point is most often located at isocentre (the common point of rotation for the gantry, collimator and couch; see Figure 1-9), which is usually 100 cm source to axis of measurement distance (SAD) for a linac (where the source is the x-ray target; see Figure 1-1). The reference point is sometimes located at the depth of maximum dose,  $d_{max}$ , in the measurement medium (see Figure 1-7). The secondary collimators (Figure 1-1) define the reference radiation field to be 10 cm by 10 cm at the plane of isocentre. See Figure 2-3a for a graphic representation of this set up. As an example, for a 6 MV beam,  $d_{max}$  is roughly 1.5 cm, so the distance from the source to the surface of the measurement medium, the SSD, is 98.5 cm (since SAD=100 cm).

A calibration factor, denoted as K, typically set to a value of 1 cGy / MU for the reference conditions, and so the conversion of MU to dose may be given by

$$K = \frac{D(d_{max}, SAD = 100cm, fs_{ref})}{MU} \quad \text{Equation 2-1}$$

where D is the dose to the reference point (SAD is 100 cm, depth is  $d_{max}$ ) and the field size is the reference size ( $fs_{ref}$ ), usually 10 x 10 cm<sup>2</sup>.

Dosimetric factors are employed to determine the dose to points other than the reference point, for field sizes other than the reference field size. As a starting point, if the point of measurement is kept as 100 cm SAD and  $d_{max}$ , but the field size changes, then the change in dose to the measurement point can be determined using a measured factor called the relative dose factor, or RDF (see Figure 2-3b). The RDF can be defined as

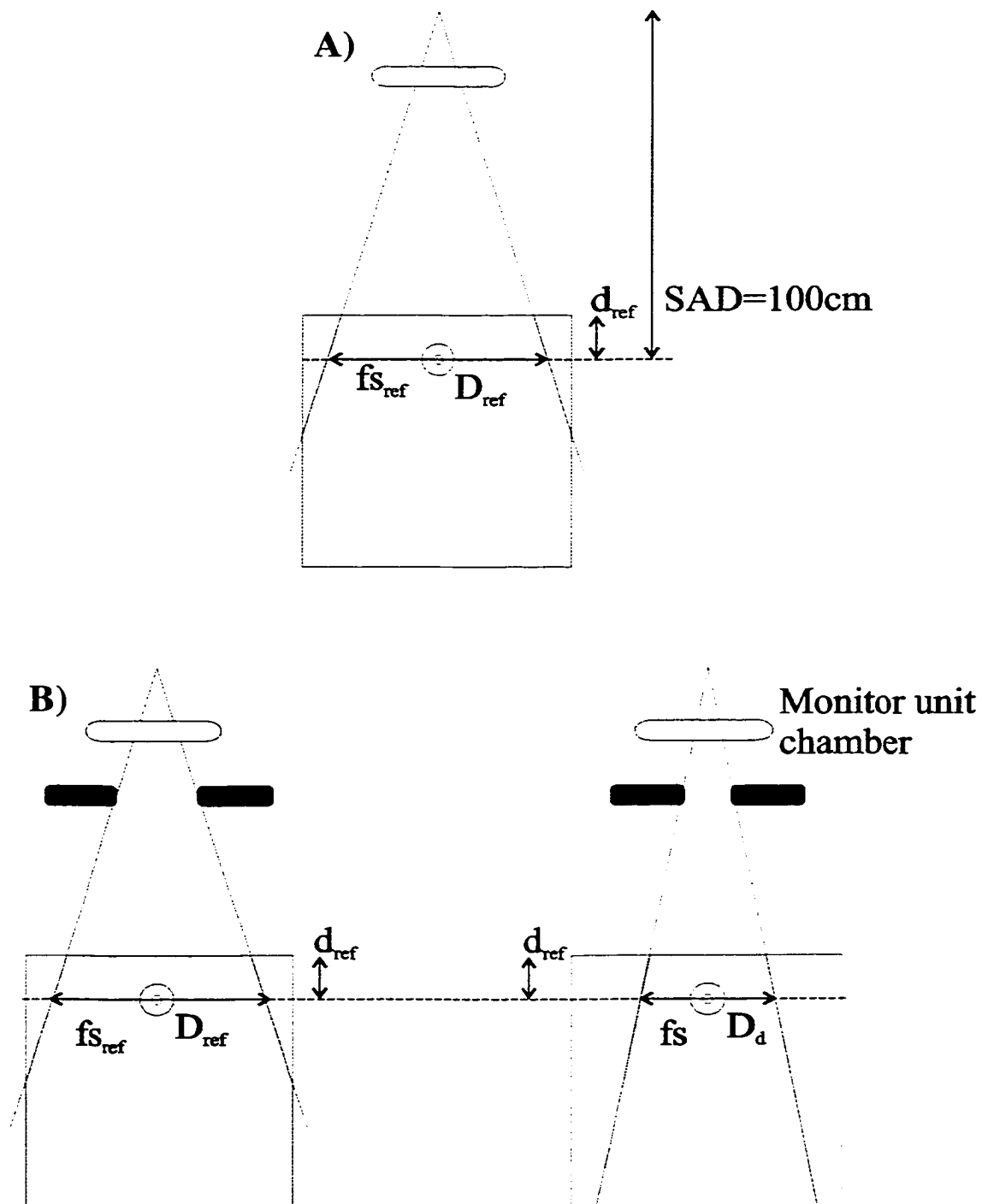


**Figure 2-3** A) Reference dose definition conditions. B) Definition and measurement technique for obtaining the value for the relative dose factor (RDF).

$$RDF(d_{max}, SAD = 100cm, fs) = \frac{D(d_{max}, SAD = 100cm, fs)}{D(d_{max}, SAD = 100cm, fs_{ref})} \quad \text{Equation 2-2}$$

where the dose to a field of size 'fs', at a constant depth  $d_{max}$  and SAD of 100 cm, is taken relative to the dose to the same point, at the same depth and SAD, for a field of some reference size ( $fs_{ref}$ ). As an example, if the field size is set to 20x20 cm<sup>2</sup> then the RDF would be a unitless ratio of roughly 1.05 (the exact value would vary depending on the treatment unit).

The RDF factor may be further subdivided into two separate factors [Khan 1994]. These reflect the change in machine output with jaw settings ( $S_c$ ), called the collimator scatter factor (see Figure 2-4), and the change in the amount of scatter within the measurement medium with changing field size ( $S_p$ ), called the phantom scatter factor (see Figure 2-5). The collimator scatter factor may be expressed as

$$S_c(SAD, fs) = \frac{D^{air}(SAD, fs)}{D^{air}(SAD, fs_{ref})} \quad \text{Equation 2-3}$$

where  $D^{air}$  is the dose for a particular field size in-air, with only a minimal amount of surrounding medium, for a field size fs relative to a measurement at the reference field size  $fs_{ref}$ . The SAD is kept at 100 cm. Knowing the values for  $S_c$  and RDF, it is now possible to obtain  $S_p$ . Measuring  $S_p$  directly would be somewhat impractical, so instead it may be calculated as per

$$S_p(d_{max}, SAD, fs) = \frac{RDF(d_{max}, SAD, fs)}{S_c(SAD, fs)} \quad \text{Equation 2-4}$$

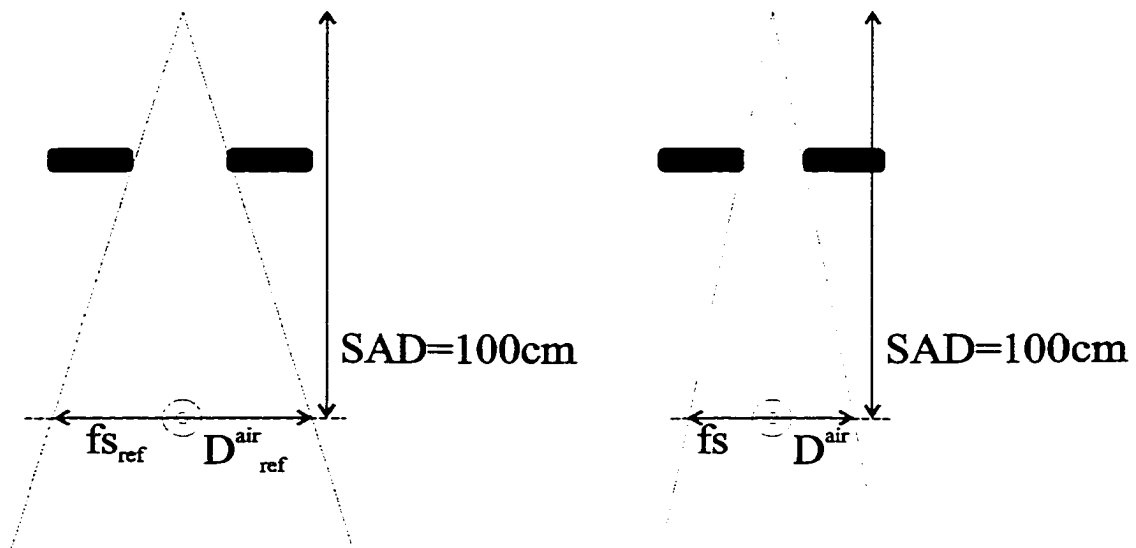


**Figure 2-4** Definition and measurement technique for obtaining the collimator scatter ( $S_c$ ).

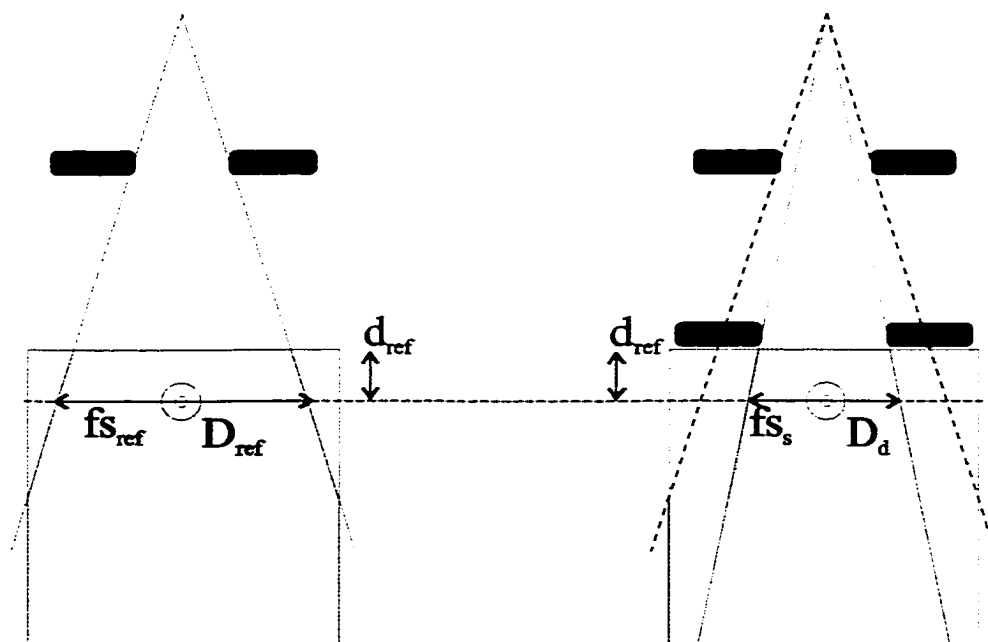


**Figure 2-5** Definition and measurement technique for obtaining the value for the phantom scatter ( $S_p$ ).

If measurements are taken “in-air” and on the CAX with a given fixed field size at the SAD of 100 cm, the variation of output with distance  $z$  from this SAD is given by the inverse square factor, as per

$$D_z = D_{SAD} \cdot IS(z, SAD) = D_{SAD} \cdot \left( \frac{SAD}{SAD + z} \right)^2 \quad \text{Equation 2-5}$$

where IS is the inverse square factor (see Figure 2-6).

If dose measurements are made off the central axis, then the dose to these off-axis points may be calculated relative to the CAX, as in

$$AOF(x, d) = \frac{D(x, d)}{D(CAX, d)} \quad \text{Equation 2-6}$$

The measurement of AOF is usually made at depth  $d$  in the measuring medium for the largest available field size (see Figure 2-7).

If the distance to the point of measurement is kept constant (i.e. SAD is constant) and the field size at isocentre is kept constant, but the amount of overlying medium varies (SSD changes), then the output varies by a factor called the tissue phantom ratio, or TPR (see Figure 2-8). The TPR is used to calculate dose in isocentric delivery techniques, and is defined for measurements at isocentre by

$$TPR(d, fs) = \frac{D_d(d, fs)}{D_{ref}(d_{ref}, fs)} \quad \text{Equation 2-7}$$

where  $D_d$  is the dose at depth  $d$  and  $D_{ref}$  is the dose at the reference depth, for a given field size  $fs$ . The TPR is often used, as it is roughly independent of the SSD. If the

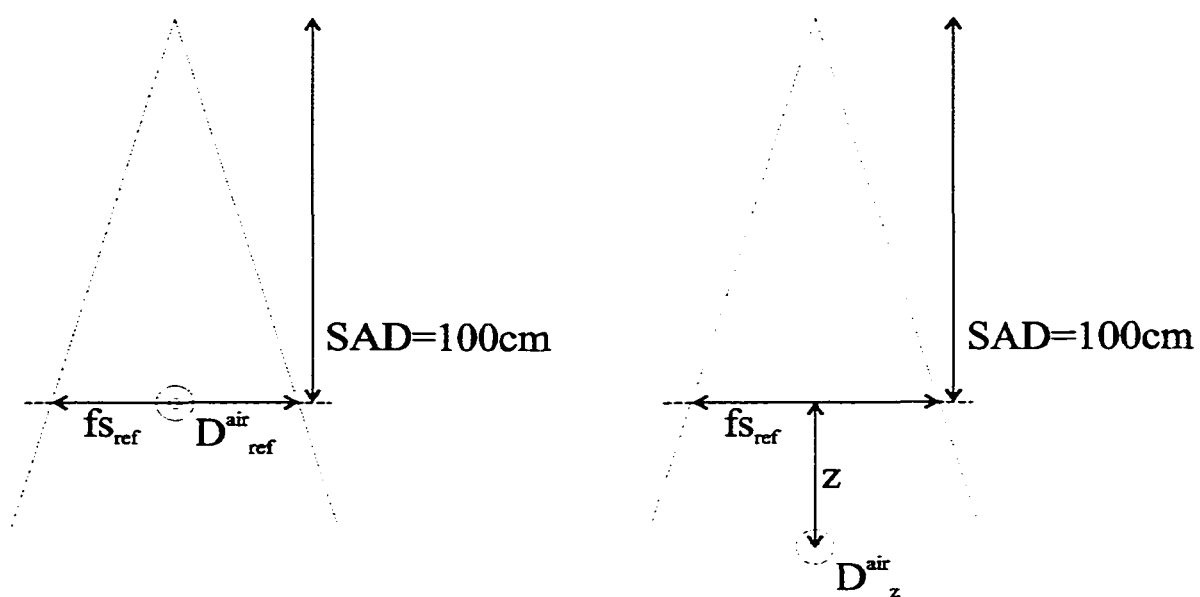


**Figure 2-6 The definition for the inverse square factor (IS).**

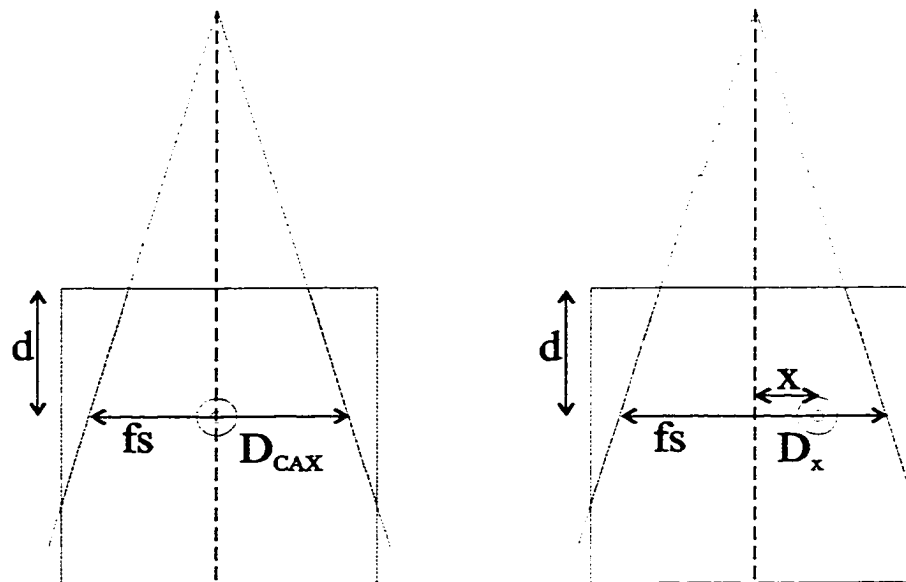


**Figure 2-7** Definition and measurement technique for obtaining the value for the asymmetric output factor (AOF).

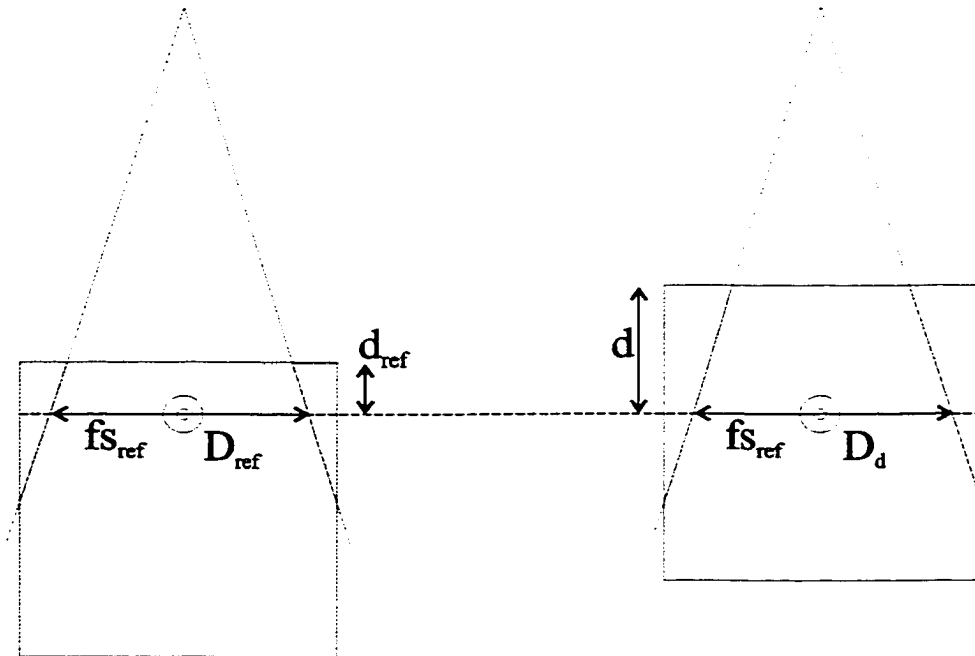


**Figure 2-8** Definition and measurement technique for obtaining the tissue phantom ratio (TPR)

reference depth is taken as  $d_{max}$ , then this factor is known as the tissue maximum ratio (TMR).

Combining the above factors, we have for a point at some depth  $d$ , distance  $x$  from the CAX, and for an SAD not necessarily equal to 100 cm, the dose is related to the calibrated output of the machine by the following relation

$$D(d, fs, x, SAD) = MU \cdot K \cdot TMR(d, fs) \cdot S_c(fs) \cdot S_p(fs) \cdot IS(SAD) \cdot AOF_d(x) \quad \text{Equation 2-8}$$

where  $fs$  is defined at isocentre,  $d$  is the depth of the measurement point and  $x$  is the distance from the CAX.

Several options for treatment planning and/or dose computation were employed in this work. Use was made of the Alberta Treatment Planning (ATP) system, a 2D TPS developed in-house. Results from ATP were compared to single field measurements (both open and dynamic fields). Use was then made of ATP as a check on planar dose calculations for multi-field dynamic deliveries.

ATP uses an empirical dose calculation routine, as described above. As well, use was made of a specialised routine enabled during the commissioning of the dynamic wedge and enhanced dynamic wedge. This routine takes a segmented treatment table (STT), which describes jaw motions as a function of MUs delivered, and constructs a virtual compensating filter based on this information. This method is expected to work well, since the filter incorporates no beam hardening and thus should well approximate a dynamic filter. One caveat is that the profile imported as an STT into the planning system should be the idealised STT (i.e. no accounting for any variations in energy fluence), since no attempt is made within ATP to model variations in  $S_c$  with the variable field size which would occur with an actual STT delivery. These correction factors are discussed in section 3.2.

### 2.2.2 Monte Carlo based algorithms

Ideally, dose may be computed from basic physical principles by Monte Carlo simulation of particles using CT density maps of the patient. Monte Carlo simulation involves sending a large number of photons through a virtual phantom and calculating the probability, voxel by voxel, of an interaction. Depending on the type of interaction, the scattered photon and electrons are then followed through virtual space. This is done for the initial incident photon and all its daughter particles until their energies have fallen below a certain cut off energy. This process is then repeated for many (on the order of  $10^8$ ) subsequent photons. There are several examples of Monte Carlo codes which are available for calculating transport in simple geometries such as EGS4 or MCNP. A more complex example of such software, extending the calculations to clinically realistic geometries, is the BEAM code, which uses EGS4 as its base, in order to model therapy units. There are even prototype treatment planning systems like the PEREGRINE system (see Figure 2-9), which employs massively parallel computing to complete treatment plans in reasonable times for clinical use.

### 2.2.3 Convolution / Superposition based algorithms

One step removed from the Monte Carlo technique is dose calculation by convolution (see Figure 2-10). A convolution dose calculation uses a dose spread kernel to relate energy fluence to deposited dose (see section 4.1 for more on energy fluence and dose). Dose spread kernels may be pre-calculated for various media by Monte Carlo simulation. For the calculation of dose from a mono energetic source in a homogeneous medium, the convolution is defined [Shiu 2000] as

$$D(\vec{r}) = \iiint_{vol} T_p(\vec{r}') d(\vec{r} - \vec{r}') dV$$

**Equation 2-9**

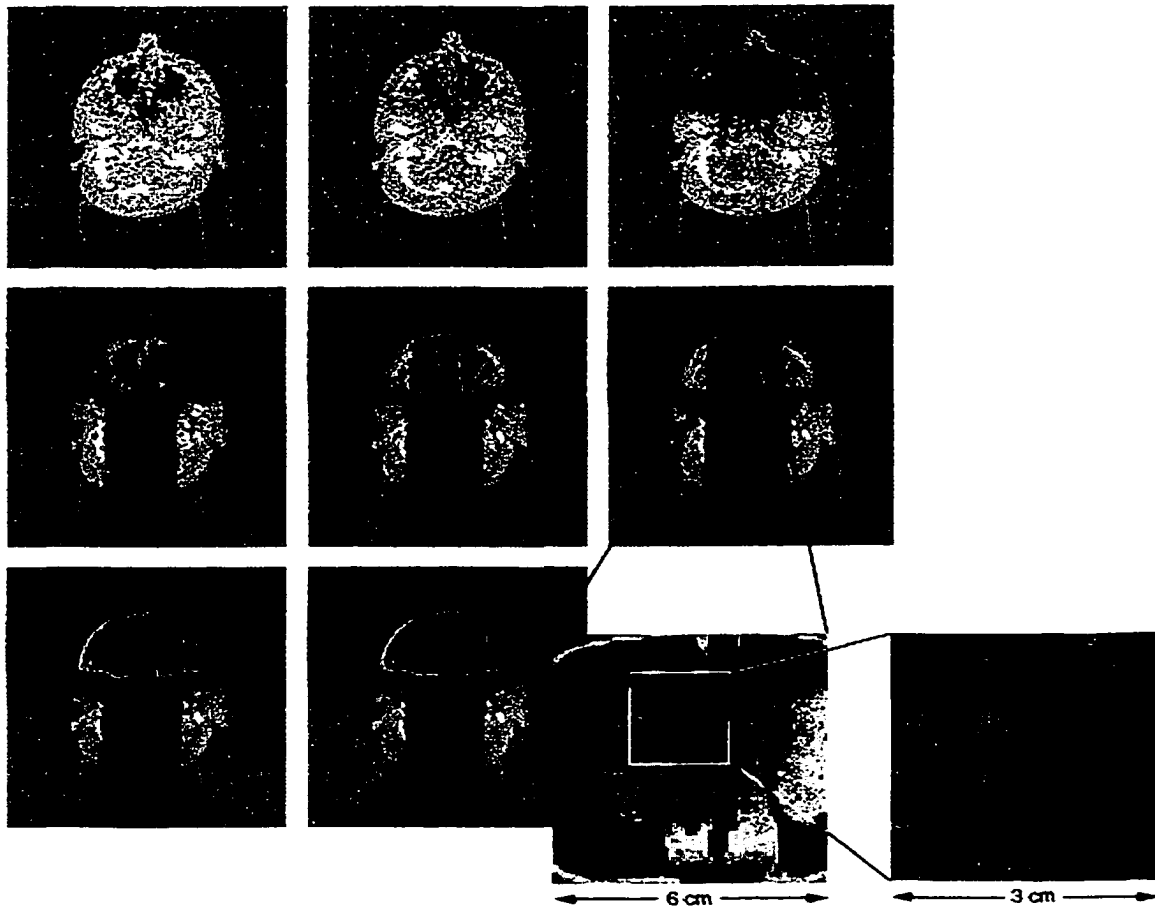


**Figure 2-9** Dose calculation by Monte Carlo methods using the Peregrine system, as a function of increasing photon histories.

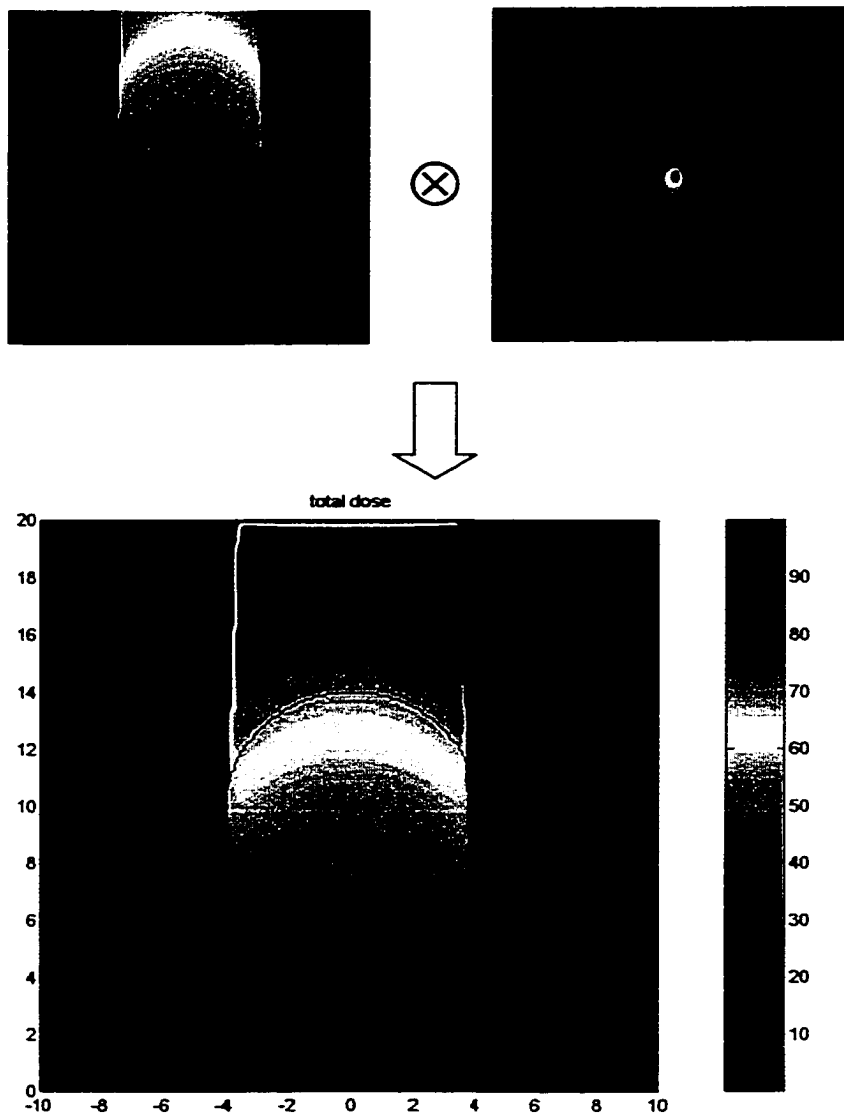


**Figure 2-10** The convolution of a TERMA distribution (A) with a polyenergetic dose spread kernel (B) to yield a dose distribution (C).

where  $D$  is the dose at some point  $r$  (see Figure 2-10c), which results from the interaction of the energy released by primary photons,  $T_p$ , at points  $r'$  (see Figure 2-10a), which deposit their energy according to the dose deposition kernel  $d$  (see Figure 2-10b). It should be noted that the expression above is valid for a single incident photon energy, and for a polyenergetic beam, one should sum individual kernels over the spectrum of incident photon energies.

A number of authors [Mackie 1985, Field 1987, Battista 1992] have worked extensively on making convolution one of the most prevalent techniques in 3D TP systems. Mackie et al have calculated a library of kernels using the EGS4 Monte Carlo code [Mackie 1988]. Photons of differing energies were forced to interact at the centre of a 60 cm radius sphere of water. The energy deposited in radial volume elements from 0 to  $\pi$  degrees (in separations of 7.5 degrees) and for various radii were calculated. Once this had been accomplished, the appropriate weighting and summing of mono energetic kernels could be used to construct a polyenergetic kernel.

An example of a commercial TPS that employs a convolution / superposition calculation scheme is the one used at this Institute, Helax TMS (MDS Nordion). This program is capable of handling as retracted missing tissue compensators and IMRT fields, and exports the resulting energy fluence profile as a modulation matrix. This matrix describes the relative weightings of incident beamlets across a 2D plane normal to the beam incidence. These weights are normalised to the primary energy fluence at isocentre. Helax is a full 3D TPS based on a convolution / superposition algorithm. The particulars of the system are exhaustively discussed in the literature [Ahnesjö 1992a, Ahnesjö 1992b, Ahnesjö 1994, Ahnesjö 1995]. The general details of convolution are presented in the following sections 2.2.3.2, 2.2.3.3, and 2.2.3.1.

Use was made in this work of a simplified convolution dose calculation scheme with correction factors, and the particulars are outlined in section 2.2.3.1 and in Chapter 5.

### 2.2.3.1 Single convolution approximation

A two dimensional single convolution approximation (SCA) dose calculation routine is employed in this work [Holmes 1993]. The SCA is a method to calculate an approximate dose distribution using a slice through a single polyenergetic convolution kernel [Mohan 1985], along with a depth dependent effective mass attenuation coefficient. The calculation of the TERMA and dose is accomplished by making several approximations, along with the application of certain correction factors. The relative dose distributions calculated by this method are compared to measurements, as well as an independent 2D TPS (see chapter 5). The dose calculations are performed on a slice by slice basis for 3D dose calculations.

A simple 2D TERMA (defined in the section 2.2.3.3) to dose convolution program was developed for use in this work. It runs on a PC in a high level programming environment (MATLAB, Math Works Inc). It assumes some approximations for the calculation of TERMA, namely a depth dependent effective mass attenuation coefficient and a constant energy spectrum as a function of depth and distance off-axis.

The effect of beam divergence for cases studied is relatively minimal for the field sizes and SSDs employed. Divergence in the TERMA is nonetheless modelled for the planar case, where the planes are in the leaf motion direction. For multi-slice plans, the effect of divergence is not accounted for in the non leaf motion direction, although again the effect is assumed to be minimal at the distances encountered in this work. There is no attempt at kernel tilting.

### 2.2.3.2 Fourier theory

The planning and dose calculation methods used in this work depend on Fourier transforms and associated theorems, namely convolution, the radon transform and the central slice theorem.

The Fourier transform of a function  $h(x)$  is often stated as

$$H(k) = \int_{-\infty}^{\infty} h(x) e^{ikx} dx \quad \text{Equation 2-10}$$

where  $h(x)$  is a function of the spatial variable  $x$  and  $k$  is the spatial frequency.

All Fourier transforms used in this work are really discrete fast Fourier transform (DFFTs). One problem with the use of the DFFT is the ringing associated with the discrete version of the Fourier transform. This is known as the Gibbs phenomenon [Bracewell 1995]. This problem is easily understood if the discontinuous pixel edges of the discrete approximation of a continuous figure are thought of as corresponding to a high spatial frequency characteristic of the data space. This shows up in the Fourier transform as an ultra high frequency component.

The convolution of two functions [Press 1989],  $a(x)$  and  $b(x)$ , is defined as

$$a(x) \otimes b(x) = \int a(x') b(x - x') dx' \quad \text{Equation 2-11}$$

where  $a$  is function of  $x'$ , and  $b$  varies as a function of the distance between  $x$  and  $x'$ . This can be pictured as the sum of the effect at  $x$  due to  $a$ , which has a spread function  $b$ . The convolution of a Heaviside step function with a Gaussian spread function is shown in Figure 2-11.

The convolution theorem states that this operation can be performed in Fourier space as the product of the two functions, that is

$$a(x) \otimes b(x) \Leftrightarrow A(k)B(k) \quad \text{Equation 2-12}$$

where  $A(k)$  and  $B(k)$  are the Fourier transform of  $a(x)$  and  $b(x)$ , respectively.

The correlation of two functions is found by taking the product of the Fourier transform of one function and the Fourier transform of the complex conjugate of the other function, that is

$$\text{Corr}(a(x), b(x)) = A(k)B^{\dagger}(k) \quad \text{Equation 2-13}$$

where the  $\hat{\phantom{x}}$  denotes the complex conjugate. The correlation can be described [Press 1989] as being a function of the lag, or shift in position, between two similar functions  $a(x)$  and  $b(x)$ .

### 2.2.3.3 KERMA, TERMA and Dose deposition

The determination of dose by a convolution algorithm requires the calculation of TERMA, a quantity related to KERMA. KERMA is a quantity that is closely related to radiation dose if charged particle equilibrium is established. Its name stands for **K**inetic **E**nergy **R**elaxed per unit **M**Ass, and is defined as

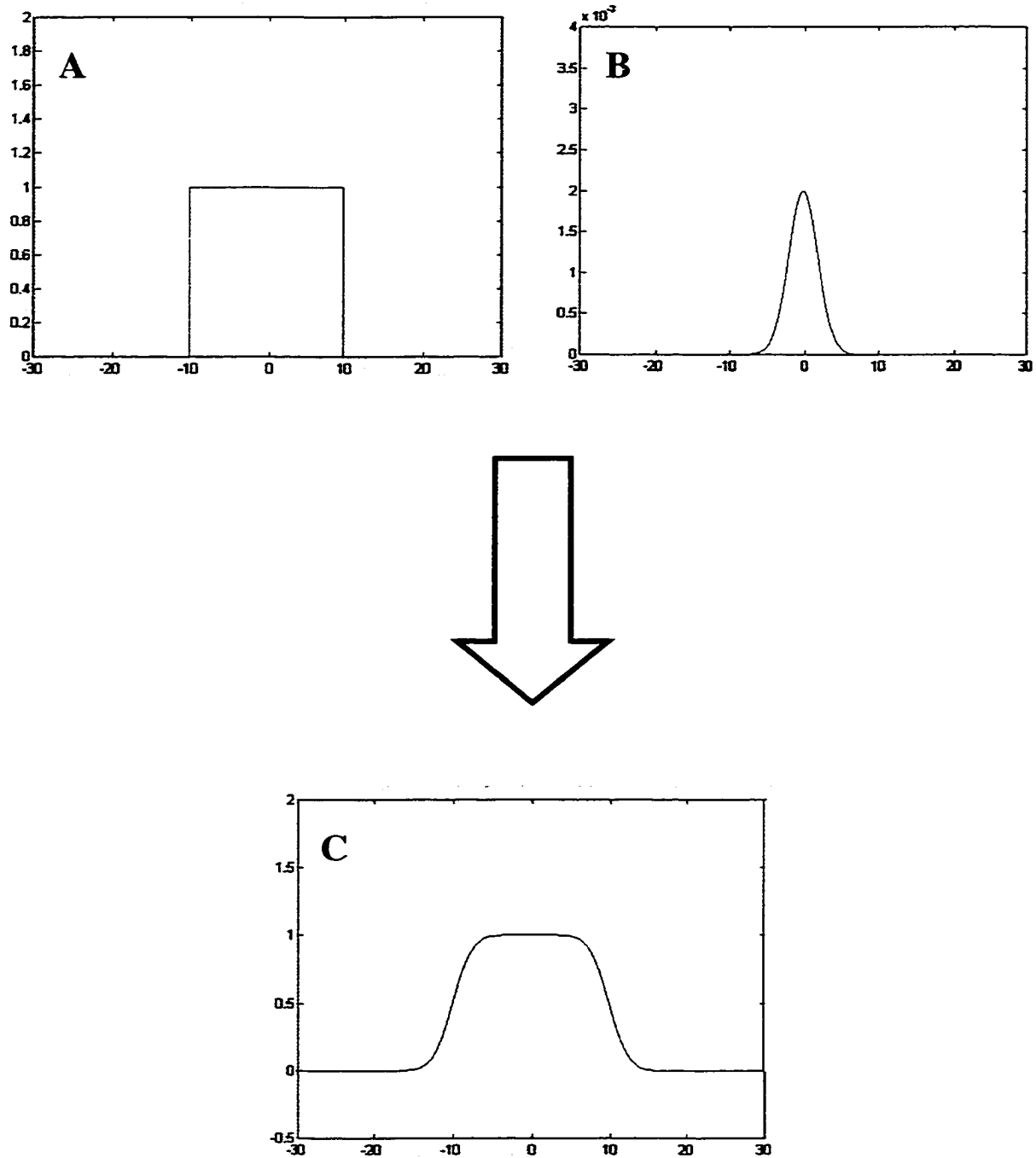


**Figure 2-11** The convolution of a unit value Heaviside function (a) with a Gaussian (b) to yield the 'smeared' distribution (c).

$$K = \frac{dE_{tr}}{dm} = \left( \frac{\mu_{tr}}{\rho} \right)_{E,Z} \Psi \quad \text{Equation 2-14}$$

where  $E_{tr}$  is the energy transferred to charged particles in an infinitesimally small volume of mass  $m$ . This quantity differs from dose (energy absorbed per unit mass), in that the energy released at any given point in a medium may not remain at that point. For example, the energy may be transferred to an electron via a Compton interaction, and that electron may travel some distance before depositing all of its kinetic energy in the medium via numerous Coulomb interactions. TERMA may be defined as the Total Energy Released per unit Mass, and is the combination of radiant and non radiant (i.e. kinetic) energy released at the point of interaction. It is this quantity that is used in convolution since the dose spread kernel used is based on the energy deposited by electrons and scattered photons when a photon interacts at a given point. TERMA is defined similarly to Equation 2-14, except using the total  $\mu$  value, not just  $\mu_{tr}$  for the energy transferred to charged particles, as in

$$TERMA = \frac{dE}{dm} = \left( \frac{\mu}{\rho} \right)_{E,Z} \Psi \quad \text{Equation 2-15}$$

Looking at Figure 2-10a, we see an example of the calculation of the beam TERMA.

It is assumed that primary photons are removed from the beam according to exponential attenuation of the form

$$\Psi(x, d) = \Psi_0(x) e^{-\mu_{eff} \cdot d} \quad \text{Equation 2-16}$$

where  $\Psi_0$  is the energy fluence incident on some medium at point  $x$ ,  $d$  is the path length through the medium which the primary energy fluence has travelled, and  $\mu$  is

the attenuation coefficient of the medium. It is also assumed that the primary photons removed deposit their energy relative to the point of interaction according to an invariant polyenergetic kernel. It is also assumed that the primary energy fluence spectrum does not change appreciably with depth. In this work, an effective depth dependent  $\mu$  value is used. This is used in conjunction with a simple exponential attenuation approximation of the TERMA.

### **2.3 The inverse plan**

As discussed in section 1.3.4, the inverse problem arises from the question concerning the combination of beams and beam intensities that will yield a desired dose distribution within a PTV. The process of inverse planing seeks an answer to this question by determining the incident energy fluence profiles required which will yield a dose distribution which is as close as possible to the requested one. The answer that is arrived at depends in some measure on the choice of constraints that one puts on this inverse problem. A variety of techniques has been proposed to address this question [Webb 1991, Lind 1990, Bortfeld 1990, Holmes 1991, Lee 1997, Hristov 1997, Liu 1999]

In order to optimise any set of equations, there must be a set of constraints, either equality or inequality constraints, or a 'fitness function' of some sort, which will ultimately allow for cardinal (i.e. quantitatively ranked in some absolute sense) or ordinal (i.e. ranked in comparison to other plans) sorting of potential solutions. The optimisation problem is unbounded without constraints, such as the constraint of minimisation of treatment time in the calculation of dynamic jaw motions [Convery 1992]. The constraints in the search for an optimal IMRT treatment may assume various forms. Constraints may be of the form of specifying that the dose to a particular adjacent normal structure must be less than or equal to some particular dose. A fitness function may evaluate such things as least squares deviation of the

dose delivered in a particular volume compared to the prescribed dose for that volume.

For treatment planning purposes, a number of beam parameters may be varied in the search for an optimal solution, namely the number of beams as well as beam energy, direction, weight, as well as beam intensity across the field (i.e. the energy fluence profile). Once the delivery technique is chosen, the dose delivery must be optimised according to the aforementioned fitness function, within the bounds of the constraints. A physical or biological fitness function for evaluating the result of the treatment plans is often used. These objective functions are covered in section 2.4. Numerical techniques (e.g. simulated annealing) may be used at this stage to arrive at a solution once the criteria are in place.

For dose delivery, one may formulate the dose delivered in terms of the incident energy fluence  $\Psi$ , which is broken into beam elements, sometimes referred to as bixels [Webb 1997]. A transfer matrix or kernel  $W$ , akin to a convolution kernel, dictates how the energy from bixel  $j$  spreads dose to point  $i$ . One can then state that the dose  $d$  is given by

$$d_i = \sum_j W_{ij} \Psi_j \quad \text{Equation 2-17}$$

This means that the solution to the inverse problem can be stated as

$$\Psi_{required} = W^{-1} d_{desired} \quad \text{Equation 2-18}$$

The problem with this approach is that the desired dose is often given as dose to a region with zero dose outside of that region. This would require beam energy fluence profiles with negative energy contents (the negative portion would remove the

entrance and exit dose from other beams above and below the volume of interest, as well as any scatter out of the volume of interest). A simple inversion does not therefore yield a proper physical solution.

The inverse planning technique used in this work relies on an analogy to CT image reconstruction. The reconstruction of a planar image from projections is based on the Fourier slice theorem (discussed in section 2.3.1). A reconstruction is not performed, however, since the desired dose distribution is defined rather than calculated. The projections are used to define the energy fluence profile that would yield this defined dose. If these profiles could include negative energy fluence input, the reconstruction would be quite faithful to the defined distribution. Since negative energy fluence represents a non-physical portion of the solution it is discarded and the optimally realisable solution is arrived at iteratively.

Dynamic delivery solutions to this problem may be somewhat different from each other. There can be several solutions using differing approaches to delivery, some involving a few dynamic ports, or perhaps an arc rotation delivery that irradiates a larger volume of normal tissue to a smaller dose. The question of which is better from a normal tissue complication standpoint, a large dose to a smaller volume or small dose to a larger volume, is a question under debate in the area of conformal radiotherapy [Zaider 1998]. In this work, the planning and delivery assume a full arc rotation about the phantom (thus irradiating a larger volume to a lower dose).

### 2.3.1 Projection, Radon transform, Filtering and Smoothing

It has been recognised for some time that inverse planning has a great deal in common with image reconstruction [Cormack 1987, Brahme 1988]. Profile calculation and optimisation can be seen as a physical analogue of the mathematical back projection operation used in tomographic reconstruction. An example of a

tomographic reconstruction of a disc is given in Figure 2-12. The reconstruction is shown for 2(A), 10(B), 18(C) and 72(D) out of 72 equally spaced projections.

The Fourier slice theorem states that the 1D Fourier transform of the projection of a distribution,  $d(x,y)$ , is a line of the 2D Fourier transform of the distribution, evaluated along a line at an angle corresponding to the angle the projection was taken along [Bracewell 1995], that is

$$p(\theta, a) = \int d(x, y) dr = \iint d(x, y) \delta(x \sin \theta - y \sin \theta - a) dx dy \quad \text{Equation 2-19}$$

where  $\theta$  is the angle that the projection is taken at,  $a$  is the distance from the axis of rotation about which the projections are taken, and  $x$  and  $y$  are the co-ordinates of the original 2D object distribution (see Figure 2-13).

This projection is known as the Radon transform. Now, using the delta function and the definition of the Fourier transform, this function becomes

$$P(\theta, k) = \iint d(x, y) e^{-ik(x \sin \theta - y \sin \theta)} dx dy \quad \text{Equation 2-20}$$

in frequency space ( $k$ ), or in real space ( $x,y$ ), we have

$$d(x, y) = \frac{1}{4\pi^2} \iint P(\theta, k) e^{-ik(x \sin \theta - y \sin \theta)} |k| d\theta dk \quad \text{Equation 2-21}$$

where  $|k|$  is the ramp filter. The ramp filter arises from the change of variables, and can also be thought of as required for removing the star artefact blurring [Bracewell 1995]. The star artefact would result from an over representation of the low spatial

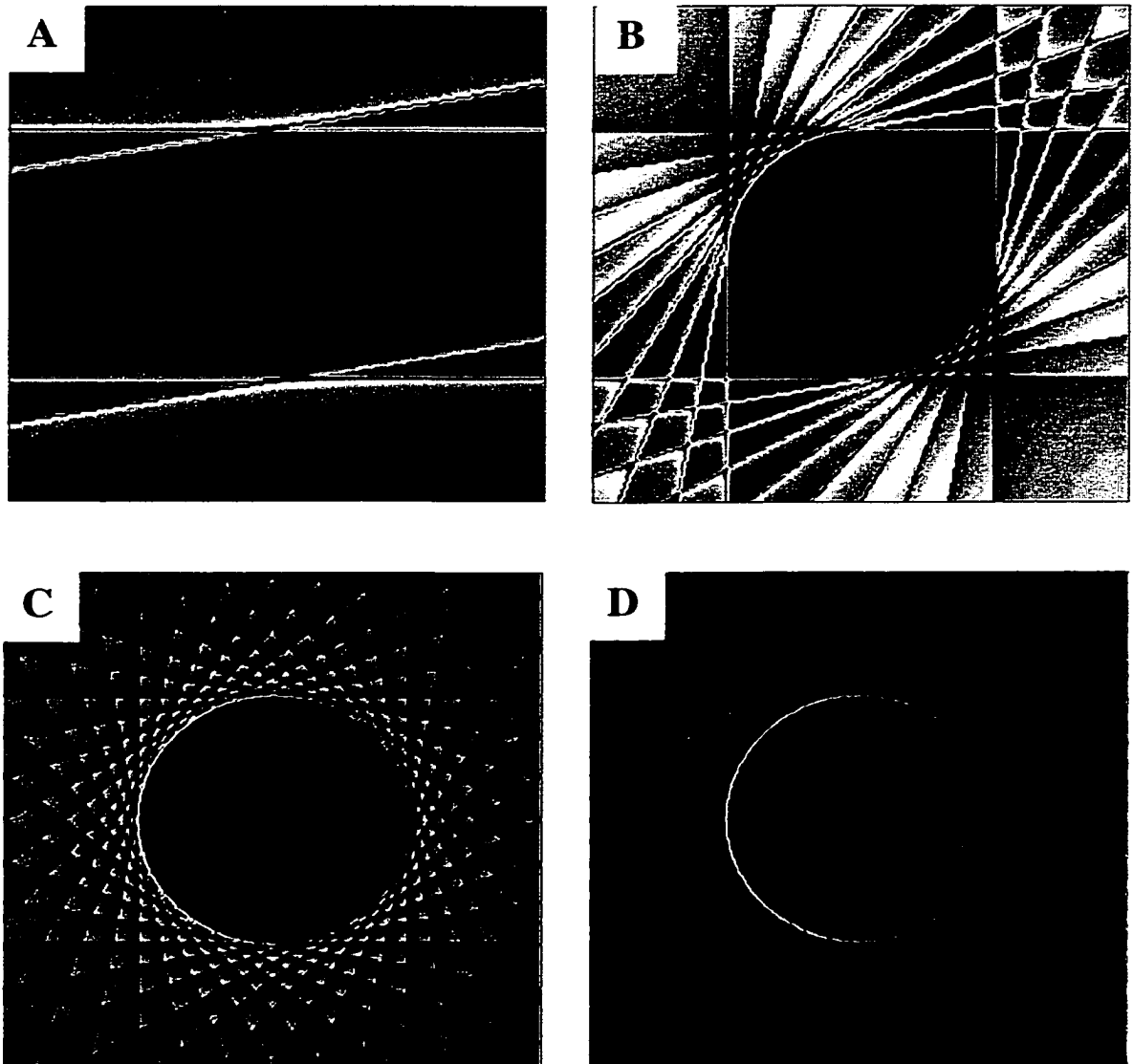


**Figure 2-12** Reconstruction of a circular distribution from its projections. The result is show for a) 2, b) 10, c) 18 and d) 72 out of 72 equally spaced projections.

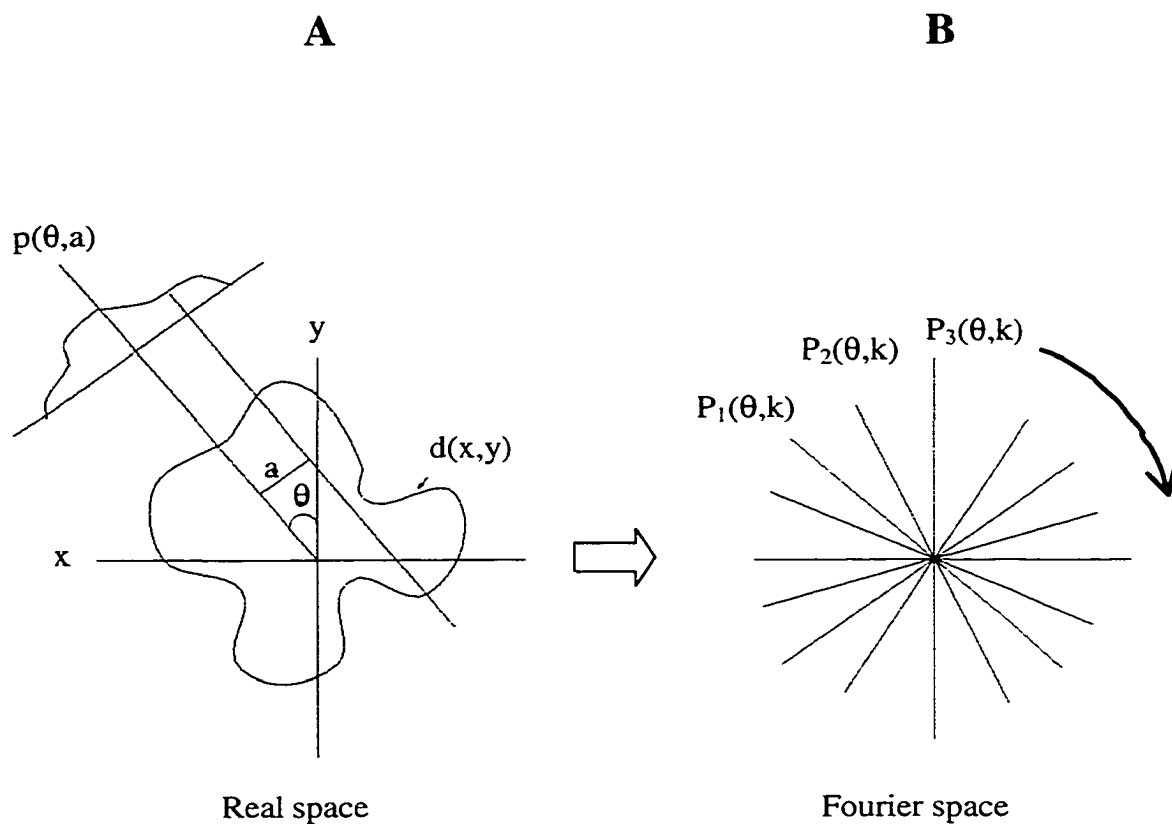


**Figure 2-13** A) a distribution  $d(x,y)$ , along with the projection of  $d(x,y)$  from an angle  $\theta$ , at distances  $a$  from the point of rotation. B) The reconstruction of the image in A by forming the 2D Fourier transform at various angles, and then taking the inverse Fourier Transform.

frequency component (this would occur at the origin of Figure 2-13b, where the projections all cross one another).

This theory is used in the present work not to reconstruct a dose from projections, but rather to determine what energy fluence profiles must be incident on a phantom in order to produce a desired dose distribution. It is the ramp filtered profiles (the filtered back projections) at each angle that are the required beam profiles needed in order to achieve the desired dose distribution. The resultant profiles have negative values, which, tomographically, are necessary for the faithful reconstruction of the image. For dose reconstruction, these negative portions of the beam can be seen as an attempt to erase the entrance and exit dose around the tumour. As such, they represent a non-physical portion of the solution, which must be discarded. Discarding the negative portion of the solution perturbs it from the ideal, and hence, in order to achieve the optimal physically realisable solution, one must iterate to a final solution.

### 2.3.2 Initial profile prediction

Initial calculations of the required energy fluence profiles are performed in a 2D Matlab routine. The initial required incident energy fluence profiles are calculated using attenuation corrected filtered back projection of the desired dose distribution. Attenuation profiles and dose projections are computed separately. Each profile is convolved with a smoothing kernel, then subjected to a mean value filter. These latter two steps are required to reduce variations in signal that give rise to spurious noise in the back projection step and to better approximate a continuous function. Attenuation and dose profiles are then multiplied together to yield the primary energy fluence projection. The primary energy fluence projection is then back projected to yield the required incident energy fluence profile. The back projection filter used is a ramp filter, multiplied with a Butterworth filter in order to reduce high spatial frequency artefacts. The non-physical portion of the solution is discarded, and that which remains is used as an initial guess to the solution of the inverse problem. This is

repeated for a large number of equally spaced projections (the question of how many is sufficient is addressed in section 5.5.2).

### 2.3.3 Profile refinement through iterative search techniques

The techniques used for initial profile estimates are an imperfect approximation to a perfect inversion. This is due to both the non-continuous implementation of the technique, as well as to the inclusion in the idealised solution of non-physical components (i.e. negative beam intensities) which must be discarded. This means that the solution on the first iteration, while being of the correct general form, is not optimal. The convergence toward an optimal solution is achieved after several iterations during which the shortcomings of the initial solution are corrected.

The search method used to find the solution to the inverse problem may take a number of forms. The optimisation technique can be, broadly, of three main types: heuristic optimisation, stochastic optimisation or deterministic optimisation.

Heuristic optimisation is the oldest of optimisation techniques, a euphemism for trial and error. This is the type of optimisation performed routinely by treatment planners in the forward planning process. With unmodulated or simply modulated (i.e. wedged or missing tissue compensator) beams shaped only by blocks or MLC, acceptably close solutions may be arrived at quickly by an experienced treatment planner. The likelihood of success of such planning, given the number of degrees of freedom associated with an IMRT plan, however, seems remote.

Stochastic methods are directed forms of trial and error that should settle in on a solution that is at or is close to the global minimum after a large number of iterations. Such methods include simulated annealing and genetic algorithms. Deterministic methods include such techniques as the Simplex method and quasi

Newton methods. A brief overview of three popular techniques used to converge to the optimal solution is presented in sections 2.3.3.1, 2.3.3.2, and 2.3.3.3.

### **2.3.3.1 Genetic Algorithms**

The idea of the genetic algorithm (GA) was popularised by Dawkin's in the book 'Artificial Life' [Dawkins 1989], and is often based on his Blind Watchmaker's program. Genetic algorithms are a computational analogue to a physical paradigm. The analogy is made to Darwinian evolution, with the organisms representing solutions to a function for which one wishes to find the global minimum. The organisms' 'genetic material' is a string of parameters, which serve as input for the function we wish to optimise. The 'organisms' are tested by use of a 'fitness function', and those that are deemed fit will survive to 'reproduce'. Here, reproduction represents pairing with another fit solution and the two 'organisms' exchange portions of their parameter strings. This method is iterative and stochastic. The stochastic component gives these methods the ability to escape from sub optimal local minima. For GAs, the stochastic component comes not only with the randomness of the break point in the 'genome' when mating fit solutions, but also the possibility for random mutations in the genome that is introduced with each mating.

Some of the possible operators that may be used on the population and varied in the GA optimisation include crossover, mutation, cloning, spontaneous generation, deletion, and family size. The fitness operator will also play a large role in how optimal the final solution is. How well the process converges to a truly optimal solution will also depend in part on how well diversity is maintained through each iteration, and how well maintained good characteristics are, and how quickly new characteristics are introduced.

The genetic algorithm technique has been applied to the various problems in treatment planning [Ezzell 1996, Langer 1996]. For problems in radiation therapy, the

genome of the ‘organisms’ may correspond to such things as beam weight or beam angle. The relative merits of this optimisation technique are closely related to that of the other stochastic optimisation discussed here, simulated annealing. The relative merits of these two techniques are therefore discussed at the end of section 2.3.3.2.

### **2.3.3.2 Simulated annealing**

Simulated annealing, as with genetic algorithms, is a computational analogue to a physical paradigm. Simulated annealing [Metropolis *et. al.* 1953, Press *et. al.* 1989], sometimes called combinatorial minimisation, is an optimisation technique of the stochastic-iterative variety which was the first to solve the rather famous travelling salesman problem. It has a few variants, such as Ingber’s very fast simulated re-annealing and the generalised simulated annealing algorithm of Bohachevsky *et. al.*; refer to Morrill 1995. These are based on the same principle, which is the computational analogy to the physical process from which it draws its name (i.e. slow cooling of a lattice into the lowest possible energy state). An initial guess of the solution is defined, and then one randomly computes changes to the initial guess. This method, as with genetic algorithms, is iterative and stochastic.

One defines an objective function to determine whether the initial feasible vector will change its state to a new value -- this will allow all vectors to change their state to some other state. This change is always made for any solution which is more optimal, but not always made for ‘uphill’ guesses which temporarily move away from an optimal solution. A probability function determines the likelihood of an ‘uphill’ change. The probability that any given vector will change its state upward gets smaller with each successive iteration, and the probability of an individual change depends on how much larger the objective function becomes.

This technique has been applied to numerous problems in medical physics [Sloboda 1992, Rosen 1995, Morrill 1995]. It is one of the more popular of the recent optimisation algorithms to be applied to some inverse problems.

The probability, because of the statistical thermodynamics analogy being used, is based on the Boltzmann probability distribution, namely

$$P(E) \sim e^{-\frac{E}{kT}} \quad \text{Equation 2-22}$$

In the case of simulated annealing, the energy  $E$  corresponds to the value of the objective function being minimised, and  $T$  is the ‘temperature’ -- a user defined parameter whose value drops at some rate as a function of the number of iterations. Since this is a minimisation problem, the goal is to achieve the lowest value of  $E$  possible. As with physical annealing, the system ‘slowly’ (in terms of number of iterations, not necessarily in terms of calculation time) settles into a near-global minimum. The probability of any change is

$$p = e^{-\frac{(E_2 - E_1)}{kT}} \quad \text{Equation 2-23}$$

where  $E_2$  is the value of the new guess and  $E_1$  is the value of the previous guess. One can see that for any values of  $E_2 < E_1$ , one gets  $p > 1$ , so the change is certain. If  $E_2 > E_1$ , it is still possible for the objective function to change to this new value even though it is larger than the current solution. It is this feature of the technique that allows one to avoid getting caught in a local minimum (see Figure 2-14a), and to continue to strive toward a global minimum (see Figure 2-14b). The convergence time for this method is usually on the order of a small power of  $N$ , where  $N$  is the number of points defining the initial feasible vector [Press *et. al.* 1989]. Simulated annealing will converge on a solution with a relatively minimal, if not absolutely minimum,

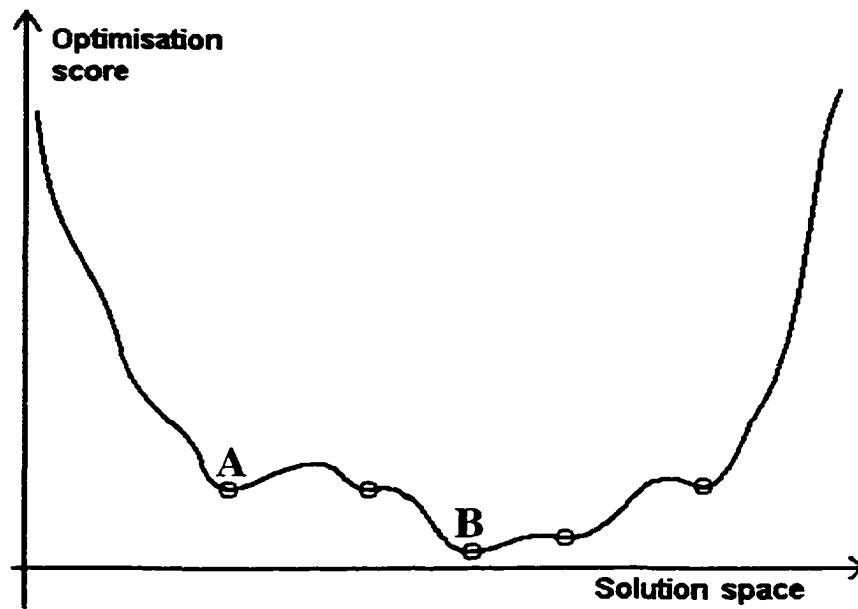


**Figure 2-14** A simple representation of the solution space of a 1D function. There are two minima shown A) a local minimum, of which there are several and B) a global minimum

objective function value that often cannot, in practice, be improved upon to any great degree. Genetic algorithms share these two features (i.e. slow convergence and likely to realise global optimum).

### 2.3.3.3 Quasi Newton Methods

The popularity of the stochastic methods is based on their ability to converge to a global minimum in the solution space. Their chief drawback is that they are ‘computationally expensive’ (i.e. their convergence times are comparatively quite long). Deterministic methods have the benefit of fast convergence, and may converge to exactly the same solution as stochastic methods.

A number of deterministic methods are based on the Newton’s method of multidimensional function minimisation. The Newton’s method is based on taking the first few terms of a Taylor expansion for a given function to give a quadratic approximation to the function. Let us assume that the minimum occurs at some point  $x_{\min}$ . If the estimate of this value after  $k$  iterations is  $x_k$ , which is a distance  $\delta$  from the true minimum point  $x_{\min}$ , the form of the function is

$$\begin{aligned}
 F(x_k + \delta) &= F(x_k) + \delta F'(x_k) + \frac{1}{2} \delta^2 F''(x_k) + \dots \\
 &\approx F(x_k) + \delta F'(x_k) + \frac{1}{2} \delta^2 F''(x_k)
 \end{aligned}
 \tag{Equation 2-24}$$

It is assumed that this polynomial provides, at least locally, a good approximation to the function. The minimum for this function occurs approximately where one has a minimum value for  $\delta$ . The value of  $\delta$  needed to make the step from  $x_k$  to  $x_{\min}$  is

$$\delta = -\frac{F'(x_k)}{F''(x_k)} \quad \text{Equation 2-25}$$

so the step at each iteration is

$$x_{k+1} = x_k + \delta = x_k - \frac{F'(x_k)}{F''(x_k)} \quad \text{Equation 2-26}$$

This is the Newton method of function minimisation.

Another function minimisation technique is the method of steepest descent. This method originated with Cauchy in 1845 and uses the gradient of the function in question and an initial starting guess of the function variables, and looks for the largest gradient from this point. Although this will likely converge to a solution, it requires many iterations to do so. There are a number of useful variations on this method, however. These may employ only the gradient or approximations to the Hessian, and as such are termed Quasi-Newton methods.

In this work, a quasi Newton method was used. There are two main reasons for this choice. One reason is the greater speed in computation of the gradient technique compared to the stochastic technique discussed. The other reason is that, depending on the choice of objective function, the minimum that is converged upon may be the same as the global minimum [Olivera 1998]. The choice of objective function is discussed in section 2.4.

In terms of the optimisation of the energy fluence profile, this search technique had the form of

$$\Psi_{i+1}(\theta, a) = \Psi_i(\theta, a) + R_\theta \left[ \left( \frac{\rho}{\mu} \right) e^{-\mu} \{ B(d_{planned} - d_{j,k}) \} \right] \quad \text{Equation 2-27}$$

where  $\theta$  is the angle that the projection is taken at, 'a' is the arc distance from the axis about which the projections are taken,  $R_\theta$  is the Radon transform taken at angle  $\theta$ , 'd<sub>planned</sub>' is the dose that is planned for point (j,k), 'd<sub>j,k</sub>' is the calculated dose to this point at iteration i, and B represents the binary mask (see Figure 2-1) of the region of interest. The binary mask is a matrix of ones and zeros, where the ones constitute an 'image' of the region of interest.

#### 2.3.3.4 Computational artefacts

In order to correct for computational artefacts, a high resolution calculation matrix is used and a degree of filtering of the data is employed. The high resolution aids back projection in two ways. It serves to better approximate a continuous structure. As well, it enhances the high end of the high frequency component, reducing the Gibbs phenomenon to a smaller portion of the overall signal.

As mentioned, the initial evaluation of the primary energy fluence projection (attenuation profile and dose projections) is convolved with a smoothing kernel, then subjected to a windowed mean value filter. While these steps are required to reduce signal variations that would otherwise give rise to noise in the back projection, they also degrade the solution by altering the true projected profile. The width of the smoothing kernel and width over which the mean filter is computed are reduced at each iteration, until they leave the input unchanged at the final iteration. As well, the cut off frequency of the Butterworth filter that is used to reduce high spatial frequency artefacts is also increased at each step. These steps have the effect of preserving more high spatial frequency at each step. This can be thought of as achieving gross

resolution in the early stages of optimisation, and finer resolution as the optimisation progresses.

## **2.4 Plan evaluation**

Treatment planning can be seen as an attempt to optimise radiation delivery on the basis of a combination of physical and biological considerations. Plans are to some degree already evaluated on biological considerations, such as the likelihood of achieving local tumour control and the chance of inducing morbidity in normal tissue. At the same time, plans are also evaluated on physical considerations, such as the level of dose delivered to a volume of interest and degree of dose homogeneity achieved in that region.

While there have been attempts to quantify and model biological factors [Kallman 1992, Soderstrom 1993] such as tumour control probabilities (TCPs) and normal tissue complication probabilities (NTCPs), there is not yet a great deal of data with which to verify many of the assumptions that these models rest upon. In practice, treatment plans tend to be based on the experience of the radiation oncologist, on the evolving record in the literature and on the outcome of clinical trials of which there are a growing number, both in-house or multi-institutional.

Despite these challenges, an accurate biological response model is highly desirable in treatment planning. Various mathematical models have been proposed to quantify the response of tumour and normal tissue cells to irradiation. These models are in turn used to calculate the probability of achieving complication-free tumour control. One popular biological constraint or figure of merit, often called  $P_+$  [Ebert 1997], is calculated as

$$P_+ = TCP - NTCP + \delta (1 - TCP) NTCP \quad \text{Equation 2-28}$$

where  $\delta$  is a weighting parameter. The NTCPs are often calculated using methods along the lines of Lyman [Lyman 1985], and employ complication probabilities extracted from the literature. TCPs are usually derived in a manner similar to Schultheiss [Schultheiss 1983]. Other biological values such as the equivalent uniform dose (EUD) [Ebert 1997] may also be calculated and used in plan evaluation. Anatomical factors, such as the structure of an organ (i.e. serial or parallel), may further impact plan evaluation. These factors may be used in iterative calculation schemes to converge on the treatment plan which achieves the highest probability of control

The cumulative dose volume histogram, often simply called the dose volume histogram (DVH) [Lyman 1985] provides an often used quantitative measure of the degree of dosimetric coverage. Aside from use in physical optimisation, DVHs can also be reduced from a complex shape to a single dose-volume equivalent. Once this is done, the values for  $TD_{50}$  and  $TD_5$  (the doses that result in complication rates of 50% and 5%, respectively, after 5 years) can be used in biological models to calculate TCPs and NTCPs. These biological constraints may then be used to optimise treatment plans accordingly. These probabilities are derived from clinical data and based upon the calculation from some particular model.

Despite the promise that biological models and figures of merit may hold, most plans today are still based on physical optimisation of the dose delivery. Again, this is done on the basis of the level of doses delivered and the degree of dose homogeneity achieved within the PTV, as well as the amount of dose delivered to tissue outside this region (both to normal tissue and sensitive structures). Physical optimisation carries the inherent assumption that the prescribed dose and treatment volumes are biologically optimal, and seeks to achieve this plan. Any biological considerations are made a priori and often on the basis of experience or mounting evidence in the literature or in clinical trials, and as such are not explicitly modelled.

The optimisation of all deliveries in this work is done purely on a physical basis. That is to say that the objective is to achieve as uniform a dose as possible within a target volume. The objective function used to evaluate the fit is given by the quadratic dose objective function, also known as the least squares objective function,  $F$ , which can be formulated as

$$F = \frac{1}{N \cdot M} \sum_{i=1}^M \sum_{j=1}^N (d_{planned} - d_{i,j})^2 \quad \text{Equation 2-29}$$

where  $d_{planned}$  is the desired dose on the dose matrix of the region of interest (which has  $N \cdot M$  elements) at point  $(i,j)$  and  $d_{i,j}$  is the calculated dose at that point. This function,  $F$ , evaluates the overall closeness of the fit of the calculated dose during the iteration process to the desired dose.

Other researchers have shown that for the iterative process based on the image reconstruction analogy [Holmes 1994], the iterative process itself is equivalent to solving the problem for a least squares (quadratic) objective function. For this reason, Equation 2-29 is not explicitly evaluated during the iterative process, since the process inherently minimises the objective function. As well, the planning process used here is implemented solely as a means to achieve profiles for desired dose distributions, and the question of how optimal the solution is extraneous to the main thrust of this thesis. It is sufficient that the forward dose calculation correctly translates the energy fluence profiles that are arrived at by this process into the correct dose distribution. If the dose calculation works sufficiently well, then comparisons can be made between planned and delivered dose distribution.

The question of correctly delivering the profiles arrived in this chapter is addressed in the following chapter.

## Chapter 3 Beam delivery

There are numerous dynamic beam delivery options available commercially, for both clinical and research purposes. At the Institute where this work was performed, there are a number of these dynamic beam options available for use. Some of these, such as the enhanced dynamic wedge (EDW) (see Figure 1-8), employ the variation of a single machine mechanical parameter during beam delivery and are becoming more routinely used. Other options, such as the Varian Dynamic Beam Delivery (DBD) toolbox, are more advanced and used in a research capacity. The DBD toolbox is a limited release piece of research software, which allows for the modulation of numerous machine parameters concurrently while the beam is on. This Institute also has clinical Dynamic MultiLeaf Collimator (DMLC) software, which allows for the input of Segmented Treatment Table (STT) files for the MLC. These STTs may be generated for IMRT fields by our 3D TPS, but user calculated STTs may also be employed.

In this chapter, the delivery techniques used are covered, as well as the modelling of correction factors needed for the proper delivery of the required energy fluence profiles, which were calculated for the desired dose distributions. Refer to section 2.3 on inverse planning for further details on the calculation of the required energy fluence profiles.

### **3.1 Step and shoot vs. sliding window technique**

Delivering intensity modulated radiation therapy (IMRT) fields using an MLC may be accomplished in one of two ways. Both of the methods mentioned here are discussed widely in the literature and rest upon slightly different assumptions for the derivation of the required positions and motions in order to achieve the prescribed IMRT intensity profiles.

One method that is favoured by some [De Neve 1996, Boyer 1997] is the ‘Step and Shoot’ delivery method. This technique delivers multiple sub field regions by moving the jaws to define the first of these segments, then turning the beam on for a set number of monitor units, turning the beam off, then repeating this procedure for subsequent field segments. Numerous segments per field are required, typically on the order of ten to twenty. This method requires the calculation of the necessary jaw sequencing and weighting of the subfields to achieve some net planned energy fluence profile which, when combined with other IMRT fields, will yield a net desired dose distribution within the patient. A simple technique for achieving this is to split up the energy fluence map to be delivered into equal intensity levels. For example, to deliver a treatment in levels of 10% of the maximum energy fluence of the field would require binning of the field in 10 intensity levels. These levels would be treated as individual MLC shapes, starting with the first 10 %, where all regions are exposed. This is followed by an MLC shape which defines regions receiving >10% of the maximum dose, followed by an MLC shape which defines regions receiving >20%, and so on, ending with the last 10% where only those regions receiving the maximum field intensity are exposed. Delivery time and complexity depend on the degree of field modulation and the number of bins used, as well as how efficiently the MLC leaf sequences are planned.

The ‘Sliding Window’ technique [Ling 1996] sweeps opposing MLC leaf pairs across the field during a continuous beam on. Since the calculation of required leaf motions inherently accounts for delivery time optimisation [Spirou 1994], these DMMLC fields should be more efficient than the ‘Step and Shoot’ variety (how much more depends on the leaf sequencing algorithm used for the ‘Step and Shoot’ field segments). While time required for delivery will be less than that for the ‘Step and Shoot’ technique, it will still depend on the complexity of the required profile.

The ‘Sliding Window’ technique was employed for this work.

### **3.2 MLC and DMLC modelling**

The inverse planning calculation computes the required input energy fluence profiles, which must be delivered to achieve the desired dose distribution. To deliver these energy fluence profiles, STTs are calculated (see Figure 3-1). An STT is a list of the position of the machine parameters as a function of the cumulative number of MUs that are to be delivered by the time these positions are reached. In order to calculate the required STT to produce the correct relative energy fluence profiles, the energy fluence delivered by MLC fields and beam profiles must be well modelled.

In order to deliver the desired energy fluence profile, energy fluence must be related to the number of MUs delivered. The MUs are delivered as a function of machine parameter setting according to an STT. For a given MU setting, energy fluence output of an MLC field is known to vary as the aperture varies (as per the factors in discussed in section 2.2.1). The number of MUs required for each subfield in order to deliver the correct relative energy fluence profile depends on the application of a number of correction factors. These correction factors will ensure that the desired relative energy fluence profile is delivered.

In order to faithfully deliver prescribed energy fluence profiles using DMLC,  $S_c$  for MLC fields and field distributions (relative beam energy fluence profiles) of the MLC sub fields must be sufficiently well modelled. In this work the number of MUs to be delivered for each subfield is modified, according to the  $S_c$  factor (see section 3.2.2.1). This is required in order to predict the summed effect of the numerous and varying field shapes called for in the course of the delivery of dynamic fields. It is the sum of individually modelled static MLC sub fields that are used to model the overall output of the dynamic treatment. The  $S_c$  correction factor and field distributions are modelled using a projected focal and extra-focal source model (discussed in the following section).

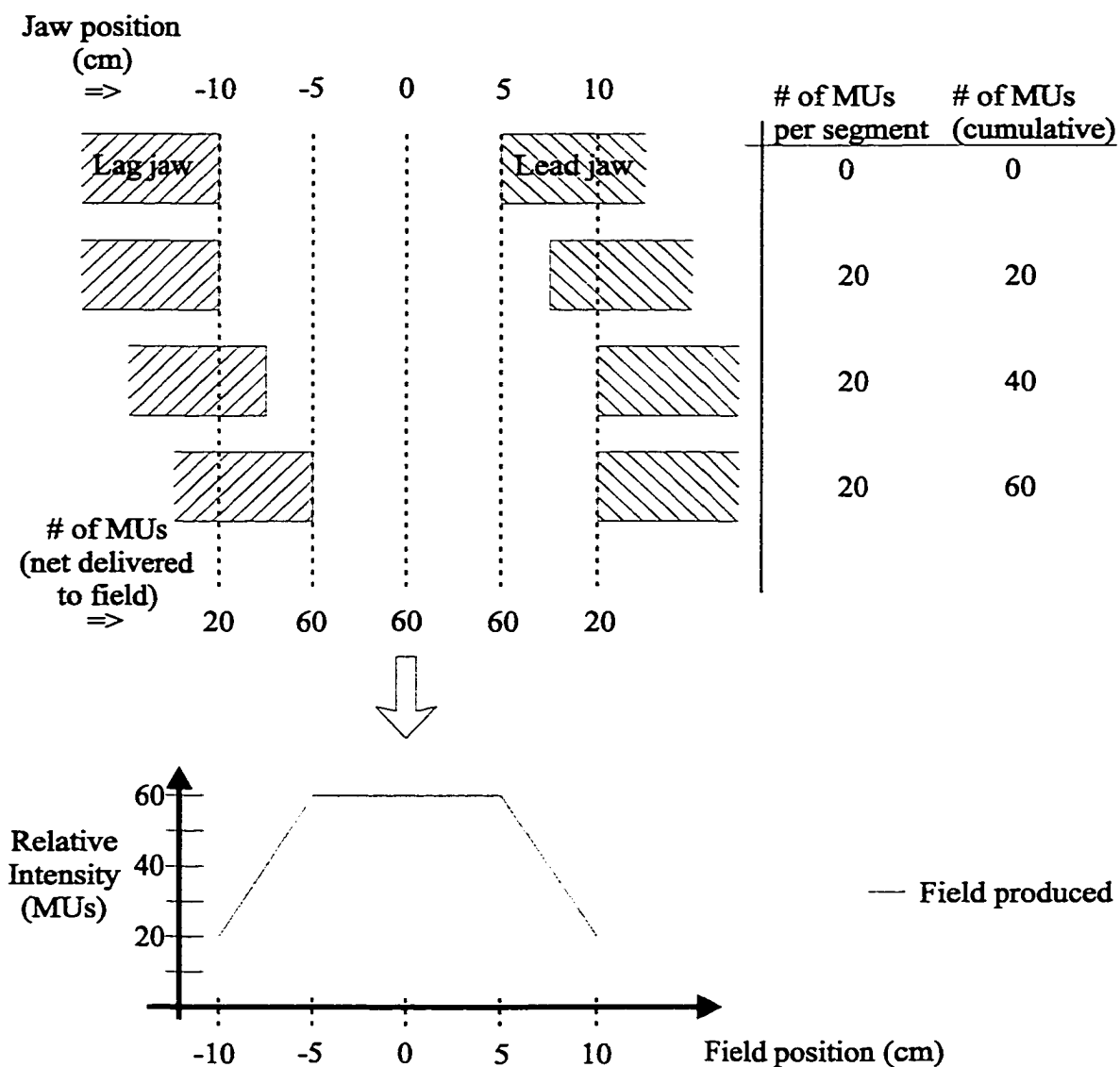


**Figure 3-1** A simple case of a dynamic treatment STT, shown for a pair of jaws and four control points.

In the IMAT delivery case, for a single projection from a given angle, the machine parameter varied is simply the MLC leaf positions. The leaf positions listed in the STT are known as ‘control points’, and there is uniform speed between control points. The required leaf positions as a function of the number of MUs delivered are initially calculated at the incident energy fluence profile’s resolution. For example, the number of MUs that will have been delivered will be calculated at 101 positions for each leaf, for a 10 cm wide field with 2 mm resolution. These positions are then sampled to form a smaller number of control points at equal MU intervals, due to a limitation in the maximum allowable number of control points in the STT. The number of control points required for good fidelity to the planned profiles is between 20 and 30, depending on the complexity of the profile [Budgell 1999]. A typical number used in this work is 26.

A 52 leaf MLC, with 1 cm thick leaf projections at isocentre (100 cm SAD), is employed in the course of this work.

### 3.2.1 The focal and extra-focal source model

It has been proposed that the variation in machine output as a function of collimator position can be modelled by assuming that a linac beam arises from two sources. These two sources are a main focal source, located at the target, and a diffuse extra-focal source located below the target at the plane of the flattening filter [Munro 1988, Sharpe 1995]. The extra-focal source is not a source per se, but rather an effective source arising from scattered photons originating primarily in the beam flattening filter. Modelling is then based on the idea that the variations in output and field intensity are due to the changing contributions from these two sources at the point of measurement. The change in head scatter may then be modelled as a change in the amount of the effective extra-focal and focal source that can be seen at the plane of measurement (see Figure 3-2 and Figure 3-3).

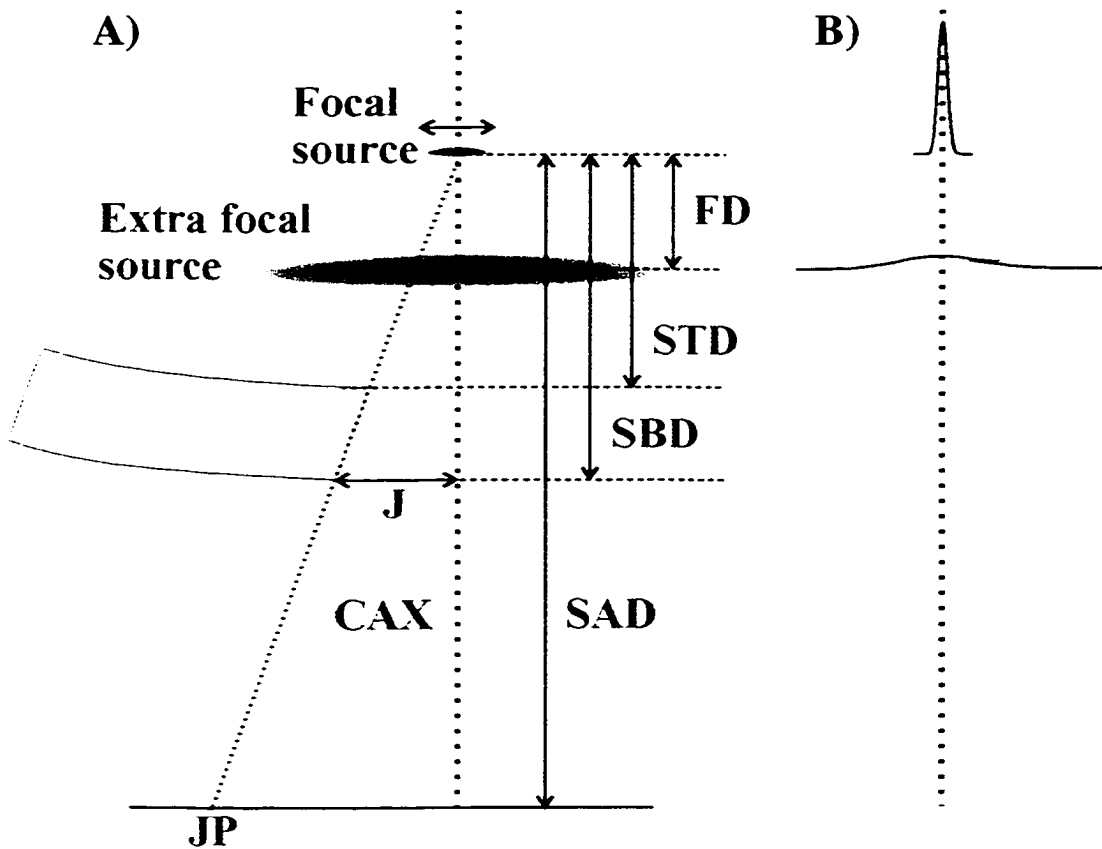


**Figure 3-2** Effective focal and extra-focal source model of linac output. A) The assumed geometry of the source distribution B) Representation of the relative distributions and weighting of the focal and extra-focal sources

Various source models have been proposed by a number of authors to account for both the change in relative linac output with field size and the variation in field distribution with jaw settings. Some of these models are based on assumed distributions such as a combination of  $1/r$  and linear distribution of the extra-focal source with heuristically defined parameters [Yu 1996]. Some authors have attempted to base their model on physical assumptions about the source of the head scatter [Hounsell 1998] which predict a largely linear distribution for the extra-focal source, with an added exponential function to model the output of larger fields.

Other researchers have made extensive measurements to characterise the focal and extra-focal source distributions. Various investigations [Jaffray *et al.* 1993; Loewenthal *et al.* 1993; Lutz *et al.* 1988] have found that the effective source distribution associated with the target (i.e. the focal distribution) is Gaussian and roughly symmetric. For a Varian 6 MV beam the FWHM value of the focal (target) distribution is about 1.4 mm ( $\sigma = 0.6$  mm). One investigation [Jaffray *et al.* 1993] reported that while most of the radiation (about 95% for a  $10 \times 10$  cm<sup>2</sup> field) originates from a focal spot, with the aforementioned standard deviation, the rest seems to result from a broadly distributed Gaussian extra-focal source with a  $\sigma$  of roughly 10 mm. Other researchers have found differing values for this extra-focal contribution [Sharpe 1995]. Monte Carlo modelling of the treatment head has characterised many other sources of scatter, in addition to the beam-flattening filter, originating in the treatment head [Anhesjo 1994, Anhesjo 1995, Liu 1997].

For this work, a multi-component extra-focal source with a combination of linear and Gaussian distributions is used. This approach was chosen in an attempt to account for the various complex distributions that exist in the treatment head. Experimental 6MV beam values, taken from the literature, for the distributions of the focal and extra-focal radiation,  $S_f$  and  $S_{e.f.}$ , as well as for their relative weightings,  $w_{t_f}$  and  $w_{t_{e.f.}}$  were used as a starting point for this model. The weighting and parameters required to describe the components of the extra-focal source were arrived at by

exhaustive search over a range of weights and values. The values were evaluated by their least squares difference with respect to measured data for in-air relative output and open field distributions. The advantage of this technique is that it employs already existing clinical data to derive these factors.

### 3.2.2 Geometric projection to source plane

Once an appropriate model is arrived at for the focal and extra-focal sources, the output and distribution of arbitrary field shapes is rendered computable by projecting the area of the field defining aperture (secondary collimator, MLC) to the planes of the sources (see Figure 3-3). This is done by making certain assumptions about the view of the focal and extra-focal source as seen from the plane of measurement. Sufficient information is available on the geometry and dimensions of the treatment head of a linear accelerator to allow the construction of a simple model for projecting the aperture defining the field as seen from the plane of measurement back onto the planes of both the focal and extra-focal source (i.e. flattening filter and the x-ray target).

#### 3.2.2.1 Collimator Scatter Factor

The combined effect of having both the MLC and secondary collimators is modelled by projecting both apertures. The smaller of the two fields is always used to define the calculation aperture. The collimator scatter factor ( $S_c$ ) at a given point (x,y) within a field is then

$$S_c(x, y) = S_{ef} \cdot [A_{jaws} \cdot A_{MLC}] + S_f \cdot [A_{jaws} \cdot A_{MLC}] \quad \text{Equation 3-1}$$

where A is a binary matrix of ones and zeros that represents the area defined by the projection of the collimating jaws and MLC onto the plane of interest, S is the source

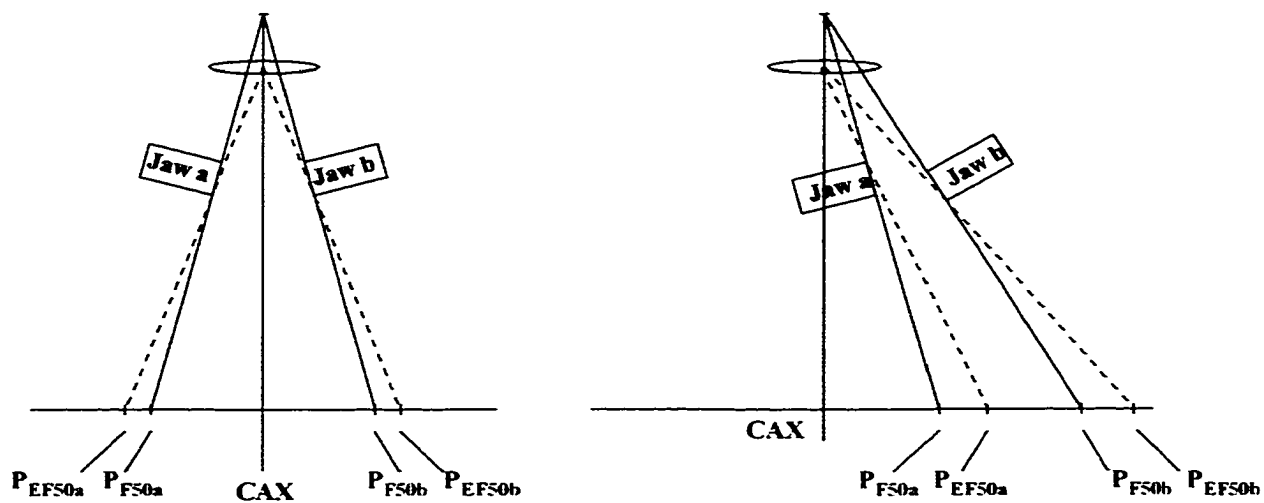


**Figure 3-3** Projection of 50% occlusion point for focal and extra-focal sources as a function of jaw position for A) symmetric and B) asymmetric jaw setting

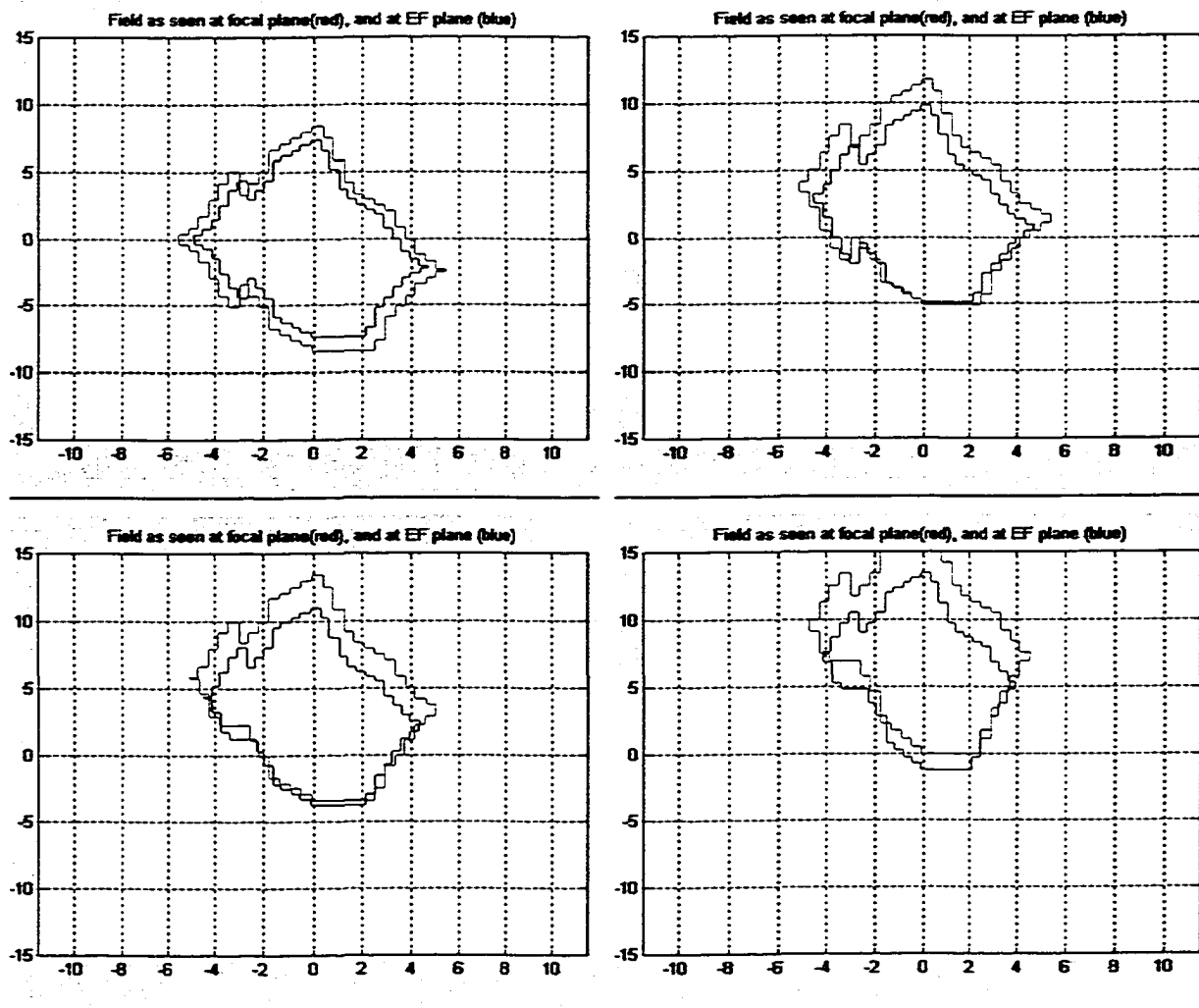


**Figure 3-4** Projections of an example MLC aperture shape from 100 cm SAD onto the focal (red) and extra-focal (blue) source planes, as seen from A) isocentre B) -4 cm off axis C) -6 cm off axis D) -10 cm off axis

distribution. These matrices are multiplied together, point by point. Since the areas  $A$  defined by the apertures at the plane of the sources may be represented as a 2D array of ones and zeros (a binary mask), the element by element product of the two matrices will give the minimum overlap region (effectively a logical AND operation). These areas are multiplied by the source distribution to give the relative energy fluence for that point relative to the other points in the field.

One prediction of this projection model is that the secondary collimator jaws should dictate the field output for all but the smallest field, since the MLC is closer to the plane of measurement and therefore can subtend a much larger area at the planes of the sources. The validity of this model, and comparisons of output versus field size for both MLC and collimating jaws are discussed in 5.2.2.1. The calculation of the output, both in terms of the relative in-air energy fluence profile and in terms of the variation in energy fluence per MU with field size, the  $S_c$  value, are discussed in the following two sections.

### 3.2.2.2 Relative Energy Fluence Profile

For this work the field distributions are modelled by the projection of relative areas of the focal and extra-focal sources as “seen” from the plane of measurement. This projection may be performed on a point by point basis, projecting the area of the aperture onto the plane of the effective sources (as per Equation 3-1). The point by point projection is, however, a time consuming process. Instead, as an approximation, the field distribution is obtained by

$$\Psi = wt_f \cdot (\Psi \cdot H_{f50}(x_1, x_2)) \otimes S_f + wt_{ef} \cdot (\Psi \cdot H_{ef50}(x_1, x_2)) \otimes S_{ef} \quad \text{Equation 3-2}$$

where  $wt_{f,ef}$  are the focal and extra-focal source weightings,  $\Psi$  is the energy fluence that would be measured at various points in the absence of collimation (i.e. data

measured from a large field scan), and  $H_{f,ef}$  is the Heaviside function (e.g. see Figure 2-11), whose edges are set by the positions of the end of the opposing leaf pairs, denoted  $x_1$  and  $x_2$ , in the plane of interest. Recall that  $*$  denotes a convolution, and  $S_{f,ef}$  is the distribution for the focal or extra-focal source, projected and scaled to the measurement plane. Adding an MLC transmission value to points lying outside the collimated region further modifies this output, and provides more realistic distributions, as will be discussed in Chapter 5.

### 3.2.2.3 Dose Output

The dose distributions calculated in this work by the SCA method, with corrections, are tested versus measured values, as well as those from an independent 2D TPS, and are discussed in Chapter 5. Since, however, this is not a true convolution and correction factors are applied to achieve correct dose distributions, no attempt was made to relate the calculated energy fluence directly to absolute dose.

It was decided to perform the dose per MU calculation separately from the dose calculation module in order to develop it as a method of performing a second check on IMAT deliveries. Dose per MU calculations for IMRT are problematic, as they are considerably different and more complex than traditional delivery techniques. Other authors have proposed various techniques for performing these sorts of calculations [Xing 2000, Boyer 1999]. The reference point used for dose per MU calculations should be in a low gradient region.

Since the dose calculations performed in the iterative inverse planning section are expected to yield the correct relative dose distribution, the absolute dose output is obtained through an empirical calculation (see section 2.2.1). In order to calculate the dose delivered by the IMAT delivery, it was decided to do so based on calculating the dose per MU to an appropriate point in the distribution and scale the relative distribution by this amount.

The dose for individual projections for a DMLC / IMAT delivery is computed at a point P some radial distance  $p$  and depth difference  $\Delta d$  from the centre of rotation (which is set to be isocentre in this work) where  $p$  and  $\Delta d$  are calculated by

$$p = x \cos \theta + y \sin \theta \quad \text{Equation 3-3}$$

$$\Delta d = y \cos \theta - x \sin \theta \quad \text{Equation 3-4}$$

where  $(x,y)$  is the co-ordinate of any general point of interest in the rotated reference frame where we wish to compute the dose, and  $\theta$  is the angle of the projection (as defined in Figure 3-5).

The total dose output to any point, shown for the general off axis case, for a DMLC / IMAT delivery should therefore be given by

$$\frac{D}{MU} = \sum_{i=1}^N CF_i(p) \cdot TPR_i \cdot AOF_i(p) \cdot S_{p_i} \cdot S_{c_i} \cdot IS(d) \cdot wt_i \quad \text{Equation 3-5}$$

where  $D$  is the dose,  $MU$  is the number of monitor units delivered,  $N$  is the number of projections,  $TPR$  is the tissue phantom ratio for that projection,  $AOF$  is the asymmetric output factor at the distance  $p$  for the point in that projection,  $S_c$  is the head/collimator scatter factor based on the largest collimated field size (defined by the largest extents of the leaves during the dynamic delivery),  $S_p$  is the phantom scatter factor based on the largest collimated field size, and  $IS(d)$  is the inverse square correction factor at depth  $d$ .  $CF_i$  is the dynamic compensator factor, and relates the ratio of the dose from largest collimated field size to the dynamic field.

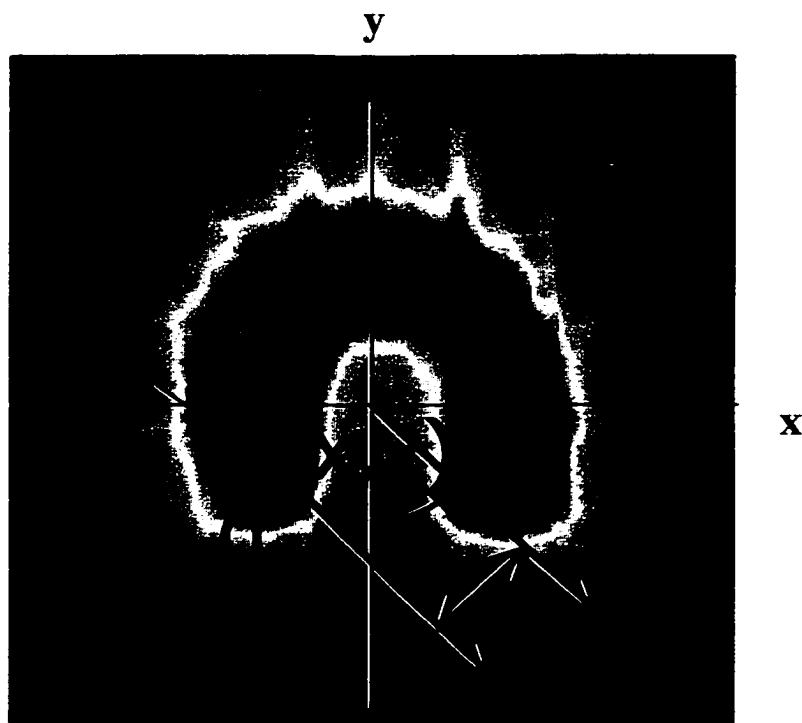


**Figure 3-5** The co-ordinates of a dose calculation point P for a planned dose distribution. This point's position is shown for a given projection relative to isocentre, in terms of a radial distance  $p$  and depth difference  $\Delta d$  from the isocentre.

$CF_{dyn}$ , the dynamic compensator factor for projection  $i$  and at point of interest (distance  $p$  and depth  $d$  from isocentre; see Figure 3-5), is computed as

$$CF_i(p) = \frac{\sum_{j=1}^M (\Psi_p)_j - (\Psi_p)_{j-1}}{\Psi_{total}} + TF \left[ 1 - \left( \frac{\sum_{j=1}^M (\Psi_p)_j - (\Psi_p)_{j-1}}{\Psi_{total}} \right) \right] \quad \text{Equation 3-6}$$

where  $M$  is the number of segments defining the dynamic treatment,  $\{\sum(\Psi_p)_j - (\Psi_p)_{j-1}\} / \Psi_{total}$  is the fraction of the total primary energy fluence delivered by projection  $i$  at distance  $p$  from isocentre,  $TF$  is the transmission factor through the MLC leaves and  $\Psi_{total}$  is the total energy fluence incident on the phantom during the entire delivery from projection  $i$ . This is a simple approximation to  $CF_{dyn}$  which holds best for fields which spend a portion of their delivery as an open field of largest collimated field size.

A more complex calculation, written in terms of the intensity (in MUs), could be written as a more explicit sum of static fields. This may be stated using the individual  $S_c$  values for the fields that expose the point of interest for  $\Delta I$  MUs out of the total number of MUs for the overall delivery, as per

$$CF_i(p) = \frac{Sp(fs_{eff}) \sum_{j=1}^M \Delta I(p) \cdot S_c(fs_j)}{I_{total} \cdot S_c(fs_{open}) \cdot S_p(fs_{open})} + TF \left[ 1 - (I^{st} term) \right] \quad \text{Equation 3-7}$$

$S_p$  is the phantom scatter factor based on the effective field size,  $fs_{eff}$ . The effective field size in the leaf motion direction is computed as

$$fs_{eff} = res \cdot \sum_{i=1}^N \frac{\Psi_i}{\Psi_{ref}}$$

**Equation 3-8**

where  $\Psi_{ref}$  is the median of the  $N$  non zero values of the desired energy fluence profile and  $res$  is the resolution at which the field is represented. The number of leaves used determines the dimension in the non-leaf motion direction. This is an approximate method of dealing with the scatter to the point of interest.

The weight of projection  $i$ ,  $wt_i$ , of  $N$  total projections is computed according to

$$wt_i = \frac{\frac{I}{(S_c)_i} (\Psi_i)_{max}}{\sum_{j=1}^N \frac{I}{(S_c)_j} (\Psi_j)_{max}}$$

**Equation 3-9**

The relative dose to all points is calculated in the dose calculation performed during the inverse planning procedure. The dose which is predicted to be delivered per MU setting is calculable by scaling the relative planned doses by the value computed above for the point  $(x,y)$ .

### 3.2.3 Leaf motions

Methods for determining the leaf motions required to realise a desired energy fluence profile are outlined, with varying simplifying assumptions, in the literature [Spirou 1994, Ling 1996, Lijun 1998]. More recent publications address the issue of correction function [Mohan 2000], although they are addressed in a dissimilar fashion. The method used in this work employs correction factors to improve adherence to the desired profile, and is detailed here.

These methods entail starting by calculating the ideal motions based on a number of simplifying assumptions. For all fields for which the motions are computed, the weighting of the subfields are normalised to give an equal energy fluence output per MU. From equations 2-8 and 4-15 it can be seen that the MU setting is proportional to the energy fluence. Because of this, the energy fluence profiles are often referred to as intensity profiles, and measured in MUs [Convery 1992, Spirou 1994, Mohan 2000]. Note that the non-uniformity of the in-air energy fluence output is corrected by reducing all points off the CAX by an in-air asymmetric output factor (AOF), as per

$$I_{net}(x) = \frac{I_{desired}(x)}{AOF_{air}(x)} \quad \text{Equation 3-10}$$

The intensity is often given in terms of monitor units, since the output at all points is normalised to the value for a 10 x 10 on the central axis where this quantity is related to a known energy fluence. The basic profile is defined by motions of leaf a and leaf b, where leaf a leads the sweeps across the field, and leaf b lags (see Figure 3-1 for example). The relation is given as

$$I_{net}(x) = I_b(x) - I_a(x) \quad \text{Equation 3-11}$$

where  $I_{net}$  is the 'intensity' of the desired profile, and  $I_a$  and  $I_b$  are the number of MUs delivered during the time when leaf a exposes the point x and leaf b covers it again. To determine the values for  $I_a$  and  $I_b$ , the method used is based on the assumption that, for positive profiles gradients  $\Delta I(x)$ , the leading leaf (leaf a, in this case) moves at a maximum velocity and for negative gradients, the lagging leaf (leaf b) moves at a maximum velocity. This can be expressed, for a positive gradient, as

$$I_a(x) = \sum_{x_{start}}^x I_a(x) + I_{min} \quad , \quad I_b(x) = I_a(x) + I_{net}(x) \quad \text{Equation 3-12}$$

where  $I_{min}$  is the number of MUs delivered while the leaf moves at a maximum velocity. A similar expression can be made for negative gradients. This method assumes a constant dose rate for the calculations, although this is not critical to the delivery as the delivery software modulates the delivery to ensure that required monitor units are delivered between control points. This method for calculating the leaf motions can be found in a number of places [Spirou 1994, MacKenzie 1996 MSc thesis].

The effect of imperfect collimation and transmission through the MLC leaves are herein after termed simply as ‘penumbral effects’. This effect has recently been explicitly addressed, albeit in a differing fashion, by other authors [Mohan 2000]. The effect of the energy fluence profile changes across the fields due to these penumbral effects is accounted for after the initial motions are calculated. At this point, a calculation of what the delivered profile will look like is made, using the method of section 3.2.2.2 for a large number of static fields. The desired profile is compared to the calculated prediction, and the profile that is input into the leaf motion routine is modified based on the predicted energy fluence profile, and the motions are recalculated. These corrections are then applied iteratively until an acceptable solution is found, as per

$$I_{i+l}(x) = I_i(x) + [I_{net}(x) - I_i(x)] \quad \text{Equation 3-13}$$

Finally, the effect of the varying  $S_c$  value due to varying MLC field sizes during delivery is accounted for by increasing the weighting of these subfields by the collimator scatter factor ( $S_c$ ). This final correction is applied by increasing or decreasing the intensity to this segment when the controller file is written. The

cumulative maximum value is adjusted appropriately at this time as well. The value of the intensity is modified, given that  $S_c$  varies according to field size, as per

$$STT(MU, fs)_i' = STT(MU, fs)_i + \frac{STT(MU, fs)_i}{S_c(STT(MU, fs)_i)} \quad \text{Equation 3-14}$$

where the field size for the STT entry  $i$  allows one to compute the change in the relative MU setting for this segment. The effect of backscatter into the monitor chamber [Hounsell 1998b] is not included, as it is not a factor for this design of monitor chamber [Duzenli 1993].

Another problem encountered with the delivery of DMLC fields is the so-called tongue and groove effect [Wang 1996, Webb 1997, van Santvoort 1996]. This problem arises from the tongue and groove regions (see Figure 3-6) where adjacent leaves interlock with each other. Points within the region below the leaves where they interlock may be exposed to a higher than expected energy fluence since they are only half blocked when only one leaf is above it (thus attenuating the beam with either the tongue or the groove). The solution is to synchronise the leaves so this does not occur. Various techniques to do this are outlined in the literature [see Lijun 1999]. The technique of van Santvoort is employed when appropriate due to its simplicity.

Other possible effects of other factors on delivery that have been noted are “timer error” [Biggs 1998] and hardware specific limitations [Cho 2000]. It is unclear what the impact of the “timer error” would be in the deliveries employed here, but it has been found to be dose rate dependent, and is assumed to be mitigated by the lower dose rates used in this work. The hardware specific limitations listed in the literature were not a concern for the unit used (such as with the minimum leaf gaps), or else were specifically included in the calculations (such as with the leaf velocities).

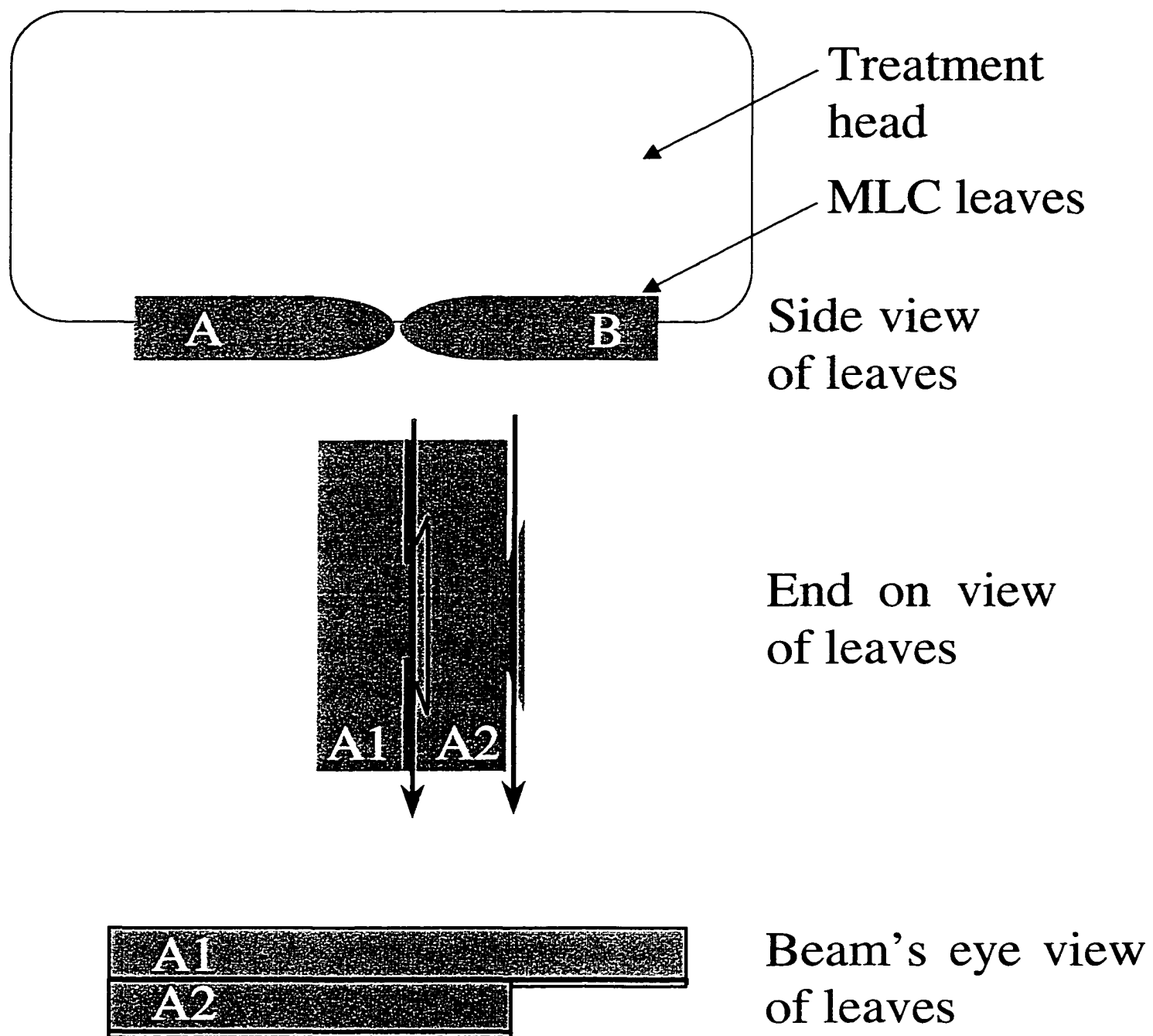


**Figure 3-6** The tongue and groove effect.

### **3.2.3.1 Discrete approximation to continuous motion**

It is known [Leavitt 1990b, MacKenzie 1996] that the delivery of dynamic fields may be approximated by the sum of discrete static fields, for a sufficiently small step size between fields. By extension, this should also mean that any cumulative effects of dynamic deliveries may be modelled as the sum of the effect for a discrete sampling of static fields. This should apply to the linac output as a function of both MLC and gantry motions, and is applied to both the relative profiles output and collimator scatter effect. The effect of this discrete sampling is discussed in Chapter 5 (see section 5.2.2.3).

### **3.2.3.2 Kinematics**

Motions of the MLC leaves are calculated with respect to a total number of monitor units per delivery. With the application of appropriate correction factors as per section 3.2.3, this corresponds to energy fluence incident on the patient / phantom surface.

MLC controller software controls the actual MLC motions. This software reads an ASCII file that defines leaf positions in the field and the number of cumulative MUs that should have been delivered when these positions are reached. These are termed control points, and the controller seeks to move the leaves linearly between these points. A sufficient sampling of control points is essential to accurate profiles generation, and it has been found [Budgell 1999] that roughly 30 points is good for moderately complex profiles. As well, it has also been noted in that equal MU spacing of control points is roughly equivalently useful as other spacing schemes. All motions are calculated assuming a fixed dose, and any delivery correction factors are accounted for outside the process of calculating the basic leaf motions.

The leaf speed (in mm/sec) for a change in position  $\Delta x$  which occurs over a given number of MUs can be divided by the dose rate (in MU/sec) to give

$$\frac{\text{mm}/\text{sec}}{\text{MU}/\text{sec}} = \text{mm}/\text{MU} \qquad \text{Equation 3-15}$$

which is the leaf speed in mm/MU. For a fixed dose rate, a number of MUs is proportional to a period of time. If the required leaf speed between two points in the dynamic delivery (in mm/sec) exceeds the maximum achievable speed (in mm/sec), a decrease in the dose rate serves to increase the effective leaf speed (in MU/sec). This is also true for any other machine parameter. The maximum speed at which any machine parameter can change may be stated in mm/MU (or, equivalently, degrees/MU for gantry rotation). Dropping the MU rate may accommodate segments requiring a speed exceeding the maximum machine parameter speed. Examples of maximum mechanical speed maximums are 35 mm/sec for leaf motion 5 degrees/sec for the gantry motion.

If the dose rate drops to accommodate DMLC speed limitations, the gantry will slow; this will have the undesirable effect of increasing arc time. One way to avoid this is by synchronising the arc delivery to the DMLC delivery such that the dose / angle relationship is designed to give continuous arcing. Given a known maximum dose rate, and given that the velocity of the gantry may be maintained at a maximum by synchronising it with the motions of the leaves, one may achieve a full single arc in minimum amount of time. The results of this technique are discussed further in Chapter 5.

### **3.3 Intensity modulated arc therapy**

The use of intensity modulated arc therapy (IMAT) was first proposed in 1995 [Yu 1995]. The proposal was to perform an inverse plan on a tumour site, then treat it by a series of successive passes where the MLC would define the outline of various intensity levels on each pass. For example, the inverse planned profiles could be broken into five equal intensity levels. The outline of these five separate intensity outlines would be delivered in five separate passes of the gantry arcing about the patient. This was shown to be possible in principle by performing an inverse plan using a commercial treatment planning system (Corvus), then delivering the prescribed profiles in five passes.

Although the technique of Yu has been demonstrated in principle, and some clinical trials are underway, there exist a number of problems with this approach. The time required for this delivery has been quoted as being about fifteen minutes, using five passes of the gantry. This value would increase linearly with the number of intensity levels used. As few as three passes have been employed, but the complexity and precision of the delivered profile decreases with fewer arcs. As well, the number of passes could double for a bifurcated tumour.

The typical treatment slot allotted for treatment at this Institute is about twelve minutes. This includes the time required for patient transit in and out of the treatment room, set up time and the actual “beam on” time. Reducing overall treatment time to the smallest value possible is therefore highly desirable. Furthermore, increasing the automation such that the delivery is part of a single beam delivery, as opposed to multiple arcs or multiple IMRT fields, reduces the treatment complexity.

The solution that is proposed in this work is to combine several of the techniques already developed by the author [MacKenzie 1996] into a single modified IMAT delivery. The idea is to use a single gantry rotation to delivery all the required

intensity profiles at once. A treatment plan is based on twenty-four profiles equally spaced in a  $2\pi$  geometry about the phantom. These multiple ports could then be delivered using a sliding window DMLC, with the direction of the sweep reversed from one projection to the next, during the continuous rotation about the phantom. The sweep direction is flipped in order that the leaf positions for the next profile to begin, roughly, where the leaves from the previous profile end. The profiles are planned in the middle of the arc where they will be delivered, and each profile segment is delivered over a  $\pi/12$  ( $15^\circ$ ) portion of the entire  $2\pi$  ( $360^\circ$ ) arc.

## Chapter 4 Verification

Validation of this work is contingent upon dosimetric verification. To this end two dosimeters are chiefly employed, namely ion chambers and radiographic film. As well, a number of different scanning tools were employed. From a dosimetric verification standpoint, it is best to confirm results by more than one dosimetric modality. This ensures a degree of independence in the verification of any cited results.

In order to verify the predictions of the dosimetric calculations and to justify the various corrections that are made to the field, one must be able to assess, accurately and reproducibly, the relative fluence or dose delivered during a dynamic treatment. This requires having both calculation routines, discussed in Chapter 3, and dosimeters, discussed here, that are capable of handling dynamic treatments. There have been a number of studies using a variety of dosimeters with dynamic fields, especially as they relate to dynamic wedge and enhanced dynamic wedge [Elder 1995, Leavitt 1997]. Given the temporally varying nature of the dynamic field, a good dosimeter should be capable of giving the integrated dose to a profile in a reasonable amount of time.

### 4.1 *Dosimetric concepts*

#### 4.1.1 Ionising Radiation Fields

Ionising radiation can be defined as radiation (e.g. photons or electrons) with energy of a few eV and above, as this is enough energy to eject the most loosely bound electrons from an atom's valence shell. Electrons so liberated will in general have some fraction of the energy imparted to them left over as kinetic energy. This energy will be transferred to atoms in the vicinity by numerous Coulomb interactions.

Photons are referred to as indirectly ionising radiation, as they impart their energy to media in relatively few large interactions. The electrons they set in motion interact with many other atoms, depositing a certain amount of energy per unit mass (i.e. dose). These electrons are referred to as directly ionising radiation.

In addition to the empirical factors discussed in section 2.2.1, a number of fundamental dosimetric concepts need to be introduced in order to discuss further the reasons for dosimetry choices made in the course of this work.

Radiation measurements for clinical purposes are performed in a mass of material, which is designed to emulate the radiological properties of the human body. Such masses are referred to as phantoms. Since the soft tissues of the human body are predominantly water, phantoms are typically water equivalent in terms of their interaction with ionising radiation. To this end, measurements are often performed in water or in a radiologically water equivalent plastic (e.g. Plastic Water™ or Solid Water™). Measurements performed in the course of this work were carried out in a variety of phantoms.

In order to quantify any beam of radiation, one must first define a number of terms that describe its energy spectrum and intensity. One may define a quantity called the fluence as the expectation value of the number of particles ( $N_e$ ) across a given area ( $dA$ ),

$$\Phi = \frac{d}{dA} N_e$$

**Equation 4-1**

which is typically given in units of  $m^{-2}$ . In order to describe how the fluence may vary with time, one may further define a quantity called the fluence rate, or flux density

$$\phi = \frac{d}{dt} \Phi$$

**Equation 4-2**

and this is usually given units of  $\text{m}^{-2}\text{s}^{-1}$ . The energy carried by the field across some small area may be described in terms of energy fluence

$$\Psi = \frac{d}{dA} E$$

**Equation 4-3**

The flux of energy across a given area over some period of time is the energy fluence rate

$$\psi = \frac{d}{dt} \Psi$$

**Equation 4-4**

For a polyenergetic beam, one must integrate over the energy spectrum as well as time in order to obtain the total energy carried by the field.

Historically, one of the earliest means of defining the energy of a beam of photons was its ability to ionise a given quantity of air. This quantity, called exposure, is defined as

$$X = \frac{dQ}{dm}$$

**Equation 4-5**

$dQ$  is the total charge produced by electrons that are set in motion by photons in a mass  $dm$  of dry air at standard temperature and pressure. Exposure is measured in C/kg (SI units) or in Roentgens, which is the historical unit of exposure, where  $1 \text{ R} = 2.58 \times 10^{-4} \text{ C/kg}$ . Exposure does not, by definition of the International Commission

on Radiation Units and Measurements (ICRU), include ionisation arising from Bremsstrahlung.

A quantity that is closely related to radiation dose is KERMA, which stands for Kinetic Energy Released per unit MAAss, and is defined as

$$K = \frac{dE_{tr}}{dm} \qquad \text{Equation 4-6}$$

This quantity differs from dose (energy absorbed per unit mass), as the energy released at any given point in a medium may not be deposited at that point. For example, energy may be transferred to an electron via a Compton interaction, and that electron may travel some distance, depositing its kinetic energy in the medium via numerous Coulomb interactions along its pathlength.

Radiation dose,  $D$ , is expressed in units of energy deposited per unit mass, and is defined as

$$D = \frac{dE_{dep}}{dm} \qquad \text{Equation 4-7}$$

This differs from KERMA in that it is the energy *deposited* at a point in a medium from charged particles, and is measured in SI units of Gray (J/Kg). Historically, dose was measured in rads (100 ergs/g) – this is the reason for the continued widespread use of cGy (where 1 rad = 1 cGy). In order to give an idea as to scale in terms of radiobiological effects (RBE), typical radiotherapy treatments give somewhere in the neighbourhood of 50 to 80 Gy in 2 Gy daily fractions, whereas a single whole body dose in the region of 5 Gy is usually fatal.

#### 4.1.2 Photon Interactions in Matter

As photons pass through matter, they may undergo a number of interactions. There are basically five major interactions of radiation with matter: photoelectric effect, Compton interaction, pair production, Rayleigh scattering, and photonuclear interactions. For each of these effects, one can say that, if an incident beam of intensity  $I_0$  particles is incident on  $N$  nuclei per unit area (most often measured in barns, in the case of cross-sections; 1 barn =  $10^{-24}$  cm<sup>2</sup>), and results in a transmission of particles  $I_{trans}$ , then the total atomic interaction cross-section is defined as

$$\sigma_a = \frac{I_{trans}}{(I_0)(N)} \quad \text{Equation 4-8}$$

The atomic interaction cross-section,  $\sigma_a$ , may be converted to the linear attenuation coefficient,  $\mu$ , for this interaction by using the relation

$$\mu = \frac{N_A \rho}{A} \sigma_a \quad \text{Equation 4-9}$$

where  $Z$  is the atomic number,  $N_A$  is Avogadro's number and  $A$  is the atomic weight;  $\mu$  is the linear attenuation coefficient. The combined linear attenuation coefficients for all the pertinent effects is the sum of the individual linear attenuation coefficients for each of the photoelectric ( $\tau$ ), Compton ( $\sigma$ ), pair production ( $\kappa$ ), Rayleigh ( $\sigma_{coh}$ ), and photonuclear ( $\sigma_{p.n.}$ ) interactions; so

$$\mu = \mu_\sigma + \mu_{\sigma_{coh}} + \mu_{p.n.} + \mu_\tau + \mu_\kappa \quad \text{Equation 4-10}$$

The mass attenuation coefficient ( $\mu/\rho$ ) has units of  $\text{cm}^2/\text{g}$  and describes the linear attenuation apart from the influence of density. The  $\mu$  term is the linear attenuation coefficient. The fractional loss of photon fluence across a distance  $dx$  is then given as

$$\frac{d\Phi}{\Phi} = -\mu dx \quad \text{Equation 4-11}$$

In other words, the transmitted intensity through a length of material  $L$  is

$$\Phi = \Phi_0 e^{-\mu \cdot L} \quad \text{Equation 4-12}$$

The various interactions mentioned above tend to dominate in different incident energy domains, as well as atomic number domains of the absorber. Some do not contribute appreciably to energy deposition. Roughly speaking, the photoelectric effect dominates at low energies (e.g. 0-100 keV), the Compton effect dominates at medium energies (e.g. 100 keV - 5 MeV), and pair production dominates at very high (high for the purposes of radiotherapy, at least) energies (e.g. 5 MeV +). The photonuclear effect has a very low contribution for radiotherapy energies, and Rayleigh scattering tends to be unimportant for dose deposition.

The deposition of dose in a given volume element is ultimately the result of the transfer of energy from the radiation field to the medium via charged particles. The transfer of energy from x-ray photons to a medium results when these photons set charged particles (e.g. electron) in motion through various interactions. Deposition of energy is a two step process, with the photons giving rise to energetic particles (i.e. KERMA), which in turn impart energy to the medium or to other particles via multiple Coulomb events (i.e. dose).

If there exists the condition of charged particle equilibrium (CPE) then for every charged particle that leaves a volume of interest, another one of the same type and with the same energy expectation value enters. This means that even though the energy imparted to some particles in a volume of interest may be deposited outside that volume by these particles, for every one of those particles that deposit some of their dose outside that volume, another particle which was set in motion outside the volume of interest will deposit an equal amount of energy inside the volume.

#### 4.1.3 KERMA and Dose

As has already been noted, the transfer of kinetic energy to a particle in a medium (KERMA) is not the same as dose deposition. The energetic particles may, after acquiring kinetic energy, move along a path giving up this energy through many small Coulomb interactions. The path will terminate when the particle comes to rest, and this may occur some distance from where it was initially set in motion. Consequently, it may be that much of the energy that the particle received in a volume of interest is deposited outside that volume. The energy released may also be re-radiated as a photon, which again may leave the volume of interest before imparting some or all of its energy.

Recalling that KERMA is defined as the energy transferred to the medium, we can further refine this as

$$K = K_c + K_r$$

**Equation 4-13**

which is to say that KERMA has two components: a collision component ( $K_c$ ) and a radiative term ( $K_r$ ).

At the lower range of the energy of charged particles that are set in motion in a given medium (almost entirely electrons), energy is transferred to the medium via numerous collision interactions. The collision KERMA is related to the energy fluence

$$K_c = \left( \frac{\bar{\mu}_{en}}{\rho} \right)_{E,Z} \psi \quad \text{Equation 4-14}$$

where  $\left( \frac{\bar{\mu}_{en}}{\rho} \right)_{E,Z}$  is the mass attenuation coefficient (which is a function of energy E of the particles, and atomic number Z of the medium). Where charged particle equilibrium exists one may equate primary dose to KERMA, as per

$$D = K_c = \left( \frac{\bar{\mu}_{en}}{\rho} \right)_{E,Z} \psi \quad \text{Equation 4-15}$$

## 4.2 Dosimeters

Although a point detector would be required in order to truly measure energy fluence; one may attempt to take measurements that are as close to being point measurements as possible. This means using a minimum amount of buildup (i.e. the amount of material needed to achieve transient CPE), with a suitable small active volume (i.e. the region where dose is measured).

As well, an integrating dosimeter is required in order to evaluate the performance of any dynamic techniques. The dosimetry techniques used in these studies were chiefly of two types: film measurements and ion chamber array

measurements. Some use was also made of a single ion chamber for point measurements and profile scans.

Many of the considerations for the measurement of dose are the same as those for the measurement of fluence, most notably the requirement that, for dynamic fields, the dosimeter be able to handle time integrated fields.

#### 4.2.1 Film

Film dosimetry is based on the response to radiation of an emulsion of microscopic grains of the crystal silver bromide (AgBr) on a cellulose substrate. When film is exposed to ionising radiation, those portions of the silver bromide crystal lattice that interact with charged particles are converted to neutral silver, and the liberated bromide ions diffuse into the gel matrix of the film. The neutral silver constitutes a latent image of the field. Developing converts the rest of the silver in the grains to neutral silver. This reaction occurs in all the grains, but as it acts much more rapidly in areas with a latent image, the developing is terminated after a very brief time so that only the latent image is revealed. The film is then treated with a stop bath to halt the developing process, and the undeveloped AgBr is then removed with a 'hypo' solution, leaving the opaque silver grains.

The developed film can be scanned with a light source, and the intensity of the light transmitted through the film is then measured. The optical density (OD) is defined in terms of the incident and transmitted light as

$$OD = \log \left( \frac{I_0}{I_t} \right)$$

**Equation 4-16**

where  $I_0$  is the incident intensity of the light and  $I_t$  is the transmitted intensity (see Figure 4-1). Optical density is then converted to dose using a calibration function. Film dosimetry for radiation fields has a long history, dating back to the discovery of radiation. The relative response of film was characterised early on by Hurter and Driffield, and this response function is thus named the H and D curve (see Figure 4-2).

Film has a number of advantages over other detectors, as well as a number of drawbacks. Film is very dependent on the emulsion (batch characteristics), processing conditions and energy spectrum of the incident radiation [Williamson 1981]. It does, however, have a fair ease of use, very high spatial resolution, good reproducibility, and not only serves as an integrating dosimeter, but also gives a permanent record of the field, once it is processed.

The utility of film in the study of dynamic fields has been widely noted [Leavitt 1990, 1994a,b,c, Klein 1995, Wang 1996], mostly due to the speed with which film may be used, its relative facility of use, and the ease with which it acquires time integrated dosimetric information. While difficulties associated with using film for photon dosimetry are also well documented [Anderson 1979, Williamson 1981, Hale 1994, Leavitt 1994b,c], it is possible to achieve reasonable results using film dosimetry, through proper calibration techniques (within 2 or 3 % of the ion chamber values [Williamson 1981, Hale 1994]).

The calibration of film is based on the H and D film response curve. Within a certain dose region, the response of film to increasing dose is roughly linear (notwithstanding energy degraded photons). It is possible to construct a curve of optical density versus dose based on films exposed to fields producing known doses in the medium. This curve, in turn, allows for the use of film for the determination of dose to points within the medium when irradiated by other fields, provided there are similar exposure conditions (e.g. same depth, photon spectrum).

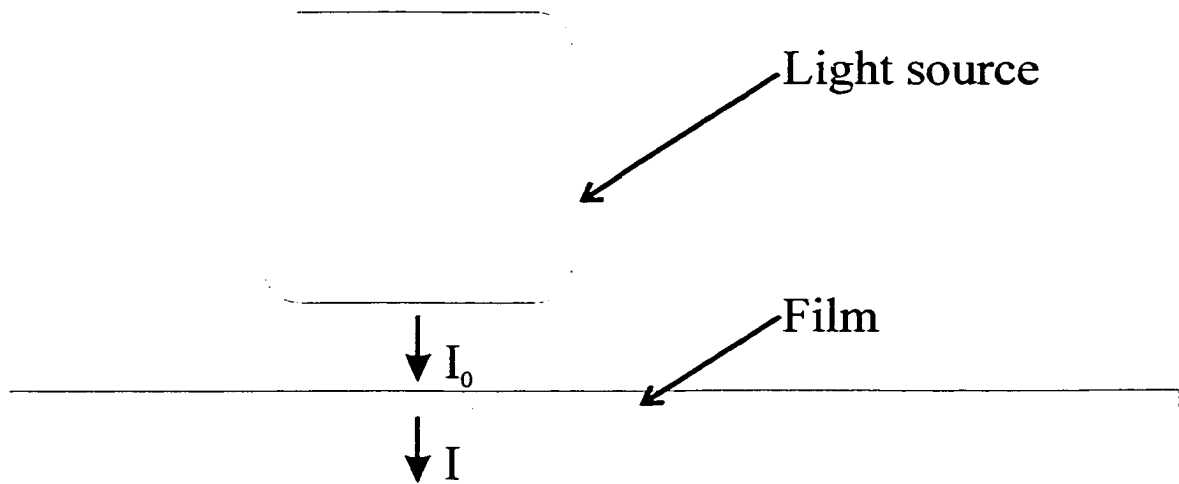


**Figure 4-1** Measurement of the optical density (OD) of a radiographic film.

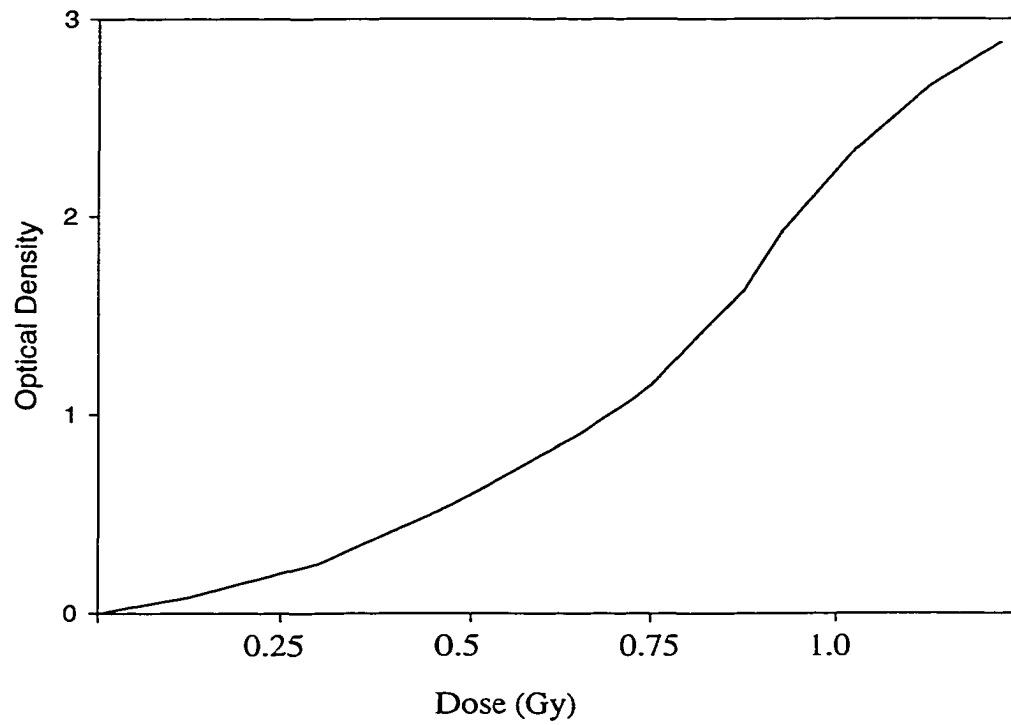


**Figure 4-2** The characteristics of a typical dose to optical density response curve of film, known as the Hunter and Driffield, or H & D, curve.

An H&D curve was constructed for any desired single depth in phantom, due to depth dependent variations in film response [Hale 1994]. The method employed in this work for BEV planar films is as follows. Several films, utilising the same field size as the films to be converted, are exposed parallel to the beam, in arbitrary 20 MU increments (e.g. 20 to 140 MU). A finer sampling of response was used in the non-linear region of the H&D curve (both in the low and high dose regions; see Figure 4-2). The dose values at the depth of interest are calculated from the MU settings using the empirical dose conversion factors outlined in section 2.2.1, and the OD to dose conversion curve then constructed. These films give a depth specific conversion function for profiles.

As well, conversion curves are constructed for rotational treatments by delivering 360° arcs with a 10 x 10 cm<sup>2</sup> field setting, and with incremental MU settings (as above). These MU settings for the arc are converted to dose using the empirical dose conversion factors outlined in section 2.2.1, and the measured OD is used to construct an H&D curve. Doses for these arcs are also confirmed by point ion chamber measurements. The results are compared to planned distributions and measured values (see 5.4). This technique is similar to that used by others [Burman 1997, Tsai 1999b] for verification of a tomotherapy dose using the Nomos system.

In order to achieve maximum reproducibility with film, all films are processed at the same time (i.e. the same night, all within a maximum of two or three hours of each other), and a set of calibration films is acquired for each measurement session. As well, all films are drawn from the same film batch. This is necessary as the accuracy of film dosimetry drops for films processed separately, as well as for films taken from different batches [Waggener 1982]. For each film, a small portion is cut off and processed, unexposed, to provide a background fog reference.

#### 4.2.2 Ion chamber and ion chamber array

The ion chamber has long been recognised as the gold standard for dosimetric measurements. This recognition exists for a number of reasons: high precision, relatively little energy dependency, relative ease of use, and good long term stability. Furthermore, readings taken from an ion chamber can, upon calibration at a national standards lab (NRC for Canada), be readily and reliably converted to dose [AAPM 1983, AAPM 1999] through the use of cavity theory. Cavity theory seeks to describe the effect of replacing part of the medium of interest with a measuring cavity of a different medium; the reader is referred to any basic text on radiological physics (e.g. Attix 1986). Ion chambers are also popular for relative measurements as well, since the electrometer readouts they produce are directly proportional to dose when CPE exists. The major drawback associated with the ion chamber use is that they require electronic equilibrium in order to give meaningful data, an assumption of cavity theory. As well, they do not lend themselves to easy acquisition of time dependent field data (the collection of which requires a number of time consuming point measurements in order to achieve reasonable spatial resolution).

The basis of ion chamber operation is the measurement of the ionisation of the air inside its volume. For typical practical ion chambers, this is a small volume of air, typically on the order of 0.1 - 3 cm<sup>3</sup> [Attix 1986]. The mean amount of energy expended to produce a single ion pair in dry air at NTP,  $W$ , is equal to 33.97 eV (33.97 J/C). This value is roughly invariant over a wide range of electron energies and gas pressures. The ionisation measured can be converted to the exposure,  $X$ , for a certain amount of collected charge and known mass of air. This value of exposure can, knowing the value of  $W$  per charge  $e$ , be related to dose by

$$D_{air} = \left( \frac{\overline{W}}{e} \right) \cdot X = K_c \quad \text{Equation 4-17}$$

under the assumption of CPE.

Cylindrical chambers consist of a central charged wire and an outer charged shell held at a fixed potential (usually around 300 V) with respect to one another. The wall of the chamber is made of a high density material with many of the radiological properties of air. The central electrode collects the charge generated in the air volume. The charge thus collected is proportional to the radiation dose deposited within the chamber volume and can be related to the dose that would have been given to the medium at that point, using cavity theory as discussed at the start of this section (4.2.2). For practical ion chambers, the volume of air used is quite small, so the signals are typically small (on the order of  $10^{-9}$  Coulombs).

Some use is made of a linear ion chamber array (Wellhöfer CA24). This array features 23 ion chambers with a 2 cm spacing between chambers. The ion chamber array allows for (relatively) fast acquisition of point measurement profiles of dynamic fields. The ion chamber array has been outfitted with a number of brass buildup caps, also referred to as brass mini phantoms [see, for example, Hounsell 1998]. This was done in order to allow for the collection of relative in-air energy fluence profiles -- this approximation is assumed to hold true due to small beam cross-section and minimum build up used.

The practical time limitations on single point measurements of a true dynamic beam delivery are lessened for single dynamic profiles when using an ion chamber array. This is due to the fact that the data is now being collected at a minimum 2cm resolution, as this is the spacing of the 23 chambers in this ion chamber array. Moving the array and repeating the measurement can therefor increase the measurement sampling resolution. The ion chamber array easily gives a reading with high accuracy and 2mm spatial resolution in minutes for the average dynamic field (assuming 100MU, 0.3-0.5 minutes per dynamic field, 10 acquisitions).

The use of ion chambers for the evaluation of radiation fields is commonplace. This is mostly due to the reliability and reproducibility of such measurements, as well as the ability to convert measurements to absolute dose.

The chief drawback for the use of a single ion chamber in the evaluation of a dynamic field is their inability to do rapid integrated measurements of temporally variant fields. It is possible to collect data for a single point, and move the ion chamber to collect data from other points, but this becomes quite time consuming if good spatial resolution of the field is desired. Furthermore, if a summation of static fields is being used to simulate a dynamic treatment, where field production can take on the order of twenty minutes, then this limitation is unacceptable. As well, charge leakage from the electrometer would make this technique non-viable for dynamic simulations. Another drawback of the ion chamber is that it requires electronic equilibrium in order maintain a calibration traceable to the national laboratory.

### ***4.3 Phantoms and set-up used***

The phantoms used chiefly throughout these investigations were of two types: cubical and cylindrical. Cubical phantoms were either in the form of a water tank (48 cm<sup>3</sup>) or slabs of water equivalent plastics (minimum 25 cm<sup>3</sup>). The cylinder used for these investigations was cut into sectional discs, and was composed of water equivalent plastic (polystyrene), and was 20 cm in diameter.

The polystyrene cylinder phantom was used for film dosimetry of multi-field deliveries. Films were cut to match the outline of the cylinder and encased between two discs, and were then light packed in a dark room using opaque black vinyl tape. Other discs are stacked around these to yield a phantom of approximately 30 cm in length.

The cylinder was then placed on a 10 cm thick slab of Styrofoam™, which was located at the edge of the treatment bed. The Styrofoam™ was placed such that most of it was hanging over the end of the bed, with a large counter balance (roughly 45 kg of lead) placed on the end remaining on the bed. The set up is shown at various stages of delivery in Figure 4-3. This set up allows the gantry to arc completely around the phantom without interference from the treatment couch (i.e. without having any portion of the arc delivery that passes through the couch or couch rails). The Styrofoam™ is assumed to be radiologically air equivalent (a simple attenuation measurement shows a 0.9 % attenuation for 10 cm of Styrofoam™).

#### **4.4 Measuring systems**

A Wellhöfer™ water tank scanning system was used extensively in these investigations, in conjunction with a single ion chamber and an ion chamber array. The water tank measures 48 cm by 48 cm by 48 cm, and is made of acrylic plastic tank which can be rotated and translated, and filled with water for use as a water phantom, or emptied to measure in-air profiles. This system is capable of moving a dose probe to  $\pm 0.1$  mm precision in positioning.

The Wellhöfer™ film scanning system was used to do the initial film measurements and verification. It is also capable of  $\pm 0.1$  mm precision in positioning. A Vidar film scanning system was used to do much of the final film measurements and verification. It differs from the Wellhöfer™ film scanning system in that it employs a line source for measurement of optical density, instead of a 'point source'. A single scan takes on the order of 5 seconds, and scans are acquired at a user defined resolution. In this work, the films were scanned at 75 dpi, or about 0.34 mm per pixel, and the images are saved as 8-bit bitmaps. As with a conventional scanner, a series of calibration films were also exposed, and these converted to bitmaps. Pixel value is correlated to dose, and a user defined fitting function is generated and inspected to

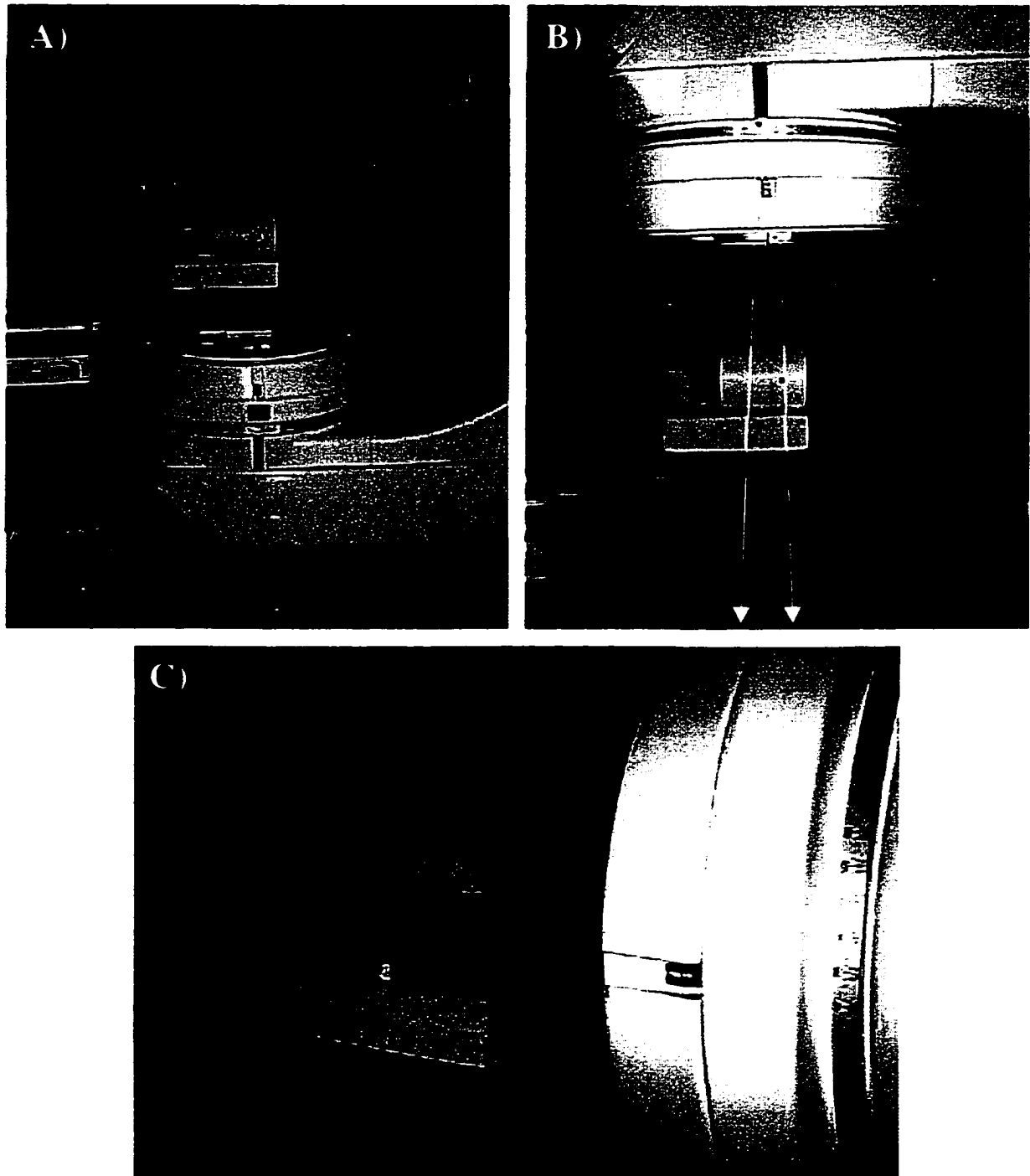


**Figure 4-3** Experimental set up used for the delivery and verification of IMAT dose distributions. Shown at A) starting position for delivery, B) at midpoint of arc (along with depiction of field area covered), and C) at 90 degrees.

view the fit to the calibration points. A complete table of pixel value to dose is then generated, and conversion and resampling to a desired resolution was done with a commercial math package.

Measured transverse slice dose distributions and calculated / predicted dose distributions are represented by two-dimensional arrays. Comparison between two fields was done, if necessary, by sampling the arrays to the same resolution. A linear interpolation scheme was employed throughout for any resampling. A two step process was used to align any two fields. The first step was to use an edge detection scheme to create a binary map of the two fields. These binary maps were then used with a Fourier correlation (see section 2.2.3.2) to determine the offset, and using this offset value the fields were then aligned. The degree of agreement was then assessed. The idea for this technique was inspired by a paper on work, similar in principle, on the alignment of electronic portal images for quantifying patient set up [Jones 1991].

## Chapter 5 Experimental results

The central thesis of this work is that one may, in principle, deliver intensity modulated arc therapy (IMAT) treatments in a single gantry rotation with the use of sliding window dynamic multileaf collimator (DMLC). The demonstration of this type of delivery has required the development of a number of components. Planning, modelling and delivery aspects have focused chiefly on the 2D planar dose distribution case, with some concluding attention paid to the extension to the 3D case, which is treated as a multiple 2D slice case. As such, some of the methods used in the modelling are approximate, and could be improved upon, but serve adequately for this work.

The components needed for this work have been developed, and each is to some degree independent of the others. For example, the inverse planning calculations may be considered separate from the delivery calculations, and the dose calculation used in the inverse planning step could be replaced with another dose calculation scheme without unduly affecting the end result. As well, the calculations needed for the delivery may be considered separately from the dosimetry of the fields. It is therefore important to consider these sections somewhat independently of each other, and any one section may be improved upon in future investigations.

In the following sections, an attempt is made to examine the work in the order in which it was developed, which is largely the order in which the various steps are required for the delivery (see Figure 5-1). A general inverse planning technique is needed to determine required beam energy fluence profiles for delivering a desired dose distribution. Beam modelling is required for the dose calculations, and dose calculations in turn are required for the iterative aspect of the inverse planning section. Beam modelling is required again for leaf motion calculation and STT program to ensure beam energy fluence profiles match the desired profiles as closely as possible. Finally, dosimeters and a dosimetric calculation method appropriate to

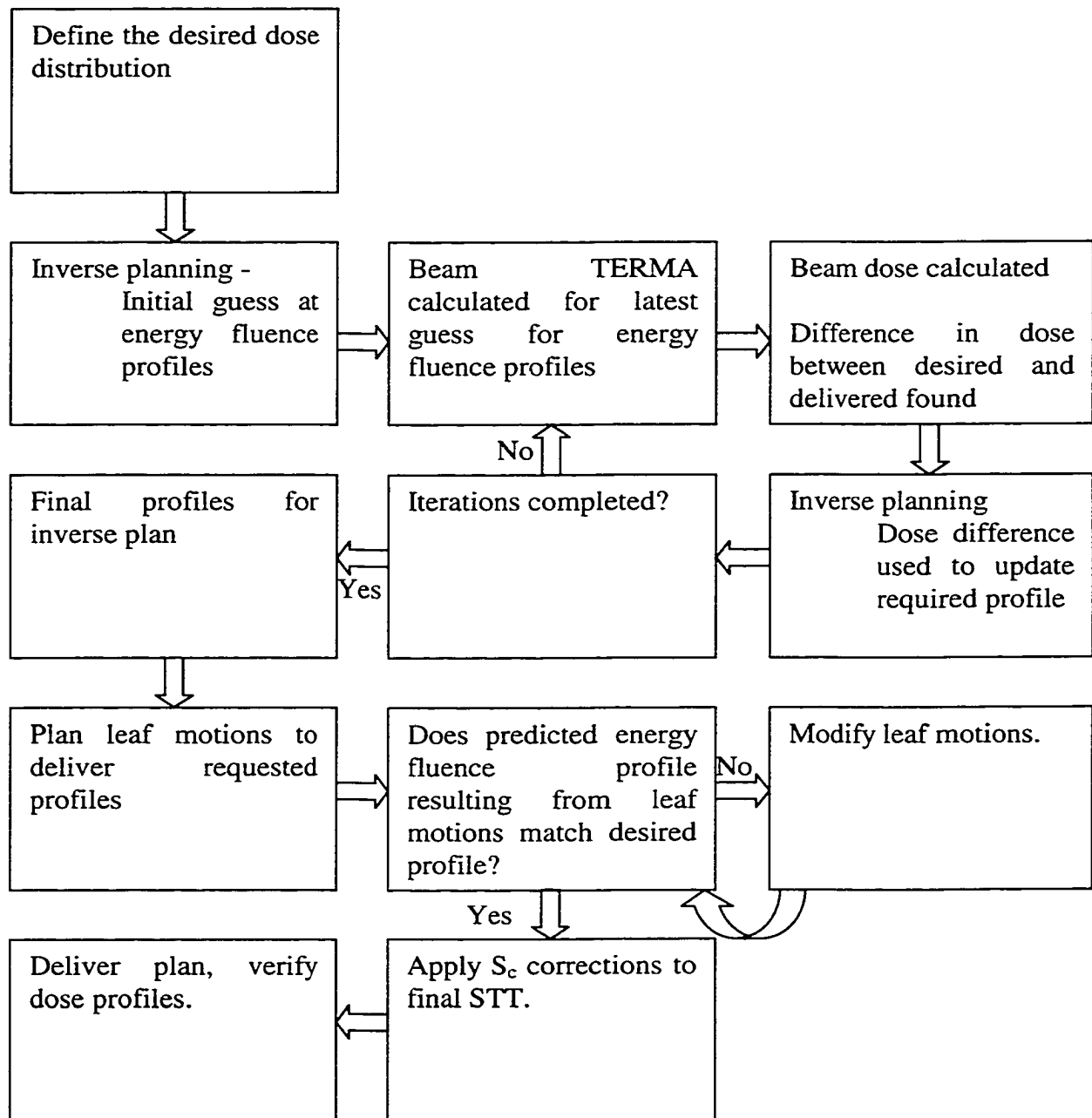


**Figure 5-1** Flowchart for the general calculation process for the planning of the IMAT fields.

IMAT are used to verify the final product of this work, namely the delivery of planned dose distributions to a desired region using IMAT.

## **5.1 Inverse planning**

Inverse planning is required in order to calculate the energy fluence profiles required to generate a desired dose distribution. The general method used along with the underlying theory is outlined in section 2.3 (in particular sections 2.3.1, 2.3.2, and 2.3.3.3).

### 5.1.1 Reducing computational artefacts

Sources of computational artefacts may, for example, include round off error or inherent assumptions of the calculation routine (i.e. in dose calculation, projection of dose region, and approximation of the region of interest as a continuous object). The round off error is assumed to be negligible when using double precision. Problems associated with assumptions of the calculation routine are assumed to be minimal, since the results of the calculation routine have been examined in some detail. The chief source of computational artefacts, which is addressed in this section, is due to the Gibbs phenomenon (see 2.2.3.2). This problem arises due to the assumption of a continuous object in the filtered back projection technique used here.

Comparing an idealised back projection to what is actually realised demonstrates the effect of the various artefact reduction techniques. Consider as an object a disc. It is known [Bracewell1995] that the ideal projection of a disc is of the form

$$P(a) = 2a\sqrt{1 - R^2/a^2}$$

**Equation 5-1**

where  $R$  is the radius of the disc, and  $a$  is the position where the projection is evaluated. By applying a ramp filter to this projection, one obtains the ideal back projection, which is noiseless due to its ideal nature. This ideal projection and its back projection were used to evaluate the various techniques employed here.

The effect of the Gibbs phenomenon is shown in Figure 5-2. The projections of an idealised disc (green line) and its discrete approximation (blue line) are shown together at left. The filtered back projection of these profiles are shown at right. The effect of the Gibbs phenomenon was reduced in several ways. The Radon projection profile's approximation to a continuous object improves with increased resolution. This has the effect of pushing the Gibbs artefact into higher spatial frequency domains, and lower amplitudes. The effect of this is seen in Figure 5-2, where the resolution of a discrete disc is increased from 0.5 cm (Figure 5-2A) to 0.05 cm (Figure 5-2D). This is done, however, at the expense of increasing the calculation time by a factor of 4 for every doubling of the resolution. The maximum resolution that was eventually used was 0.05 cm. This choice was made as it yielded good results while still keeping the overall calculation times acceptable (on the order of an hour per slice planned), and still posed few of the memory allocation problems which occurred with the larger array sizes.

Next, prior to applying the FFT, the Radon projection profile to be transformed was fitted and smoothed. The fitting is done as a piecewise series of cubic polynomial fits to sections that are  $3N$  pixels in length, where  $N$  was, after some experimentation, eventually set to be 5. The middle section of the polynomial fit was used to replace the projection, provided that the local error was less than some threshold value  $T$ , as per

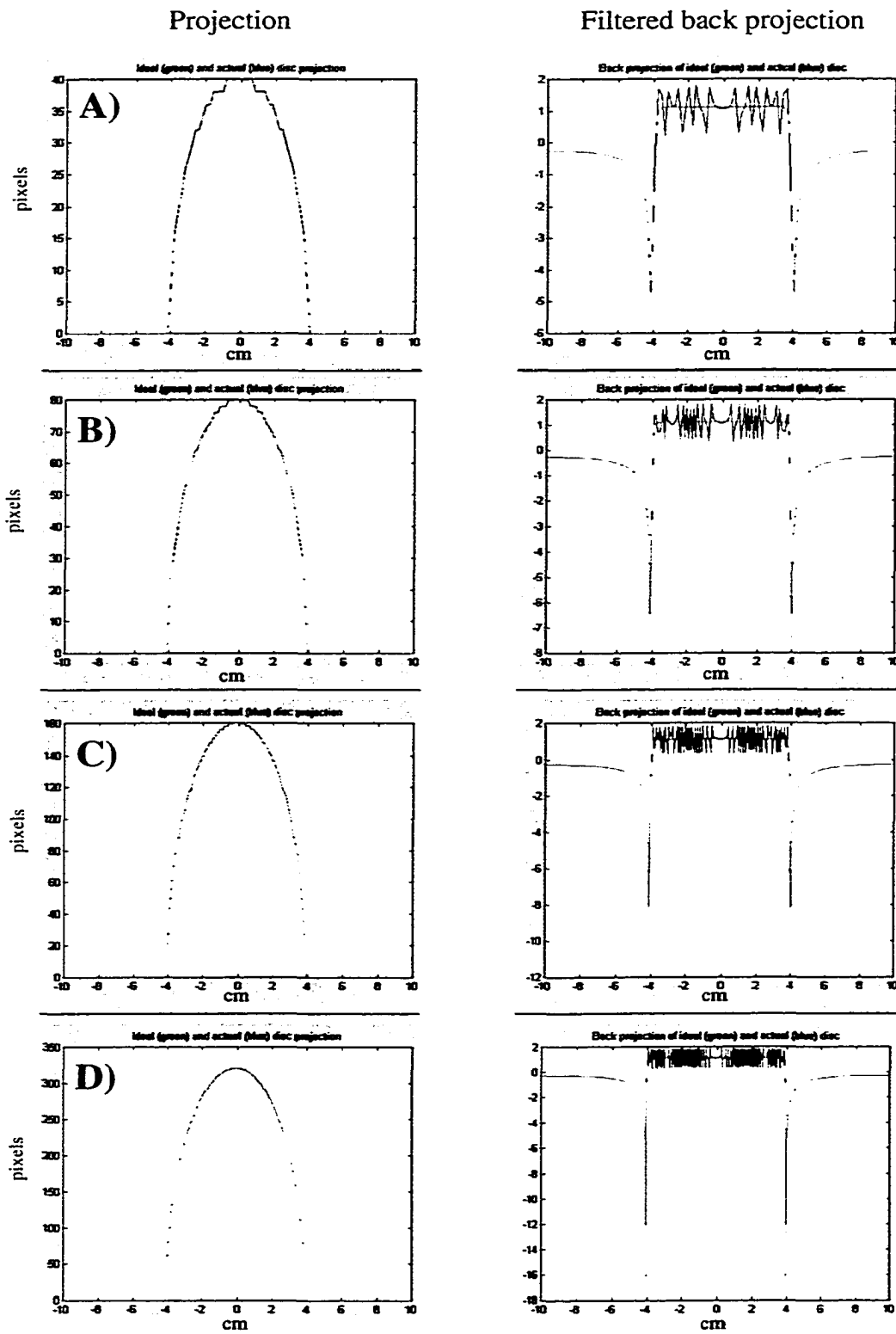


**Figure 5-2** Effect of increasing resolution of projections (left) on computational artefact in filtered back projections (right). Resolutions shown: A) 0.5 cm B) 0.2 cm C) 0.1 cm and D) 0.05 cm.

$$T \leq \frac{|P_{orig} - P_{fit}|}{P_{orig}} \quad \text{Equation 5-2}$$

The value for T was eventually set to be 0.015 or 0.01, at calculation resolutions of 0.1 and 0.05 cm, respectively. The choice of the values for both T and N were somewhat subjective, but chosen to preserve as much of what appeared to be the true projection profile as possible. This technique removes some, but not all, of the jaggedness of the projected profiles. A degree of smoothing was still required to further reduce the Gibbs artefact.

Smoothing was accomplished in part by convolving the resultant projection with a smoothing kernel, which resulted in a more uniformly varying profile at the expense of degrading the fidelity to the original projection. The form of the kernel was chosen to be a Gaussian, and so the operation had the form of

$$P_{smooth} = P_{orig} \otimes \left( \frac{1}{2\pi k^2} e^{\frac{-x^2}{2k^2}} \right) \quad \text{Equation 5-3}$$

where k is the smoothing parameter. As k goes to 0, the Gaussian tends to a delta function, and thus there is no smoothing with the convolution.

A median filtering was also applied, to remove any spikes in the signal, where the width of the median window is set to some value  $w_{med}$ . This assumes that any spikes in the signal are spurious, but the value  $w_{med}$  is decreased upon each iteration, preserving more of the original projection.

These methods are used in the early iterations of inverse planning, and the degree of smoothing is reduced during the latest stages of the iteration, such that more

and more of the original projection is preserved. This corresponds to calculating the low spatial frequency components of the required profile at the early stages, and filling in the high frequency components at the later stages of the calculation.

Finally, the ramp filter,  $|\omega|$ , is combined with a low pass Butterworth filter in order to remove some of the high spatial frequency noise remaining from the spurious portion of the solution due to the discrete approximation. This has the form

$$\frac{|\omega|}{\sqrt{1 + (\omega/\omega_0)^M}} \quad \text{Equation 5-4}$$

where  $\omega$  is the frequency,  $\omega_0$  is the cut off frequency of the Butterworth filter, and  $M$  is an attenuation parameter. The value chosen for the attenuation parameter was  $M=10$ , after some variation, in order to provide rapid fall off.

The effect on the appearance of the Butterworth filter due to varying the parameter  $\omega_0$  is shown in Figure 5-3. On the left of this figure is the Butterworth filter, and on the right is the Butterworth filter combined with the ramp filter. The values of  $\omega$  shown along the x axis range from  $-\pi/2$  to  $+\pi/2$ , with  $\omega=0$  at the centre. One can see that for high values of  $\omega_0$  there is effectively no low pass filtering, and so the ramp filter is unchanged (see in Figure 5-3A). As the  $\omega_0$  value is decreased there is a decrease in the amount of the high frequency component that is passed through the filter. During iteration the value of  $\omega_0$  is initially set at a low value and increased with successive iterations to a high value (so, for example, appearing initially as in Figure 5-3D, and finishing as Figure 5-3A).

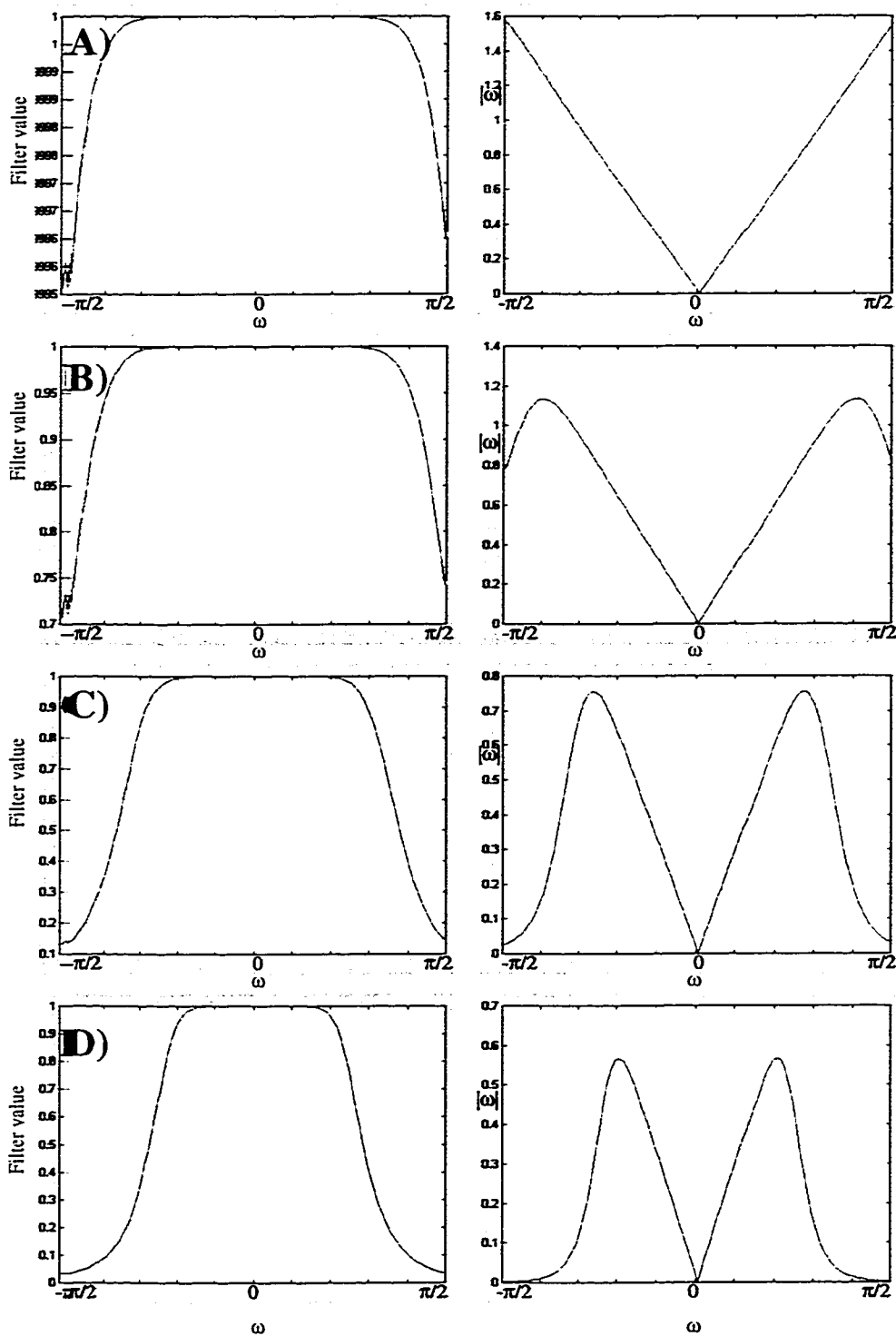


**Figure 5-3** Butterworth filter with a cut off value,  $\omega_0$ , of A) 2 B) 1.5 C) 1.0 and D) 0.5, alone (at left) and in conjunction with the ramp filter (right);  $M=10$  (see Equation 5-14).

The effect of using this low pass filter, in conjunction with the high pass (i.e. Ramp) filter, on the positive portion of a back projected disc is shown in Figure 5-4. The appearance of the Butterworth filter combined with the ramp filter is shown at left, and the result of using this filter on the ideal (green line) and discrete (blue line) projection of the disc are shown at right. It can be seen that as the value of  $\omega_0$  is varied from 1 (Figure 5-4A) to 0.2 (Figure 5-4C), that the amplitude and frequency of the noise decreases. One may also note that there is a loss in the fidelity of the edge reconstruction in the ideal back projection as the  $\omega_0$  value is decreased (refer to especially green line at right, Figure 5-4C).

The effect of the various smoothing and filtering operations, coupled with low pass filtering is demonstrated in Figure 5-5. All discrete disc back projections (blue lines) are compared to the ideal unfiltered disc back projection (green lines). The unfiltered back projection is shown in Figure 5-5(A). The back projection with a degree of low pass filtering is shown in Figure 5-5(B). The effect of combining the low pass filter with the smoothing operations discussed above is shown in Figure 5-5(C). The effect of further increasing the smoothing is shown in Figure 5-5(D).

The obvious drawback of the highly filtered back projection is that it initially fails to accurately reproduce the high spatial frequency edge details on the first pass. This is an iterative reconstruction process, however. This means that the central portion of the region of interest is built up on the first pass, and the difference between desired and calculated distribution and profile back projected and is used to update the projection profile on the following iteration. The degree of noise is low, as is the preservation of edge detail in the first few iterations, where the filtered back projections have the appearance of D in Figure 5-5. The edge (i.e. higher spatial frequency) detail is built up during the latter iterations, where filtered back projections have the appearance of C in Figure 5-5. This admits some noise in the reconstruction, but with an increasingly smaller component of the final solution.

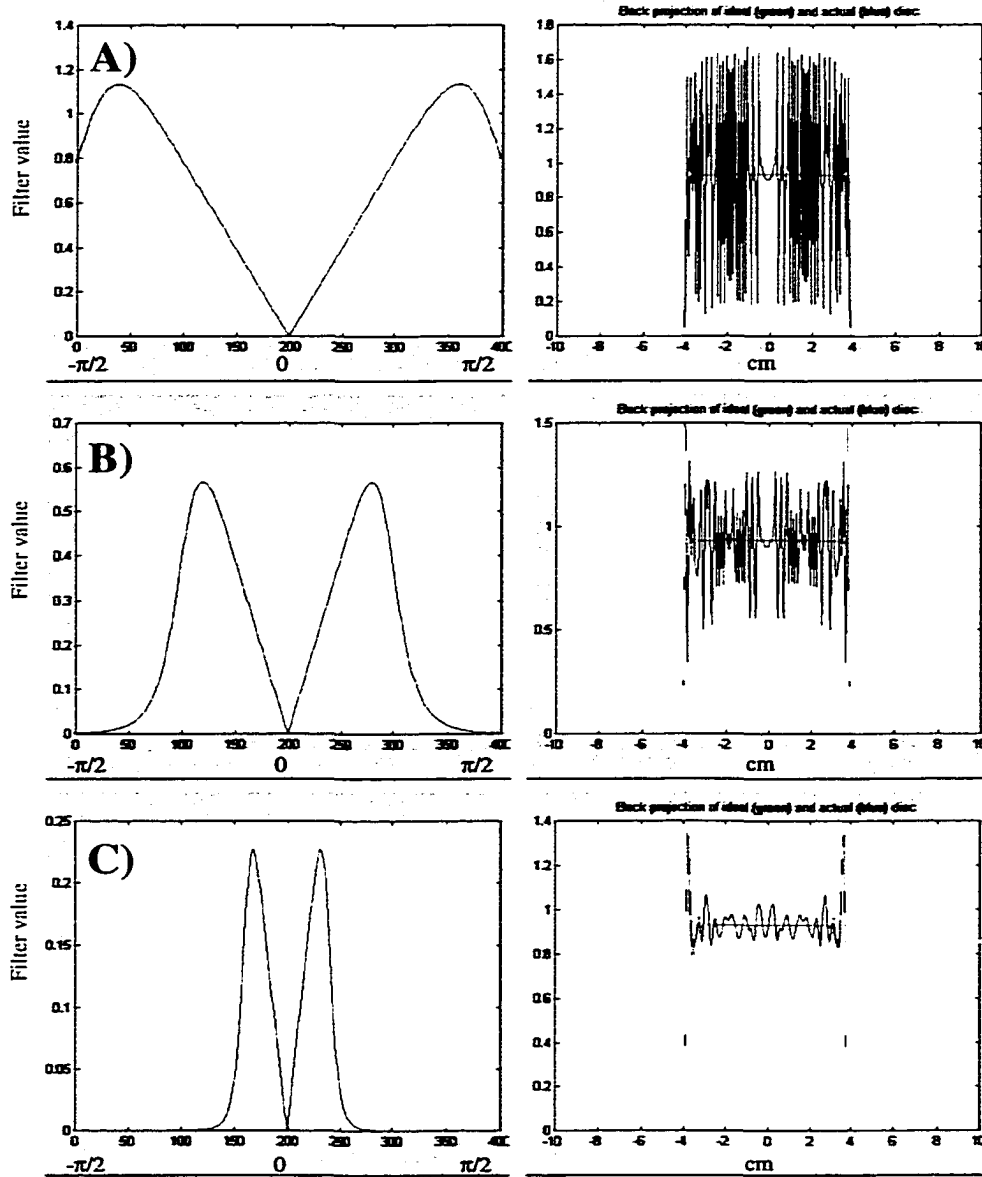


**Figure 5-4** Effect of combined high pass (Ramp) and low pass (Butterworth) filter (at left) on the filtered back projection of an ideal disc projection (green) and a discrete disc projection (blue) for cut off values,  $\omega_0$ , of A) 1.0, B) 0.5, C) 0.2

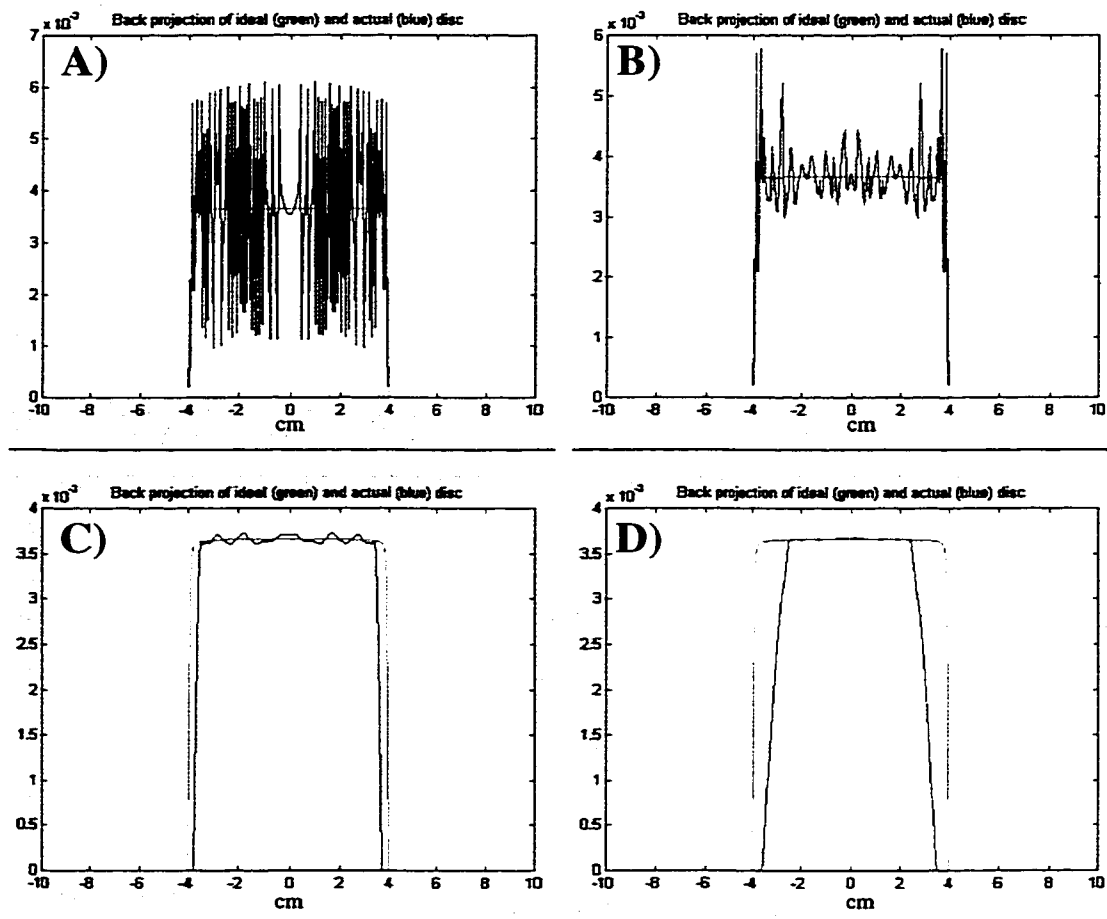


**Figure 5-5** Effect of increasing degree of low pass filtering and smoothing on a discrete disc projection (blue), shown with the ideal projection (green). Cases shown are A) no filtering or smoothing B) just low pass filtering C) same low pass filtering and some smoothing and D) same low pass filtering and increased smoothing

The performance of this calculation technique as it relates to the calculation of required beam energy fluence profiles is discussed in relation to specific examples in section 5.5 and section 5.6. The beam energy fluence profiles and dose calculation, which are used in the inverse planning, are discussed in the following section.

## **5.2 Beam modelling**

The inverse planning and dose calculation methods employed in this work are inherently 2D in nature (i.e. for single transverse slices). They are employed solely for the purpose of demonstrating the principle of the delivery of IMAT fields by a sliding window DMLC technique. The model employed for calculating the beam energy fluence profiles is not, however, inherently limited to single leaf pairs. Similarly,  $S_c$  is calculated according to the MLC aperture, and so is not necessarily limited to the single plane.

Given that the dose and planning sections are limited to a single plane, the focus of this work has been on the planning, delivery and verification of 2D planar IMAT fields. For the delivery of these 2D planar distributions, a set of ten opposing leaf pairs are synchronised to limit the effect of variations due to adjacent leaves moving in a differing manner. This has the effect of reducing the problem of modelling to a single plane. Calculation of the beam profile in the plane of the leaf motion is therefore handled separately on a leaf pair by leaf pair basis.

Some investigation was also carried out on multi-planar delivery, although this is planned as multiple single slices, with the assumption that the required dose distributions do not vary greatly from slice to slice.

Beam modelling was performed initially for the in-air energy fluence profiles of static fields. Calculations were performed for both relative profile distributions, as

well as machine output as a function of field size. Once this was done, the modelled profiles could then be used in the calculation of dose by first calculating TERMA based on these energy fluence profiles, and then convolving TERMA with the dose spread kernel. The results of energy fluence profile modelling and dose distribution calculations are discussed in the following sections.

### 5.2.1 TERMA and dose calculation

Unlike other inverse planning schemes of this type [Brahme 1988, Bortfeld 1990, Holmes 1994], beam divergence was included in the dose calculation. It was decided this would be appropriate in order to minimise the complication of comparing the results of the final dose calculation routines developed for this work with both measurements and the results of other independent treatment planning systems. The inclusion of divergence is accomplished simply at the beam TERMA calculation stage by sampling the in-air beam energy fluence profile as it would be projected at 100 cm source to axis distance (SAD) and expanding or contracting this profile in lateral dimensions. This is done to simulate how the unattenuated incident energy fluence would appear at different distances from the target. The expansion or contraction is accomplished by re-spacing the sampled points (see Figure 5-6), according to

$$\frac{res * 100}{SSD + z}$$

**Equation 5-5**

where “res” is the profile resolution, SSD is the distance from the source to surface of the phantom space, and z is the depth in the phantom. Interspersing points are arrived at by linear interpolation of the profile. The total energy removed from the x-ray beam in primary interactions (hereinafter referred to as TERMA [Ahnesjo 1989]; see section 2.2.3.3) was calculated using the divergent path length (see Figure 5-7) for each of the points in the array, as per

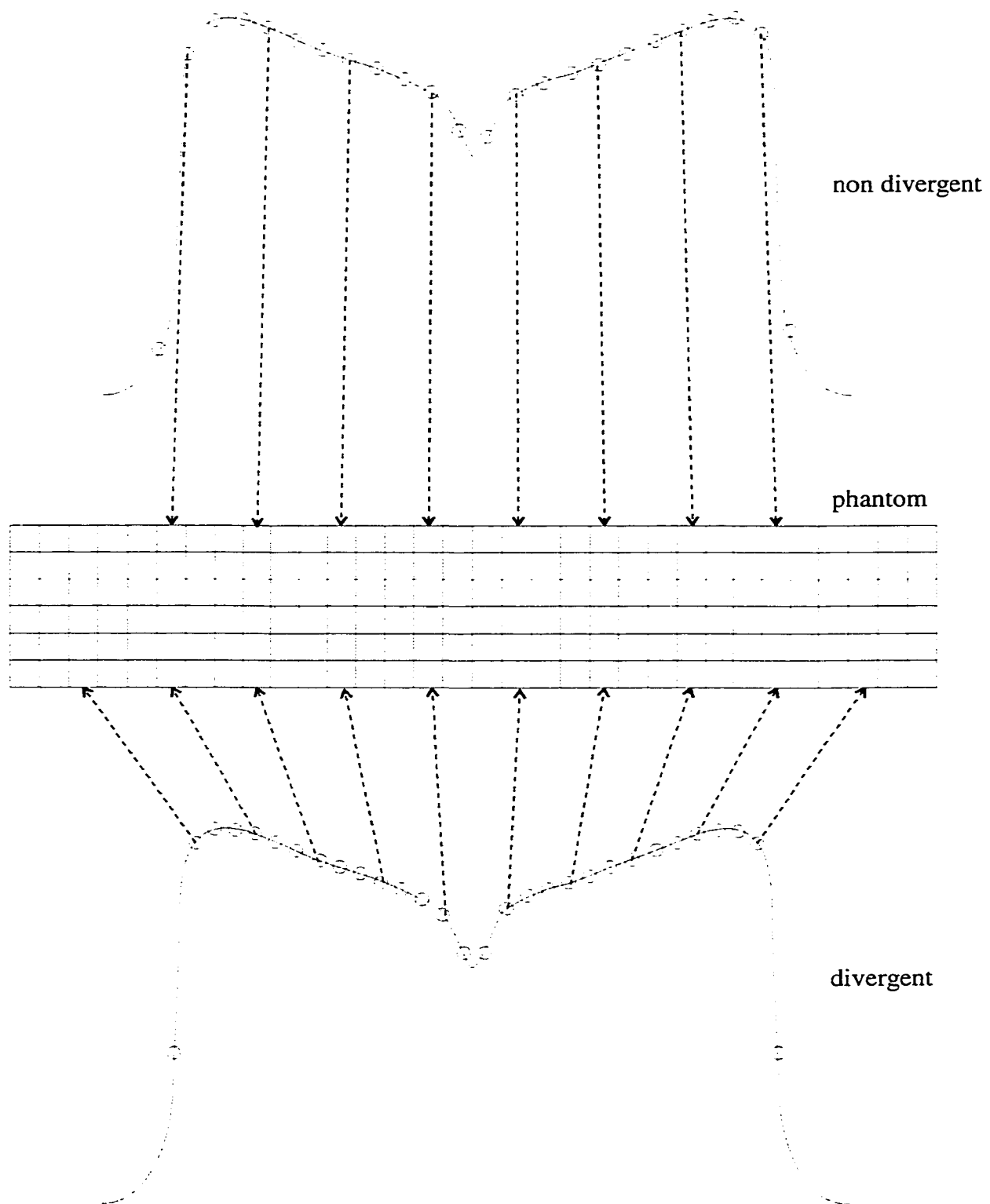


**Figure 5-6** Effect of resampling the non-divergent projection of the incident energy fluence profile, as it would be seen at isocentre.

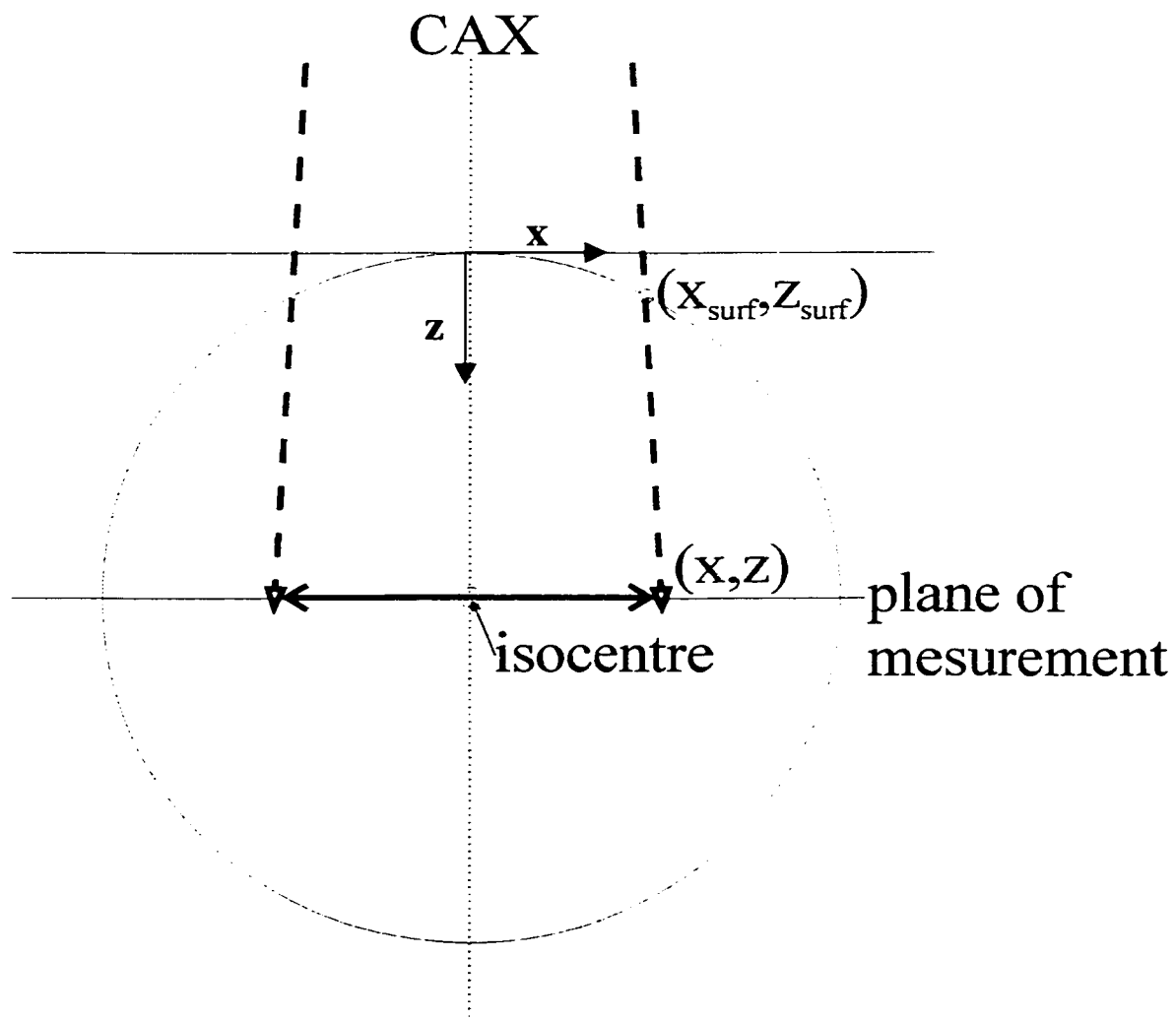


**Figure 5-7 Phantom co-ordinates for TERMA calculations**

$$T(x, d) = \left(\frac{r}{r_0}\right)^2 \left(\frac{\mu_{eff}(d)}{\rho}\right) \Psi_0(x) e^{-\mu_{eff}(d)d} \quad \text{Equation 5-6}$$

where  $d$  is  $\sqrt{(x-x_{surf})^2+(z-z_{surf})^2}$ , the ray line depth of the point,  $(\mu_{eff}/\rho)$  is the mass energy absorption coefficient,  $x_{surf}$  is the horizontal co-ordinate of the point where the diverging beam enters the phantom,  $\Psi_0$  is the incident energy fluence and  $\mu_{eff}$  is the depth dependent effective attenuation coefficient [Mohan 1985].

The effective mass attenuation coefficient employed for the TERMA calculation,  $\mu_{eff}$ , uses a depth dependent mono energetic approximation. The values of  $\mu_{eff}$  used were taken from tabulated values of Monte Carlo simulation work found in the literature [Mohan 1985]. It is similar to an effective single value used clinically at the Institute where this work was carried out, which represents the average value over the shallow depths (~10 cm) for a 6 MV beam. Once TERMA is calculated at all points in the phantom, dose is calculated by convolving TERMA with a 2D slice of the 6MV polyenergetic dose spread kernel [Mohan 1985]. The dose calculation particulars are laid out in sections 2.2.3.1 (the single convolution dose approximation). Briefly, the relative dose is computed by convolution of TERMA with the dose spread kernel, as per

$$D(x, z) = T(x, z) \otimes k(x, z) \quad \text{Equation 5-7}$$

Initial calculations were performed for energy fluence, TERMA and dose distributions for simple rectangular open fields. Once this was accomplished, the modelling of dynamic fields was then addressed. The comparisons of measured and calculated profiles, both in-air (i.e. energy fluence profiles) and in phantom (i.e. dose profiles), are discussed in the following section.

## 5.2.2 Open field distribution, $S_c$ and dose calculation

It is assumed that if the energy fluence incident on the surface of the phantom is known, one may then calculate the dose in the phantom. Therefore, in order to calculate the dose distribution from a dynamic delivery, one must first determine the net energy fluence for such a field. In order to model the net energy fluence delivered from a dynamic delivery, the net energy fluence may be viewed as the sum of the energy fluence from a large number of discrete static fields. The proviso for this is that the  $S_c$  and relative distribution of individual fields are sufficiently well modelled for static fields. The modelling of single static fields is addressed in this section, and the summation of static fields to calculate the net effect is addressed in section 5.2.2.3.

### 5.2.2.1 $S_c$ values for MLC

One of the considerations in beam modelling is the variation in output with secondary collimator jaw position and MLC leaf position. These variations may be modelled by considering the area of the extra-focal plane that can be “seen” from the plane of measurement. It can be seen (see Figure 5-8) how a smaller MLC field may subtend an equal area of extra-focal source due to the geometry of the treatment head. Experimental measurements of these variations are shown in Figure 5-9.

It can be seen from Figure 5-9 that the relative output is dominated by the secondary collimating jaws, except for the smallest of MLC fields. For the MLC measurements the secondary collimating jaws were fixed, defining a  $15 \times 25 \text{ cm}^2$  field. It was found that the variation in  $S_c$  at the plane of measurement for the MLC leaves being completely retracted (so the field was defined by the jaws alone) to the output with an MLC field of  $4 \times 6 \text{ cm}^2$ , amounts to a 2% reduction in  $S_c$ . Compare this to the change in  $S_c$  over the same range of field sizes defined by the

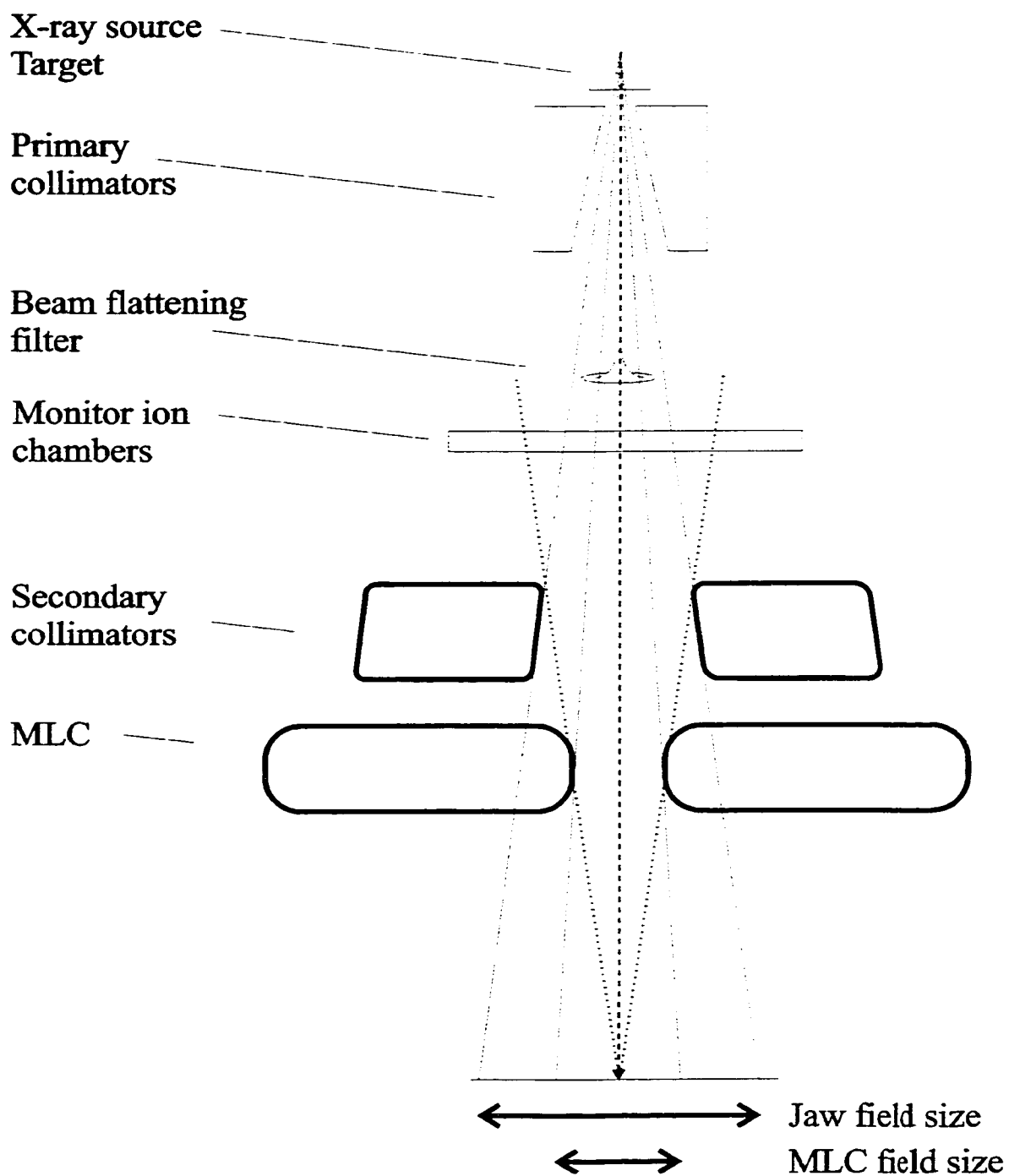


**Figure 5-8** Equal areas of extra-focal plane (at level of flattening filter) subtended by different jaw and MLC field size settings

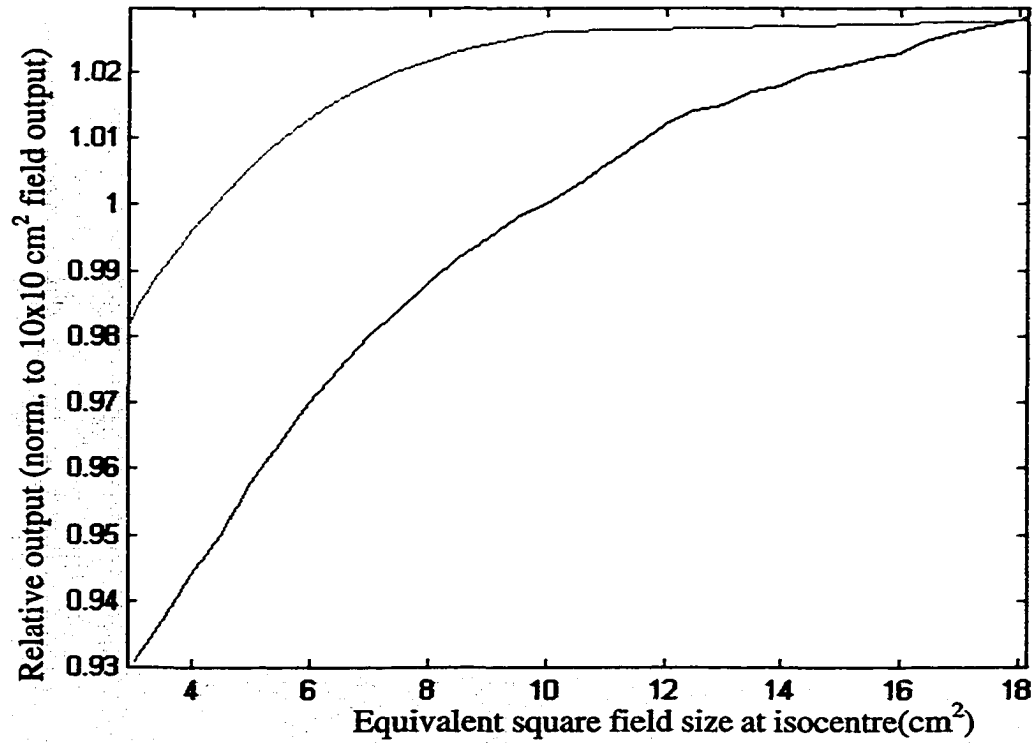


**Figure 5-9** Change in  $S_c$  for a variable MLC aperture with jaws fixed at  $15 \times 25 \text{ cm}^2$  (green line) versus the change in  $S_c$  for variable jaws (MLC fully retracted) over the same aperture variation (blue line).

secondary collimators (blue line, Figure 5-9) -- this is on the order of 7%. Again, the reason for this is that the area of the secondary source seen from the plane of measurement varies as the field defining apertures are varied (see Figure 5-8). Since the MLC is lower than the secondary collimators, the area subtended by a small MLC field can be larger than the region subtended by a much larger secondary collimator setting.

As a result of the finding above, it was decided to use a fixed setting for the collimating jaws (15cm x 25cm, XxY) for all the dynamic treatments delivered in this work. The rationale for this was to preclude having to account for the large variations in the output that occurs due to variation in secondary collimating jaw position. This also meant accepting a certain level of transmission through the MLC leaves *outside the region of interest*. This is on the order of a few percent of the primary beam, and hence of little consequence as it is, again, outside the region of interest.

The relative in-air output (i.e.  $S_c$  value) may be calculated by projecting the area of the aperture from the point of interest onto the plane of the effective sources. Certain assumptions about the distribution of the extra-focal source, as well as the weighting of the source, were made according to values found in the literature, as per section 3.2.1. The values for the parameters that describe the components of the extra-focal source were then arrived at by an exhaustive least squares fit to values for  $S_c$  measured in-air with an ion chamber fitted with a brass build-up cap (see section 4.2.2). For the extra focal component, 2.855 was the value used for the linear component maximum radius and 4.0 was the  $\sigma$  for Gaussian component. The value employed for  $w_{t_{ef}}$  was 0.08. The  $S_c$  values were for both jaw and MLC apertures, and the fitting was done over a range of values suggested in the literature. The closeness of the final fit to measured values is given in Table 1, in which the  $S_c$  measurements for various MLC apertures are given along with fitted values in Table 1. This source distribution is used in the calculation of the in-air beam energy fluence profiles, as per section 5.2.2.2.

	Field Size	Calc Sc	Meas Sc	% diff
jaws	4	0.9510	0.944	0.7
	4.5	0.9553	0.950	0.6
	5	0.9587	0.958	0.1
	5.5	0.9634	0.964	0.1
	6	0.9681	0.970	0.2
	6.5	0.9729	0.975	0.2
	7	0.9791	0.980	0.1
	7.5	0.9836	0.984	0.0
	8	0.9879	0.988	0.0
	8.5	0.9891	0.992	0.3
	9	0.9938	0.995	0.1
	9.5	0.9971	0.998	0.1
	10	1.0000	1.000	0.0
	15	1.0176	1.021	0.3
20	1.0303	1.032	0.3	
MLC	2	0.9583	0.965	0.7
	3	0.9815	0.983	0.1
	4	1.0009	0.996	0.5
	5	1.0114	1.007	0.4
	6	1.0171	1.012	0.5
	7	1.0229	1.018	0.5

**Table 1**  $S_c$  measured and predicted by extra-focal source model.

The measured  $S_c$  data in Table 1 is a subset of data that were acquired for a large range of square and rectangular MLC field sizes. It was found that the relative output could also be accounted for as a function of their respective equivalent field sizes (normalised to the output of a 10x10 cm<sup>2</sup> field, defined solely by the collimating jaws). The equivalent square field size [Khan 1994] is given by

$$sq_{eq} = \frac{2AB}{A+B} \quad \text{Equation 5-8}$$

where A and B are the length and width of the rectangular field, and  $sq_{eq}$  is the length of the side of the equivalent square field. These data were fitted to a fourth order polynomial, which is

$$\begin{aligned} & -2.832 \times 10^{-6} (sq_{eq})^4 + 1.504 \times 10^{-4} (sq_{eq})^3 \\ & - 3.070 \times 10^{-3} (sq_{eq})^2 + 0.02905 (sq_{eq}) + 0.9204 \end{aligned} \quad \text{Equation 5-9}$$

The comparison of the values obtained using this polynomial with measured data is given in Figure 5-10. The fitted polynomial was employed for the  $S_c$  correction of the MLC subfields in the STT calculation stage. The correction is only required at this stage in order to standardise the output of the individual segments. The segments are initially spaced equally in terms of MU settings. Altering the relative weighting of the segments at the STT calculation stage has the effect of normalising the actual output so the segments are, in fact, spaced equally with respect to output, which is what is desired in order to achieve the desired energy fluence profile. The polynomial  $S_c$  method was employed due to its relative accuracy, as well as speed and ease of implementation.

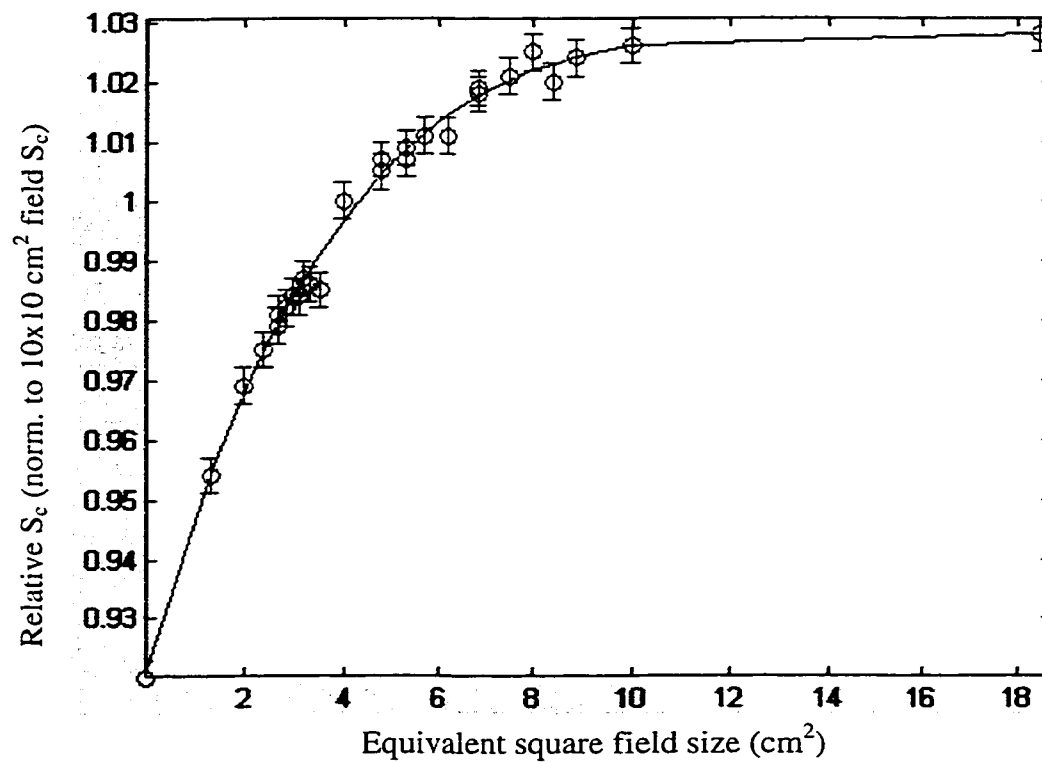


**Figure 5-10** Relative  $S_c$  of rectangular MLC field shapes (red circles with error bars) vs. their respective equivalent square shapes, along with fitted polynomial (blue line).

### 5.2.2.2 Open field energy fluence profiles

A further step in beam modelling is the characterisation of the variation in beam profiles as a function of distance from the central beam axis for variable MLC apertures in the plane of measurement. Combining this with the depth variation in TERMA allows one to fully characterise TERMA in the phantom in both dimensions (recall from section 2.2.3.1 that the planning is done on a slice by slice basis).

It was expected that the field distribution would be well modelled by a projection of the relative amount of source seen from the plane of measurement. Recall from section 3.2.2.2 that this projection may be approximated by

$$\Psi = wt_f \cdot (\Psi \cdot H_{f50}(x_1, x_2)) \otimes S_f + wt_{ef} \cdot (\Psi \cdot H_{ef50}(x_1, x_2)) \otimes S_{ef} \quad \text{Equation 3-2}$$

This technique has been applied to a number of test field cases, which were measured in-air with an ion chamber and high Z buildup cap (also called a mini phantom; see section 4.2.2). The results of these comparisons for three representative fields are shown in Figure 5-11. The measured profiles of these fields are shown in Figure 5-11A. The comparison of calculated to measured profiles are quite favourable. The maximum discrepancy for the symmetric cases, the 10x10 and 10x6 cm MLC fields shown in Figure 5-11B and Figure 5-11C, respectively, are on the order of 0.3 % of the value at the central axis, excluding the high gradient region. For the asymmetric case (the 10x4 MLC field shown in Figure 5-11D), the discrepancy is slightly larger, increasing to 0.5% toward to edge distal to the CAX. These calculations are also used in modelling the dynamic motions of the leaves as the sum of a large number of static fields (see section 5.2.2.3).

### 5.2.2.3 Calculation and delivery of single DMLC energy fluence profiles

Required energy fluence profiles were calculated for an elliptical eight beam delivery (see Figure 5-21, profiles A, B and C). These required profiles are calculated as per sections 5.1 and 5.5, although for the purposes of this section the desired dose distribution is not important, nor is the ability to produce the desired dose distribution. The question of the validity of the summed delivery over multiple gantry angles is addressed in section 5.5 and section 5.6. This section is concerned with the ability to deliver a single desired energy fluence profile.

Leaf motions are initially calculated as per section 3.2.3.2. Once the motions are computed using the most basic assumptions (no change in output with field size, perfect step function collimation of the beam), correction factors are then applied to achieve an improved in-air energy fluence profile. The profiles are calculated for the single plane delivery case, and as such delivery is performed by calculating the motions required for a single leaf pair, and synchronising the motions of a set of ten leaf pairs to deliver these profiles. The resulting energy fluence profile was then measured in-air using an ion chamber array with brass buildup caps.

The results from the delivery of the uncorrected calculated leaf motions are shown for two of the eight profiles in Figure 5-12 (due to the symmetry of the plan, there are only three distinct profiles, and the third profile is essentially a flat profile, and is a fairly uninteresting case). Desired profiles are shown in blue, while the measured profiles are given in green. The measured in-air beam profiles are both clearly quite different from the desired energy fluence profiles, with the differences reaching upwards of 10% and higher of the relative profile maximum in some regions.

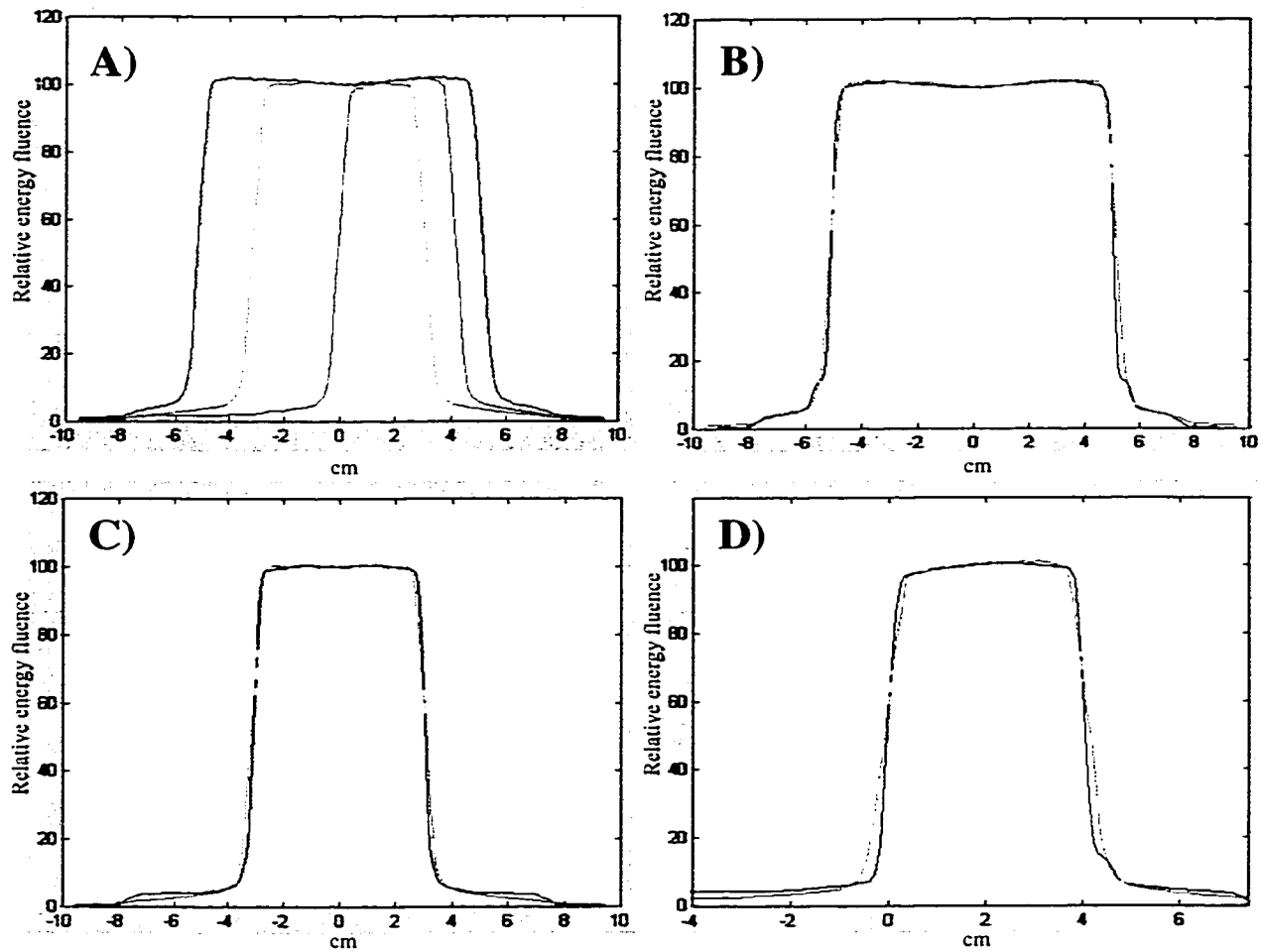


**Figure 5-11** A) Three measured beam energy fluence profiles: 10x10 (blue), 10x6 (green) and an asymmetric 10x4 (red); measured (green) vs. calculated (blue) values for B) 10x10 C) 10x6 D) 10x4 asymmetric. Secondary collimating jaws are fixed at 15x25 (XxY) cm<sup>2</sup>.

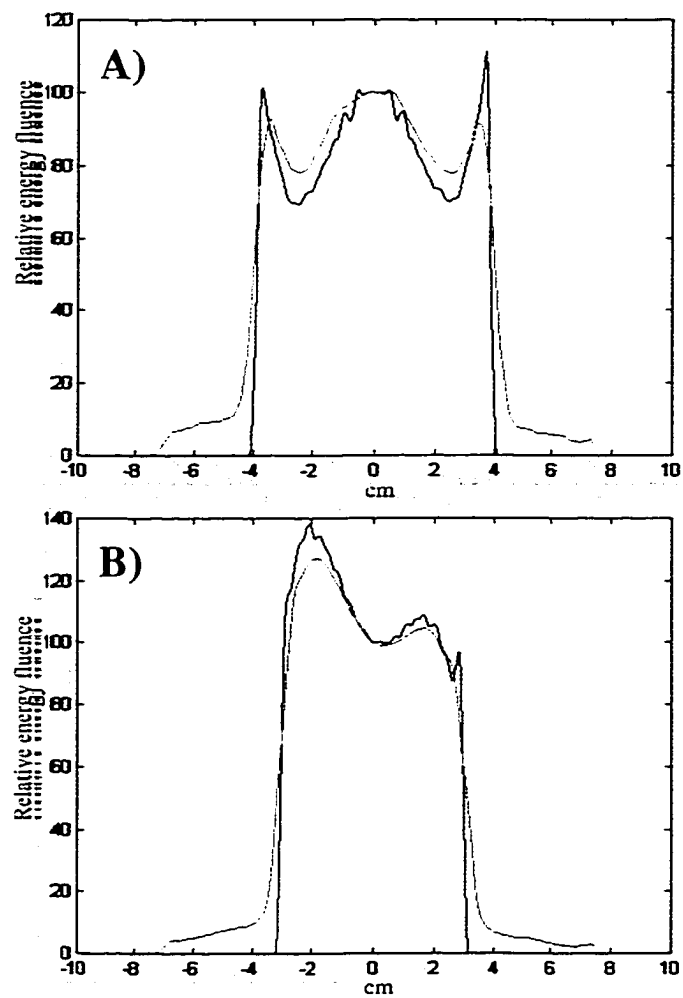


**Figure 5-12** Planned (blue) and measured (green) energy fluence profiles for two single projections (A and B) of required profiles for planar dose deliveries of an elliptical dose distribution.

The first correction tested was the Sc correction, which accounts for the change in energy fluence output versus field size. The method of applying this correction is outlined in 3.2.2.1. The effect of accounting for this correction is shown Figure 5-13. Comparing to Figure 5-12 one can see a slight improvement in the 'spike' at the right edge of the field for Figure 5-13A, a slight improvement in left side 'hump' of Figure 5-13B. The discrepancies that remain in these profiles examined in Figure 5-13 are assumed to be due to what is termed the penumbral effect (see section 3.2.3), which is addressed below.

The second correction tested was the penumbral correction, which accounts for the variation in the delivered beam energy fluence profile from the desired beam energy fluence profile due to collimation and transmission effects. In order to apply this correction, one must first calculate the leaf motions without corrections, as done previously. Once this is done, the methods of section 3.2.2.2 are applied to calculate the energy fluence profile for each of the sub fields of the delivery. These are summed to give a prediction of the net delivery of all these sub fields. If this process is done for a sufficiently large number of control points, and the modelling of the in-air profiles is sufficiently good, then the predicted profile should match the measured one. The basis for the penumbral corrections is the ability to predict the in-air profiles for a given set of leaf motions, and this prediction is then compared to the desired profile. If the desired profile does not match, the profile that is used in the STT calculation is modified and new leaf motions are calculated. The process may be repeated iteratively.

In order to compute the predicted profile, we first assess how many control points are sufficient to define this prediction. The effect of the number of control points used in this prediction calculation for the penumbral correction is shown, for the profile in Figure 5-12 B, in Figure 5-14. It can be seen that the solution arrived at improves, in terms of the symmetry and smoothness, as the number of control points is increased.

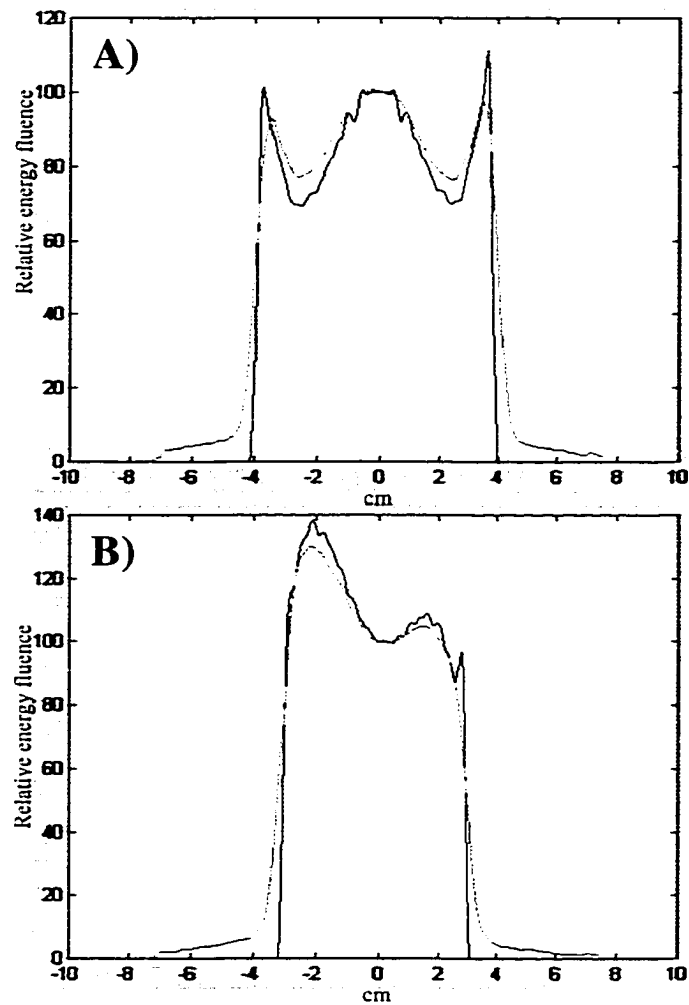


**Figure 5-13** Planned (blue) and measured (green) energy fluence profiles for two single projections (A and B) of required profiles for planar dose deliveries of an elliptical dose distribution.

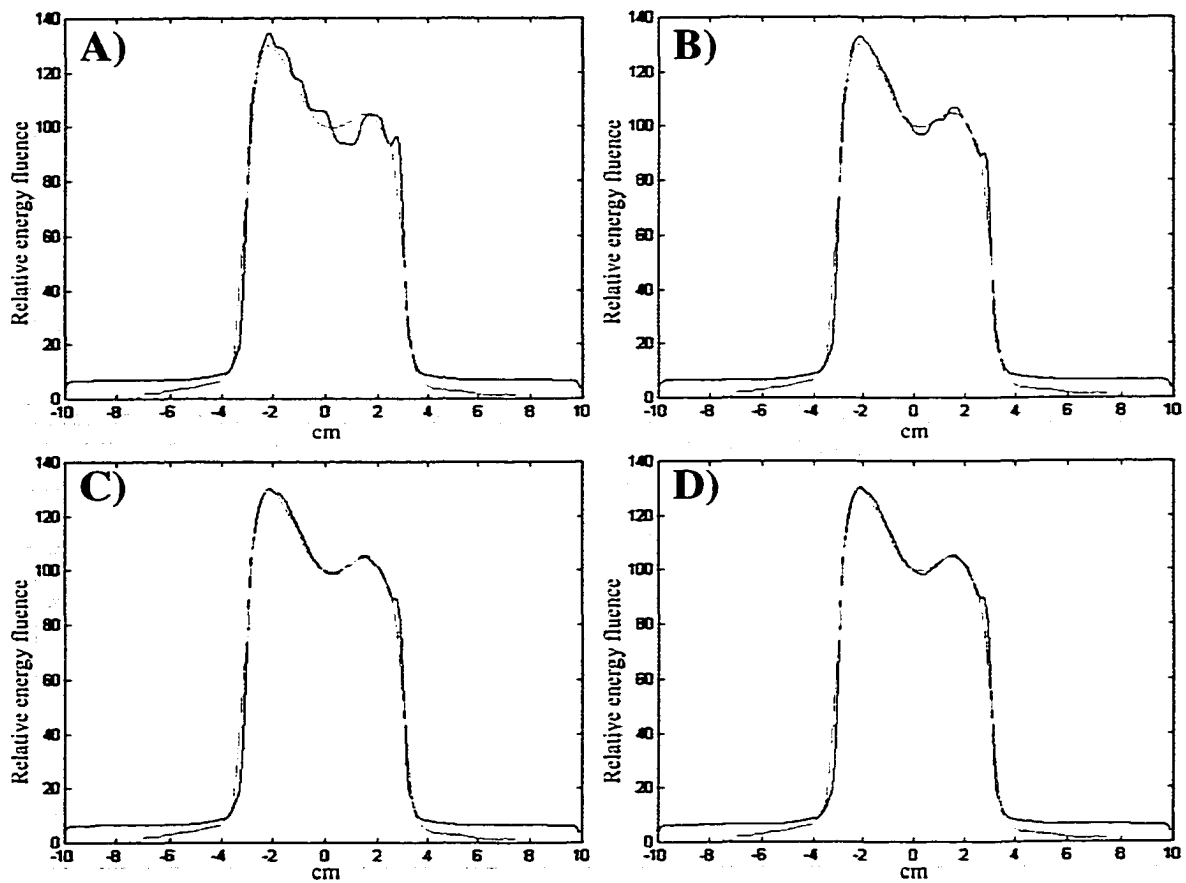


**Figure 5-14** Prediction calculation of a beam energy fluence profile of an uncorrected delivery for the penumbral correction, based on a sum of static fields for A) 13 fields, B) 26 fields C) 51 fields and D) 101 fields.

There is only a slight increase in calculation time associated with using more points; roughly ten seconds for thirteen control points, versus about a minute for 51 control points. It can be seen in Figure 5-15 that, comparing the predicted beam energy fluence profile from this method to the in-air measurement of the actual output for an uncorrected delivery, the results are quite favourable. There is a slightly larger discrepancy for the profile shown in Figure 5-15A, especially in the higher gradient regions, but an over-exposure of the two ‘valleys’ in the profile is predicted. Given the ability to predict the uncorrected output, this difference may be taken to account to improve the delivery.

The results of applying the two corrections are shown in Figure 5-16 and Figure 5-17. The comparisons made are between the desired beam energy fluence profile (shown in red), the uncorrected profile delivery (shown in green) and corrected deliveries. The first delivery corrects solely for the  $S_c$  factor (shown in A, in blue). This resulted in an improvement in the output in the small field regions at the field edges, but not a greatly improved delivery overall. Applying the penumbral and  $S_c$  correction together (shown in B, in blue) results in very good agreement for one profile (Figure 5-16), and substantially improved agreement in the other (Figure 5-17).

The corrected leaf motions for the profiles shown in Figure 5-12B and Figure 5-12C are shown in a beam’s eye view in Figure 5-18 and Figure 5-19, respectively.

#### **5.2.2.4 MLC field dose profiles**

Percent depth dose (PDD) and dose profiles were extracted from the calculated 2D planar dose matrix. Agreement was first assessed between the calculated PDD and measured data in water. Agreement was then assessed between the calculated dose profiles and measured data.

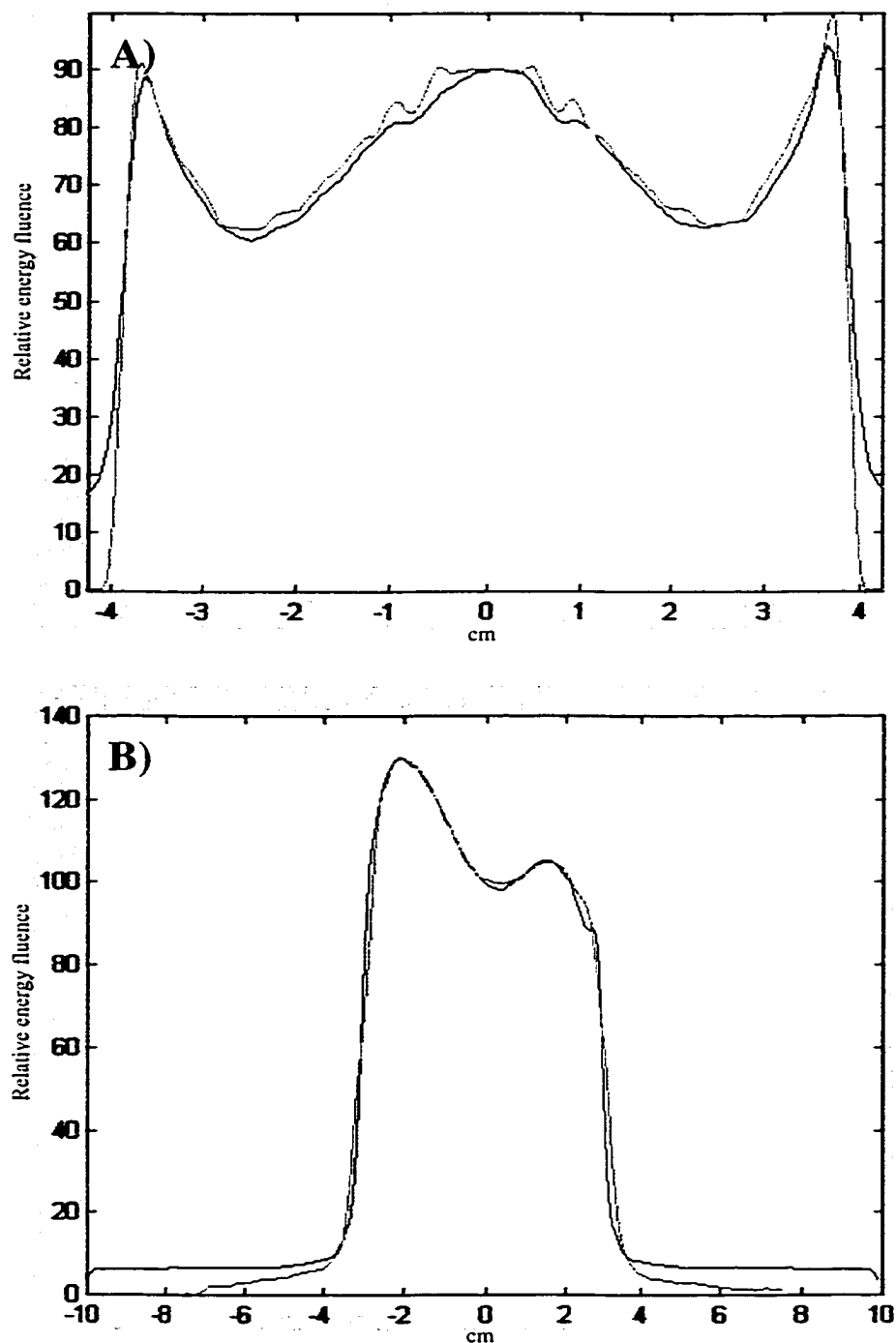


**Figure 5-15** Predicted beam energy fluence profile using sum of calculated static fields (blue) compared to measured value (green) for an STT delivery with the  $S_c$  correction, but without the penumbral correction.

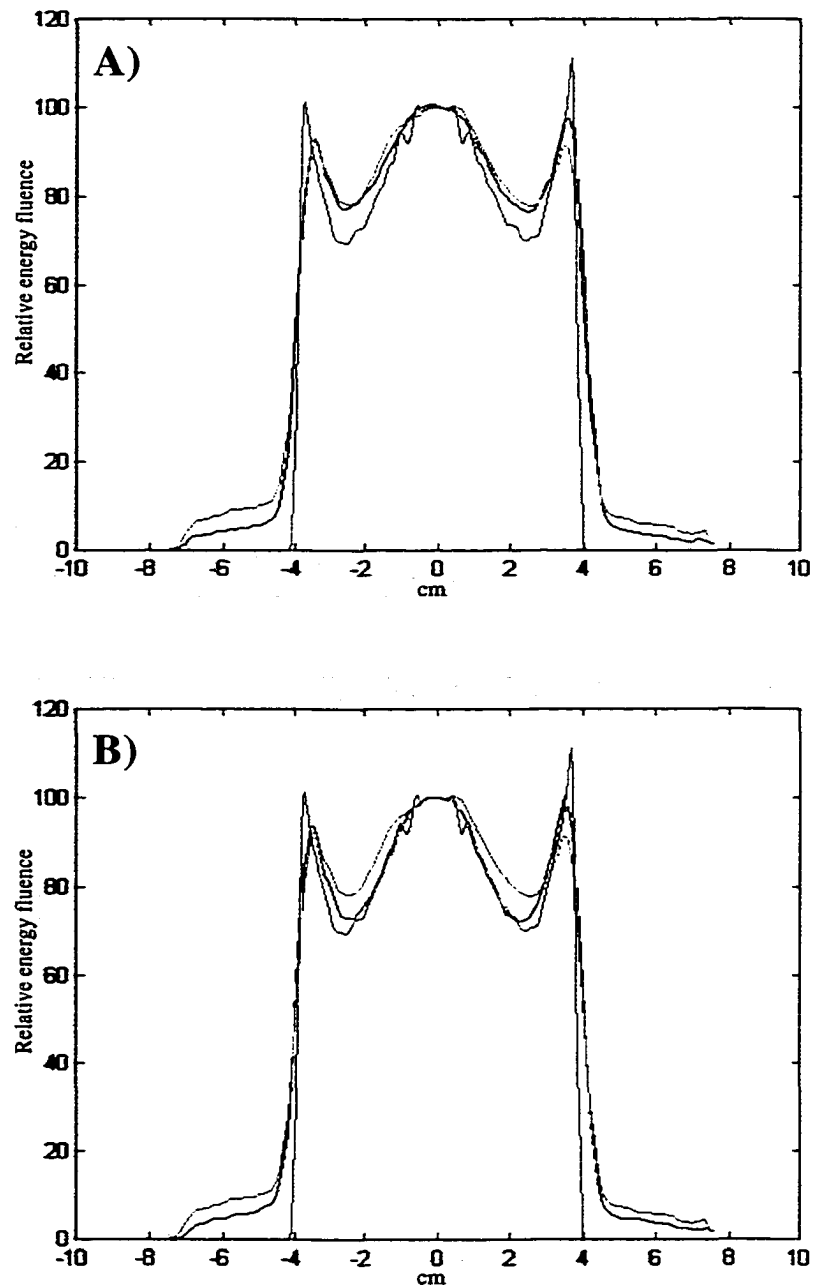


**Figure 5-16** Comparison of desired beam energy fluence profile (red) with the uncorrected profile delivery (green) and A) the Sc corrected profile (blue) and B) the penumbral and Sc correction (blue).

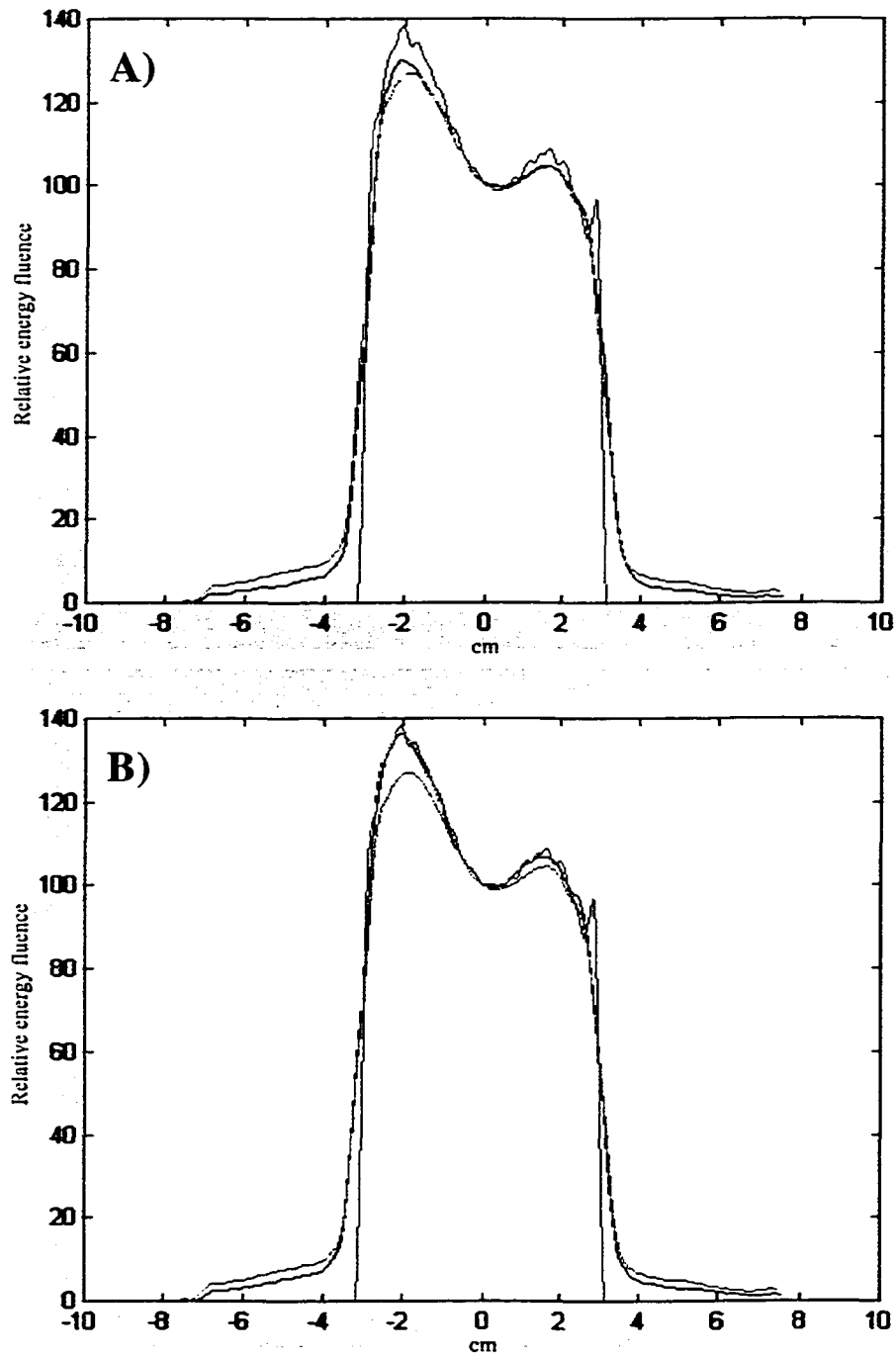


**Figure 5-17** Comparison of desired beam energy fluence profile (red) with the uncorrected profile delivery (green) and A) the Sc corrected profile (blue) and B) the penumbral and Sc correction (blue).

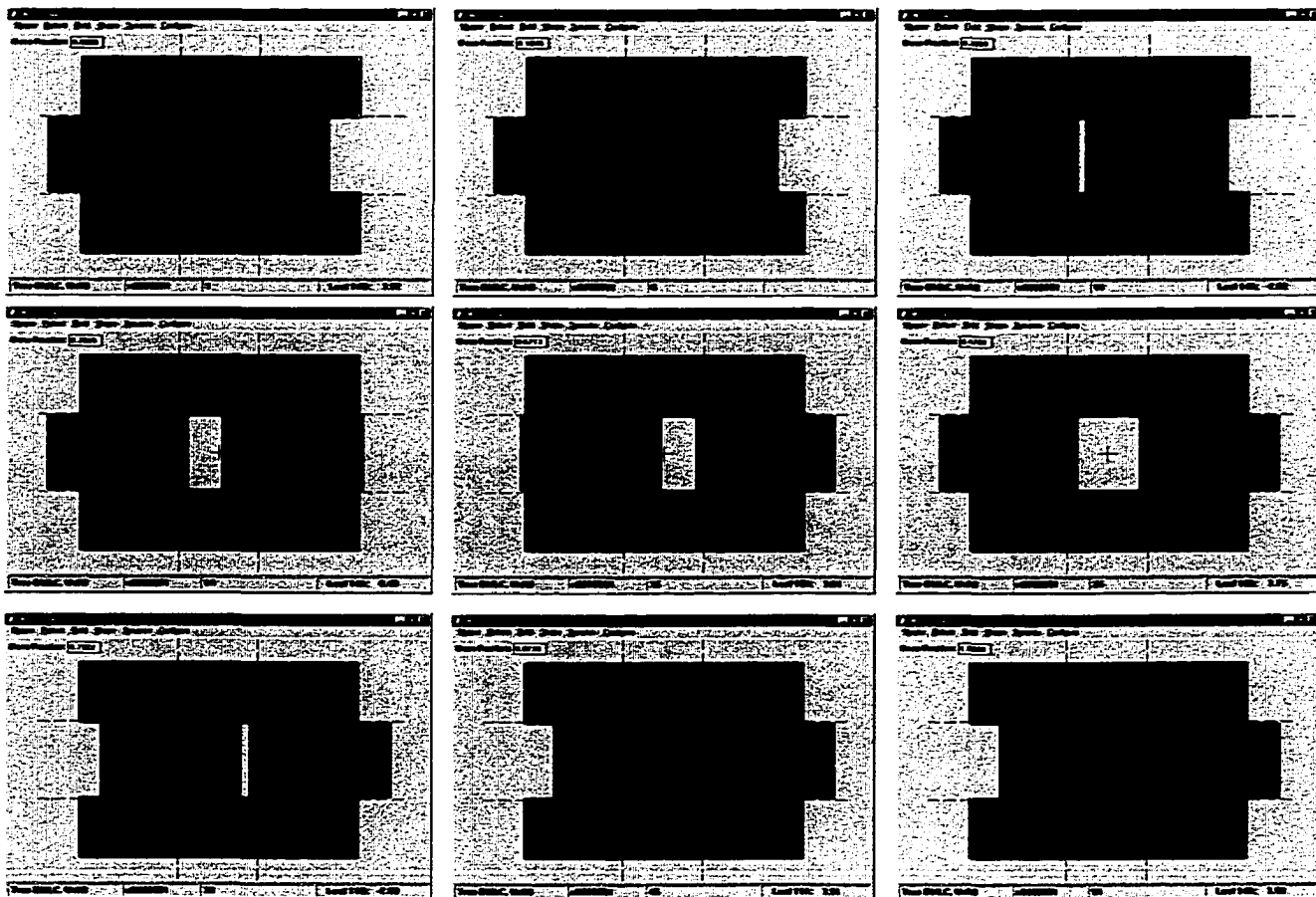


**Figure 5-18** Beam's eye view of planned leaf motions for profile shown in Figure 5-21A.

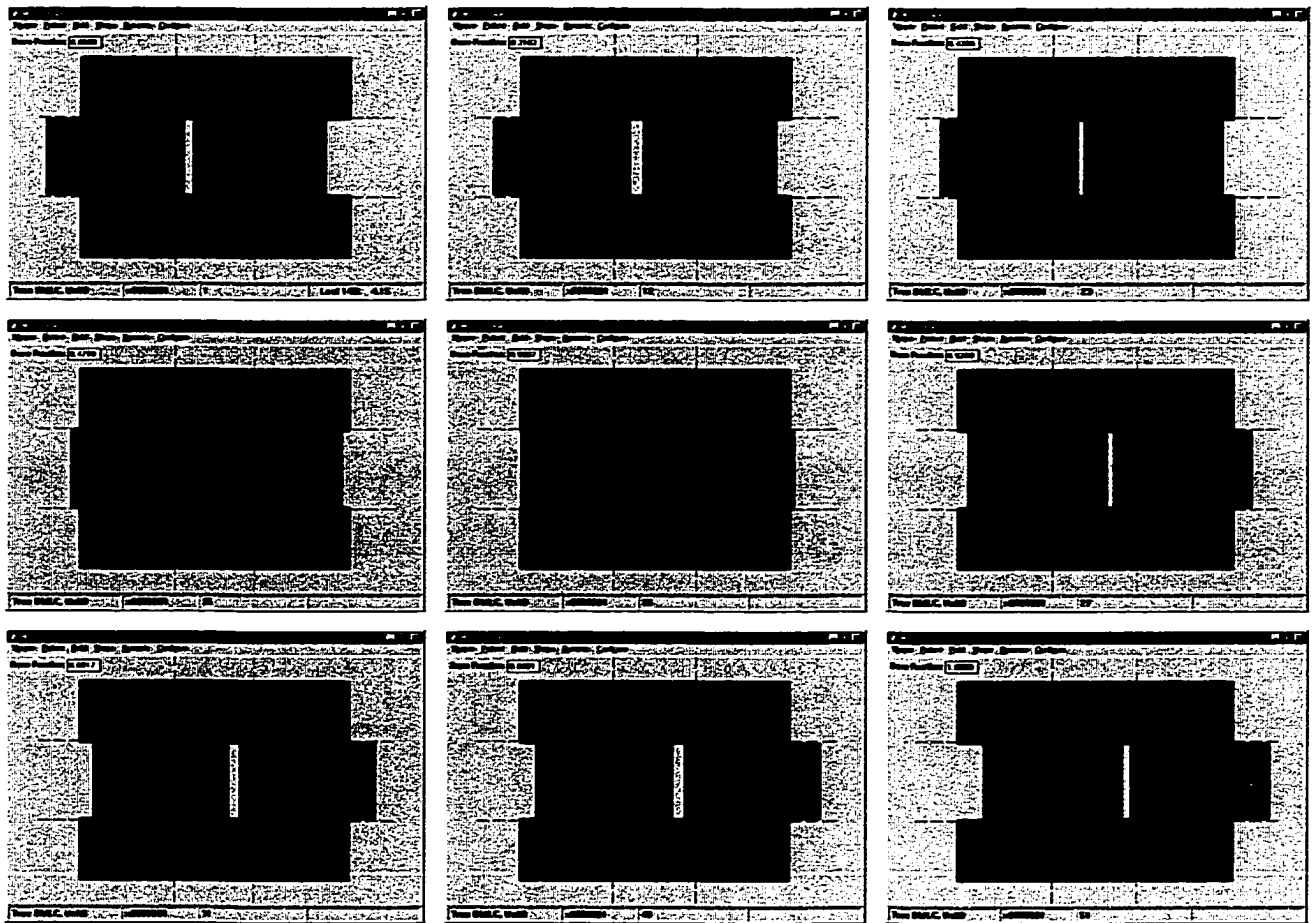


**Figure 5-19** Beam's eye view of planned leaf motions for profile shown in Figure 5-22.

When calculated PDDs were compared to measured values, a discrepancy was noted. This was not surprising, since 2D planar dose calculation (the 2D single convolution approximation; see section 2.2.3.1) fails to account for the changes in lateral scatter from planes parallel to the calculation plane which occur with varying field sizes. This technique can therefore fail to give the correct PDD characteristics for certain fields. Depth dependent correction factors have been used by others employing planar convolution [Homes 1993]. It was decided to re-scale the calculated PDD as a function of field size based on measured PDD values in order to alleviate the discrepancy between the measured and calculated values.

Comparisons of calculated and measured dose profiles at depth were performed. The comparisons of calculated and measured dose profiles are shown in Figure 5-20 for four MLC fields of various sizes: a 10x10 cm<sup>2</sup> symmetric field, a 10x6 cm<sup>2</sup> symmetric field, a 10x4 cm<sup>2</sup> symmetric field and a 10x4 cm<sup>2</sup> asymmetric field with a 4 cm off-axis shift. These measurements were taken in a water tank phantom with a scanning ion chamber probe, at a depth of 10cm, at 90 cm SSD. Calculated dose profiles are arrived at by the convolution method outlined in section 2.2.3.1. The calculation of energy fluence profiles is discussed in section 5.2.2.2. From these profiles the TERMA may then be determined, as per Equation 5-2. Once the TERMA is calculated throughout the phantom, then the overall dose distribution may be calculated by convolving the TERMA with the dose spread function.

There is a minor discrepancy in the high gradient region of each of the four cases shown in Figure 5-20. This may be due in part to the perturbation of the measurement by the finite size of the detector, an effect discussed in numerous articles [Garcia-Vicente 1998, Metcalfe 1993, Sibata 1991]. This may also be due in part to a slight underestimate of the lateral scatter by the calculation routine. It was felt that the discrepancies were acceptable for the purposes of this investigation.

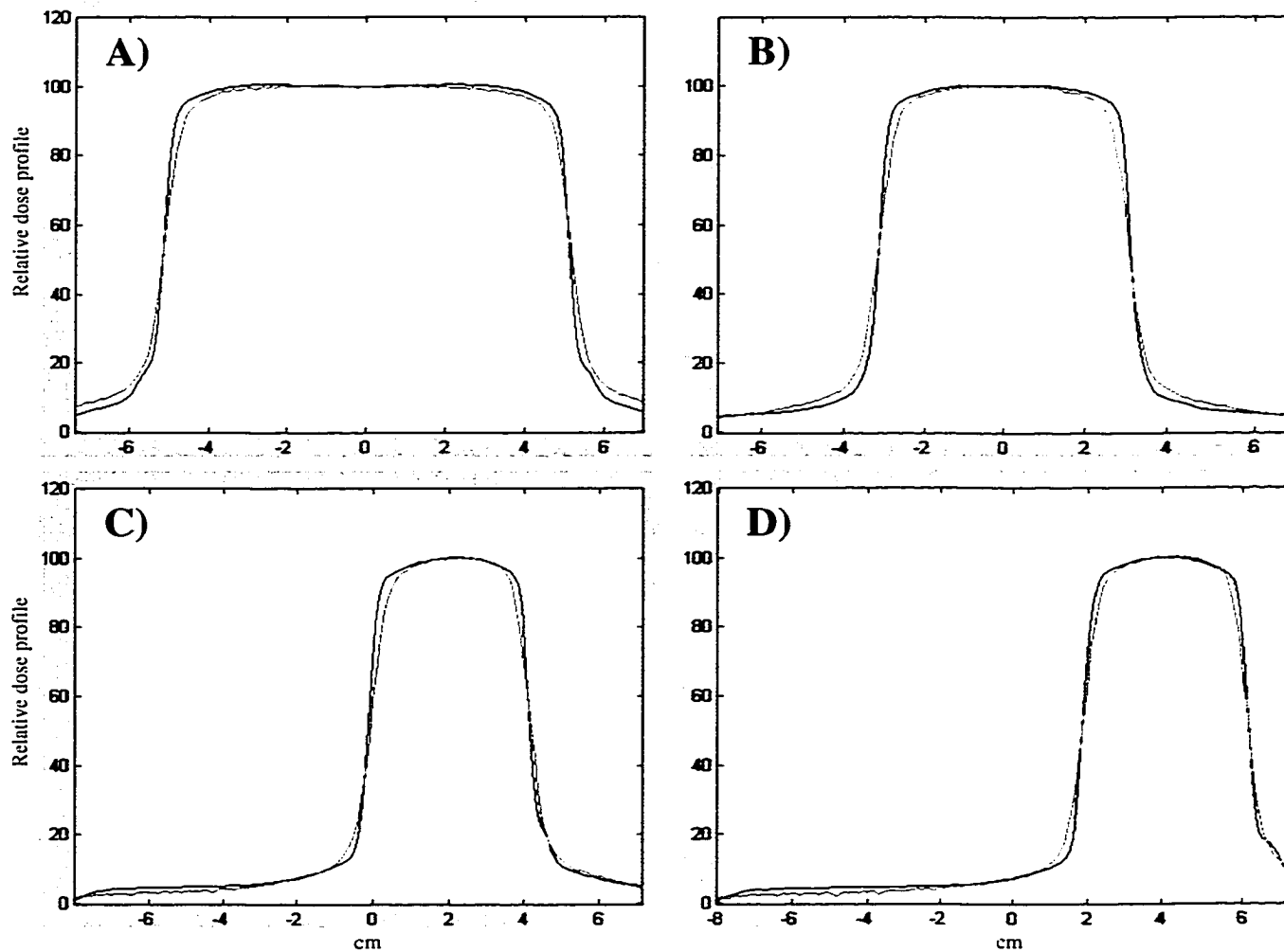


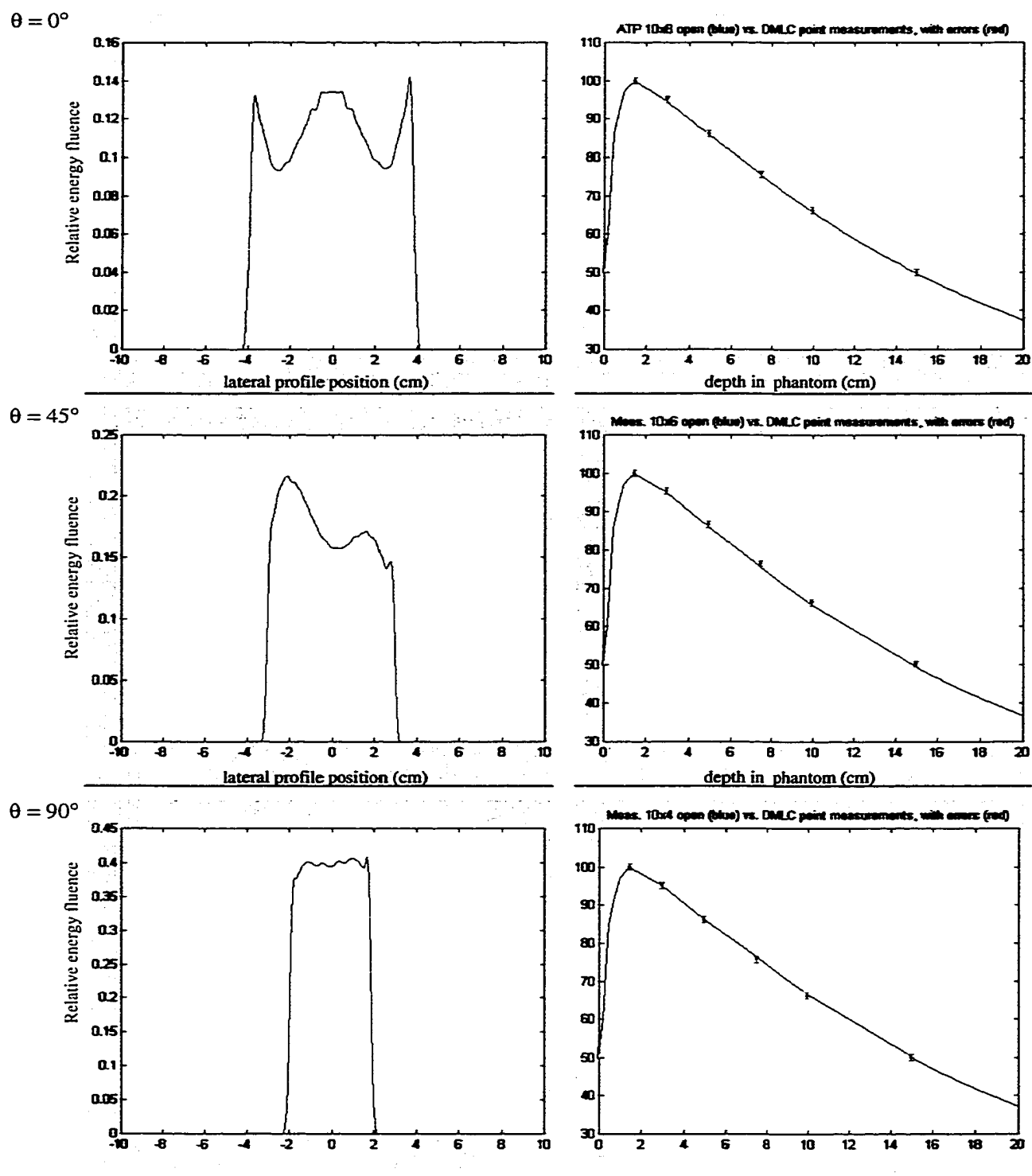
**Figure 5-20** Measured (green line) and calculated (blue line) dose profiles for various MLC apertures, namely  $10 \times 10 \text{ cm}^2$ ,  $10 \times 6 \text{ cm}^2$ ,  $10 \times 4 \text{ cm}^2$  (2 cm off-axis shift), and  $10 \times 4 \text{ cm}^2$  (4 cm off-axis shift).

### 5.2.3 Dynamic field distribution, output and dose calculation

Measurements were performed to assess the PDD of dynamic fields. It was expected that the PDD for simple dynamic fields would be, largely, equal to that required for an open field of the largest extent defined by the dynamic jaws or leaves. This is based on experience with the dynamic and enhanced dynamic wedge [Huntzinger 1994, Leavitt 1994b], as well as on previous experimental results with more complex beam profiles [MacKenzie 1996].

Point doses (see Figure 5-21) at various depths along the central beam axis (CAX) were measured for several of the single projections required to deliver an elliptical dose to a single slice. MLC motions were calculated according to the method detailed in section 5.2.2.3, and the fields were delivered on a water tank. It was found that the PDD of the dynamic fields corresponded to the relative point measurements for an open field, within the bounds of error of the point measurements. The open field used for comparison is defined by the largest leaf setting values used over the course of the delivery of that field. Note that for point measurements, errors are estimated from the reproducibility of electrometer readings; the standard error on a series of measurements was used as a gauge for this value. For low gradient regions, the error due to slight variations in chamber positioning is negligible (on the order of 0.5 mm).

The PDD of the more complex dynamic field of Figure 5-22A was measured using the method described above, along the ray line from the off-axis point marked by the red arrow. The results are far less favourable (see Figure 5-22B) when comparing the point measurements to the open field, defined by the largest aperture defined by all segments comprising the delivery. This is most likely due to the relatively low scatter contributions to the PDD from segments of the energy fluence profile close to the CAX in comparison to the overall scatter in the field. Improved



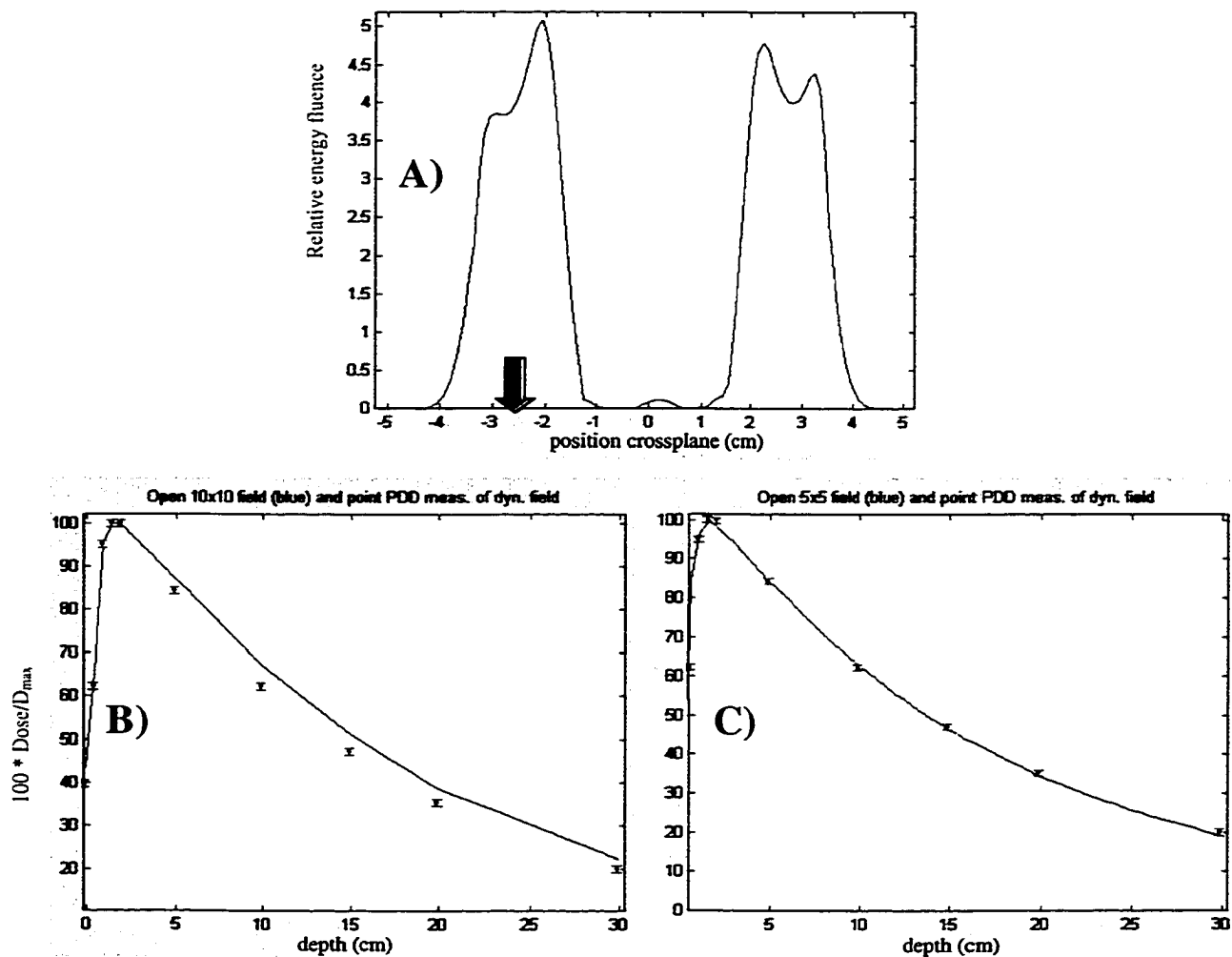


**Figure 5-22** Point measurements with error bars (red points) and measured PDDs for open fields of same maximum dimensions (shown in B, blue line), as well as for an effective field size (shown in C, blue line) for a complex energy fluence profile input (shown in A).

agreement between calculation and measurement may be achieved by using the effective open field size rather than the largest aperture subtended. Recall that the effective open field width,  $fs_{eff}$ , was defined as

$$fs_{eff} = res \cdot \sum_{i=1}^N \frac{\Psi_i}{\Psi_{ref}} \quad \text{Equation 3-8}$$

where all  $N$  values of the relative energy fluence profile  $\Psi_i$  are compared to some reference value in a weighted sum, and multiplied by the field resolution, denoted 'res'. Doing this for the profile in Figure 5-22A yields favourable agreement (see Figure 5-22C). This is an approximate correction which will suffice best for fields which do not depart greatly from the fields of the sort shown in Figure 5-21, where  $fs_{eff}$  tends to the value for the open fields defined by the maximum extents of the leaves. Fair agreement is nevertheless seen for a fairly complex profile (e.g. Figure 5-22). Possible improvements to this method are discussed in Chapter 6.

Based on these results, the effect field size is used for all dynamic fields. This holds true with the earlier results since, for the cases examined in Figure 5-21,  $fs_{eff}$  tends to the field size defined by the largest extents of all the dynamic segments.

### **5.3 Absolute dose for DMLC fields**

The dose calculation technique employed in this work is a combination of theoretical values and empirical measurements. Once the TERMA (see Equation 5-6) has been calculated using the corrections and modelling found in section 5.2, the dose may be computed. The dose calculation particulars are laid out in sections 2.2.3.1 (the single convolution dose approximation) and 3.2.2.3 (the calculation of dose per MU). Briefly, the relative dose is computed using a convolution of the TERMA with the dose spread kernel, as per

$$D(x, z) = T(x, z) \otimes k(x, z) \quad \text{Equation 5-7}$$

Recall from section 3.2.2.3 that it was decided to perform dose per MU for the monitor unit calculation separately from the dose distribution calculation. The dose per MU is determined using

$$\frac{D}{MU} = \sum_{i=1}^N CF_i(p) \cdot TPR_i \cdot AOF_i(p) \cdot S_{p_i} \cdot S_{c_i} \cdot IS(d) \cdot wt_i \quad \text{Equation 3-5}$$

The dose per MU results were checked by comparison with measurement (for single field projections). Dose distributions were evaluated by comparison to measurement (for single fields) and by comparison to an independent TPS (for multiple field projections).

The dose output per MU setting was calculated as per section 3.2.2.3. The validity of the formulas presented there are contingent upon a few approximations. These include the use of a flat phantom TPR for small to medium size (e.g.  $\leq 10$  cm) fields incident on *relatively* large cylindrical (e.g.  $\geq 20$  cm) phantoms. As well, it is critical that appropriate values be used for the dynamic compensator factor,  $CF_{dyn}$ , as well as for  $S_c$  and  $S_p$ .

The use of flat surface TPRs in cylindrical geometry was tested experimentally. Recall that TPR is the ratio of the dose measured for a given depth and field size at a fixed SAD to a reference depth at the same SAD and for the same field size (see section 2.2.1 and Figure 2-8).

For a  $10 \times 10$  cm<sup>2</sup> field incident on a flat polystyrene phantom surface, the ratio of the dose measured with an ion chamber at 10 cm depth, 90 cm SSD, to that measured at  $d_{max}$  (1.5 cm), 98.5 cm SSD (100 cm SAD) with the same field size was  $0.788 \pm 0.001$ . This measurement was repeated for a  $10 \times 10$  cm<sup>2</sup> field incident on a

cylindrical polystyrene phantom. The averaged ratio of the dose from anterior and posterior projections on the isocentric phantom to the dose measured for the same field size incident on a flat phantom surface at  $d_{\max}$  was  $0.785 \pm 0.001$ . While these readings are not within the stated error ranges of one another, this is almost certainly due to the slight and expected perturbation (i.e. lack of scatter) introduced by replacing the flat surface with a curved one. The variation between the two values is, however, only 0.4 % for this field size, which is representative of the largest field sizes used in the experimental deliveries. The result of this indicated that the TPR for a flat phantom approximates, with a very small error, the TPR for cylindrical phantom, for moderately sized fields.

Measurements of the dynamic compensation factor (see section 3.2.2.3) were performed using a small volume ion chamber (Protea corp., 0.1 cc, 4 mm diameter) in a water equivalent plastic (Solid Water™). Measurements were made first for the dynamic delivery. The reading was then repeated, keeping the same MU setting, for the static MLC field, whose size was determined by the largest extents of a dynamic field (as per the definition of  $CF_{\text{dyn}}$  in Equation 3-6).

Recalling the discussion in section 3.2.2.3, a formula for the calculation of the dynamic compensation factor was presented. Values for the dynamic compensation factor,  $CF_{\text{dyn}}$ , were calculated as per Equation 3-6 for a number of dynamic deliveries. Values were also calculated using the sum of static fields technique as per Equation 3-7, using distributions and  $S_c$  as predicted in sections 5.2.2.1 and 5.2.2.2. For the first of the series of profiles shown in Figure 5-21, the measured value of  $CF_{\text{dyn}}$  was  $0.213 \pm 0.004$ .  $CF_{\text{dyn}}$  was calculated using the two methods (Equation 3-7 and a sum of static fields) to be 0.210 and 0.207, respectively. For the last of the series of profiles shown in Figure 5-21, the measured value of  $CF_{\text{dyn}}$  was  $0.500 \pm 0.004$ . This value was calculated (Equation 3-6, sum of static fields) to be 0.493 and 0.489, respectively.

The method of Equation 3-6 works fairly well in these particular cases but it was found that for profiles of increasing complexity, such as the one shown in Figure 5-22, that agreement worsened for the value given by Equation 3-7, but was better for the sum of static fields technique. For this particular field, the value for the simplified (Equation 3-7) calculation of  $CF_{dyn}$  was 0.4069, and for the sum of static fields, the value was calculated to be 0.3529. The measured value was  $0.361 \pm 0.004$ , which is just within two error ranges ( $2 \sigma$ ) of the second calculated value. Using the sum of static fields  $CF_{dyn}$  value for the dose per monitor unit calculation, the computed dose per monitor unit value is 0.2798 cGy / MU. The dose per monitor unit value for this delivery was measured by obtaining an ion chamber measurement for both a 10x10 field at  $d_{max}$ , at 100 cm SAD, as well as the ion chamber measurement for the delivery in question at the specified depth and distance from the CAX, and taking the ratio of the two readings. The value found to be  $0.2868 \pm 0.0006$  cGy / MU, or about 2.4 % higher than the computed value.

Using the measured value for  $CF_{dyn}$  in place of the computed value, and leaving all other computed factors the same, the calculated dose per monitor unit is then 0.2862. This computed value is within error of the measured one, with a 0.2 % difference. This is not surprising, as the  $CF_{dyn}$  relates the dynamic field output to that of an open field whose extents are defined by the largest leaf extents. If this is done accurately, then determining the dose becomes a question of using well known empirical values for doing so, and is thus a trivial matter.

#### **5.4 Verification dosimetry**

Two main dosimeters were employed in this work: ion chamber and film. The ion chamber serves as the reference dosimeter because measured values from an ion chamber can be related back to energy fluence and dose (see section 4.2.2). For the single profile measurements of section 5.2.2.3, an ion chamber array was used

throughout. For the multiple field 2D planar dose measurements, as in sections 5.5 through 5.7, film is used exclusively as it is the only dosimeter available to us that provides a rapid and high resolution integrated dose measurement.

Film measurements were calibrated against optical densities for known doses, which were confirmed by ion chamber measurements, according to the technique outlined in section 4.2.1. Measurements were then performed with the two film dosimetry systems, as per section 4.4.

Comparison of the two film dosimetry systems is shown in Figure 5-23. It is necessary to perform this comparison, as the Vidar film scanner being employed to perform dosimetry was not equipped with software intended for this purpose. The comparison is done for the film of a concave IMAT delivery, although the choice of distribution here is arbitrary, as it simply needs to be shown that the two systems give the same result. The two scans, once calibrated to their respective H&D curves, give essentially the same isodose pattern, although a slight rotation in the film was present between the two systems due to physical alignment limitations.

Film scanning was initially performed with a Wellhöfer scanning densitometer which performs line scans at 15 mm/sec. This translates into roughly 25 minutes to scan a 20x20 cm<sup>2</sup> area, with 2 mm spaced scans. During the course of this investigation, a second film scanner (Vidar) became available. Based on the Vidar film scanner's considerably shorter scan acquisition time, as well as its favourable comparison to the standard film scanner, the former was used throughout the rest of the investigation for film dosimetry.

The calibration procedure for the films of the IMAT deliveries, again, involves a series 10x10 cm<sup>2</sup> fields which are delivered in 360 degree unmodulated arcs. These arcs are delivered with various MU settings to construct a rotational delivery H & D curve. The depth dependence of the film response is mitigated for the rotational

delivery, due to the superposition of beams from differing directions. This effect is demonstrated in Figure 5-24B.

Once a series of calibration films was exposed, one of these arc films was converted to a dose distribution using the calibration data. Once the measured dose for a uniform arc was obtained, it was then compared to a TPS calculated dose for an identical arc delivery. The TPS has been tested experimentally for such fields to a degree sufficient to validate its use for clinical treatment. This provides a suitable comparison, since the arc is well approximated by a large number of incident rotated static open fields, due to the adequate modelling of open fields by the in-house TPS. The comparison between measured and calculated values for a line dose taken through the centre of rotation (see Figure 5-24A) for the arc delivered on a cylindrical phantom is shown in Figure 5-24B. Good agreement is evident, although the scanned film is somewhat noisy (having a standard error of 1.9 cGy, out of the 100 cGy delivered at isocentre).

For the purposes of comparing planned to the measured doses, the method outlined in section 4.4 was used. The calculated dose array and the measured dose array were sampled to the same resolution, and padded with zeros to the same size. The alignment of the calculation space for the planned dose distribution to that of the measured dose distribution was realised through Fourier correlation to determine the offset between the two. Once the appropriate shift was applied to align the fields, the comparison of the two could proceed. The technique has been applied for all comparisons, and is shown for the concave dose delivery in Figure 5-25.

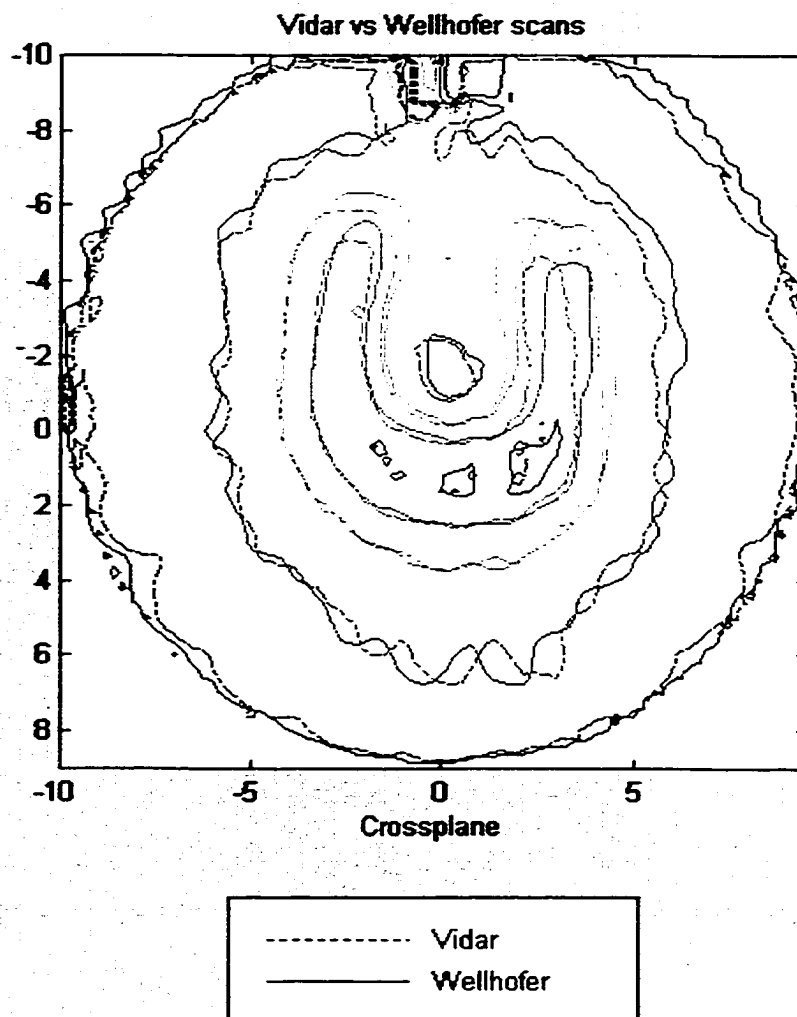


**Figure 5-23** A comparison of two film dosimetry system measurements for a single plane delivery of a concave dose distribution using IMAT.

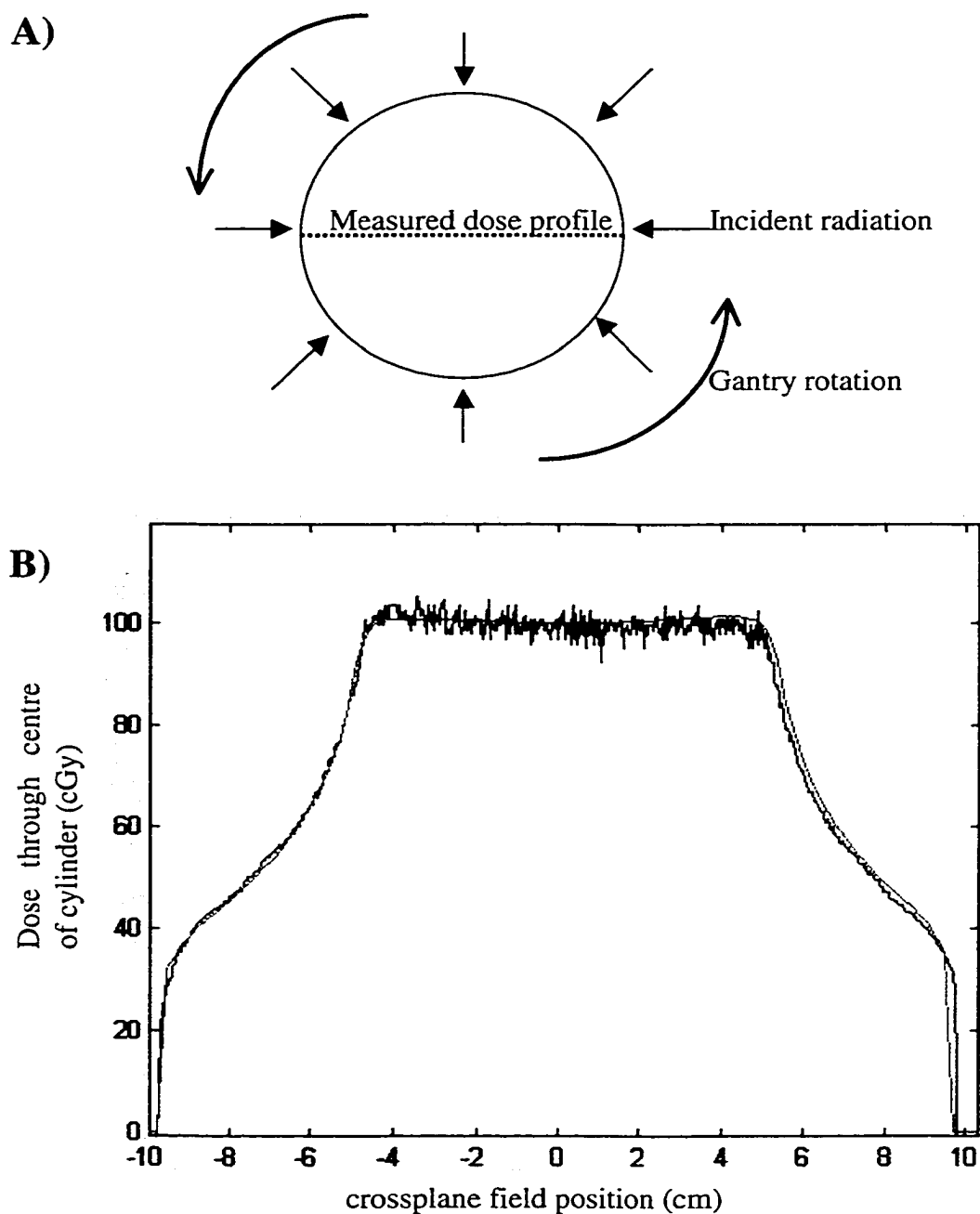


**Figure 5-24** A) Measurement of a line dose profile through the experimental phantom for a static 360° arc delivery B) Comparison of dose profile from calibrated film measurement (blue) with in-house TPS (ATP, in green) for an arc distribution to the test phantom.

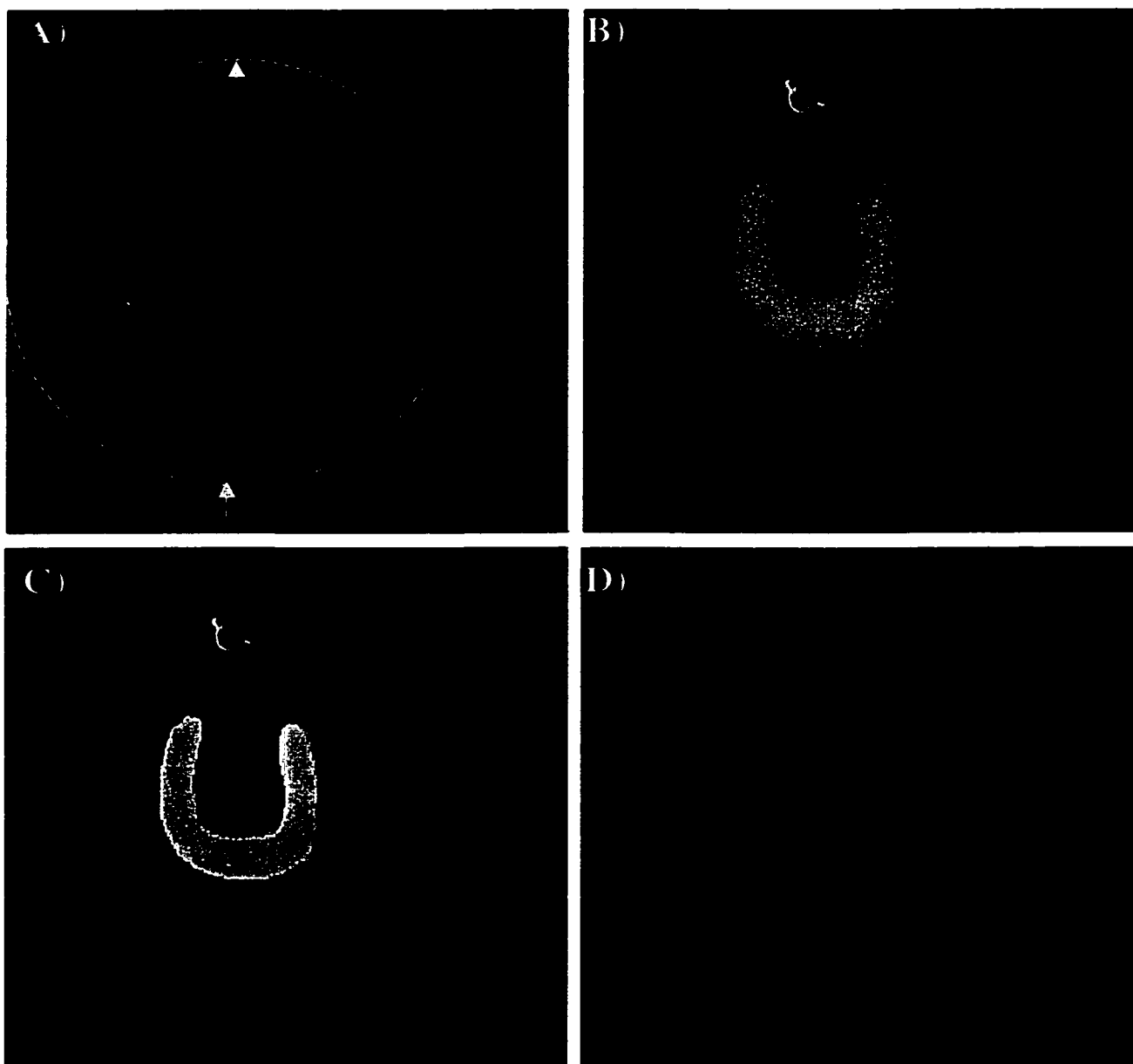


**Figure 5-25** Illustration of the use of Fourier correlation for the alignment of the calculation space with the measured dose region. The shift between the calculation space (A) and measured outline (B) is determined. The planned region of interest is overlaid on the measured distribution (C), and the dose to this region is then extracted (D) for comparison.

## **5.5 Delivery of simple planar dose distributions**

Delivering a desired dose distribution to a single plane constituted the initial full test of the planning, delivery and verification of intensity modulated arc using this DMLC technique. Profiles were planned to deliver a desired planar dose distribution to a single transverse slice through the phantom. Dynamic multileaf collimator motion was determined based on a synchronised bank of ten opposing leaves to deliver this 2D dose distribution.

The first simplified delivery consisted of an elliptical dose distribution, centred about the isocentre (see Figure 5-26). The isocentre was made coincident with the centre of the phantom used for measurements. A first trial at multi-field delivery was planned and delivered for an eight field delivery. This was done to test the ability of the planing and dose calculation for a simple multi-field case, and to test the dosimetry of multi-field deliveries. This also provided the generation of some of the profiles used in earlier sections (see section 5.2.2.3). Subsequent deliveries were accomplished with more projections, as explained in section 5.5.2; the results of these deliveries are given in section 5.5.4. More complex dose distributions were also delivered, and the results from these deliveries are examined in section 5.6.

### **5.5.1 Verification of the simple multi-field delivery**

As a second check on the calculated dose distribution for a multi-field planar dose distribution, some use was made of the in-house TPS to confirm the doses calculated for the input energy fluence profiles.

The in-house treatment planning system has been modified to allow importing of segmented treatment tables (STTs) for dynamically modulated fields. The intended purpose of this was to allow the modelling of dynamic wedges, but file input can be

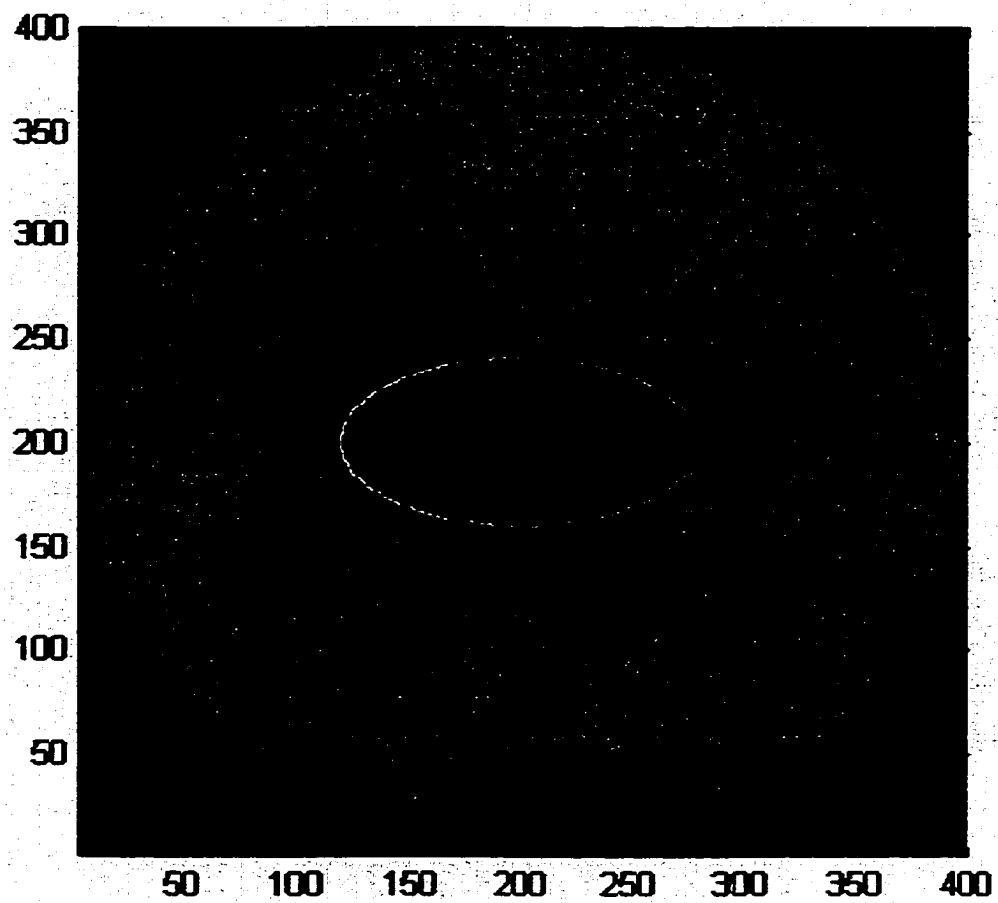


**Figure 5-26** Desired dose delivery region (shown in red) in the experimental phantom (shown in green)

adapted to represent arbitrary beam profiles. The system models dynamic wedges using an effective compensator thickness given by

$$t(x) = \left[ -\frac{HVL}{\ln 2} \right] \cdot \ln \left[ \frac{\Psi(x)}{\Psi_{max}} \right] \quad \text{Equation 5-10}$$

where  $t(x)$  is the compensator thickness at position  $x$  in the field, HVL (half value layer) is the thickness that gives a transmission of one half of the incident beam intensity,  $\Psi(x)$  is the desired energy fluence at point  $x$  after passing through the compensator and  $\Psi_{max}$  is the maximum energy fluence in the profile. This calculation method assumes no beam hardening (i.e. no change in the x-ray spectrum), so the HVL value is arbitrary.

The planar dose distribution predicted by the TPS developed in house (ATP) for the eight field IMRT treatment is shown in Figure 5-27. The shapes of the compensators for the incident energy fluence profiles at 0, 45 and 90° (starting at 'noon' and moving clockwise) may be compared to the profiles in Figure 5-21 (this plan is the source of these profiles). The resultant dose distributions from the calculation on the PC based planning system and the in-house TPS are shown in Figure 5-28. There is good agreement throughout, with a slight shift evident between the two. The shift appears to be a problem in aligning the edges of the data spaces. As well, there is a limitation of the in-house planning system with regard to the greatest resolution that can be used, forcing the original PC calculation to be sampled at a coarser resolution, which may also have introduced a slight shift. Nevertheless, there is a favourable congruence in the four small 40% isodose level 'hot spots' (the roughly elliptical shapes, in light blue), as well as in the highest dose regions.

Results of the calculations and deliveries in section 5.2.2.3 validate the correction factors applied to dynamic field deliveries for single projections. Employing these corrections, the simple eight field central elliptical dose delivery was

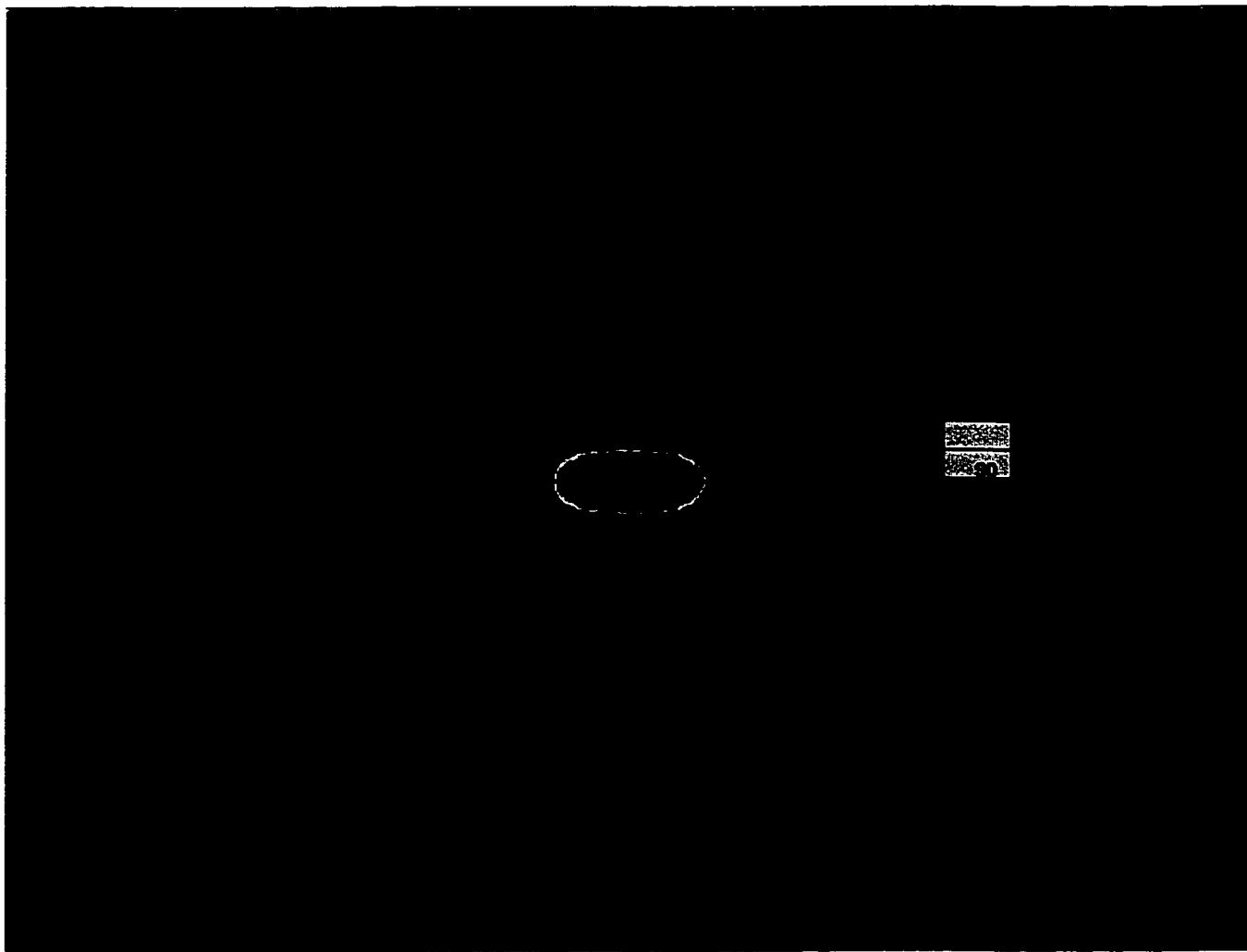


**Figure 5-27** Inverse plan based on eight projections designed to deliver a centred elliptical dose delivery, using in-house TPS. Profiles are planned in PC routine and imported into in-house TPS for purposes of comparison. Intensity profiles at gantry angles 0, 45 and 90 degrees are shown in Figure 5-21.

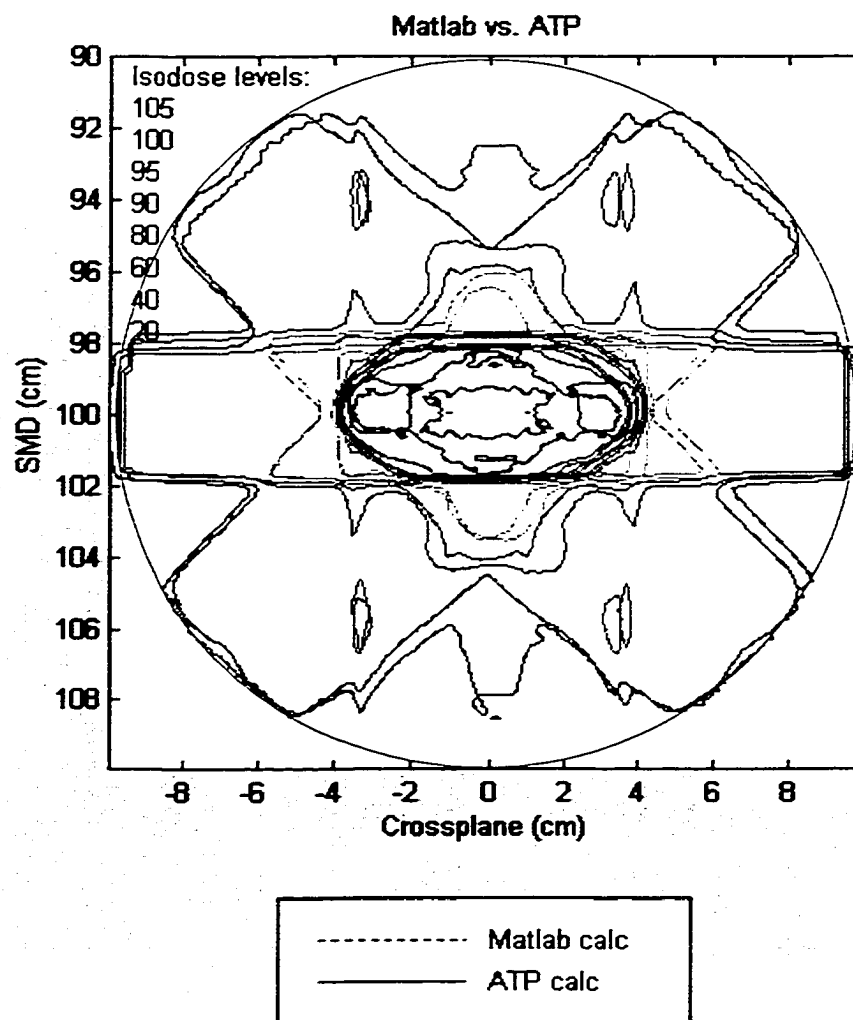


**Figure 5-28** Comparison of two isodose distributions calculated by an in-house treatment planning system (ATP) and by the PC based routine used in this work.

performed (see Figure 5-27 and Figure 5-28). Film measurements were calibrated according to the technique outlined in section 4.2.1 and section 5.4.

Once the calculation and measured dose arrays are aligned, several techniques were used for evaluating the delivery with respect to the stated goal. Firstly, a difference map of the planned versus delivered dose is generated, for both the overall phantom dose, as well as the desired target region. As well, a cumulative dose-area histogram (DAH) is used to evaluate dose coverage for any given slice. Finally, a differential histogram of local dose errors is generated, along with the mean dose difference and the standard error.

The difference map, DAH and differential local error histograms (see Figure 5-29) were generated for the film measurement of the eight field plan shown in Figure 5-27 and Figure 5-28. The difference map shows an error in the dose difference inside the region of interest. This discrepancy between the predicted and measured dose distribution is seen as a slight over estimation of the dose per MU which should have been delivered, as per Equation 3-5 in section 3.2.2.3. It was calculated that, for the delivery of 260 MUs, that the dose would be 108.5 cGy. From Figure 5-29C, we see that this mean local dose difference is  $1.65 \pm 2.81$  cGy. This appears to be good dose coverage, and the DAH (Figure 5-29B) shows good coverage over the area of interest.

The next matter addressed was the number of projections required to approximate a continuous rotational delivery. Once the appropriate number of projections for planning and delivered is determined, we look at the delivery and verification of two other simple distributions, a similar elliptical dose distribution centred about the isocentre, as well as an elliptical distribution centred about a point offset the isocentre.

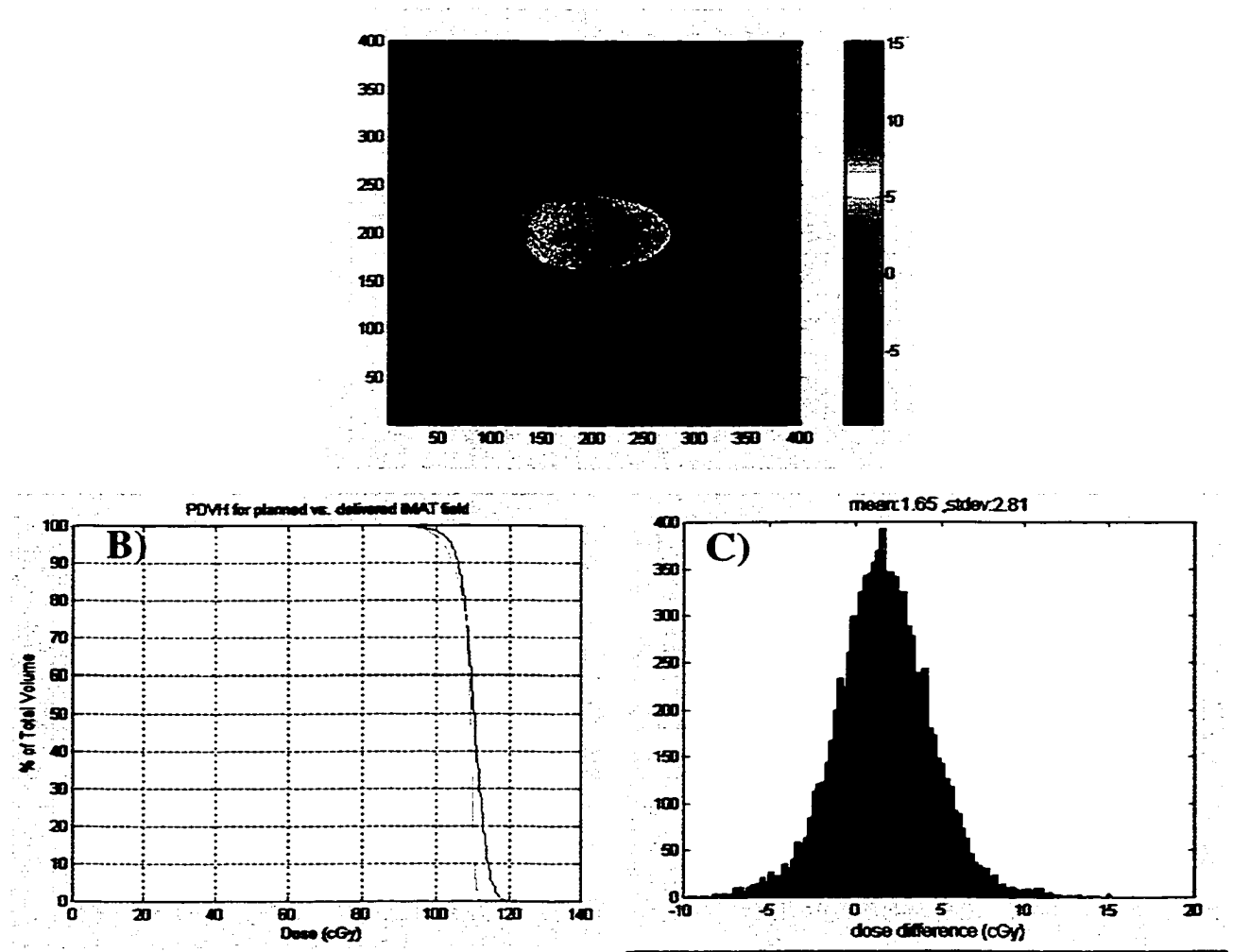


**Figure 5-29** Dosimetric comparison between planned and delivered dose to a central elliptical target. A) Dose difference between planned and delivered in region of interest B) Cumulative dose area histogram of planned (blue) and measured (green) values values C) Histogram of local dose difference between planned and delivered doses.

### 5.5.2 Approximation of continuous motion

There are a number of factors and assumptions that may affect the delivery of planned profiles in an intensity modulated arc delivery. The ability to convert the planned profiles into leaf motions that deliver the desired energy fluence profiles is an important step in the delivery. As well, the assumption is made that a certain number of planned projections are sufficient to approximate a continuous rotation. The former assumption was addressed in section 5.2.2.3 by measuring single projection deliveries in-air. The latter assumption is addressed here.

The approximation of continuous motion by a sufficient number of static beams is a fairly obvious one. Most, if not all, TP systems model fields that are delivered while executing a uniform gantry rotation (often simply referred to as arc delivery) by a large number of static fields. In the case of our in-house TPS, the user specifies the amount of overlap between any two consecutive fields (default overlap is 75%), then the number of fields to be employed is determined. The dose distribution for this arc delivery is then calculated from each of these beams and summed. In the example shown in Figure 5-30, a continuous 10 by 10 cm<sup>2</sup> field is arced around a 20 cm diameter phantom that is nearly cylindrical, and this arc is approximated by the sum of one hundred and eighty one static beams. The isodose lines in Figure 5-30 (as well as for Figure 5-31 and Figure 5-32) are for 100, 80, 60, 50, 40, and 20 percent of the maximum dose. In Figure 5-31, one can see the continuous rotation approximation improving as the number of fields employed is increased from four, to eight, to sixteen and to twenty-four beams for the delivery. The 24 and 181 beam delivery approximations are compared in Figure 5-32. It can be seen that while there are slight differences in the two approximations, these differences are small enough that one may conclude that beyond twenty-four profiles, for a cylindrical geometry, the trade-off in increased computation time is not warranted. This has also been borne out in

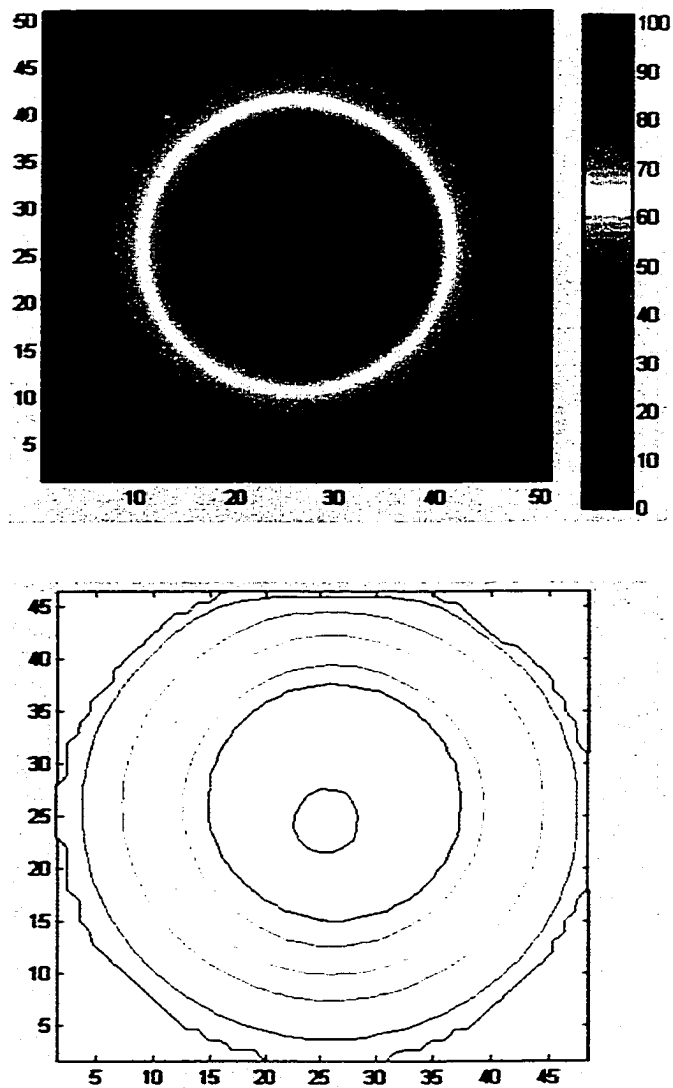


**Figure 5-30** Continuous arc approximation using 181 individual static fields. The isodose lines are for 100, 80, 60, 50, 40, and 20 percent of the maximum dose (in order, starting at the centre and moving out).

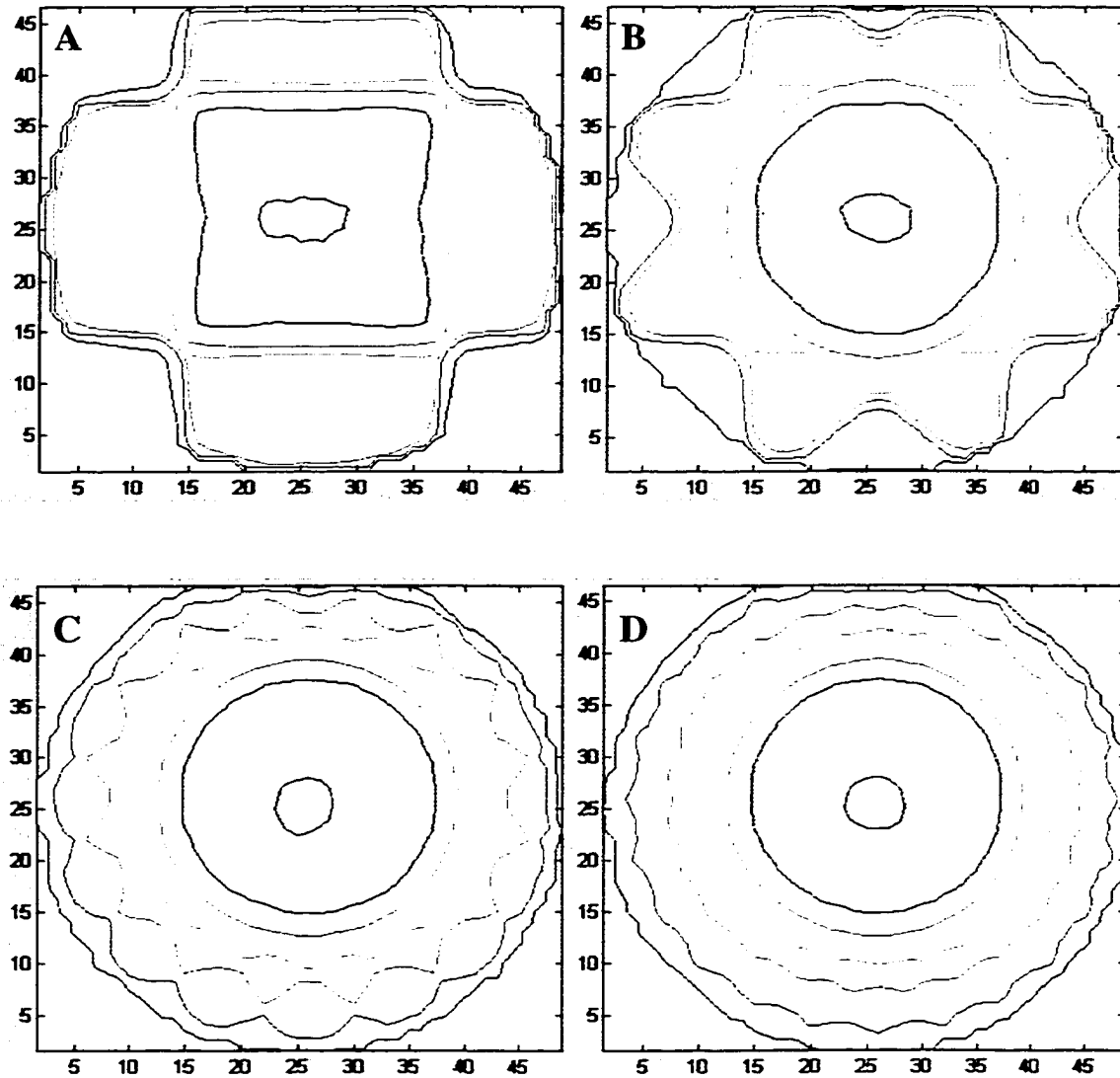


**Figure 5-31** Continuous arc approximation as the number of fields goes from a) 4 fields b) 8 fields c) 16 fields d) 24 fields. The isodose lines are for 100, 80, 60, 50, 40, and 20 percent of the maximum dose.

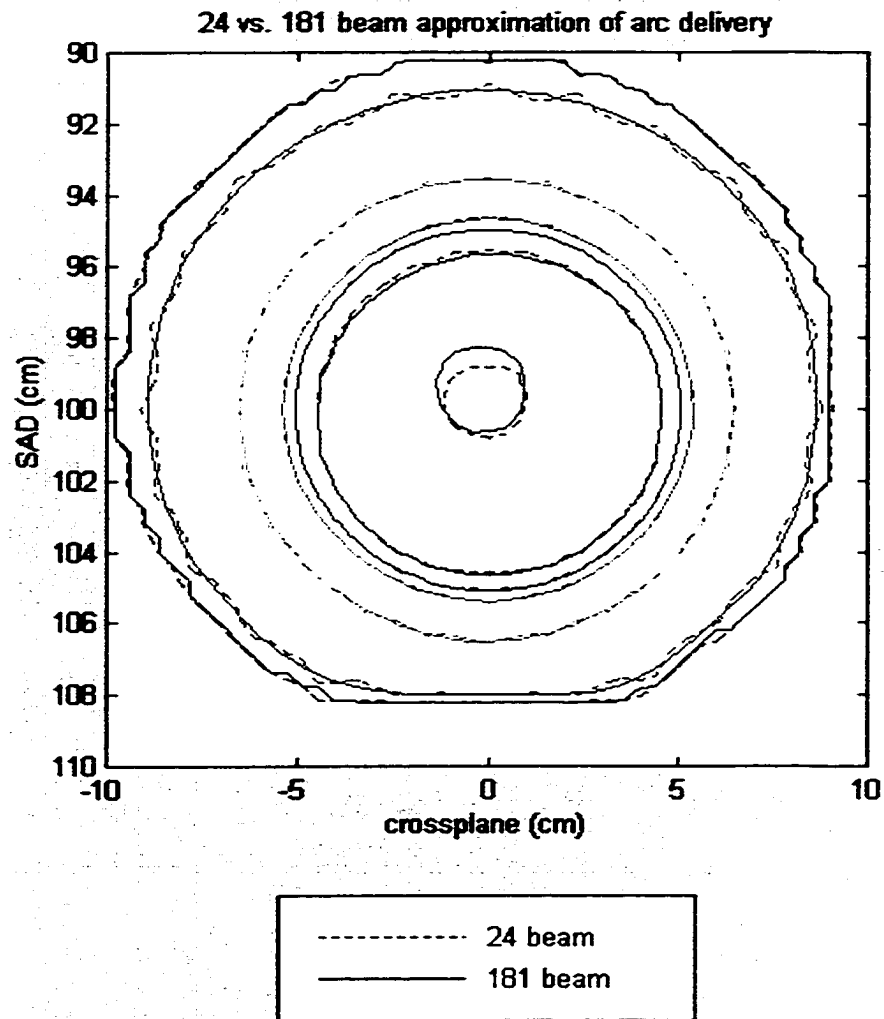


**Figure 5-32 Comparison of the 24 beam (dashed line) and 181.**

the delivery phase for even complex planar dose distributions (i.e. twenty-four fields appears to suffice to deliver complex dose distributions). Twenty-four beams were used for the remainder of planning and delivery cases investigated.

### 5.5.3 Planning of simple distributions: convergence and calculation times

All calculations were performed in a high level interpreted math package (Matlab, MathWorks). As such they are expected to run somewhat slower than compiled routines, and calculation and convergence times should therefore be considered as relative times, and possible to improve upon. All calculations were performed on a PC with a Pentium III 500 MHz processor running Windows NT 4.0.

Two plans were calculated to deliver a homogeneous dose distribution to elliptical regions of interest. One distribution is centred about the centre of rotation, which is coincident with the centre of the phantom (Figure 5-33A). The other distribution is off set from the centre of the phantom (Figure 5-33B). Results of the iterative technique used are shown in Figure 5-34, and Figure 5-35 for two desired dose distributions. The desired dose distribution in each case is a homogeneous dose to the region defined by the area shown in D). The convergence to a final solution occurred, as discussed in section 5.1.1, as the iterations progressed and the various artefact reduction parameters were reduced to limit the degree of smoothing and filtering. After some experimentation, the number of iterations to be used was set at sixteen. The examples shown employ that number of iterations. It was found that similar results were achieved with fewer iterations, but the dose uniformity was degraded. Similarly, a solution could be calculated using fewer projections, but again the solution was degraded; that is to say noisier beam energy fluence profiles were

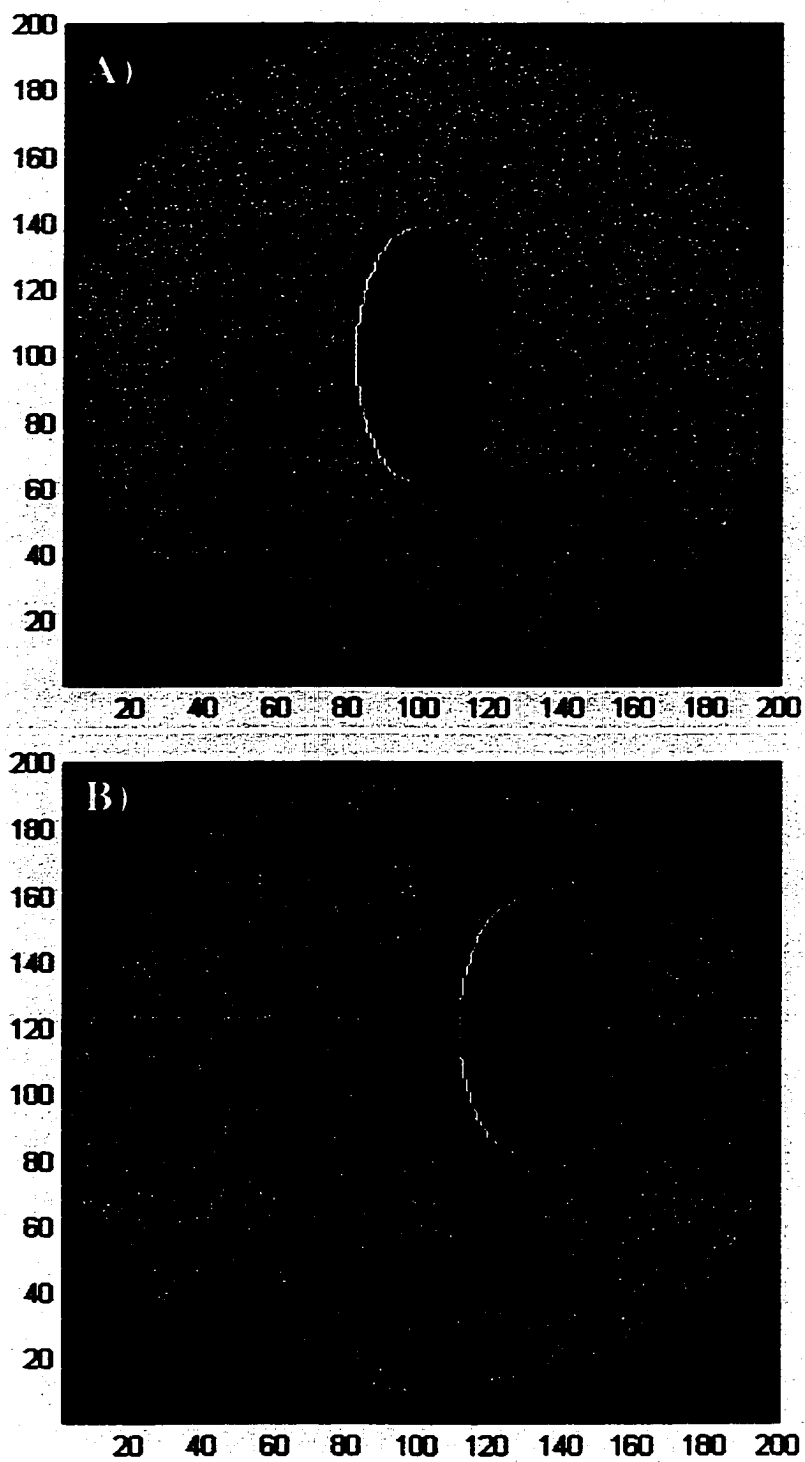


**Figure 5-33** Planned region of interest (in red) within the phantom (green) for elliptical dose delivery A) centred about isocentre and B) off isocentre

produced, and a less homogeneous dose resulted. The number of projections was also chosen because of the fair approximation of continuous rotation that could be achieved, and because of the greater fidelity of the reconstruction that is achieved as the number of projections increases.

Looking at Figure 5-34 and Figure 5-35, one can see the inverse planning process progress as we calculate the initial solution (A), iterate to the 8<sup>th</sup> pass (B) and finally arrive at the desired dose distribution (C). Note that the colour bar used shows the relative dose achieved in A -C (normalised to unity), and the dose difference in relative units from unity (i.e. 0.01 corresponds to 1% difference) between the final calculated and desired dose (D). As the solution iterates from the initial to final solution, the noise reduction techniques used are such that they have the effect of smoothing out high spatial frequency noise due to the discrete nature of the projections. As mentioned previously, this also has the unwanted effect of filtering the high frequency component of the solution, which corresponds to the finer edge detail of the final dose distribution. One can see this edge detail being improved as the algorithm iterates to the final solution, and the filtering and smoothing are decreased. The final dose difference from the desired dose (D) can be seen to be within a few percent of the uniform unity dose.

Calculation times were on the order of 80 minutes per slice calculated, using the computing resources listed above. This is using sixteen iterations, a resolution of 0.05 cm, and 24 beam projections. The calculation time could be greatly reduced by compiling the scripts used, but this was not done, as the total calculation time has no affect on the solutions themselves.

The results of the delivery of the planned distribution shown in Figure 5-34 and Figure 5-35 are discussed further in the following section.

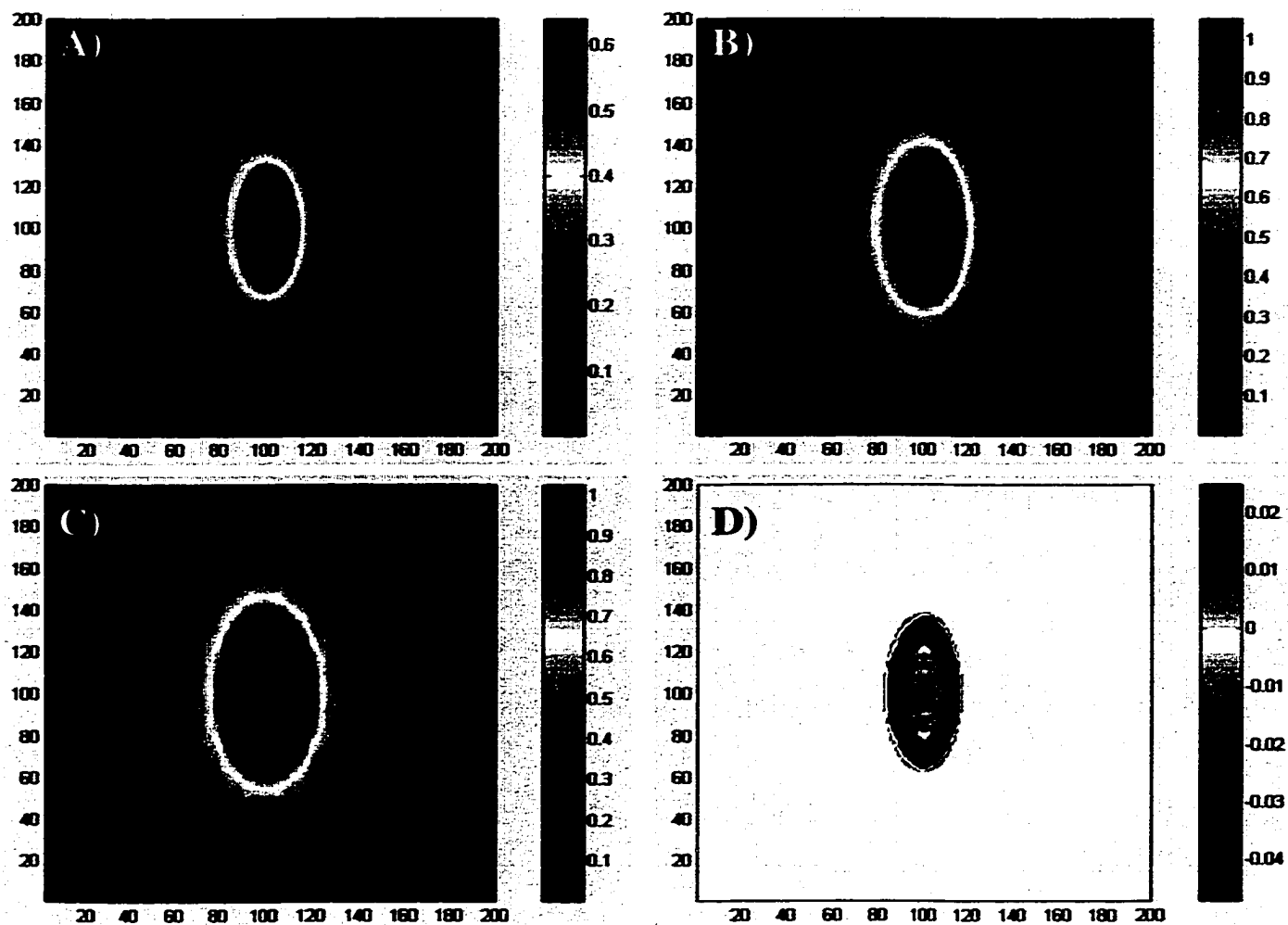


**Figure 5-34** Inverse plan based on 24 projections for a centred elliptical dose delivery. Relative dose distribution is shown at the A) first iteration, B) eighth iteration and C) last (sixteenth) iteration. D) Relative dose difference shown between planned and desired distributions (units of the axes are pixels).

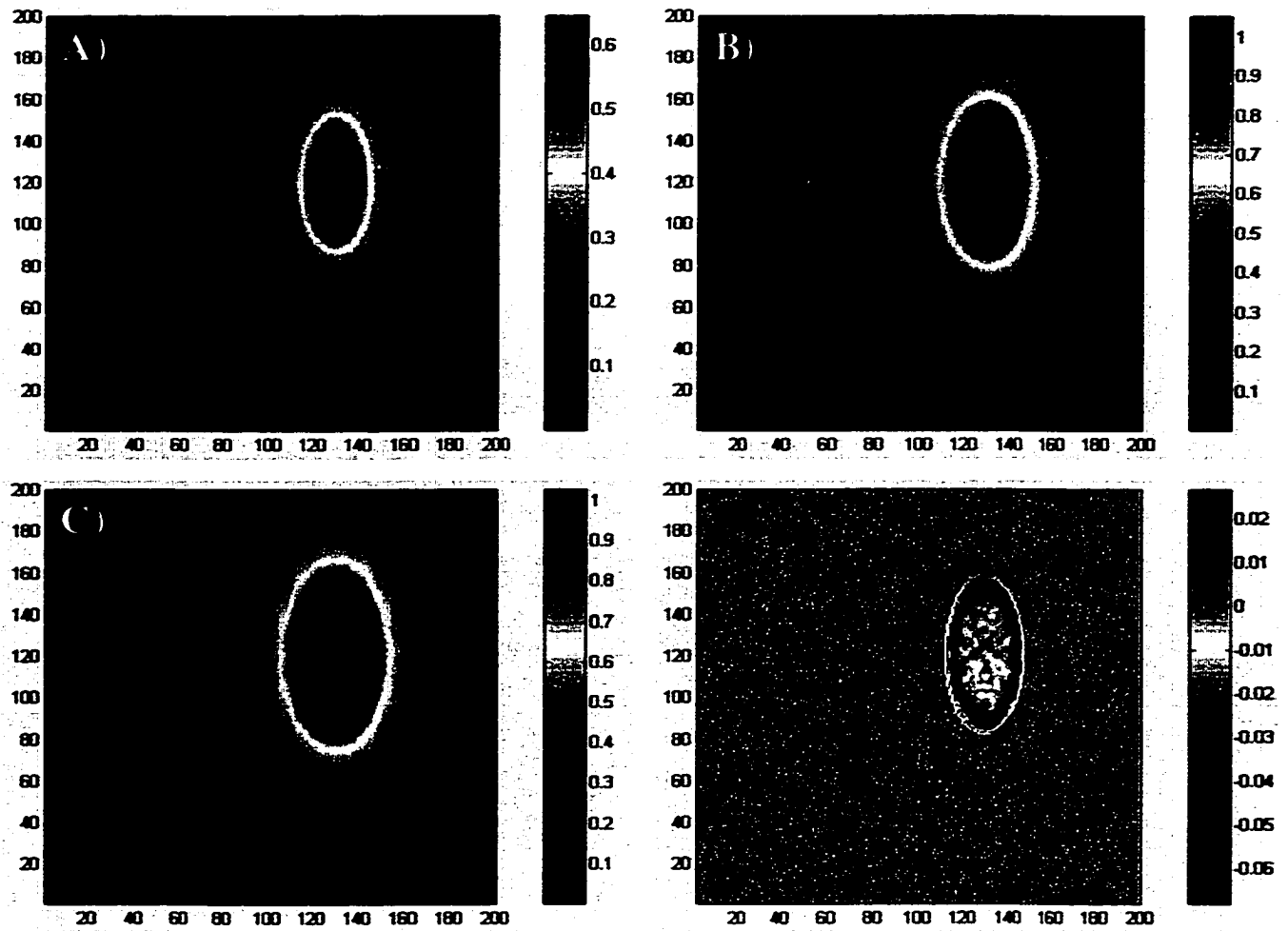


**Figure 5-35** Inverse plan based on 24 projections for an off-centre elliptical dose delivery. Relative dose distribution is shown at the A) first iteration, B) eighth iteration and C) last (sixteenth) iteration. D) Relative dose difference shown between planned and desired distributions (units of the axes are pixels).

#### 5.5.4 Delivery of planned profiles

Aside from the synchronisation of a bank of MLC leaves for the delivery of the single plane, a further synchronisation is also required due to the use of multiple machine parameters during beam delivery. In this work, two controller files are executed simultaneously. One is designed to control the gantry (and potentially other parameters such as the collimating jaws), and the other is used to control the leaf positions of the MLC. In order to avoid creating a conflict over the dose modulation and to keep the gantry speed at a maximum value, the arc control is calculated based on the DMLC motion. Once the required energy fluence profiles have been calculated, the leaf motions required may also be calculated. From the leaf motions, the dose per MU setting may be calculated (refer to section 3.2.2.3). Knowing the total dose (and therefore total number of MUs) to be delivered, along with the actual maximum leaf velocities, the leaf trajectories required to keep the dose rate at a maximum are found (as per section 3.2.3).

Due to slightly fluctuating dose rates, presumably when the leaf acceleration was non-zero [Svenson 1994], the actual deliveries could not be delivered in a continuous arcing fashion. Once the dose rate changed from its constant (maximum), this caused the gantry to slow, and sudden changes in gantry motion caused gantry motion to cease. This in turn caused the treatment to cease, as the gantry was outside its dose - position tolerance limits for the treatment.

This difficulty in achieving a true IMAT delivery should be viewed as a mechanical or dose rate control limitation of the present equipment. It is not an inherent problem with this concept for delivery of IMAT fields. IMAT fields were, however, delivered using a discrete 15 degree step and shoot method, combined with the sliding window fields.

The results of the planned delivery of the simple elliptical dose distribution from twenty-four projections are shown in Figure 5-36 and Figure 5-37. The predicted dose distributions used for comparative purposes are based on the planned distribution, which is then scaled by the dose to a reference point, using the dose per MU value from Equation 3-5.

The first of these deliveries is for an elliptical dose distribution centred about the isocentre, which was made to coincide with the centre of the phantom. The dose difference between planned and measured dose distributions is arrived at by taking the planned dose distribution, scaling by the calculated dose per MU times the number of MUs used, and subtracting the measured dose distribution. Using the binary map of the region of interest (see section 2.1) and multiplying it by the measured and planned dose distributions yields the dose difference in the region of interest. This dose difference is given in Figure 5-36B, and provides one measure of the agreement between planned and delivered dose distributions. As can be seen by looking at the difference map, the dose homogeneity is good, and even at the edges where the variation is on the order  $\pm 5$  cGy. The largest differences occur in the posterior - anterior direction (along the major axis direction of the ellipse). This may be related to the slight attenuation of the beam by the Styrofoam phantom support.

Finally, the dose coverage of the region of interest may also be seen to be quite good, and close to the desired dose, by examining the cumulative dose area histogram (Figure 5-36C). As well, the local difference histogram (Figure 5-36D) can be seen to be quite small, and the mean value is easily within a standard error range of the predicted dose delivery. The predicted dose is arrived at using the calculated dose distribution scaled by the dose per MU as calculated by the methods outlined in 3.2.2.3. The mean dose difference between the predicted and measured values is 0.329 cGy, with a standard error of 1.47 cGy (0.4% difference,  $\pm 1.6\%$ ).

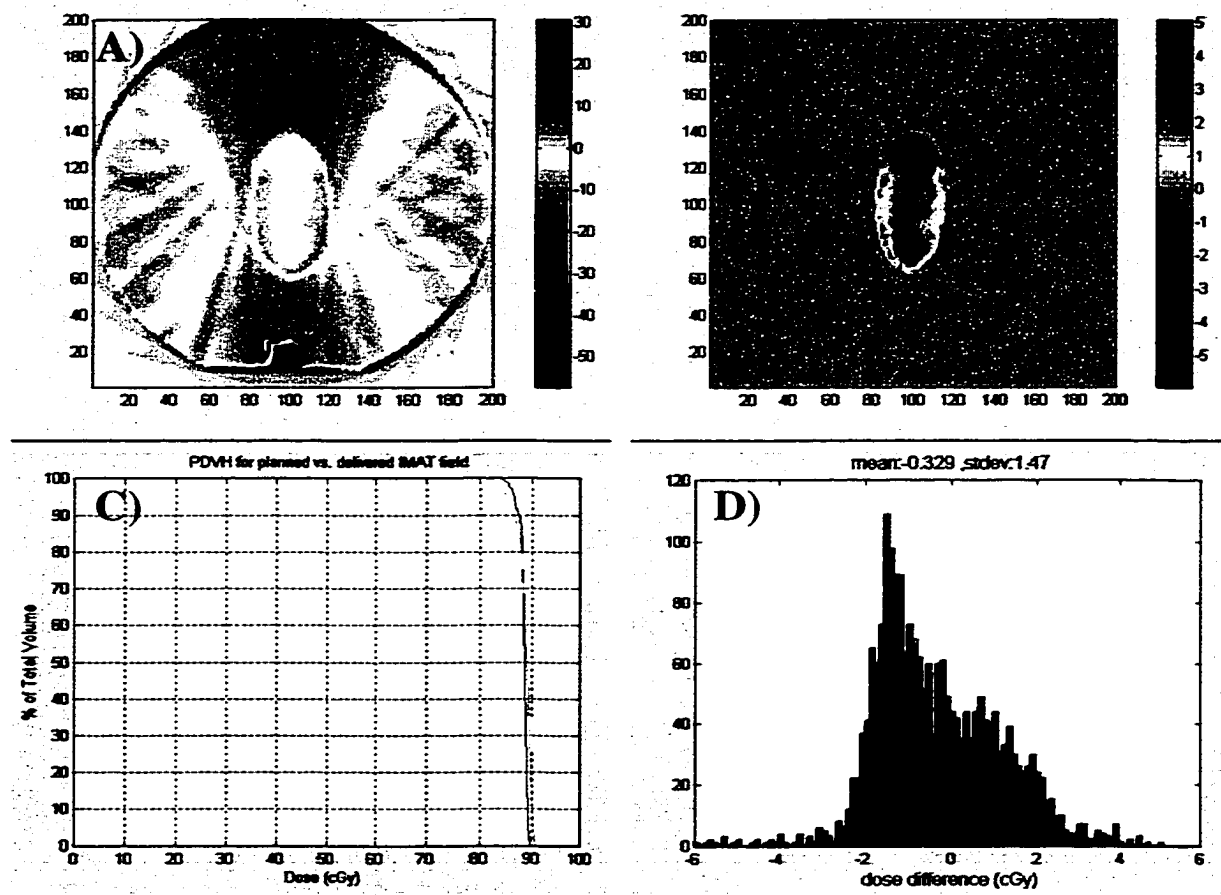


**Figure 5-36** Results of dose delivery for simple elliptical dose distribution centred about the isocentre. A) dose difference between planned and delivered B) dose difference between planned and delivered in region of interest C) Cumulative dose area histogram of planned (blue) and measured (green) values D) Local error histogram showing local pixel differences between predicted dose and measured dose.

The next simple dose delivery was that of an elliptical dose distribution of the same dimensions as the one discussed above, but with its centre translated away from isocentre. The results from this delivery are given in Figure 5-37.

The results of this delivery are quite good as well. The dose difference in the region of interest (Figure 5-37B) again shows an overall high degree of homogeneity and good agreement with the desired dose distribution. There is, once again, a polarisation of high and low doses along the major axis of the ellipse. The cumulative dose area histogram (Figure 5-37C) has a broader appearance, indicating a larger dose range over the region of interest. This is further quantified in the local difference histogram (Figure 5-37D), where we see that the discrepancy is higher than in the centred ellipse, and the standard error is also higher, again indicating a less homogeneous dose. The mean dose difference between the predicted and measured values is -2.16 cGy, with a standard error of 2.54 cGy. The delivery is nevertheless under one standard error range from the predicted dose delivery, and the mean difference constitutes only roughly 2.4 % of the predicted dose.

### ***5.6 Delivery of complex planar dose distributions***

The investigation of more complex distributions constitutes a more complete test of intensity modulated arc deliveries by this method. Two complex dose distributions were planned and delivered: an irregular ‘butterfly’ shaped dose distribution, an irregular shape incorporating slight concavities as one might encounter in clinical reality. A second and more challenging delivery was planned for a highly concave distribution. The desired homogeneous dose distribution regions are shown in Figure 5-38A for the irregular ‘butterfly’ distribution, and in Figure 5-38B for the concave dose distribution.

The planning of these deliveries is shown in Figure 5-39 and Figure 5-40. A feature present in these inverse plans, not seen in the previous two twenty-four beam

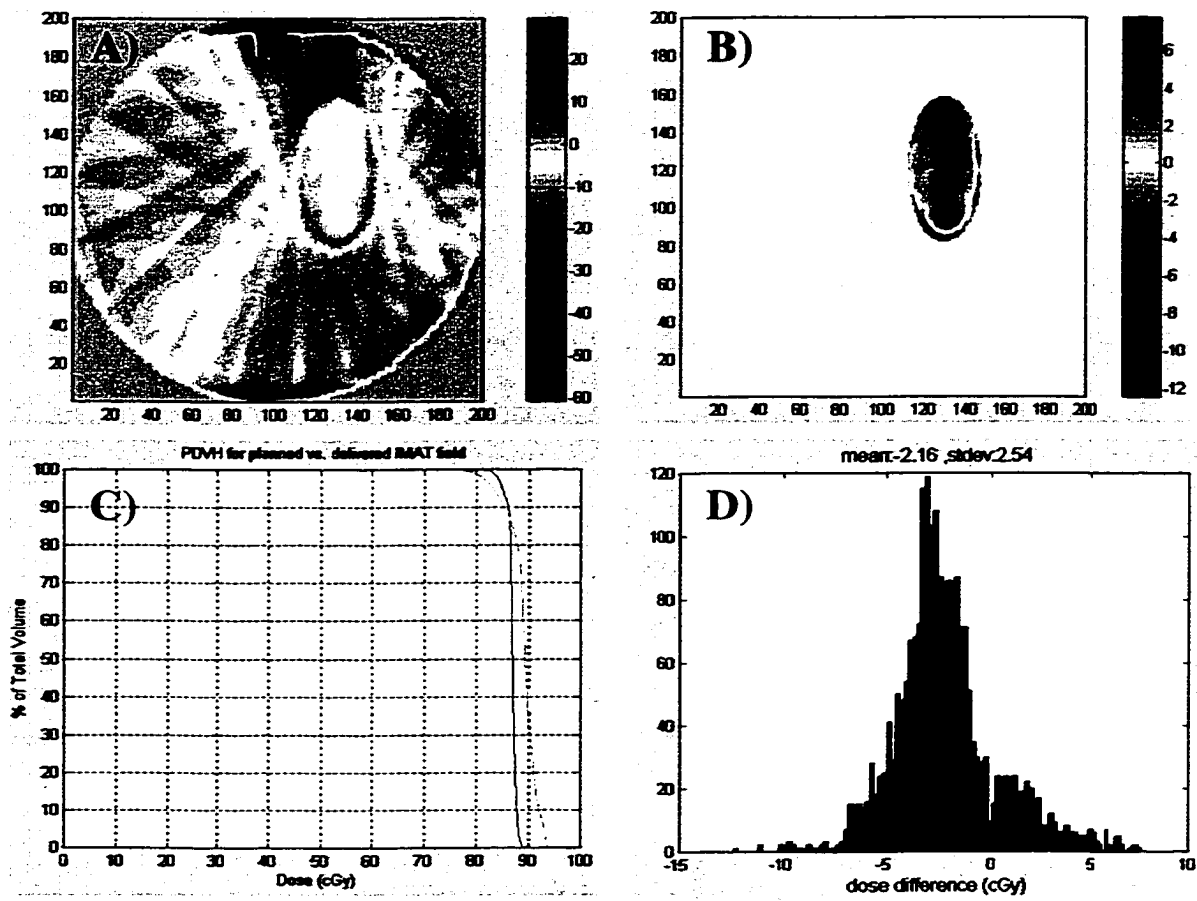


**Figure 5-37** Results of dose delivery for simple elliptical dose distribution centred about a point off the isocentre. A) dose difference between planned and delivered B) dose difference between planned and delivered in region of interest C) Cumulative dose area histogram of planned (blue) and measured (green) values D) Local error histogram showing local pixel differences between predicted dose and measured dose.

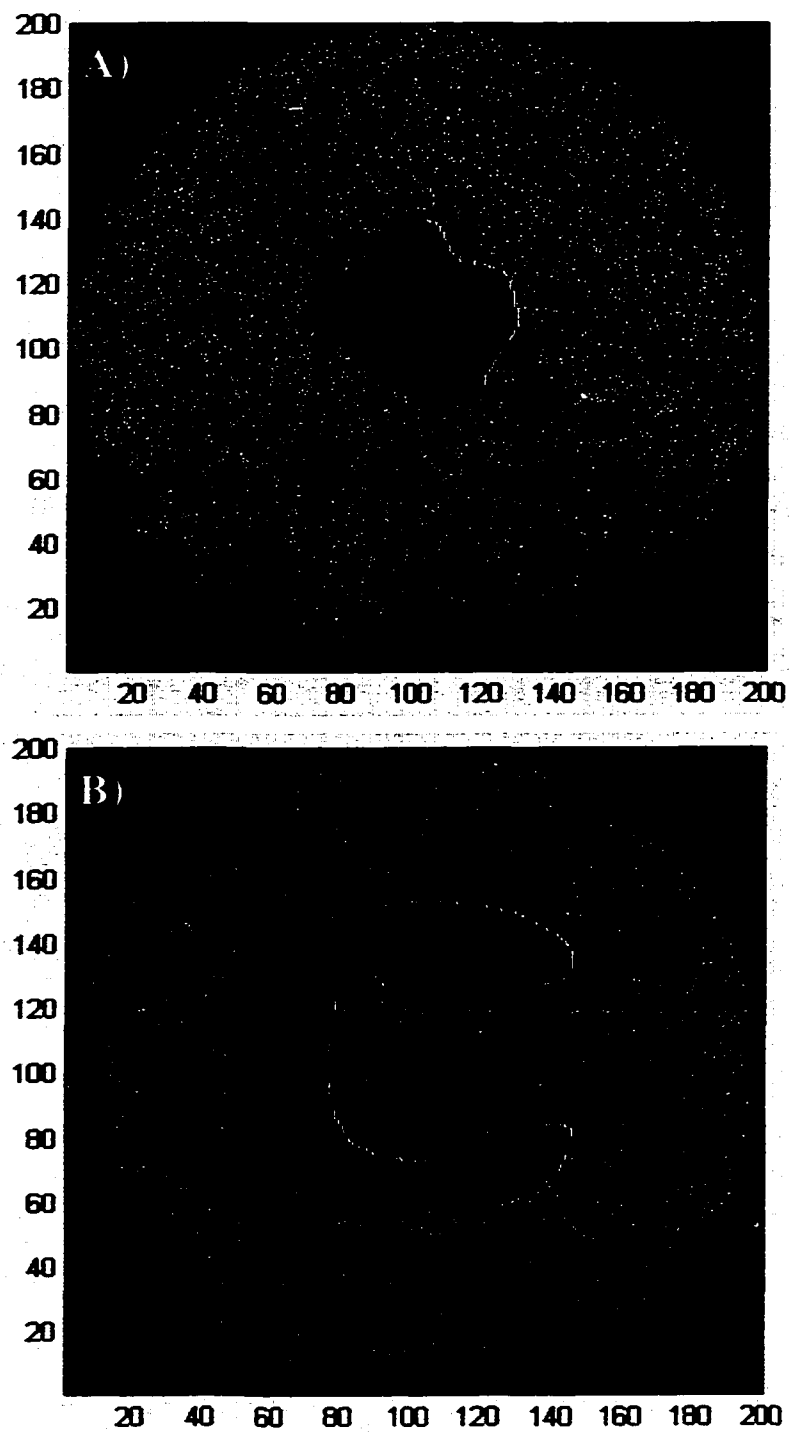


**Figure 5-38** Planned region of interest (in red) within the phantom (green) for A) an irregular dose distribution and B) a concave dose distribution.

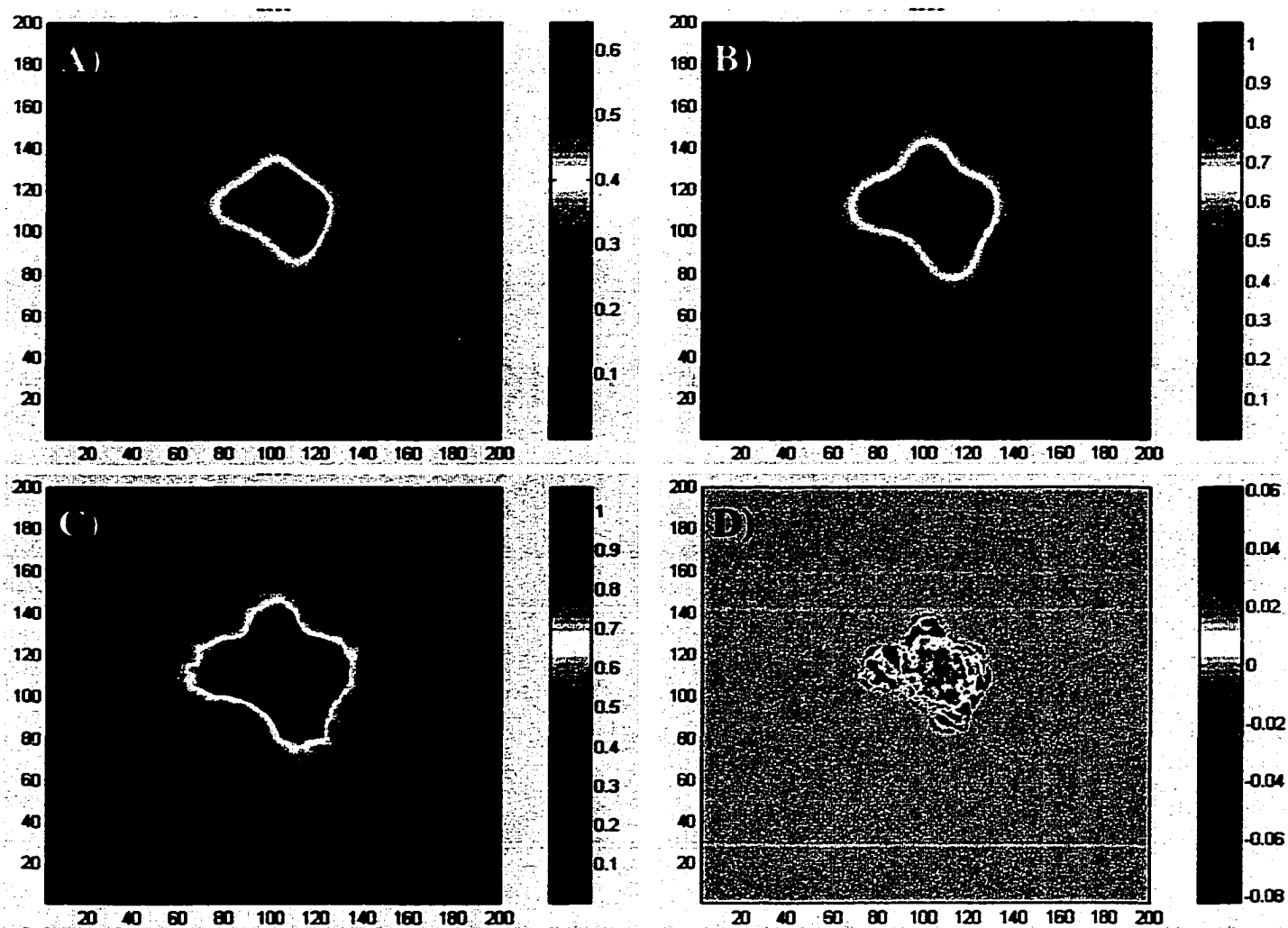


**Figure 5-39** Inverse plan based on 24 projections for an off-centre ‘butterfly’ shaped dose delivery. Relative dose distribution is shown at the A) first iteration, B) eighth iteration and C) sixteenth and final iteration. D) Relative dose difference shown between planned and desired distributions (units of the axes are pixels)

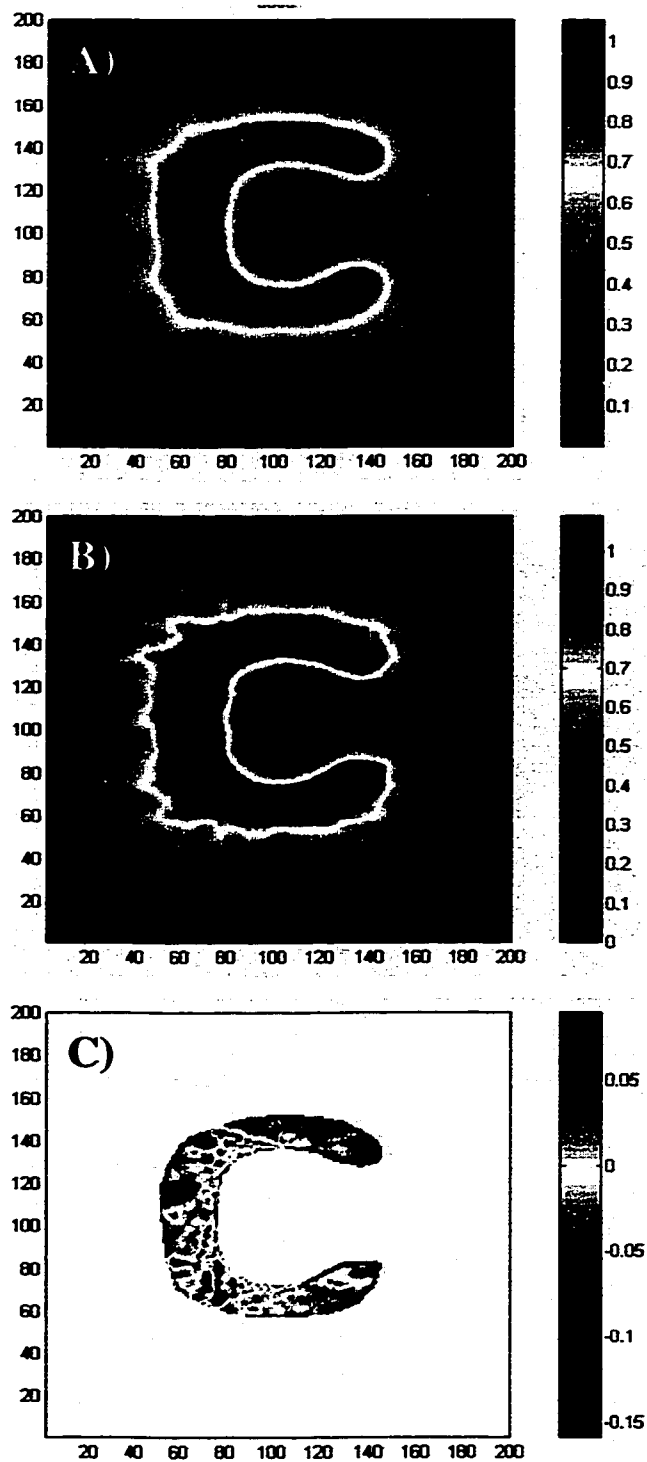


**Figure 5-40** Inverse plan based on 24 projections for a concave dose delivery. Relative dose distribution shown at A) eighth iteration and B) sixteenth and final iteration. C) Relative dose difference shown between planned and desired distributions (units of axes in pixels).

plans, is an increased level of streaking. The more complex plans seem to be more prone to computational artefacts in the planning stages. These streaks seem to have a value of roughly 5% greater than the unity dose that is planned. There is also a very slight lack of coverage in the plan in some of the edge pixels. These shortcomings of the plans are discussed further in Chapter 6. The effect of this streaking is discussed here with respect to the effect on the delivery of these planned dose distributions.

The results of measured dose distributions from these inverse plans versus the predicted dose distributions are given in Figure 5-41 and Figure 5-42.

The results of the irregular dose distribution planned in Figure 5-39 are shown Figure 5-41. The dose differences are shown in Figure 5-41A and Figure 5-41B. The largest dose differences come, as before, from the points near the edge of the region of interest. A difference with this plan, compared to those previously presented, is the difference that arises due to the streaking present in the planned distribution. This streaking does not appear in the delivered dose distribution for two reasons. Firstly, the sharp variation in the final planned fluence profiles exist due to computational artefacts and were smoothed by the application of a median filter. This served to mitigate, but not entirely remove, these variations. A second effect is the natural smoothing that occurs in the sampling of the delivery profile into discrete control points. The net effect of this is to provide a smoother dose distribution delivery.

From Figure 5-41B and Figure 5-41C it can be seen that the dose coverage is relatively homogeneous, and within the standard error of the planned dose distribution. The mean dose difference between the predicted and measured values is 1.45 cGy (1.6% shift), with a standard error of 2.22 cGy (2.4% error). The larger dose differences are confined to points along the edge, as well to the overestimate of the dose from the spurious streaking within profiles.

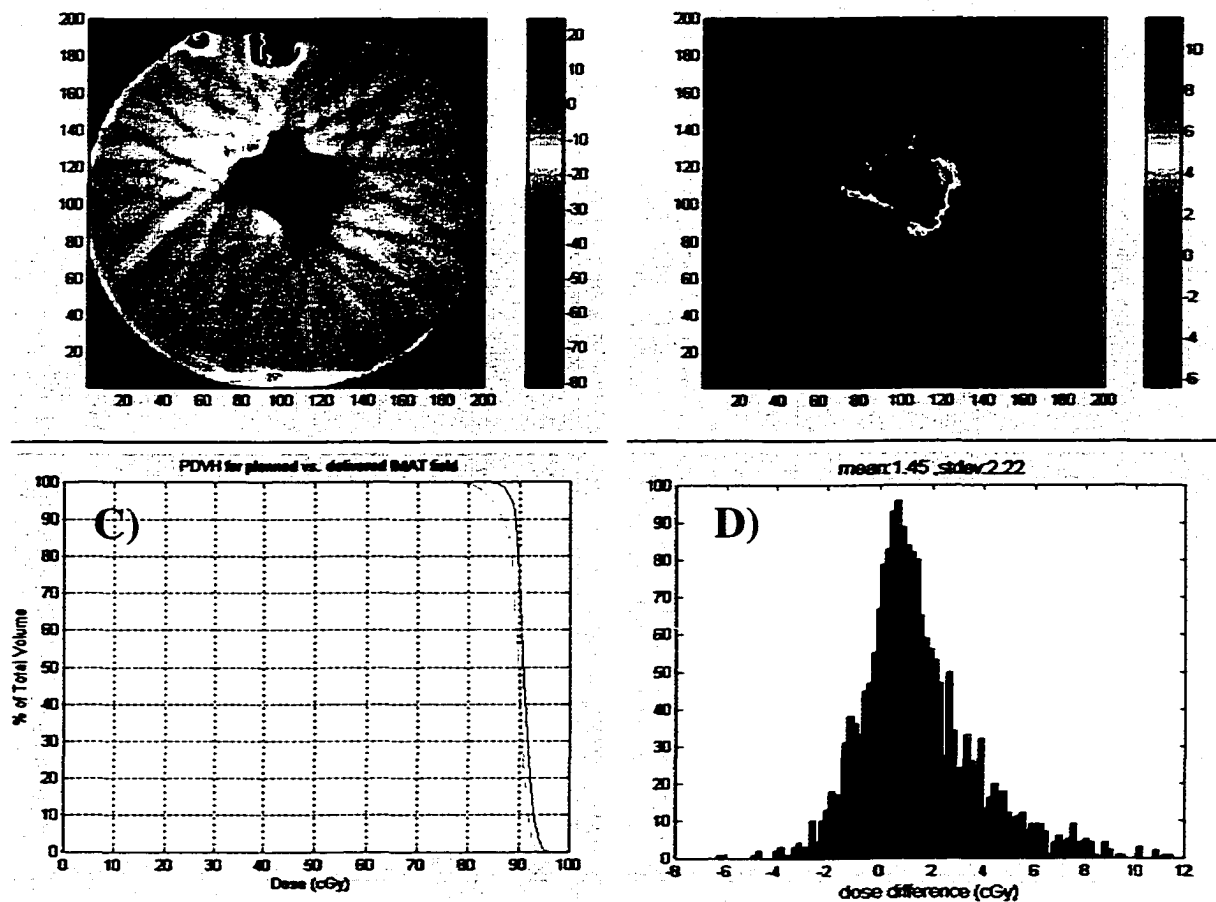


**Figure 5-41** Results of dose delivery for a complex off-centre ‘butterfly’ dose distribution. A) dose difference between planned and delivered B) dose difference between planned and delivered in region of interest C) Cumulative dose area histogram of planned (blue) and measured (green) values D) Local error histogram showing local pixel differences between predicted dose and measured dose.

The most complex of the dose deliveries attempted is the concave dose distribution, the results of which are summarised in Figure 5-42. The mean dose difference between the predicted and measured values is 5.81 cGy (6.0 % shift), with a standard error of 3.04 cGy (3.2 % error). This discrepancy is higher than that of the other distributions, as is the standard error. There is one large edge artefact, which is most obvious in Figure 5-42B, which is the hot spot denoted in red. The dose coverage, as evidenced by the dose area histogram of Figure 5-42C, is good although the magnitude of the dose is less than what was predicted for the MU setting used. The result is quite good considering the high complexity of the dose distribution that is sought in this case. It is more difficult to make comparisons in this case, as the streaking in the planned distribution gives rise to differences in the dose difference map, which are not meaningful differences. The implications of this are discussed further in Chapter 6.

In order to assess the effect of the streaking artefact in the planned distribution on the level of agreement between the planned and measured dose distribution, the measured distributions were compared to the desired uniform distribution, scaled by the predicted dose delivery. In Figure 5-43, the dose difference and local dose error histogram are given for the two simple dose distribution deliveries. In Figure 5-44, the dose difference and local dose error histogram are given for the two complex dose distribution deliveries. From these comparisons, one can see that the mean is not markedly different, nor is the standard error in dose difference, for the simple deliveries. This is not surprising, as the planned distributions for these fields were relatively artefact free. For the complex deliveries, the standard error in dose difference is again relatively unchanged. For the mean dose difference, the difference for the 'butterfly' distribution drops from 1.45 to 0.3 cGy, and for the concave delivery, the difference drops from 5.8 to 3.8 cGy. It therefore appears that part of the increased difference between the planned and measured is partly due to computational artefacts in the planned distributions.

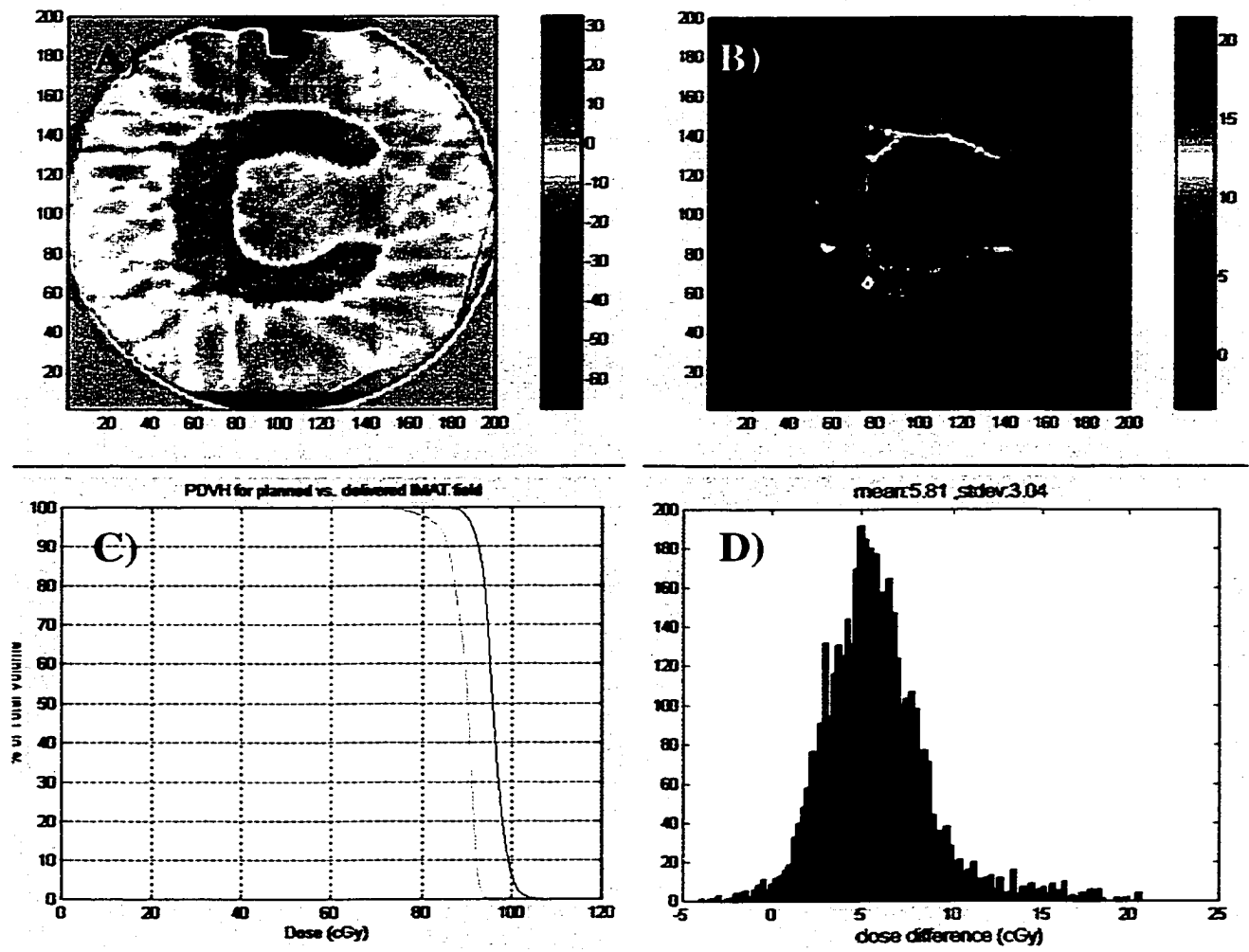


**Figure 5-42** Results of dose delivery for a complex concave dose distribution. A) dose difference between planned and delivered B) dose difference between planned and delivered in region of interest C) Cumulative dose area histogram of planned (blue) and measured (green) values D) Local error histogram showing local pixel differences between predicted dose and measured dose.

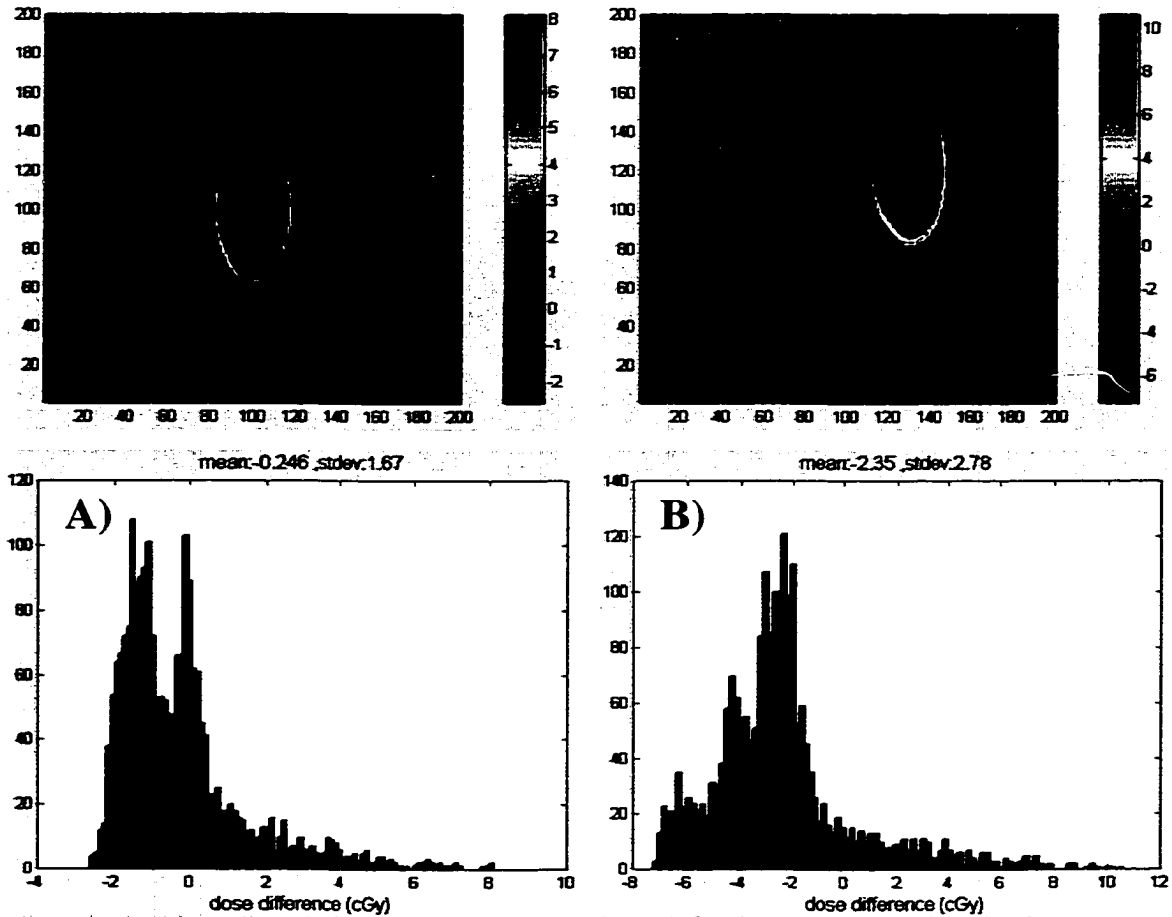


**Figure 5-43** Local dose error histogram using the desired dose distribution, scaled by predicted dose, for simple dose deliveries A) centred elliptical dose distribution and B) off-centre elliptical dose distribution

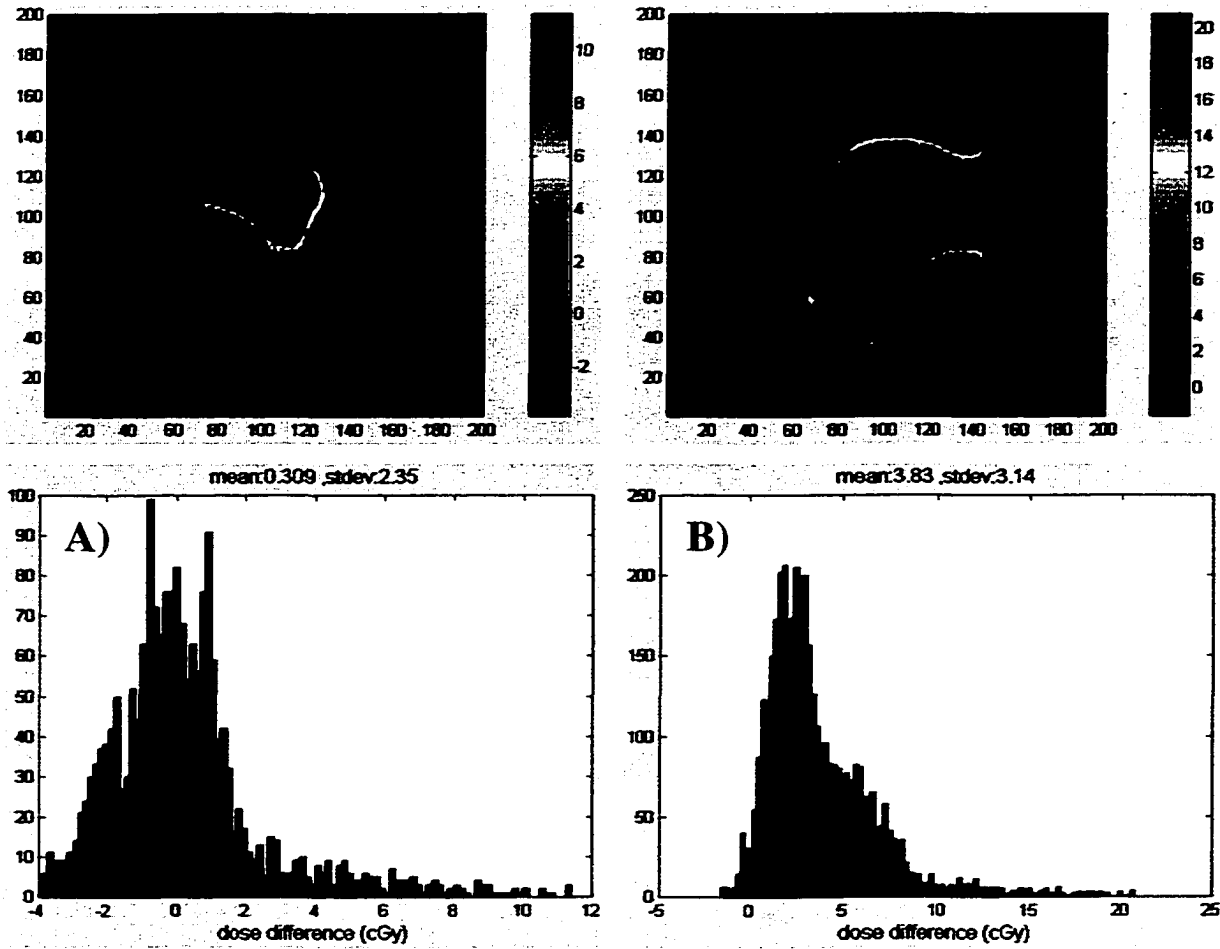


**Figure 5-44** Local dose error histogram using the desired dose distribution, scaled by predicted dose, for complex dose deliveries A) irregular 'butterfly' dose distribution and B) concave dose distribution

### **5.7 3D multi-slice delivery**

The 3D-multi-slice delivery that is presented in this section is given as a qualitative example of how this technique may be employed, in principle, to deliver a very complex 3D dose distribution. The reason that the comparison is made only in a qualitative sense is that the planning and dose calculation techniques developed are 2D in nature. Although the initial planning and calculations may be done for individual slices as presented, a full 3D dose calculation for any multi-slice plan should be done at some juncture to properly account for the effect of scatter from neighbouring slices on one another. The desired dose distributions for this delivery are shown in Figure 5-45.

The multi-slice delivery is treated, to a first approximation, as a simple extension of the planar delivery to multiple contiguous slices. For most realistic clinical cases, the variation from one slice to the next should never be as extreme as the example delivery examined here.

This 3D plan was devised to stress the ability to deliver highly irregular concave dose distributions, which vary a great deal from slice to neighbouring slice. Partly due to the high degree to which these planned dose distributions do differ from one another, and partly due to limitations in the spacing available on the cylindrical phantom, the slices were planned and measured at 2-cm intervals. The delivery was performed using 2 synchronised leaves for each slice.

In order to ascertain the ability of the algorithm to translate planned in-air energy fluence profiles for a multi-slice delivery to leaf motions, an STT file was generated for one of the twenty-four projections for a five-slice delivery. This desired

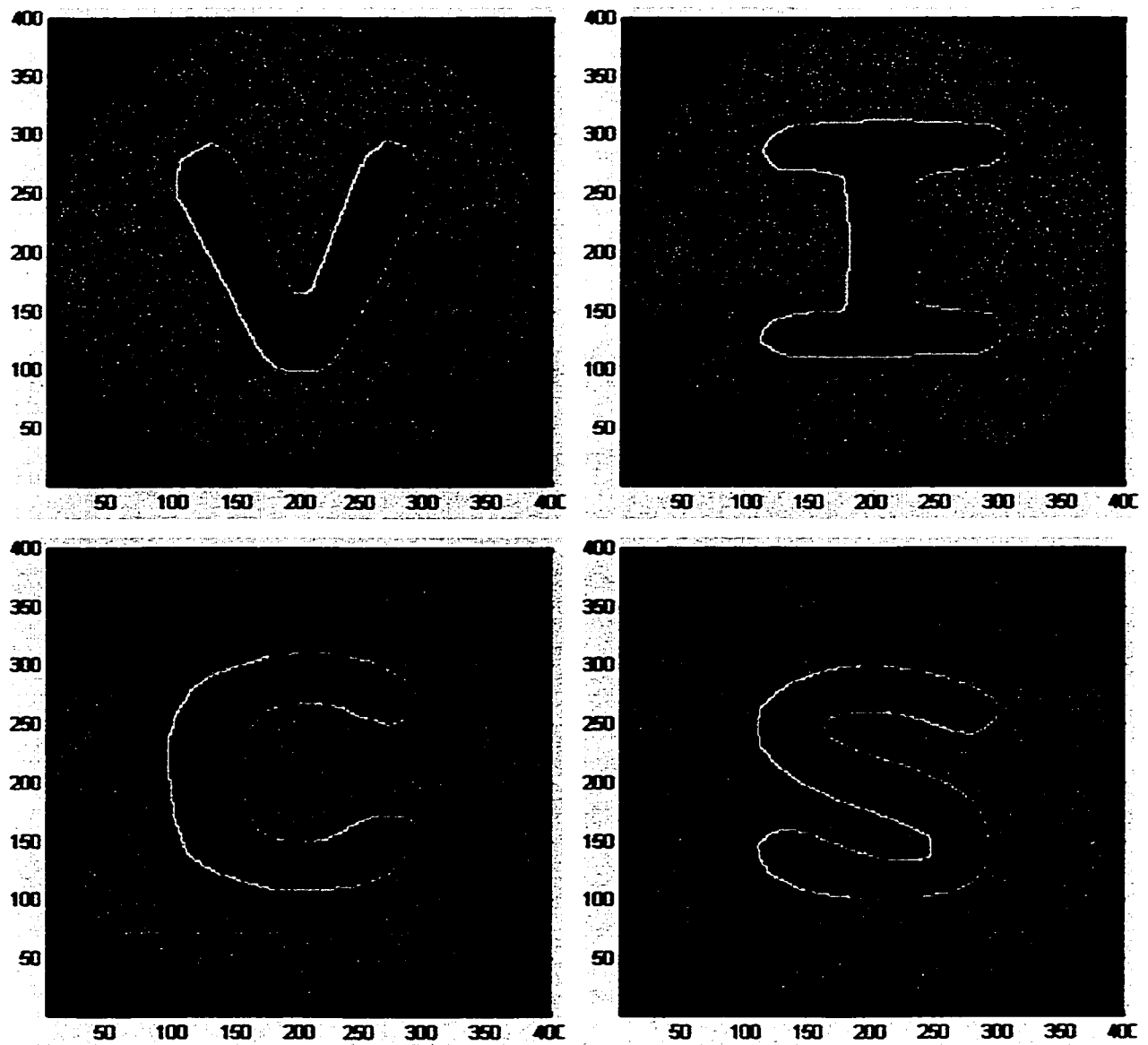


**Figure 5-45** The desired treatment regions for the multi-planar 3D dose delivery.

in-air energy fluence profile is shown in Figure 5-46A. This file was read by the software package that is supplied by the MLC vendor to validate MLC and DMMLC plans. The vendor software can generate a calculated transmission image based on the leaf motions in the file. A comparison is made, purely for the purposes of providing a qualitative check on the calculated leaf motions, with the vendor software calculated transmission image, shown in Figure 5-46B. It is readily apparent that the leaf motions for the planned 2D-energy fluence profile give a similar result.

The results of this delivery are shown in Figure 5-47B and Figure 5-47C for all five slices. Figure 5-47B shows the actual film image of this delivery, while Figure 5-47C shows the isodose distributions from these films. The red line, which encompasses the desired region of interest, represents the 90% isodose line, and corresponds to a dose of 72 cGy. The planned target dose is 80 cGy. The results of this delivery are especially good in light of the fact that the planning is done on a slice by slice basis. Results may improve for this type of delivery for more clinically realistic cases, where there may not be as much variation from slice to slice, or if a full 3D calculation is performed at some stage to account for any large slice to slice variation.

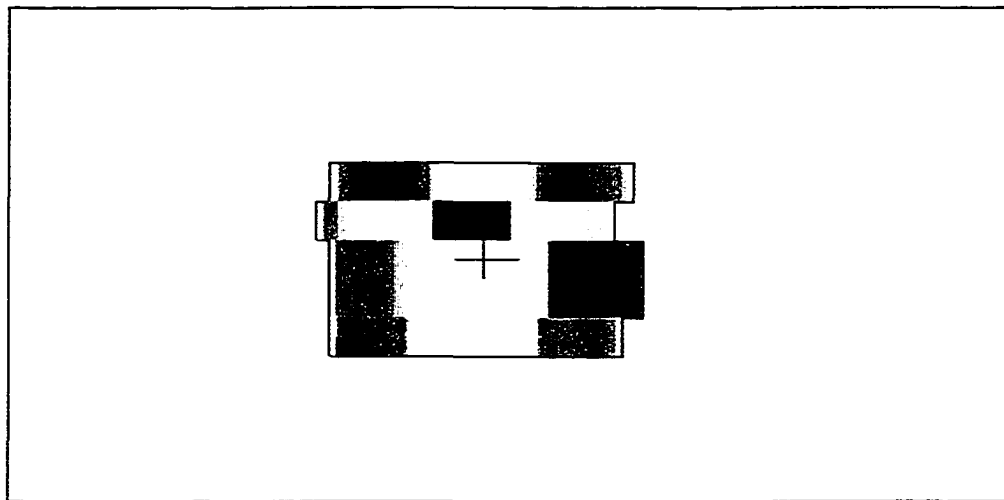
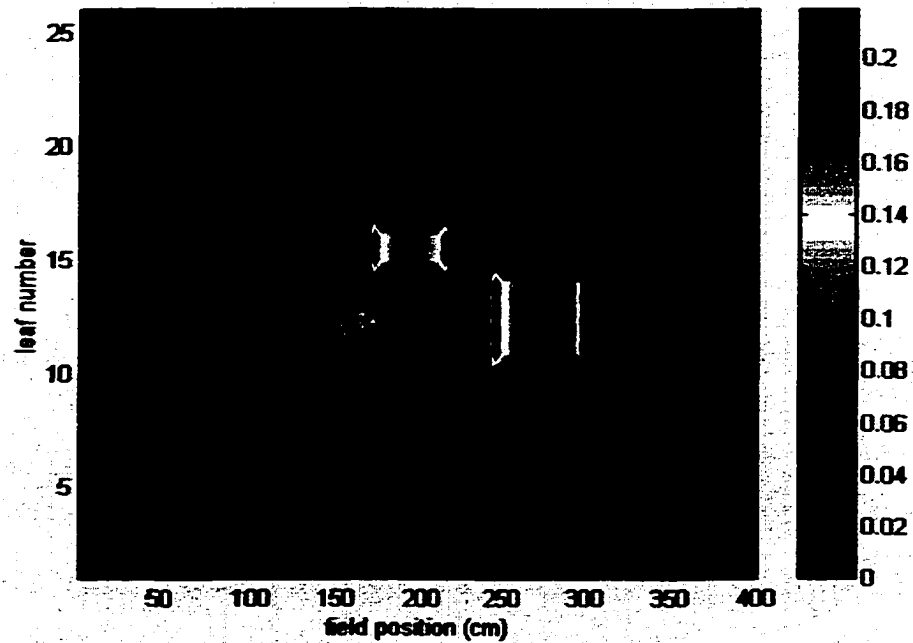


**Figure 5-46** A) Planned single projection (of 24) of required energy fluence profile for a 3D plan (5 slices planned) B) independent software confirmation of net relative intensity resulting from planned leaf motions, assuming simple summed aperture intensity model.

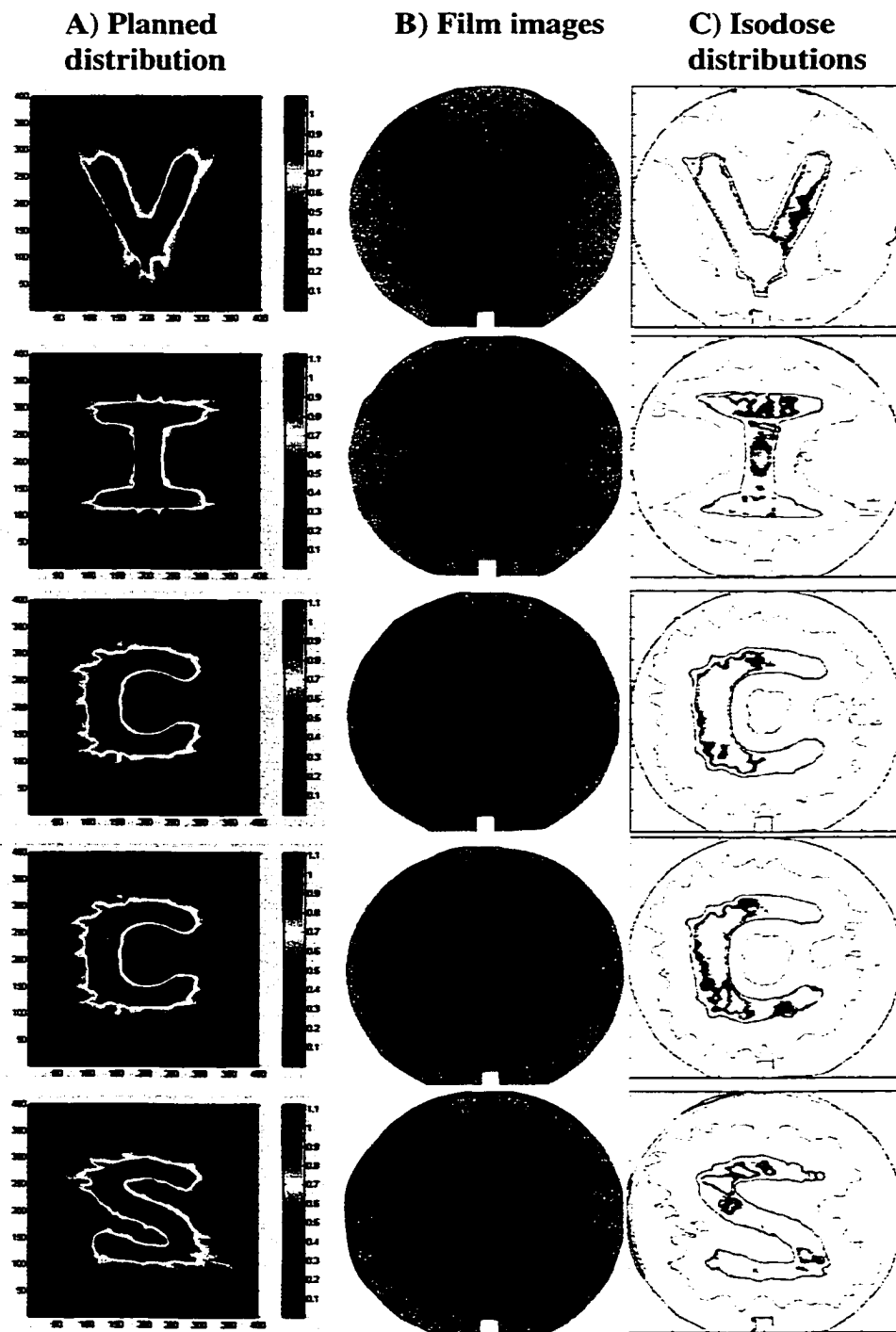


**Figure 5-47** Results from concurrent slice delivery (multi-slice, 3D plan) of highly irregular dose patterns; planned distribution (A), film images (B) and isodose levels (C) for 20 (dk. blue), 40 (lt. blue), 60 (yellow), 74 (red) and 82 (red-brown) cGy.

## Chapter 6 Discussion, conclusions and future work

The goal of this work was to demonstrate the feasibility of delivering an arbitrary dose distribution using an IMAT scheme that employs a sliding window DMLC and a single gantry pass. The ability to deliver arbitrary 2D homogeneous dose distributions in this manner was demonstrated, along with the viability of the overall planning and DMLC STT calculation technique. As well, the ability to deliver a very complex 3D multi-slice delivery has been demonstrated in principle. The development of this technique has presented some instructive challenges for planning, delivery, modelling and verification.

The success in delivering the elliptical, off-isocentre elliptical and irregular ‘butterfly’ shaped dose distributions demonstrates the ability to not only deliver simple and irregularly shaped homogeneous dose distributions, but the ability to predict the absolute dose that will be delivered for these dose distributions. The increasingly off-centre (such as the off-centre ellipse distribution of Figure 5-35) and complex profiles (such as the concave distribution of Figure 5-40) were certainly the more problematic distributions, in terms of predicting the absolute dose output of the delivery, although the former was moderately successful. The reasons for these shortcomings lie most likely with the difficulties in accurately calculating the  $CF_{dyn}$  factor for these more complex deliveries, and perhaps in the calculation of the off isocentre dose distributions themselves.

There were a number of components in the planning process that were somewhat extraneous to the validity of the overall thesis. These components, as well as the approximations used in this work, need to be improved upon in order to allow this technique to be incorporated into the clinical setting. Some of the benefits and shortcomings of the various aspects of the methods used are addressed here, along with proposed future directions for research into this technique.

The planning process has been shown to be capable of calculating the required energy fluence profiles to deliver a desired dose distribution. This process, however, still appears to admit some computational artefacts in the final solution, and calculation times are long. An improvement to the overall process may be to either improve the noise suppression technique employed in the current scheme, or adopt another inverse planning scheme. One promising candidate may be a proposed analytic scheme, which has been recently published [Oelfke 1999]. Improvements of this nature are required to alleviate the streaking problem that is seen in the final solution which, although not complicating the delivery, makes the comparison between the planned and measured distributions more problematic.

The beam modelling appeared to function well and perhaps does not need a great deal of additional modification. One aspect that could be improved is the modelling of the transmission through the MLC leaves, which is currently approximated as a constant transmission value. This should be modified to be a function of the distance from the MLC leaf end. Other authors [Mohan 2000] have employed empirical transmission factors, which, in effect, combine the source projection technique used in this work with the transmission through the MLC leaves. This is an interesting approach, which could also be explored.

The MLC source projection method for  $S_c$  and field distribution works well for the fields studied. Further investigation is required to explore its suitability for use with the planning of multi-slice deliveries. For the calculation of field distributions, the projected source distribution is convolved with the Heaviside function, and the projection is treated as a symmetric projection. In reality the projection should be slightly asymmetric. The symmetric approximation seems to function quite well, but the true geometry might be taken into account in future work.

During the course of this work, physical and software limitations were encountered with regards to beam delivery. One physical limitation which was

encountered was the inability to sustain continuous arcing. Continuous arcing of the gantry, as was originally desired, was difficult to achieve since any fluctuation in the dose rate caused the gantry to stop. Once stopped it would not resume motion, thereby causing the dose delivery to cease due to a position-dose interlock. Improved software / hardware co-ordination between gantry rotation, MLC leaf position and dose delivered is required to overcome this difficulty.

One software limitation which was encountered is the limitation with regard to the number of control points that may be used in a controller file. The number of control points is directly related to the ability to deliver a DMLC field accurately [Budgell 1999]. For the DMLC deliveries, this value is 320 control points. This limits the number of allowable control points for a single rotation delivery, with twenty-four projections, to thirteen control points per projection. For research purposes, this number was doubled by splitting the delivery into two half arcs.

Modifications could be made to the dose calculator developed within the interpreted math system. An improved dose calculation scheme could improve agreement with measurements; it would aid in the final assessment with regard to full 3D dose calculation. Desired improvements include enhanced beam handling to include 3D beam modelling by means of true 3D convolution with kernel tilting and scaling. This 3D calculation would properly assess the effect of scattered radiation from adjacent slices on each other. Kernel tilting would allow the technique to more accurately handle smaller SSDs and larger field sizes without the problems [Sharpe 1993] that were encountered with the simplified code used in this work. Kernel scaling would serve as a good inhomogeneity correction algorithm, which would aid in making this a clinically implementable technique. Such an improved 3D dose calculation scheme may also be used in conjunction with the technique used in this work. Initial optimisation of incident profiles may proceed as was done. After initial optimisation, a full 3D calculation would allow for a further iterative improvement to the solution.

A better technique for the calculation of PDD would be some form of Clarkson integration. The use of the effective field size,  $f_{s_{\text{eff}}}$ , served as an approximation for change in scatter, and it sufficed for the simpler fields encountered. This technique, however, is too basic to be applied to a general calculation scheme.

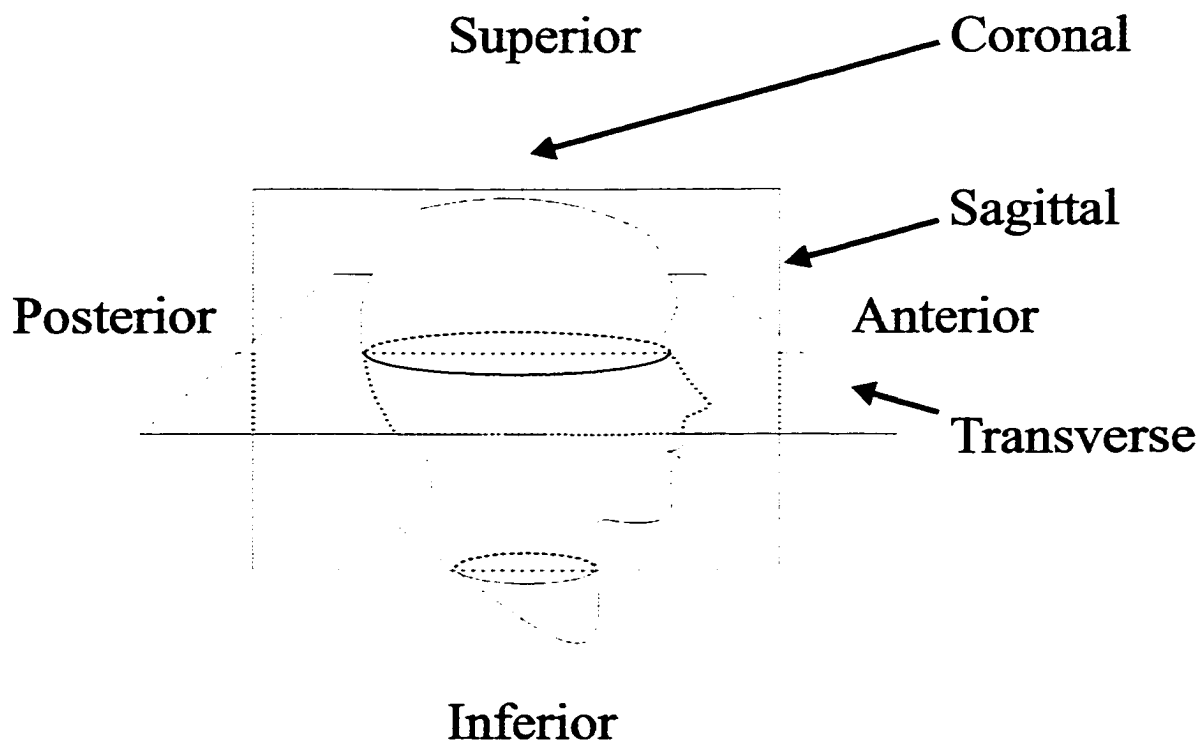
On the delivery side, a very useful extension to the technique presented here would be to introduce motion of the secondary collimating jaws as a means to reduce the amount of transmission through the MLC leaves. This would be accomplished by having the collimating jaws track the leading and lagging most leaves. This would complicate modelling by introducing a continually changing head scatter term in the calculations, but this would be calculable in a similar fashion to the penumbral and head scatter effects, which are already performed in this work.

While the dosimetry was shown to be valid, the spacing between slices was limited to 2 cm. This is a limitation of the phantom currently being used. With the finer spacing of slices available with say, a 120 leaf MLC (where the inner 80 are spaced at 0.5 cm intervals), measurements should, ideally, be repeated at a finer spacing. This brings up the practical limitation of the time required for this sort of film dosimetry for a large number of slices. The time required for this sort of dosimetry includes time required for cutting the films to fit the phantom, packing the films in the phantom and light proofing the exposed edges, as well as time for developing and scanning the films. If this is repeated for a large number of slices, the overall time for verification becomes almost prohibitive. Alternately, a 3D dosimeter, such as a polymer or Fricke gel based one, or the newer optical gel devices, may be useful. Such dosimetry is still in relative infancy, and requires a great deal of specialised expertise, and as such is beyond the scope of this thesis.

Dosimetry is required as it is used to measure delivered dose distributions and dose levels against planned distributions and levels. There was little difficulty in

achieving the desired distributions. The dose levels were not difficult to achieve for the more clinically realistic deliveries, but were off in the more complex deliveries. A further improved dose-MU calculation algorithm is evidently required for the most complex of dynamic fields.

Future directions for this work would include the moving of such techniques into the clinic, and extending the cases where it is used. One example of such an extension is rotation therapy with a small field, which may provide a good approximation to a gamma knife or linac based radiosurgery. The feasibility of multiple pass non-coplanar intensity modulated arc therapy could also be explored. As well, the combination of these techniques with variable position of the secondary collimating jaws, MLC, collimator rotation, and perhaps couch motions has yet to be explored. With such developments, the ability of producing 3D dose distributions of any shape will be more closely realised. This should yield the expected benefits of improved tumour control through dose escalation and fewer treatment complications for cancer patients.

**Chapter 7 Appendix A, Co-ordinate system of the patient**

## Chapter 8 Bibliography

AAPM "A protocol for the determination of absorbed dose from high energy photon and electron beams" *Med. Phys.* 10:741-771 (1983)

AAPM "AAPM's TG-51 protocol for clinical reference dosimetry of high energy photon and electron beams" *Med. Phys.* 25:1847-1870 (1999)

Ahnesjö A 1989 Collapsed cone convolution of radiant energy for photon dose calculation in heterogeneous media *Med. Phys.* **16** 577-92

Ahnesjö A, Knöös T and Montelius A 1992a Application of the convolution method for calculation of output factors for therapy photon beams *Med. Phys.* **19** 295-301

Ahnesjö A, Saxner M and Trepp A 1992b A pencil beam model for photon dose calculation *Med. Phys.* **19** 263-73

Ahnesjö, A. "Analytic modelling of photon scatter from flattening filters in photon therapy beams" *Med. Phys.* 21:1227-1235 (1994)

Ahnesjö, A. "Collimator scatter in photon therapy beams" *Med. Phys.* 22:267-278 (1995)

Anderson, D.W.; St. George, F. "Comparison of film and ion chamber systems for depth dose measurements for a 25 MV beam" *Phys. Med. Biol.* 24:636-638 (1979)

Attix F.H. "Introduction to Radiological Physics and Radiation Dosimetry" New York, U.S.A. John Wiley & Sons (1986)

Battista JJ Sharpe M (1992) "True three-dimensional dose computations for megavoltage x-ray therapy: a role for the superposition principle" *Australasian Physical & Engineering Sciences in Medicine*. 15(4):159-78

Biggs P "Evidence for a significant timer error on a linear accelerator: consequences for a special therapy application" *Phys. Med. Biol.* 43:3139-3143 (1998)

Bortfeld T, Burkelbach J, Boesecke R, and Schlegel W. (1990). Methods of image reconstruction from projections applied to conformal radiotherapy. *Phys. Med. Biol.* 35, 1423-1434.

Boyer A Geis P Grant W Carol M (1997) "Modulated beam conformal therapy for head and neck tumours" *Int. J. Radiat. Onc. Biol. Phys.* 39:227-236

Boyer A Xing L Ma C Curran B Hill R Kania A Bleier A "Theoretical considerations of monitor unit calculations for intensity modulated beam treatment planning" *Med. Phys.* 26(2):187-195 (1999)

Bracewell R "Two dimensional imaging" Prentice Hall (1995)

Brahme A. (1988) "Optimization of stationary and moving beam radiation therapy techniques" *Radiother. Oncol.* 12, 129-140.

Brasher P.M.A. "Alberta Cancer Registry, 1994 report" ACB, Oct. 1997

Budgell G (1999). Temporal resolution requirements for intensity modulated radiation therapy delivered by multileaf collimators. *Phys. Med. Biol.* 44, 1581-1596.

Burman C Chui C Kutcher G Leibel S Zelefsky M LoSasso T Spirou S Wu Q Yang J Stein J Mohan R Fuks Z Ling C (1997) "Planning, delivery, and quality

assurance of intensity-modulated radiotherapy using dynamic multileaf collimator: a strategy for large-scale implementation for the treatment of carcinoma of the prostate” *Int. J. Radiat. Onc. Biol. Phys.* 39(4):863-73

Carrier, R.; Cormack, D.V. “Physics of Radiation Therapy and Medical Imaging - An Historical Overview” *Physics in Canada* 51:162-168 (1995)

Cho P Marks R “Hardware sensitive optimization for intensity modulated radiotherapy” *Phys. Med. Biol.* 43, 1629-1643. (2000)

Chui, C.; Mohan, R.; Fontenla, D “Dose computations for asymmetric fields defined by independent jaws” *Med. Phys.* 15:92-95 (1988)

Convery, D.J.; Rosenbloom, M.E. “The generation of intensity modulated fields for conformal radiotherapy by dynamic collimation” *Phys. Med. Biol.* 37:1359-1374 (1992)

Cormack A. (1987). “A problem in rotation therapy with x-rays” *Int. J. Radiat. Oncol. Biol. Phys.* 13, 623-630.

Cotrutz C Kapas C Webb S “Intensity modulated Arc Therapy (IMAT) with centrally blocked rotational fields” *Phys. Med. Biol.* 45:2185-2206 (2000)

Dawkins R (1989) “The Evolution of Evolvability” in *Artificial Life*, Ed. Langton C, Redwood City, California, Addison-Wesley

De Neve W De Wagter C De Jaeger K Thienpont M Colle C Derycke S Schelfhout J (1996) “Planning and delivering high doses to targets surrounding the spinal cord at the lower neck and upper mediastinal levels: static beam-segmentation technique executed with a multileaf collimator” *Radiotherapy & Oncology.* 40(3):271-9

Derycke S Van Duyse B De Gersem W De Wagter C De Neve W (1997) "Non-coplanar beam intensity modulation allows large dose escalation in stage III lung cancer" *Radiotherapy & Oncology*. 45(3):253-61

Duzenli C MacLean B Field C (1993) "Backscatter into the beam monitor chamber: implications for dosimetry of asymmetric collimators" *Med. Phys.* 20: 363-367

Ebert M (1997) "Optimisation in radiotherapy I: defining the problem" *Australasian Physical & Engineering Sciences in Medicine*. 20(3):164-76

Elder P Coveney F Welsh A (1995) "An investigation into the comparison between different dosimetric methods of measuring profiles and depth doses for dynamic wedges on a Varian 600C linear accelerator" *Phys. Med. Biol.* 40(4):683-9

Ezzell G, "Genetic and geometric optimization of three-dimensional radiation therapy treatment planning" *Med. Phys.* 23(3), 293-305, 1996 Mar.

Field GC Battista JJ (1987) "Photon dose calculations using convolutions on real and Fourier space: assumptions and time estimates" *Proc. of Ninth Int. Conf. on Comp. in Med.*, Den Haag, Netherlands, Elsevier

Field, G.C. "Dose Calculations for Megavoltage Photon Beams Using Convolution" Master's thesis, University of Alberta (1988)

Garcia-Vicente F. Delgado JM. Peraza C. "Experimental determination of the convolution kernel for the study of the spatial response of a detector" *Med. Phys.* 25(2):202-7, 1998 Feb.

Goitein M Abrams M Rowell D Pollari H Wiles J (1983) "Multi dimensional treatment planning: II. beam's eye view, back projection, and projection through CT sections" *Int. J. Radiat. Oncol. Biol. Phys.* 9(6) 789-797

Hale, J.I.; Kerr, A.T.; Schragge, P.C. "Calibration of film for accurate megavoltage photon dosimetry" *Medical Dosimetry* 19:43-46 (1994)

Hansen V Evans P Shentall G Helyer S Yarnold J Swindell W (1997) "Dosimetric evaluation of compensation in radiotherapy of the breast: MLC intensity modulation and physical compensators" *Radiotherapy & Oncology.* 42(3):249-56

Harari P Kinsella T (1995) "Advances in radiation therapy for head and neck cancer" *Cur. Op. Onc.* 7(3):248-54

Holmes T, Mackie TR, Reckwerdt PJ, and Simpkin D. (1991). "A unified approach to the optimization of brachytherapy and external beam therapy" *Int. J. Radiat. Onc. Biol. Phys.* 20, 859-873.

Holmes T. (1993) "Tomotherapy -- A Model for the physical optimisation of external beam radiotherapy" Ph.D. thesis, University of Wisconsin-Madison

Holmes T, and Mackie TR. (1994). "A filtered backprojection dose calculation method for inverse treatment planning" *Med. Phys.* 21, 303-313.

Hounsell A. Wilkinson J (1998). "Head scatter modelling for irregular field shaping and beam intensity modulation" *Phys. Med. Biol.* 42, 1737-1749.

Hounsell A. (1998b). "Monitor chamber backscatter for intensity modulated radiation therapy using multileaf collimators" *Phys. Med. Biol.* 43, 445-454.

Hristov DE and Fallone BG. (1998) "A continuous penalty function method for inverse treatment planning" *Med. Phys.* 25, 208-223.

Huntzinger, C.J. "Dynamic wedge: a physicist's perspective" in Proceedings of the Twentieth Varian Users Meeting, Manchester (1994)

International Commission on Radiation Units and Measurements "Determination of Absorbed Dose in a Patient Irradiated by Beams of X or Gamma Rays in Radiotherapy Procedures" ICRU Report 24, Washington, D.C. (1976)

International Commission on Radiation Units and Measurements "Prescribing, Recording, and Reporting Photon Beam Therapy" ICRU Report 50, Washington, D.C. (1993)

International Electrotechnical Commission "Medical Electron Accelerators - Functional Performance Characteristics" IEC Performance Standard 976, Geneva (1989)

Jaffray, D.A.; Battista, J.J.; Fenster, A.; Munro, P. "X-ray sources of medical linear accelerators: Focal and extra-focal radiation" *Med. Phys.* 20:1417-1427 (1993)

Johns, H.E.; Cunningham, J.R. "The physics of radiology" 4th ed. Springfield, Il.: Charles C. Thomas (1983)

Jones S Boyer A "Investigation of an FFT based correlation technique for the verification of radiation treatment setup" *Med. Phys.* 18(6):1116-1125 (1991)

Kallman P, Lind BK, and Brahme A. (1992). "An algorithm for maximizing the probability of complication-free tumor control in radiation therapy" *Phys. Med. Biol.* 35, 1423-1434.

Khan, F.M. "The physics of radiation therapy" Baltimore:Williams and Wilkins (1994)

Kijewski, P.K.; Chin, L.M. ,Björngard, B.E. "Wedge-shaped dose distributions by computer-controlled collimator motion" *Med. Phys.* 5:426-429 (1978)

Klein E Low D Meigooni A Purdy J (1995) "Dosimetry and clinical implementation of dynamic wedge" *Int. J. Radiat. Onc. Biol. Phys.* 31(3):583-95

Kollar, J. "Evaluation and Modification of a Differential SAR Dose Calculation Algorithm" Master's thesis, University of Alberta (1996)

Langer M, Brown R, Morrill S, Lane R, Lee O (1996) "A generic genetic algorithm for generating beam weights" *Med. Phys.* 965-971, 23 (6)

Leavitt, D. "Dynamic beam shaping" *Medical Dosimetry* 15:47-50 (1990a)

Leavitt, D.; Martin, M.; Moeller, J.; Lee, W. "Dynamic wedge field techniques through computer controlled collimator motion and dose delivery" *Med. Phys.* 17:87-91 (1990b)

Leavitt, D. "Advances in dynamic wedge technique" in Proceedings of the Twentieth Varian Users Meeting, Manchester (1994a)

Leavitt, D. "Clinical aspects and experience with dynamic wedge" in Proceedings of the Twentieth Varian Users Meeting, Manchester (1994b)

Leavitt, D. "Ion chamber and film densitometric techniques for dynamic wedge" in Proceedings of the Twentieth Varian Users Meeting, Manchester (1994c)

Leavitt D Klein E (1997) "Dosimetry measurement tools for commissioning enhanced dynamic wedge" *Medical Dosimetry*. 22(3):171-6

Lee S Cho P Marks I Oh S (1997) "Conformal radiotherapy computation by the method of alternating projections onto convex sets" *Phys. Med. Biol.* 42, 1065-1086

Lijun M Boyer A Xing L Ma C "An Optimised leaf-setting algorithm for beam intensity modulation using dynamic multileaf collimators" *Phys. Med. Biol.* 43, 1629-1643. (1998)

Lijun M Boyer A Xing L Ma C (1999) "Synchronising dynamic multileaf collimators for producing two dimensional intensity modulated fields with minimum beam delivery time" *Int. J. Radiat. Onc. Biol. Phys.* 44: 1147-1154

Lind B Kallman P (1990). "Experimental verification of an algorithm for inverse radiation therapy planning" *Rad. Onc.* 17: 359-368

Ling C Burman C Chui C Kutcher G Leibel S LoSasso T Mohan R Bortfeld T Reinstein L Spirou S Wang X Wu Q Zelefsky M Fuks Z (1996) "Conformal radiation treatment of prostate cancer using inversely-planned intensity-modulated photon beams produced with dynamic multileaf collimation" *Int. J. Radiat. Onc. Biol. Phys.* 35(4):721-30

Liu H Mackie T McCullough E (1997). "Calculating dose and output factors for wedged photon radiotherapy fields using a convolution / superposition method" *Med. Phys.* 24, 1714-1728.

Liu Y Yin F Gao Q (1999) "Variation method for inverse treatment planning" *Med. Phys.* 26, 356-363

Loewenthal, E.; Loewinger, E.; Bar-Avraham, E.; Barnea, G. "Measurement of the source size in 6- and 18-MV radiotherapy linac" *Med. Phys.* 19:687-690 (1993)

Lutz, W.R.; Nasser, M.; Bjarngard, B.E. "Evaluation of a beam-spot camera for megavoltage x rays" *Med. Phys.* 15:614-617 (1988)

Lyman J (1985) "Complication probability as assessed from dose-volume histograms" *Rad. Res. Sup.* 8:S13-9

MacKenzie, M.A. "Production of arbitrary dose profiles using dynamic collimation" Master's thesis, University of Alberta (1996)

Mackie T Scrimger J Battista JJ (1985) "A convolution method for calculating dose for 15 MV x-rays" *Med. Phys.* 12:188-196

Mackie T Bielajew A Rogers DWO Battista JJ (1988) "Generation of photon energy deposition kernels using the EGS4 Monte Carlo code" *Phys. Med. Biol.* 33:1-20

Mackie T Holmes T Swerdloff S Reckwerdt P Deasy J Yang J Paliwal B Kinsella T (1993) "Tomotherapy: a new concept for the delivery of dynamic conformal radiotherapy" *Med. Phys.* 20(6):1709-19

Metropolis, N.; Rosenbluth, A.; Rosenbluth, M.; Teller, A.; Teller, E. *J. Chem. Phys.* 21:1087-1097 (1953)

Metcalfe P. Kron T. Elliott A. Wong T. Hoban P. "Dosimetry of 6-MV x-ray beam penumbra" *Med. Phys.* 20(5):1439-45, 1993 Sep-Oct.

Mohan R Chui C Lidofsky L (1985) "Energy and angular distributions of photons from medical linear accelerators" *Med. Phys.* 12 (5) 592-597

Mohan R Arnfield M Tong S Wu Q Siebers J (2000) "The impact of fluctuations in intensity patterns on the number of monitor units and the quality and accuracy of intensity modulated radiotherapy" *Med. Phys.* 27(6), 1226-1237.

Morrill SM, Lam KS, Lane RG, Langer M, and Rosen II. (1995). "Very fast simulated reannealing in radiation therapy treatment plan optimisation" *Int. J. Radiat. Oncol. Biol. Phys.* 31, 179-188.

Munro, P.; Rawlinson, J.A.; Fenster, A. "X-ray sources of medical linear accelerators: Focal and extra-focal radiation" *Med. Phys.* 15:517-524 (1988)

Oelfke U Bortfeld T (1999) "Inverse planning for x-ray rotation therapy: a general solution of the inverse problem" *Phys. Med. Biol.* 44, 1089-1104.

Olivera GH, Shepard D, Reckwerdt PJ, Ruchala K, Zachman J, Fitchard EE, and Mackie TR. (1998). "Maximum likelihood as a common computational framework in tomotherapy" *Phys. Med. Biol.* 43, 3277-3294.

Pigott K Dische S Saunders M (1995) "Where exactly does failure occur after radiation in head and neck cancer?" *Radiotherapy & Oncology.* 37(1):17-9

Press, W.H.; Flannery, B.P.; Teukolsky, S.A.; Vetterling, W.A. "Numerical recipes" New York, NY Cambridge Press (1989)

Reinstein L Wang X Burman C Chen Z Mohan R Kutcher G Leibel S Fuks Z (1998) "A feasibility study of automated inverse treatment planning for cancer of the prostate" *Int. J. Radiat. Onc. Biol. Phys.* 40(1):207-14

Roa W Hazuka M Sandler H Martel M Thornton A Turrisi A Urba S Wolf G Lichter A (1994) "Results of primary and adjuvant CT based 3D radiotherapy for malignant tumours of the paranasal sinuses" *Int. J. Radiat. Oncol. Biol. Phys* 28:857-865

Rosen I, Lam K, Lane R, Langer M, and Morrill S (1995) "Comparison of simulated annealing algorithms for conformal therapy treatment planning" *Int. J. Rad. Onc. Biol. Phys.* 33, 1091-1099.

Rubin, P. (Ed.) "Clinical Oncology" Philadelphia, W.B. Saunders Co. (1993)

Schultheiss T Orton C Peck R (1983) "Models in radiotherapy: volume effects" *Med. Phys.* 10:410-415

Sharpe M, Battista JJ (1993). "Dose calculation using a convolution and superposition principles: the orientation of dose spread kernels in divergent x-ray beams" *Med. Phys.* 20, 1685-94.

Sharpe M, Jaffray D Battista JJ Munro P (1995) "Extra-focal radiation: a unified approach to the prediction of beam penumbra and output factors for megavoltage X-ray beams" *Med. Phys.* 22(12): 2065-2074

Sherouse G Mosher C Novins K Rosenman J Chaney E (1987) "Virtual Simulation: concept and implementation" Proc. of Ninth Int. Conf. on Comp. in Med., Den Haag, Netherlands, Elsevier

Sherouse G Bourland J Reynolds K McMurry H Mitchell T Chaney E (1990) "Virtual Simulation in the Clinical Setting: Some Practical Considerations" *Int. J. Rad. Onc. Biol. Phys.* 19:1059-1065

Shiu A. Mellenberg D (eds.) "General practice of radiation oncology physics in the 21<sup>st</sup> century" Medical Physics Monograph No. 26, Medical Physics Publishing, Madison WI, 2000

Sibata CH. Mota HC. Beddar AS. Higgins PD. Shin KH. "Influence of detector size in photon beam profile measurements" *Phys. Med. Biol.* 36(5):621-31, 1991 May.

Sloboda R (1992) "Optimization of brachytherapy dose distributions by simulated annealing" *Med. Phys.* 19(4):955-64

Smitt M Li S Shostak C Chang W Boyer A (1997) "Breast-conserving radiation therapy: potential of inverse planning with intensity modulation" *Radiology.* 203(3):871-6

Soderstrom S. Gustafsson A. Brahme A. "The clinical value of different treatment objectives and degrees of freedom in radiation therapy optimization." *Rad. Onc.* 29(2): 148-63, 1993 Nov.

Spirou, S.V.; Chui, C.S. "Generation of arbitrary intensity profiles by dynamic jaws or multileaf collimators" *Med. Phys.* 21:1031-1041 (1994)

Svensson, R; Källman, P; Brahme, A "An analytical solution for the dynamic control of multileaf collimators " *Phys. Med. Biol.* 39:37-61 (1994)

Thames H D Schultheiss T E Hendry J H Tucker S L Dubray B M "Can modest escalations of dose be detected as increased tumour control" *Int. J. Radiat. Oncol. Biol. Phys* 1992 (22) 241-246

Tsai J Wazer D Ling M Wu J Fagundes M Dipetrillo T Kramer B Koistinen M Engler M (1999a) "A non-invasive immobilization system and related quality assurance for

dynamic intensity modulated radiation therapy of intracranial and head and neck disease," *Int. J. Radiat. Oncol. Biol. Phys* 40 (5) 1213-1230

Tsai J Engler M Ling M Wu J Kramer B Dipetrillo T Wazer D (1999b) "A non-invasive immobilization system and related quality assurance for dynamic intensity modulated radiation therapy of intracranial and head and neck disease, " *Int. J. Radiat. Oncol. Biol. Phys* 43 (2) 455-467

Urtasun, R.C. "Does improved depth dose characteristics and treatment planning correlate with a gain in therapeutic results?" *Int. J. Radiat. Oncol. Biol. Phys.* 22, 235-239 (1992)

van Santvoort J Heijmen B (1996) "Dynamic multileaf collimation without 'tongue-and-groove' underdosage effects" *Physics in Medicine & Biology.* 41(10):2091-105

Verellen D Linthout N van den Berge D Bel A Storme G (1997 ) "Initial experience with intensity-modulated conformal radiation therapy for treatment of the head and neck region" *Int. J. Radiat. Onc. Biol. Phys.* 39(1):99-114

Waggener, R.G. (Ed.) "Handbook of medical physics, vol. 1" Boca Raton, Florida CRC Press (1982)

Wang X Spirou S LoSasso T Chui C Mohan R (1996) "Dosimetric verification of an intensity modulated treatment" *Med. Phys.* 23:317-327

Webb S. (1991). "Optimization by simulated annealing of three-dimensional conformal treatment planning for radiation fields defined by multileaf collimator" *Phys. Med. Biol.* 36, 1201-1226.

Webb S. (1997). "The Physics of Conformal Radiotherapy- Advances in Technology"

Williamson, J.; Khan, F.M.; Sharma, S.C. "Film dosimetry of megavoltage beams: a practical method of isodensity to isodose curve conversion" *Med. Phys.* 8:94-98 (1981)

Xing L Chen Y Luxton G Li J Boyer A "Monitor unit calculations for an intensity modulated photon field by a simple scatter-summation algorithm" *Phys. Med. Biol.* 45: - (2000)

Yu, C. "Intensity-modulated arc therapy with dynamic multileaf collimation: an alternative to tomotherapy" *Phys. Med. Biol.* 40:1435-1449 (1995)

Yu M Sloboda R (1996) "Analytic representation of head scatter factors for shaped photon beams using a two-component x-ray source model" *Med. Phys*23:973-984

Zaider M Amols H "A little to a lot or lot to a little: is NTCP always minimised in multiport therapy" *Int. J. Radiat. Oncol. Biol. Phys.* 41, 945-950 (1998)